



# **Joint symposium of Misasa 2019 & Core-Mantle Coevolution**

**Origin, Evolution & Dynamics of the Earth &  
Planetary Interiors**

**Brancart Misasa Room 401 & 403**

**18th to 21st March**

# Program

## 18th March

9:30-9:35	X. Xue (IPM, director)	Opening remarks from IPM
9:35-9:40	T. Tsuchiya (CMC leader)	Opening remarks from Core-Mantle Coevolution

### Session 1: Geoneutrino

Chairman: H. Kagi

9:40-10:20 O. Šrámek (Charles Univ.) Invited talk

Geoneutrinos and radiogenic power in the Earth: recent advances and future prospects

10:20-10:40 W.F. McDonough (Tohoku Univ.)

W.F. McDonough\*, B. Roskovec, O. Šrámek

In search of recycled continental crust in the Mantle Transition Zone using geoneutrino measurements

10:40-11:00 H. Tanaka (ERI, U. Tokyo)

Restriction of the Core-Mantle Chemical Composition with Neutrino Observations

### Coffee break

Chairman: J.-F. Lin

11:20-11:40 M. Yamano (ERI, U. Tokyo)

M. Yamano\*, H. Hamamoto, A. Tanaka, S. Goto, T. Matsumoto

Re-evaluation of surface heat flow data in Japan for better estimation of the temperature distribution in the crust.

11:40-12:00 H. Watanabe (Tohoku Univ.)

Development of New Technology for Geo-neutrino Directional Measurement

### Lunch and Poster

### Session 2: Geochemistry and Petrology

Chairman: E. Takahashi

14:00-14:40 M.J. Walter (Geophys. Lab. Carnegie Inst.) Invited talk

M. Walter\*, J. Drewitt, H. Zhang, S. McMahon, D. Edwards, B. Heinen, O. Lord, S. Anzellini, A. Kleppe

The fate of carbonate in oceanic crust subducted into earth's deep mantle

14:40-15:00 S. Aoyama (Niigata Univ.)

S. Aoyama\*, T. Oneyama, W. Ouchi, Y. Ueno, M. Satish-Kumar

Multiple sulfur isotopes constraints on the origin of sulfide sulfur in Archean granitoids from Dharwar craton, Southern India

15:00-15:20 M. Satish-Kumar (Niigata Univ.)

M. Satish-Kumar\*, S. Aoyama

Recent developments in stable isotope measurements on high-pressure high-temperature experimental run products and natural samples

15:20-15:40 K. Fukuyama (Univ. Tokyo)

K. Fukuyama\*, H. Kagi, T. Inoue, Y. Sano, T. Shinmei, S. Kakizawa, N. Takahata, S. Hishita

Investigation of nitrogen incorporation into stishovite using implanted sample and outlook on deep nitrogen cycle

Coffee break

Chairman: R. Nomura

16:00-16:20 S. Tateno (ELSI, Tokyo Tech.)

S. Tateno\*, H. Ozawa, K. Hirose, T. Suzuki

Fe<sub>2</sub>S: the most iron-rich Fe-S compound at pressures of the inner core

16:20-16:40 K. Suzuki (JAMSTEC)

A. Takamasa, K. Suzuki\*, Y. Fukami, T. Iizuka

High precision tungsten isotope of ocean island and LIPS basalts from deep mantle

16:40-17:00 H. Sumino (Univ. Tokyo)

H. Sumino\*, T. Tanaka, H. Kuwahara, S. Kishi, R. Nomura, K. Mibe, C. Jackson, S. Tateno, H. Kagi

Noble gas partition between metal-silicate melts

17:00-17:20 T. Tsuchiya (GRC, Ehime Univ.)

T. Tsuchiya\*, A. Ohba, Z. Xiong

Ab Initio Applications to the Element Partitioning between Core and Mantle

## 19th March

Chairman: T. Okuchi (IPM)

9:00-9:40 T. Nakagawa (Univ. Hong Kong) Invited talk

On theoretical and numerical modeling of the core-mantle thermal-chemical coupling: Review and perspective view

Session 3: water

9:40-10:00 X. Xue (IPM, Okayama Univ.)

Hydrogen incorporation mechanisms in nominally anhydrous mantle minerals: NMR spectroscopy and first-principles calculation

10:00-10:20 N. Prejzav (IPM, Okayama Univ.)

N. Prejzav\*, T. Okuchi, N. Tomioka, X. Wang, C. Hoffmann

Probing hydrogen by single-crystal neutron diffraction in deep mantle hydrous minerals

Coffee break

Chairman: A. Suzuki

10:40-11:00 J. Tsuchiya (GRC, Ehime Univ.)

J. Tsuchiya\*, K. Umemoto

First principles determination of the dissociation boundary of phase H ( $\text{MgSiO}_4\text{H}_2$ ) and possible existence of ice VII at lower mantle conditions

11:00-11:20 H. Fei (BGI)

H. Fei\*, T. Katsura

High water solubility of ringwoodite at mantle transition zone temperature

11:20-11:40 S. Yamashita (IPM, Okayama Univ.)

In situ vibrational spectroscopy of the dehydration of talc in the system  $\text{MgO-SiO}_2\text{-H}_2\text{O}$

11:40-12:00 T. Ohashi (Tohoku Univ.)

T. Ohashi\*, T. Sakamaki, K. Funakoshi, M. Muranushi, C. Shito, Y. Shibasaki, A. Suzuki

Structures of hydrous sodium silicate melts under high pressure and high temperature

Lunch and Poster

Headquarter business meeting (Room 503 Juraku)

Session 4: Transport properties

Chairman: K. Kawai

14:00-14:40 A.R. Thomson (UCL) Invited talk

A.R. Thomson\*, S.A. Hunt, J. Van Driel, J.P. Brodholt, D.P. Dobson

Simultaneous deformation of Calcium Perovskite and Pyrope

14:40-15:00 Y. Nishihara (GRC, Ehime Univ.)

Y. Nishihara\*, S. Doi, D. Yamazaki, N. Tsujino, T. Yoshino, T. Kubo, M. Imamura

D111-type apparatus for high-pressure deformation experiments and its application to a rheological study of hcp-iron

15:00-15:20 N. Tsujino (IPM, Okayama Univ.)

N. Tsujino\*, D. Yamazaki, Y. Nishihara

Creep strength of bridgmanite

15:20-15:40 S. Azuma (ELSI, Tokyo Tech.)

S. Azuma\*, R. Nomura, K. Uesugi, Y. Nishihara, S. Doi, T. Arimoto, T. Irifune

Update of the rotational diamond anvil cell and deformation microstructures of lower mantle materials

Coffee break

Chairman: Y. Nishihara

16:00-16:20 S. Ritterbex (GRC, Ehime Univ.)

S. Ritterbex\*, T. Tsuchiya

Ab-Initio Investigation of Iron Self-Diffusion: Implications for the Plasticity of Earth's Inner Core

16:20-16:40 K. Kawai (Univ. Tokyo)

K. Kawai\*, A. Borgeaud, Y. Suzuki

Imaging subducted slabs in the mantle from inversion of seismic waveforms

16:40-17:00 H. Gomi (IPM, Okayama Univ.)

H. Gomi\*, T. Yoshino

Electrical resistivity and thermal conductivity of fcc Fe: Implications for the Mercury's core

17:00-17:20 K. Miyanishi (Osaka Univ.)

K. Miyanishi\*, N. Ozaki, S. Ohmura, M. Harmand, A. Krygier, T. Nishikawa, Y. Umeda, K. Shigemori, Y. Sakawa, T.

Sano, R. Kodama

Study on transport properties of liquid iron and iron alloy under high temperature and high pressure using the laser shock technique

17:40-18:00 Signing ceremony

Agreement of cooperation between the Geophysical Laboratory Carnegie Institution for Science and

Institute for Planetary Materials, Okayama University

18:30-20:30 Banquet (entry required)

## 20th March

Session 5: Seismic observation and properties

Chairman: K. Ohta

9:00-9:40 D. Mainprice (Univ. Montpellier) Invited talk

Deformation, crystal preferred orientations, and seismic anisotropy in the Earth's D" layer

9:40-10:00 S. Tanaka (JAMSTEC)

Azimuthal anisotropy in the lowermost mantle beneath Philippine from ScS-S travel times

10:00-10:20 N. Takeuchi (ERI, Univ. Tokyo)

S.K. Roy, N. Takeuchi\*, D. Srinagesh, M. Ravi Kumar, H. Kawakatsu

Topography of the western Pacific LLSVP constrained by S wave multipathing

Coffee break

Chairman: H. Terasaki

10:40-11:00 K. Ohta (Tokyo Tech.)

K. Ohta\*, A. Hasegawa, T. Yagi, Y. Okuda, K. Onga, K. Hirose, Y. Ohishi

Measurements of high pressure-temperature thermal conductivity of the Earth's lower mantle minerals in a laser-heated diamond anvil cell

11:00-11:20 H. Terasaki (Osaka Univ.)

H. Terasaki\*, I. Yamada, A. Kamiya, R. Tsuruoka, T. Kondo, Y. Higo, A. Machida

Sound velocity of liquid Fe-Ni-S-Si under pressure

11:20-11:40 Y. Nakajima (Kumamoto Univ.)

Y. Nakajima\*, D. Kinoshita, Y. Kuwayama, K. Hirose, A. Iwamoto, S. Tateno, D. Ishikawa, A.Q.R. Baron

Sound velocity of liquid Fe-P alloy under high pressure based on inelastic X-ray scattering measurements

11:40-12:00 T. Irifune (GRC, Ehime Univ.)

Sound velocities of CaSiO<sub>3</sub> perovskite ("breyite") and some implications for chemical compositions around the 660 km discontinuity.

Lunch and Poster

Misasa joint-use research Session 1

Chairman: T. Katsura

14:00-14:40 J.F. Lin (Univ. Texas) Invited talk

Internally-consistent multiple constraints on the mineralogy and seismology of Earth's lower mantle

14:40-15:00 T. Okuchi (IPM)

Nanoscale texture and transformation timescale of dense  $\text{Mg}_2\text{SiO}_4$  polymorphs in shocked meteorites: comparison between natural occurrences by high-resolution TEM and experimental results by fast XFEL diffraction

15:00-15:20 M. Kanzaki (IPM)

Low-frequency micro-Raman spectroscopy: applications to mineral sciences

Coffee break

Chairman: D. Yamazaki

15:40-16:00 B. Zhang (CAS)

B. Zhang\*, T. Yoshino, C. Zhao

The effect of water on Fe-Mg interdiffusion rates in ringwoodite and implications for the electrical conductivity in the mantle transition zone

16:00-16:20 N. Chertkova (GRC, Ehime Univ.)

N. Chertkova\*, S. Yamashita, H. Ohfujii, T. Irifune, H. Kadobayashi, Y. Yamamoto

Probing basalt- $5.75\text{H}_2\text{O}$ - $\text{CH}_4$  system by *in situ* vibrational spectroscopy

16:20-16:40 Y. Zhang (IPM)

Y. Zhang\*, T. Yoshino, A. Yoneda, M. Osako

Effect of iron content on thermal conductivity of olivine with implications for cooling history of rocky planets

Session: Development of high-pressure technique

16:40-17:00 I.C. Ezenwa (IPM, Okayama Univ.)

I. C. Ezenwa\*, T. Yoshino

Measurement of T -dependent electrical resistivity of solid and liquid Fe and Pt at fixed P

## 21st March

Misasa joint-use Session 2

Chairman: T. Yoshino

9:00-9:40 E. Takahashi (GIG) Invited talk

E. Takahashi\*, S. Gao, J. Wang, L. Li

Melting process in Hawaii plume: Report from large volume multi-anvil laboratory in Guangzhou Institute of Geochemistry

9:40-10:00 N. Tsuchiya (Iwate Univ.)

N. Tsuchiya\*, D. Yamazaki

Silicic melt formed by a partial melting experiment of mantle peridotite reacted with slab melt

10:00-10:20 Y. Nakamura (AIST)

Y. Nakamura\*, T. Yoshino, M. Satish-Kumar

Pressure dependence of graphitization: Implications for rapid recrystallization of carbonaceous material in Earth's crust

Coffee Break

Chairman: H. Gomi

10:40-11:00 K. Fujita (Osaka Univ.)

Y. Haraguchi, T. Yoshino, S. Yamashita, M. Nakamoto, M. Suzuki, K. Fujita\*, T. Tanaka

Electrical Conductivity Measurement of rhyolite and andesite glasses

11:00-11:20 Y. Mori (Okayama Univ. Sci.)

Y. Mori\*, N. Nakano, T. Yoshino

The Measurement of Seebeck coefficient under Pressure using Six-axis Multi-Anvil Press

11:20-11:40 C. Zhao (IPM)

Redox kinetics of olivine revealed by diffusion profile of oxygen fugacity and its implication to the redox evolution of the uppermost mantle

11:40-12:00 T. Yoshino (IPM)

T. Yoshino\*, W. Sun, C. Zhao, N. Sakamoto, H. Yurimoto

Electrical conductivity of hydrous olivine: revisited by various approaches

Lunch and Poster

Misasa joint-use Session 3

Chairman: N. Tsujino

14:00-14:40 T. Katsura (BGI, Univ. Bayreuth) Invited talk

T. Katsura\*, H.-F. Fei, D. Druzhbin

H<sub>2</sub>O-enhanced ionic conductivity of olivine

14:40-15:00 L. Xie (BGI, Univ. Bayreuth)

L. Xie\*, K. Nishida, T. Ishi, C. Artem, B. Dimitry, T. Katsura

Simultaneously generation of ultra-high pressure and high temperature by combining boron-doped diamond heater and sintered diamond anvils.

15:00-15:20 D. Yamazaki (IPM)

High pressure generation in the Kawai-type multianvil apparatus

15:20-15:30 X. Xue (IPM, director) Closing remarks

16:30-17:30 A. Yoneda (IPM)

The last lecture (in Japanese with English slides)

## Poster

### A01

1. A. Okamoto\*, T. Hiraga

Viscosity of Lower Mantle Estimated from the Common Diffusivity of Creep and Grain Growth

2. T. Kubo\*, M. Imamura

Grain growth textures and kinetics in pyrolytic and basaltic materials under lower mantle conditions

3. R. Sinmyo

Technical development toward understanding the melting temperature of the materials at high pressure using ultra-fast spectroradiometry

4. T. Sakai

Pressure scales at multi-megabar pressure

5. M. Nishi\*, K. Yamamoto, Y. Zhou, T. Irifune

Polycrystalline diamond sintered from ultradispersed nanodiamonds

6. Y Higo\*, T Irifune

Development of ultrasonic measurement technique toward whole lower mantle conditions

7. T. Inoue\*, M. Noda, S. Kakizawa, T. Kuribayashi, A. Sano, T. Hattori

Importance of various Al substitutions in bridgmanite

8. A. Suzuki

Stability field of hydrous aluminosilicates from the mantle transition zone to the shallow part of the lower mantle

9. H Kagi\*, T. Kubo, A. Shinozaki, T. Okada, H. Ohfuji, A. Nakao

Reaction between forsterite and nitrogen fluid at high pressure and high temperature

### A02

10. R. Iizuka-Oku\*, H. Gotou, K. Fukuyama, H. Kagi

Behavior of light elements in the early stage of Earth's evolution: In-situ high-pressure and temperature

11. T. Kuribayashi\*, Y. Zhou, T. Irifune, H. Ohfuji

Structural study on new high-pressure forms of  $Al_2SiO_5$

12. S. Tateno\*, T. Komabayashi, K. Hirose

Static compression of B2 KCl to 230 GPa and its  $P$ - $V$ - $T$  equation of state

13. S. Itoh

Quantitative analysis from stigmatic isotope imaging of SIMS

14. T. Kogiso\*, N. Akizawa

Controlling factor of whole-rock PGE concentrations in mantle peridotite

15. F. Maeda, Y. Horioka, S. Kamada\*, S. Aoyama, S. Ozawa, M. Satish-Kumar, A. Suzuki

Sulfur and carbon isotope fractionation under mantle conditions

16. N.M. Kondo\*, T. Kogiso

Major element composition of the Hadean crust: constraints from Sm-Nd isotope systematics and high-pressure melting experiments

A03

17. S. Tanaka\*, W. Siripunvaraporn, S. Boonchaisuk, S. Noisagool, K. Kawai, Y. Suzuki, T. Kim, Y. Ishihara, H.

Kawakatsu, N. Takeuchi, K. Miyagawa, R. Iritani

Completion of the seismic observation with Thai Seismic Array (TSAR)

18. S Kaneshima

S-to-P scattering in the lower mantle near subduction zones

19. M. Matsushima

Core-mantle interaction inferred from a core surface flow model

20. Y. Yamamoto\*, H. Fukami, W. Taniguchi, P.C. Lippert

Variation of the intensity of the paleomagnetic field during 38-50 Ma deduced from the marine sediments recovered from the northwest Atlantic

21. M. Obayashi\*, T. Miyoshi, J. Yoshimitsu

Toward adjoint tomography of the large low seismic velocity provinces beneath the western Pacific Ocean

22. G. Hao

Using S-P wave search the depth of mantle 660-discontinuity beneath Kuril Region where subduction slab do not exist

23. R. Iritani\*, H. Kawakatsu, N. Takeuchi

Sharpness of the hemispherical boundary in the inner core beneath the northern Pacific

24. K. Minami, K. Ueki\*, T. Iizuka, S. Enomoto, H.K.M. Tanaka

Sample-scale geochemical variation of the Inada granitic body, Ibaraki, Japan -toward the reduction of geoneutrino flux estimation errors-

A04

25. H. Dekura\*, T. Tsuchiya

*Ab initio* anharmonic lattice dynamics for Fe-bearing lower mantle minerals

Misasa

26. T. Moriguti\*, A. Yoneda, E. Ito  
Melting phase equilibrium relations in MgSiO<sub>3</sub>-SiO<sub>2</sub> system under high pressures
27. M. Sakurai\*, N. Tsujino  
Pressure effect on IR spectra of anhydrous minerals  
neutron diffraction measurements on iron-silicate-water-sulfur system
28. L. Guan\*, D. Yamazaki  
Lattice preferred orientation of akimotoite and mid-mantle anisotropy in subduction zones
29. H. Yusa\*, N. Hirao, Y. Mori, Y. Ohishi  
Latest remodeling of multi-axis DAC system for radial XRD experiments
30. Y. Yachi\*, T. Kunihiro, E. Nakamura  
DREAM & Its applications: Software for Management of Samples and Data
31. M. Osako\*, A. Yoneda  
Measurement of thermal conductivity and thermal diffusivity for mantle minerals by the pulse heating method
32. A. Yoneda\*, S. Kobayashi, S. Kamada  
Low-frequency micro-Raman spectroscopy and its application to mineral sciences
33. N. Noguchi\*, Y. Fujii, T. Saitoh, H. Okamura  
High-pressure synthesis of doped black phosphorous
34. R. Wang\*, T. Yoshino  
Electrical conductivity of diasporite, δAlOOH and εFeOOH
35. C. Liu\*, T. Yoshino<sup>1</sup>  
Intrinsic attenuation factor Q of partially molten Fe-S-O system

## Geoneutrinos and radiogenic power in the Earth: recent advances and future prospects

O Šrámek<sup>1\*</sup> <sup>1</sup>Department of Geophysics, Charles University, Prague, Czech Republic.

\*email:ondrej.sramek@gmail.com

**Introduction:** The Earth's engine is driven by unknown proportions of primordial and radiogenic energy, with the former being left over after accretion and core formation, while the latter is produced in radioactive decay of K, Th & U. Competing models of Earth's composition reveal an order of magnitude uncertainty in the amount of radiogenic power driving mantle convection and plate tectonics. This gross level of uncertainty weakens our models of the composition and dynamics of the Earth, including its thermal evolution, style and planform of mantle convection, and energetics of the core.

Measurements of the flux of geoneutrinos, electron antineutrinos emitted inside the Earth during  $\beta^-$  decays, reveal the amount of U and Th in the Earth and define its amount of radiogenic power. Flux measurements at large underground neutrino detectors confronted with geological predictions of geoneutrino emission from the Earth's crust constrain the radiogenic power deeper in the Earth.

**Earth's energy budget:** The secular loss of heat from the deep Earth has been reasonably well constrained at  $46 \pm 3$  TW [1] from careful analyses of land and sea-floor heat flow measurements. Much uncertainty remains in attempts to separate the total surface heat loss into the two major contributions, the secular cooling and ongoing differentiation (inner core growth) of the planet on one hand, and the power of radiogenic heat sources (radionuclides of U, Th, K) on the other [1]. Our current understanding offers a rather accurate estimate of radiogenic heat production in the Earth's crust of  $7 \pm 1$  TW [2] and argues for negligible to very limited radiogenic power in the Earth's core [3]. The uncertainty of a factor of  $\sim 3$  in geochemical and cosmochemical estimates of Silicate Earth's abundances of K, Th & U, translates, after subtracting the crustal component, into an order of magnitude uncertainty in radiogenic power available in the convecting mantle [4].

**Measuring geoneutrino flux:** The highest energy antineutrinos, emitted in  $\beta^-$  decays of natural  $^{232}\text{Th}$  and  $^{238}\text{U}$  decay chains, can be detected via inverse beta decay reaction with energy threshold of 1.8 MeV, in large underground liquid scintillator neutrino experiments. Detectors in Japan (KamLAND) [5] and Italy (Borexino) [6] have measured geoneutrino flux and have begun to put limits on Earth models of U & Th abundances. A simple combined analysis of KamLAND and Borexino results indicates a mantle geoneutrino signal of  $8.8 \pm 6.4$  TNU (Terrestrial Neutrino Units)

which translates to radiogenic power of  $21 \pm 10$  TW in the Silicate Earth (Fig.1) [7].

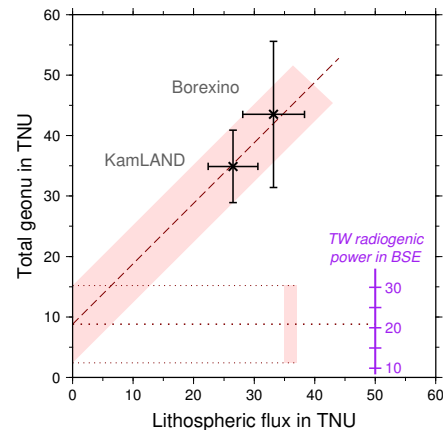


**Figure 1** Measured geoneutrino total flux (vertical axis) vs. predicted lithospheric flux (horizontal axis). The y-intercept of slope 1 line fit (red dashed) indicates the mantle signal, and translates into the Silicate Earth's radiogenic power (purple).

Three more detectors are expected to have measured geoneutrinos by year  $\sim 2020$ : SNO+ in Canada, and JUNO and Jinping in China. The combination of data from all five experiments has the potential to provide much tighter limits on radiogenic power in the Earth's mantle [8].

**Synergy between neutrino physics and geoscience:** Extracting the mantle signal from the measurement of total Earth's geoneutrino emission requires an independent accurate prediction of crustal signal which must come from geoscience. Ongoing dedicated efforts are invested in improving both the global and the regional (near detectors) models of crustal structure and composition, hence prediction of crustal geoneutrino emission.

Measuring geoneutrinos at oceanic locations, distant from nuclear reactors and continental crust, would best reveal the mantle geoneutrino flux. Performing a coarse scale geoneutrino tomography could even test hypotheses of large heterogeneous structures enriched in heat-producing elements located in the shallow [9] or in the deep mantle [4].

**References:** [1] Jaupart, C. et al., *Treatise Geophys.*, vol. 7, ch. 6 (2015). [2] Huang, Y. et al., *Geochem. Geophys. Geosyst.*, **14**, 2003 (2013). [3] McDonough, W.F., *Treatise Geochem.*, vol. 3, ch. 16 (2015). [4] Šrámek, O. et al., *Earth. Planet. Sci. Lett.*, (2013). [5] Gando, A. et al., *Phys. Rev. D*, **88**, 033001 (2013). [6] Agostini, M. et al., *Phys. Rev. D*, **92**, 031101 (2015). [7] <https://tinyurl.com/y2hj7psv> [8] Šrámek, O. et al., *Sci.Rep.*, **6**, 33034 (2016). [9] Roskovec, B. et al. arXiv:1810.10914.

## In search of recycled continental crust in the Mantle Transition Zone using geoneutrino measurements

William F. McDonough<sup>1</sup>, Bedřich Roskovec<sup>2</sup>, and Ondřej Šrámek<sup>3</sup> <sup>1</sup>Department of Earth Sciences and Research Center of Neutrino Sciences, Tohoku University, 6-3, Aramaki Aza Aoba, Aobaku, Sendai, Miyagi, 980-8578, JAPAN [wfm@tohoku.ac.jp](mailto:wfm@tohoku.ac.jp) <sup>3</sup>Instituto de Física, Pontificia Universidad Católica de Chile, Santiago, Chile <sup>4</sup>Department of Geophysics, Faculty of Mathematics and Physics, Charles University, V Holešovičkách 2, 18000 Praha 8, Czech Republic

Plate tectonics provides the framework for understanding the modern evolution of the crust and mantle system, with subduction zones linking these two major domains of the silicate Earth. Sediment recycling into the mantle at subduction zones is well established, although unknowns (e.g., past and present-day rates, amounts, depth of recycling, etc) remain significant. The present day subduction zone settings include ocean-ocean, ocean-continent, and continent-continent collisions and each of these likely have differing degrees of efficiencies of sediment recycling, as evidence by distinct differences in the remnants of meta-sediments exposed in fossil forearc regions of different collision zones. The retrieved metamorphic record of ocean-ocean and ocean-continent collision zones documents meta-sediments experiencing high-grade (granulite to eclogite facies) metamorphism. In contrast, continent-continent collisions return meta-sediments having experienced ultra high-grade (up to diamond facies) metamorphism. What is not known is the effectiveness of deep sediment recycling, past the magmatic zone, in each of these three different convergent margins.

Models that envisage successful subduction channel transport of upper crustal materials below 300 km depth, past a critical phase transition in buoyant crustal lithologies, are capable of accumulating and assembling these materials into so-called

“second continents” that are gravitationally stabilized at the base of the Transition Zone, at some 600 to 700 km depth [Kawai et al., 2013]. Global scale, Pacific-type subduction (ocean-ocean and ocean-continent convergence), which lead to super continent assembly, were hypothesized to produce second continents that scale to about the size of Australia, with a maximum potential of continental upper crustal concentration levels of radiogenic power. Seismological techniques are incapable of imaging these second continents because of their negligible difference in seismic wave velocities with the surrounding mantle. We can image the geoneutrino flux linked to the radioactive decays in such hypothesized continental lithologies with land and/or ocean-based detectors. We present predictions of the geoneutrino signal for these continental lithologies, assuming different scaled models and show that the combination of the KamLAND-JUNO-Jinping neutrino experiments are strategically positioned to discover or constrain a predicted second continent beneath eastern China. The power emissions from such second continents were proposed to be drivers of super continental cycles. Thus, testing models for the existence of continental lithologies in the Mantle Transition Zone will place constraints on mantle and plate dynamics when using land and ocean-based geoneutrino detectors deployed at strategic locations.

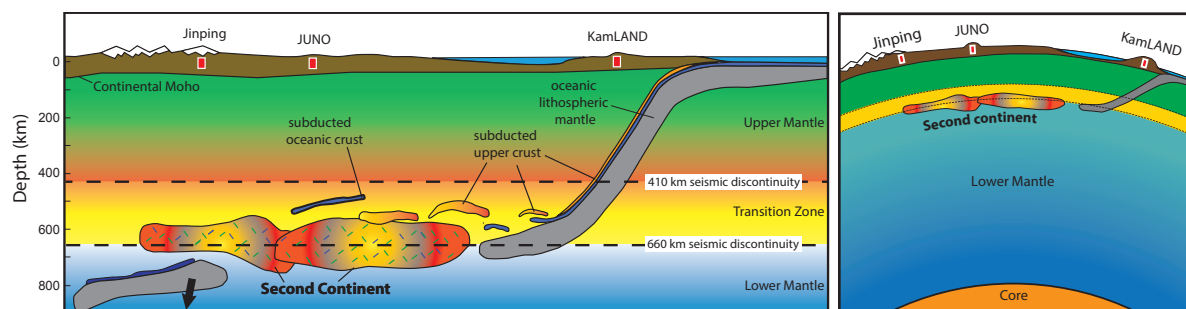


Figure 1: Left panel shows cartoon illustration of a second continent that formed under eastern China due to Pacific-type subduction occurring along the western margin of the Pacific basin. Picture is an adaptation of Fig. 5 in Kawai et al., (2013). The proximity of 3 geoneutrino experiments to this proposed second continent are shown as being underground in Japan (KamLAND) and China (JUNO and Jinping). These 3 detectors see approximately the same mantle volume and similar global crust, see right panel, which results in a major reduction in the predicted uncertainties. Local differences in the geoneutrino signals for each of these detectors are due to geological differences in the nearby lithosphere (closest 500 km) surrounding the detector; this region contributes approximately half of the detected signal.

Kawai, K., S. Yamamoto, T. Tsuchiya, and S. Maruyama (2013) The second continent: Existence of granitic continental materials around the bottom of the mantle transition zone. *Geoscience Frontiers*, 4(1), 1-6.

## Low-frequency micro-Raman spectroscopy and its application to mineral sciences

H.K.M. Tanaka\* <sup>1</sup>Earthquake Research Institute, University of Tokyo, Bunkyo, Tokyo 113-0032, Japan.

**Introduction:** Neutrinos originated in decay of radionuclide inside the Earth (geoneutrinos) were detected by the Japanese group for the first time, and the detection accuracy has been improved by purifying the liquid scintillator of the detector and reduction of the nuclear reactor background. Since the observational data at a surface of the Earth can be converted to the radiogenic power, i.e., the heat production density, this new information provides us a new vision to understand the core-mantle dynamics including the heat source of the mantle convection. The objective of this research is to create a new academic region that transversely support particle physicists and earth scientists by developing advanced neutrino-based earth observation technologies.

The geoneutrino flux in the vicinity of KamLAND detector was modeled in 2005. However, this modeling has been done by utilizing the globally averaged crustal structures and radioactive isotope concentrations. The new modelling method that incorporates the local information is underdevelopment in order to apply it to the KamLAND data. Furthermore, proof-of-principle studies are currently conducted to realize the idea of directional-sensitive detection of geoneutrinos in the future. The fundamental studies are ongoing to clarify the technological requirements for the actual implementation of this technique.

**Modeling:** The rock chemical composition database and underground thermal structure database have been generated and the probability density function was evaluated based on these (Figure 1). For the rock chemical composition database, 96 published papers and Geological Survey Japan database (including 10862 rock samples) have been used [1]. In addition, 215 rock samples have been collected from Oki, Shimane Prefecture, Megata, Akita Prefecture, and Takashima, Saga Prefecture and analyzed to study the chemical composition of the lower crust [1]. The seismic database [2] was utilized to compare the generated database with the seismic tomography results in order to model the underground lithology. By expressing the lithology at a deep underground in a form of the probability density function, and by developing all of the modules that are required to calculate the neutrino flux, the objective geoneutrino flux based on the probability model has been derived for the first time [1]. It is anticipated that the objective radiogenic heat production will be derived by subtracting the geoneutrino flux

observed with the KamLAND by the neutrino flux modeled by this objective geoneutrino flux.

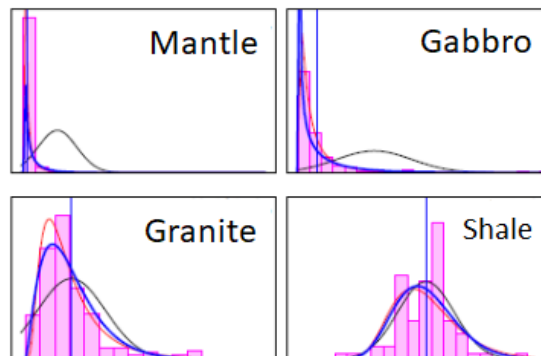


**Figure 1** Uranium concentrations in different rocks (Mantle, Gabbro, Granite and Shale) fitted by different distribution functions (gamma, log-normal and normal).

**Developments of the directionally sensitive geoneutrino detector:** A small-sized test detector was developed for demonstration of this concept. The post signal generated by geoneutrino was simulated by using a neutron beam, and this signal was successfully imaged by this test detector (Figure 2). It is anticipated that 3 dimensional structures of pseudo-geoneutrino signals will be imaged by the further developments of the data analysis algorithm and data taking electronics for detecting events with lower energies.

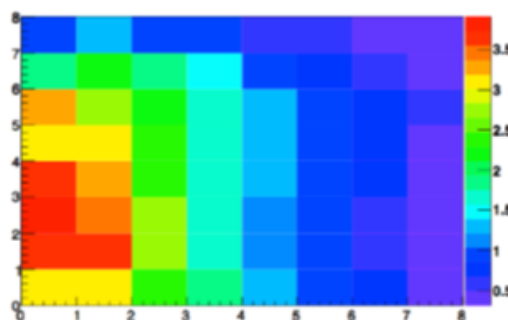


**Figure 2** Imaging results of the pseudo-geoneutrino signals generated by the neutron beam with the currently developed test detector [3].

**References:** [1] N. Takeuchi, K. Ueki, T. Iizuka, J. Nagao, A. Tanaka, S. Enomoto, Y. Shirahata, H. Watanabe, M. Yamano and H. K. M. Tanaka, *Physics of the Earth and Planetary Interiors*, in press. [2] Christensen and Mooney (1995). [3] Watanabe, H. private communications

## Re-evaluation of surface heat flow data in Japan for better estimation of the temperature distribution in the crust

M Yamano<sup>1\*</sup>, H Hamamoto<sup>2</sup>, A Tanaka<sup>3</sup>, S Goto<sup>3</sup>, and T Matsumoto<sup>4</sup>

<sup>1</sup>Earthquake Research Institute, the University of Tokyo, Bunkyo-ku, Tokyo 113-0032, Japan, <sup>2</sup>Center for Environmental Science in Saitama, <sup>3</sup>Geological Survey of Japan, AIST, <sup>4</sup>National Research Institute for Earth Science and Disaster Resilience, \*email:yamano@eri.u-tokyo.ac.jp

**Introduction:** We have been studying the subsurface temperature structure of the Japanese islands as part of a research project to assess geo-neutrino flux originating from U and Th in the crust. Seismic velocity structure has been used to infer composition of the crust, and information on the crustal thermal structure is important in this procedure since seismic velocity depends on temperature as well.

Surface heat flow is the most fundamental geophysical data for estimation of subsurface temperature structure. However, heat flow data on land in Japan had been rather sparse and not evenly distributed owing to the limitation of boreholes available for temperature measurement. This situation was improved by temperature profile data obtained in observation wells for the Hi-net seismograph network, which are densely and evenly distributed over the Japanese islands.

**Analysis of borehole temperature data:** Most of the Hi-net observation wells are shallow and subject to influence of ground surface temperature (GST) variation. We selected temperature profile data in relatively deep wells, over 150 m, in the central part of Honshu, close to the geo-neutrino observation station, KamLAND. After eliminating data apparently affected by ground water flow, we reconstructed GST history in the past at each well through inversion analysis of the temperature profile data. All the results show recent GST increase due to global warming and/or the heat island effect. The amplitude of GST increase in the last 100 years

varies by site from 1.5 to 4 K. The results of GST history reconstruction will be used for analysis of temperature profiles in shallow wells.

We have also been conducting continuous temperature measurement in the upper 100 m of two boreholes located in central Tokyo and on the coast of the Lake Biwa. The obtained data demonstrate downward propagation process of the influence of surface thermal environment variation attributable to human activity.

**Measurement of thermal conductivity:** For determination of heat flow values, we need to know thermal conductivity of formations through which temperature gradient is measured. At many stations, however, it is difficult to obtain rock/sediment samples for thermal conductivity measurement, which is a major source of uncertainty in heat flow data.

Aiming for better evaluation of surface heat flow, we started measurement of thermal conductivity of core samples collected from Hi-net wells and boreholes drilled for volcano observation. We use an optical scanning instrument, which enables nearly continuous measurement along the core, as well as a conventional box-type probe. High-density data with the optical scanning instrument provide valuable information on small-scale heterogeneity in thermal conductivity. New data for Hi-net borehole samples can be included in GST history reconstruction analysis to determine more reliable heat flow values.

**Compilation of geothermal data:** We have been compiling heat flow data in the northwest Pacific area (0 to 60 °N, 120 to 160 °E), which includes the whole Philippine Sea, Japan Sea, and Sea of Okhotsk. We have just updated the data set for publication as part of a CD-ROM. It contains 3670 data, while 3184 values were collected in the previous version published in 2004. We also collected thermal conductivity values measured on rock samples from boreholes in Japan. The compiled data will also be published in the above-mentioned CD-ROM together with geothermal gradient data in and around the Japanese islands. These databases, in combination with data from Hi-net boreholes, serve as a basis for modeling thermal structure of subduction zones around Japan.

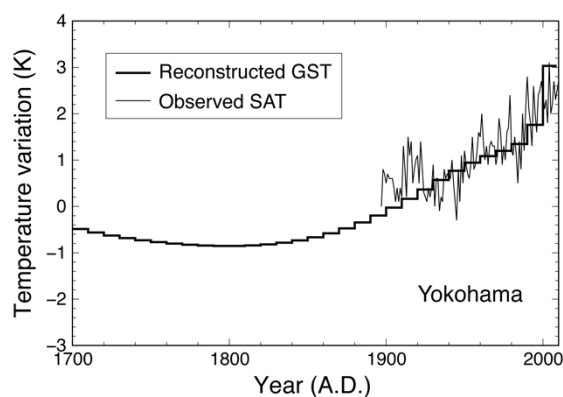


**Figure 1** GST history reconstructed from borehole temperature data at Hi-net Yokohama station compared with surface air temperature (SAT) variation observed at a nearby meteorological station.

(Template for Misasa2017 & Core-Mantle Coevolution symposium. Remove this before upload.)

## Development of New Technology for Geoneutrino Directional Measurement

H. Watanabe<sup>1\*</sup> <sup>1</sup>Research Center for Neutrino Science, Tohoku University, 6-3, Aramaki Aza Aoba, Aobaku, Sendai, Miyagi, 980-8578, Japan.

\*email:hiroko@awa.tohoku.ac.jp

**Introduction:** Neutrino is an elusive particle and it can penetrate even astronomical objects. While neutrino experiments continue to explore the neutrino properties, e.g. oscillation nature of neutrino flavor transformation, mass-square differences and mixing angles, we have begun to utilize neutrino as a tool to look into the Earth. Ant-neutrinos emitted from radioactive isotopes, geo-neutrinos, bring unique and direct information of the Earth's interior and thermal dynamics.

**Experimental Study of Geoneutrino:** KamLAND, Kamioka Liquid-scintillator Anti-neutrino Detector, has 1 kton ultra pure liquid scintillator. They reported the first experimental study of geo-neutrino in 2005 [1]. Later the geo-neutrino signals were used to estimate the Earth's radiogenic heat production and constrain the composition models of the bulk silicate Earth [2]. Following the Fukushima reactor accident in March 2011, the entire Japanese nuclear reactor industry has been subjected shutdown. This unexpected situation allows us to improve the sensitivity for geo-neutrinos [3], because anti-neutrinos from reactors, reactor neutrinos, are most serious background for geo-neutrino measurement.

**Directional Measurement :** The liquid scintillator detectors have the sensitivity for measuring total amount of geo-neutrinos from the Earth's crust and mantle. However, we do not have the technology to track the direction of incoming geo-neutrinos at present due to the high miss-identification in a neutrino's track reconstruction. The direction-sensitive detector can map out the U and Th distribution inside the Earth and this technic is also applicable to resolving crust versus mantle contributions.

Low energy anti-neutrinos are detected by the charged current reaction  $\bar{\nu}_e + p \rightarrow e^+ + n$  (inverse beta decay reaction). This is tagged by the delayed coincidence based on the prompt positron signal and delayed neutron capture signal. Although the positron is emitted almost isotopically, the recoil neutron retains the information of the coming neutrino direction. We have developed <sup>6</sup>Li-loaded liquid scintillator (Fig. 1) to (1) minimize thermal diffusion of the neutron before it is captured by other nuclei and (2) get point-like delayed signal for precise vertexes. To separate prompt and delayed signals, optical discrimination of energy deposit point by high resolution imaging devices is required.

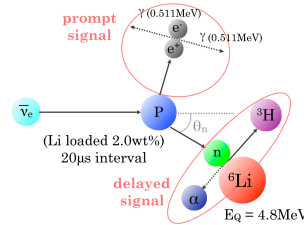


**Figure 1** Anti-neutrino detection with <sup>6</sup>Li-loaded liquid scintillator.

**Developments :** Recent progress in studying the new technology confirmed that a signify improvement in possible in neutrino tracking identification with a combination of <sup>6</sup>Li-loaded liquid scintillator and imaging detector. As shown in Fig 2, the scintillation light is collected by the mirror array and measured by pixelated photon sensor to achieve high vertex resolution, ~2 cm.

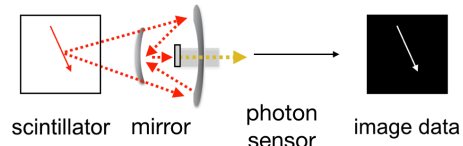


**Figure 2** Schematic view of directional measurement detector.

### (1) Mirror array

We have tried to increase the reflectance to get more photons. In FY 2017, we developed the mirror array with Al. It had about 60% of reflectance. We have developed the method of aluminum evaporation on acrylic mirror and achieved about 95% of reflectance. Since there are two refraction points between scintillator and photon sensor, the expected photons is increased by a factor of 2.5. This achievement allows us to get more statistics of the image data and increase the resolution of separating vertexes.

### (2) Photon sensor

In FY 2017, we studied about specific performance of MCCP (Multi Pixel Photon Counter). We developed cooling system to decrease noise level to use our experiment. In this FY, 3D measurement of scintillation light by two imaging detector with MCCP was started. The 3D images taken by MCCP and multi anode PMT will be compared and reported.

**References:** [1] T. Araki et al., Nature 436, 499 (2005) [2] A. Gando et al., Nature Geosci. 4, 647 (2011) [3] A. Gando et al., Phys. Rev. D 88, 033001 (2013)

## The fate of carbonate in deeply subducted oceanic crust

M Walter<sup>1</sup>, J Drewitt<sup>2</sup>, H. Zhang<sup>3</sup>, S. McMahon<sup>2</sup>, D Edwards<sup>2</sup>, B Heinen<sup>2</sup>, O Lord<sup>2</sup>, S Anzellini<sup>4</sup> and A Kleppe<sup>4</sup>

<sup>1</sup>Geophysical Lab, Carnegie Institution of Washington, Washington D.C., 20015, USA

<sup>2</sup>School of Earth Sciences, University of Bristol, Queens Road, BS8 1RJ, UK

<sup>3</sup>School of Earth and Space Sciences, USTC, 96 Jinzhai RD, Hefei, Anhui 230026, P. R. China

<sup>4</sup>Diamond Light Source Ltd, Diamond House, Chilton, OX11 0DE, UK

\*email: mwalter@carnegiescience.edu

**Introduction:** Knowledge of how carbon can cycle through exterior and interior reservoirs is fundamental for understanding its evolution through geological time and the habitability at earth's surface. The H/C ratio in earth's exosphere is higher than in the source region of primitive basalts, suggesting an enriched carbon reservoir in the mantle [1]. One possible explanation is that subduction of carbon enriched the mantle over geological time. On average basaltic crust contains ~ 2.5 wt.% CO<sub>2</sub> [2], and modeling of slab devolatilization processes indicates that subducted carbonate may survive past the volcanic front to be transported deeper into the mantle [3].

Experimental evidence shows that carbonated oceanic crust should melt in the transition zone along most subduction geotherms (Fig. 1) due to a deep depression in the carbonated basalt solidus [4]. Mineral inclusions in superdeep diamonds have trace element signatures that testify to carbonate melt in their formation providing direct evidence for this process [4]. However, along cool subduction geotherms carbonate may be transported into the lower mantle, potentially enriching the deep mantle reservoir in carbon. Here we report on laser-heated diamond anvil cell (LHDAC) experiments in the CaO-MgO-SiO<sub>2</sub>-CO<sub>2</sub> (CMSC) and FeO-MgO-SiO<sub>2</sub>-CO<sub>2</sub> (FMSC) systems at lower mantle pressures. We investigate the stability of carbonate in basaltic oceanic crust and test for decarbonation reactions involving carbonate and coexisting silica [5].

**Methods:** We report on LHDAC experiments and analysis of recovered run products by synchrotron x-ray diffraction and micro-Raman spectroscopy. Starting compositions were synthesized in the CMSC and FMSC systems by mixing carbonates with silica glass. Experiments were made in symmetric DACs with pressed discs of starting material sandwiched between discs of NaCl as a pressure medium. Samples were heated using a double-sided laser geometry and temperatures measured by spectroradiometry. Samples were held at temperature for up to 1 hour. Samples were analyzed using angle-dispersive X-ray diffraction at beamline I15 of the Diamond Light Source for phase identification. The presence of diamond in run products was determined by Raman spectroscopy at the University of Bristol.

**Results:** We find that carbonate reacts with silica to form bridgmanite ± Ca-perovskite + CO<sub>2</sub> at pressures in the range of ~40 to 70 GPa (Fig. 1). Decarbonation reactions have a negative Clapeyron slope and present a final barrier to subduction of carbonate beyond ~1500 km depth. For some geotherms solid CO<sub>2</sub>-V may be present in subducted crust over a limited depth range but will eventually breakdown to form diamond and free oxygen as slabs heat up to ambient mantle temperatures [6]. We find that the fate of carbonate in subducted oceanic crust is ultimately diamond at conditions of the deep lower mantle where it potentially may be stored on long timescales, possibly being returned to the surface in upwelling plumes. We investigate whether the deep lower mantle may become enriched in carbon in the form of diamond over geological time due to subduction of carbonate and its eventual dissociation to form diamond plus oxygen and whether release of oxygen during diamond formation can provide a mechanism for locally oxidizing the deep mantle.

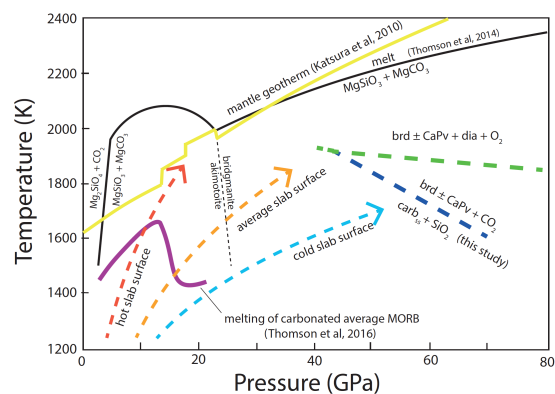


**Figure 1.** Pressure-temperature diagram showing generalised carbonate phase relations in subducted, carbonated oceanic crust [5].

**References:** [1] Hirschmann, M. and Dasgupta, R. (2009). *Chemical Geology* 262 4–16. [2] Alt, J. & Teagle, D. (1999). *Geochim. Cosmochim. Acta* 63, 1527–1535. [3] Gormon et al. (2006) *G-Cubed* doi:10.1029/2005GC001125 [4] Thomson et al (2016). *Nature* 529, 76-79. [5] Drewitt et al (2019). *Earth and Planetary Science Letters* 511, 213-222. [6] Katsura et al (2010). *Physics of the Earth and Planetary Interiors* 183, 212-218.

## Multiple sulfur isotopes constraints on the origin of sulfide sulfur in Archean granitoids from Dharwar craton, Southern India

S Aoyama<sup>1\*</sup>, T Oneyama<sup>1</sup>, W Ouchi<sup>1</sup>, Yuichiro Ueno<sup>2</sup> and M. Satish-Kumar<sup>1</sup>

<sup>1</sup>Faculty of Science, Niigata University, 2-8050 Ikarashi, Nishi-ku, Niigata, 950-2181, Japan

<sup>2</sup>Department of Earth and Planetary Science, Tokyo Institute of Technology, Meguro, Tokyo 152-8551, Japan

\*email: aoyama@geo.sc.niigata-u.ac.jp

**Introduction:** Sulfur is ultimately derived from the mantle through magmatic activity. In the surface, sulfur is mainly present as sulfate ( $S^{6+}$ ) and sulfide ( $S^{2-}$ ) in the ocean and crust. A part of these sulfur finally return back to the mantle through subduction process, however, there are little evidences of subduction of sulfur in the Archean (>2.5 Ga) period. Mass Independent Fractionation (MIF) of sulfur isotopes is found in the Archean supracrustal rocks such as sedimentary sulfide and sulfate deposits, thus MIF signatures of granitoids potentially exhibit subduction of surface sulfur in the depth of granitoid formation. Because intensive MIF signals are found in sedimentary rock records between late Archean to early Proterozoic [1], multiple sulfur isotopes of sulfide sulfur in granitoids from Dharwar craton, Southern, India were studied to understand whether sulphur has been recycled or not.

**Experimental:** From powder samples of about 80 Dharwar granitoids, sulfide sulfur was extracted by Cr(II) methods and converted into  $Ag_2S$ . The product  $Ag_2S$  was fluorinated into  $SF_6$  gas by using Kurie-point Pyrolyzer [2]. Multiple sulfur isotopes (ratios of  $^{32}S$ ,  $^{33}S$  &  $^{34}S$ ) of  $SF_6$  was analyzed by high-precision isotopic ratio mass spectrometer (MAT253, Thermofisher Scientific).

**Results and Discussion:** Eleven granitoid samples with sulfide sulfur from Dharwar were measured,  $\delta^{34}S$  were mostly positive, ranging from  $-1.4\text{‰}$  to  $+30.4\text{‰}$  (with analytical errors of  $\pm 1.5\text{‰}$ ),

$\Delta^{33}S$  ranged from  $-0.089\text{‰}$  to  $+0.071\text{‰}$  (with analytical errors of  $\pm 0.05\text{‰}$ ). Sulfur in the mantle ( $\delta^{34}S = -1.28\text{‰}$  &  $\Delta^{33}S = 0.003\text{‰}$ , [3]) alone cannot explain these variations, suggesting incorporation of other source of sulfur such as sedimentary sulfide and seawater sulfate. Based on the chemical compositions, Na/K ratios and ASI (Aluminium Saturation Index) values of granitoids tend to have little relationships with  $\Delta^{33}S$  values. On the other hand, granitoids having high Sr/Y ratios are prone to have negative  $\Delta^{33}S$  values. Because high Sr/Y ratios are the signals of melting of mafic rocks (e.g., altered oceanic crust) under the presence of garnet and/or hornblende in residue, the result implies that seawater sulfate component within the oceanic crust is subducted and partially melted to be recycled into granitoids. Such  $\Delta^{33}S$  signals of these granitoids, however, shows much smaller variations compared to those of simultaneous surface rock records, suggesting high contributions of primordial sulfur from the mantle in the late Archean period.

### References:

- [1] Johnston, D. T. (2011). "Multiple sulfur isotopes and the evolution of Earth's surface sulfur cycle." *Earth-Science Reviews* 106(1-2): 161-183. [2] Ueno, Y., *Chemical geology*, 419 (2015) 29–35 [3] Labidi, J., et al. (2013). "Non-chondritic sulphur isotope composition of the terrestrial mantle." *Nature* 501(7466): 208s-+.

## Recent developments in stable isotope measurements on high-pressure high-temperature experimental run products and natural samples

M. Satish-Kumar<sup>1</sup>, S. Aoyama<sup>1</sup>

<sup>1</sup>Department of Geology, Faculty of Science, Niigata University, Nishi-ku, Niigata 950-2181, Japan.

\*email: satish@geo.sc.niigata-u.ac.jp

For constraining the light element contents of lower mantle and core, stable isotope composition can be effectively used as an independent proxy [1, 2]. Although isotope fractionation in the deep earth occur in a narrow range, the volume of light element content in the mantle and core are extremely high, which can effectively cause significant natural isotopic compositional variations. It is necessary to accurately measure the isotope composition accurately in micro to nanomole scales, because the high-pressure experimental run products are small in volume. Recent studies have predicted the presence of isotope fractionation even at lower mantle and core *P-T* conditions, especially in magma ocean environment and during the core segregation [2, 3, 4]. Despite the necessity of the micro-volume stable isotope measurement, there is always a tradeoff between the accuracy and the sample size.

At Niigata University, a MAT-253 mass spectrometer (Thermo Fisher Scientific) was installed through the MEXT Grant-in-Aid for Scientific Research on Innovative Areas. Carbon and oxygen isotopic compositions are measured using CO<sub>2</sub> and multiple sulfur isotopic composition are measured using SF<sub>6</sub> gas. A new micro-volume inlet system was installed and fundamental parameters such as pressure effect and capillary flow effect were tested. Using the micro-volume inlet system the minimum volume required for analysis is 1 micro-mole sample gas, and the precision for carbon and oxygen isotopic composition are better than 0.1‰. The precision for sulfur isotopes is ±0.3‰ and ±0.01‰ (1σ) for δ<sup>34</sup>S and Δ<sup>33</sup>S, respectively, based on the repeated analyses of standard Ag<sub>2</sub>S (IAEA S-1). Multiple sulfur isotope measurement system consists of 1) curie point pyrolyzer for rapid conversion of small volume samples to SF<sub>6</sub> gas [5], 2) vacuum line system for pumping out non-condensable gasses, 3) gas chromatograph for purifying the SF<sub>6</sub> gas and 4) micro-volume inlet system for introduction of sample gas to ionization chamber.

Multiple sulfur isotope ratios experimental run products were measured using the new system. Metal phases were separated and sulfur was extracted using Cr(II) reduction method [6]. Preliminary results indicate that S isotope fractionations occur in the pressure range of 3–5 GPa, under high-temperature conditions corresponding to the magma ocean environment. The negative δ<sup>34</sup>S of mantle [7], can hence be

explained by sulfur isotope fractionation in a magma ocean environment.

Sulfur isotope measurements were also carried out on granitoid samples from the Archean with sulfide sulfur showing positive δ<sup>34</sup>S values. Mass independent isotope fractionation, expressed as Δ<sup>33</sup>S, was also observed, suggesting that sulfur in the mantle alone cannot explain these variations. The incorporation of surface sulfur from sedimentary rocks and seawater is proposed.

Carbon isotopic compositions of experimental run products were also measured using the mass spectrometer. We could measure isotopic compositions of carbonate and diamond separately for high-pressure samples up to 15 GPa. Further refinements are underway for ultra small volume measurements.

**References:** [1] Wood et al., *Reviews in Mineralogy & Geochemistry*, **75**, 231-250, (2013). [2] Satish-Kumar M, et al., *Earth and Planetary Science Letters*, **310**, 340-348 (2011). [3] Shahar, A. et al., *Science*, **352**, 580-582, (2016). [4] Labidi et al., *Geochimica et Cosmochimica Acta*, **175**, 181–194, (2016). [5] Ueno Y., *Chemical Geology*, **419**, 29–35 (2015). [6] Canfield D.E. et al., *Chem. Geol.*, **54**, 149-155. (1986) [7] Labidi J. et al., *Nature*, **501**, 208-211. (2013)

## Investigation of nitrogen incorporation into stishovite using implanted sample and outlook on deep nitrogen cycle

Ko Fukuyama<sup>1\*</sup>, Hiroyuki Kagi<sup>1</sup>, Toru Inoue<sup>2,3</sup>, Yuji Sano<sup>4</sup>, Toru Shinmei<sup>3</sup>, Sho Kakizawa<sup>3</sup>, Naoto Takahata<sup>4</sup>, Shunichi Hishita<sup>5</sup>

<sup>1</sup>Geochemical Research Center, Graduate School of Science, The University of Tokyo, <sup>2</sup>Department of Earth and Planetary Systems Science, Hiroshima University, <sup>3</sup>Geodynamics Research Center, Ehime University, <sup>4</sup>Atmosphere and Ocean Research Institute, The University of Tokyo, <sup>5</sup>National Institute for Materials Science Tokyo 113-0033, Japan.

\*email: ko.fukuyama@eqchem.s.u-tokyo.ac.jp

**Introduction:** Nitrogen occupies about 80% of the Earth's atmosphere and is an essential element of life. Moreover, it is suggested that nitrogen had an impact on the climate in the early Earth (e.g. Goldblatt et al., 2009; Wordsworth and Pierrehumbert, 2013). Therefore, nitrogen is an important volatile element in the early Earth evolution process and origin of the life. However, we still cannot fully understand the behavior of nitrogen in the deep Earth. For example, nitrogen is depleted compared to other volatile elements in deep mantle (Marty et al., 2012). The "missing" nitrogen is an important subject in Earth Science.

**Experimental:** In this study, we compared nitrogen incorporation into lower-mantle minerals (bridgmanite, stishovite) by high-pressure and high-temperature experiments using multi-anvil apparatus installed at Geodynamics Research Center, Ehime University under the conditions of 27 GPa and 1400 °C-1700 °C. In these experiments, we used Fe-FeO buffer in order to reproduce the redox state of the lower mantle. Two types of starting materials: a powder mixture of SiO<sub>2</sub> (quartz) and MgO and a powder mixture of SiO<sub>2</sub>, MgO, Al<sub>2</sub>O<sub>3</sub> and Mg(OH)<sub>2</sub> were used for starting materials. Nitrogen in recovered samples was analyzed using NanoSIMS installed at Atmosphere and Ocean Research Institute, The University of Tokyo.

We prepared implant standard samples in order to estimate nitrogen solubility in stishovite at National Institute for Materials Science. Implant standards were quartz glass and we used N<sup>+</sup> as implant ion species.

**Results and Discussion:** A series of experimental results revealed that stishovite can incorporate 39-418 ppm nitrogen which is larger than bridgmanite nitrogen solubility (5-50 ppm nitrogen solubility reported by Yoshioka et al. (2018)). Stishovite is formed by the transition of the SiO<sub>2</sub>-rich oceanic crustal sedimentary rocks or continental crusts transported to the lower mantle via subducting slabs. From these reasons, Our study suggests that nitrogen would continue to be supplied

to the lower mantle via subducting slabs since approximate 4 billion years ago when the plate tectonics had begun, forming a "Hidden" nitrogen reservoir in the lower mantle. Furthermore, this "Hidden" nitrogen reservoir may play a role in decreasing high-concentration nitrogen which enhanced greenhouse effect in the early atmosphere (Goldblatt et al., 2009) to the present nitrogen concentration level.

Thus, our experimental results support the young faint Sun paradox explained by high-concentration nitrogen in the early earth (e.g. Goldblatt et al., 2009; Wordsworth and Pierrehumbert, 2013) and suggest "Missing" nitrogen has been caused by forming a "Hidden" nitrogen reservoir in the lower mantle.

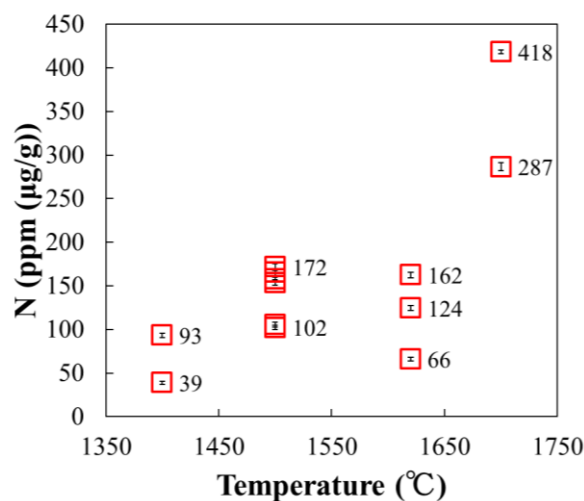


**Figure 1** Nitrogen solubility in stishovite under different temperatures

### References:

- [1] Goldblatt et al. (2009) Nat Geosci 2, 891-896
- [2] Li et al. (2013) Earth. Planet. Sci. Lett. 377, 311-323.
- [3] Marty (2012) Earth. Planet. Sci. Lett. 313, 56-66.
- [4] Wordsworth and Pierrehumbert (2013) Science 339, 64-67.
- [5] Yoshioka et al., (2018) Earth. Planet. Sci. Lett.

## Fe<sub>2</sub>S: the most iron-rich Fe-S compound at pressures of the inner core

S Tateno<sup>1,2\*</sup>, H Ozawa<sup>2,3</sup>, K Hirose<sup>1,4</sup>, T Suzuki<sup>5</sup> <sup>1</sup>Earth-Life Science Institute, Tokyo Institute of Technology, Tokyo 152-8550, Japan, <sup>2</sup>Institute for Planetary Materials, Okayama University, Misasa, Tottori 682-0193, Japan, <sup>3</sup>Nuclear Science and Engineering Center, Japan Atomic Energy Agency, Tokai-mura, Ibaraki 319-1195, Japan, <sup>4</sup>Department of Earth and Planetary Science, The University of Tokyo, Tokyo 113-0033, Japan, <sup>5</sup>Geochemical Research Center, The University of Tokyo, Tokyo 113-0033, Japan.

\*email: tateno@elsi.jp

**Introduction:** Sulfur is considered to be one of the light elements in the Earth's core as iron sulfides are universally found in iron meteorites. The phase diagram of the Fe-FeS system at the high-pressure and high-temperature ( $P$ - $T$ ) conditions of the core has particular importance to understand the composition and state of the Earth's core. Because Fe<sub>3</sub>S is known as the most iron-rich Fe-S compound at  $> 20$  GPa, the iron-sulfur core model has been discussed considering Fe and Fe<sub>3</sub>S in the solid core.

However, our previous experiment reveals that Fe<sub>3</sub>S decomposes into S-bearing hcp-Fe and CsCl (B2)-type phase above  $\sim 250$  GPa from X-ray diffraction measurements (XRD) [1]. Furthermore, TEM analysis on the recovered sample exhibits that S-poor phase, likely to be a former hcp-Fe, coexisted with S-rich phase with  $> 33.5$  atm% S. Hence, the S-rich end-member compound has not been constrained under pressure more than 250 GPa. In order to re-investigated the phase relations in Fe-FeS system, we studied phase relations in Fe<sub>2</sub>S at multi-megabar pressure range.

**Experimental:** High  $P$ - $T$  conditions were generated in a laser-heated diamond-anvil cell using double-beveled diamond anvils with 40 or 60  $\mu$  m culets. We used the Fe<sub>2</sub>S phase as the starting material, which was synthesized beforehand at high pressures in a multianvil apparatus and confirmed by microprobe analysis. SiO<sub>2</sub> glass and MgO were used for thermal insulation and pressure calibration. We loaded such sample assembly as MgO/SiO<sub>2</sub>-glass/Fe<sub>2</sub>S/SiO<sub>2</sub>-glass so that MgO was detached from an iron sample, in order to avoid possible chemical reaction at high temperature. Angle-dispersive XRD measurements were conducted at BL10XU, SPring-8. Heating was performed from both sides of the sample by employing a pair of 100 W Yb fiber lasers.

**Results and Discussion:** We performed three separate sets of experiments at pressures at 120-310 GPa and temperature up to 3000 K. When we heated the Fe<sub>2</sub>S sample being mostly amorphous by compression to 300 GPa at 300 K, the 20 new peaks appeared in a few minutes and became spotty with further heating. All peaks are assigned to the orthorhombic structure, which agrees well with  $Pnma$  symmetry phase proposed by the theoretical prediction [2]. This observation indicates that Fe<sub>2</sub>S

composition crystallizes as a single phase. In the following decompression and re-heating the sample, its stability was confirmed to be 150-310 GPa.

Our previous study [3] reported that hcp-Fe and B2 phase crystallizes in Fe-6wt% S bulk composition at 270 GPa and 2400 K. Then, the peaks from the B2 phase become weak at further heating. We re-analyzed the series of XRD datum, and found that such apparent weakening was caused due to the appearance of Fe<sub>2</sub>S phase. Indeed, in the XRD pattern collected at 3500 K, we confirmed that additional weak peaks from  $Pnma$ -Fe<sub>2</sub>S were clearly visible and the reflection from the coexisting hcp-Fe phase became intense simultaneously. This indicates that stable phase assemblage in Fe-6wt% S bulk composition changes from hcp-Fe + B2-FeS into hcp-Fe +  $Pnma$ -Fe<sub>2</sub>S. Hence, Fe<sub>2</sub>S is the sulfur-rich end-member compound after the decomposition of Fe<sub>3</sub>S at 250 GPa. The slope of eutectic melting curve should have kink at the decomposition of Fe<sub>3</sub>S. Also, pressure evolution of the eutectic composition should change as well. Since the extrapolation from lower pressure data is not applicable beyond 250 GPa, higher  $P$ - $T$  experiments are necessary to establish the phase diagram at the pressure of inner core boundary.

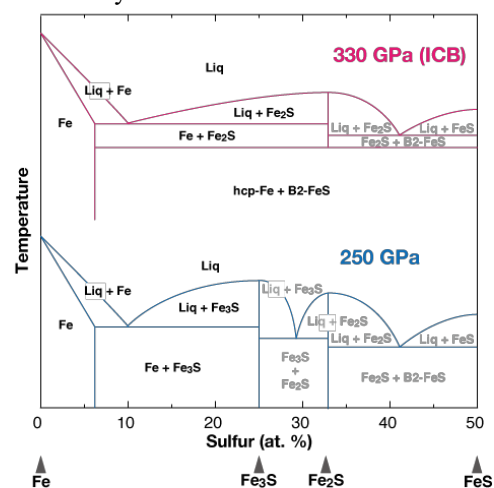


**Figure 1** Composition-temperature diagrams in the system Fe-FeS, inferred from the present study and Mori *et al.* [3].

**References:** [1] Ozawa, H. *et al.*, *Gephys. Res. Lett.* **40**, 4845 (2013). [2] Bazhanova, Z. *et al.* *Phys. Uspekhi*, **60**, 1025 (2017). [3] Mori, Y. *et al.*, *Earth Planet. Sci. Lett.*, **464**, 135 (2018).

## High precision tungsten isotope of ocean island and LIPS basalts from deep mantle

Asako Takamasa<sup>1</sup>, Katsuhiko Suzuki<sup>1\*</sup>, Yusuke Fukami<sup>1</sup>, Tsuyoshi Iizuka<sup>2</sup>

<sup>1</sup>Research and Development Center for Submarine Resources, JAMSTEC, Natsushima, Yokosuka 237-0061, Japan, <sup>2</sup>Graduate School of Science, The University of Tokyo, Hongo, Bunkyo, Japan.

\*email:katz@jamstec.go.jp

**Introduction:** Among five W isotopes, <sup>182</sup>W is a product of  $\beta$ -decay of <sup>182</sup>Hf with the relatively short half life of 8.9 m.y. As Hf and W are lithophile and siderophile, respectively, the <sup>182</sup>Hf-<sup>182</sup>W radiometric system could constrain metal-silicate (core-mantle) differentiation, especially core segregation, in the very early Earth system because of its large fractionation between metal-silicate and the short half life of <sup>182</sup>Hf. Recent improvements of analytical techniques of W isotope analyses using TIMS and MC-ICP-MS equipped with a desolvating device allow to obtain highly precise <sup>182</sup>W/<sup>184</sup>W ratios of terrestrial rocks. These led to findings of  $\mu^{182}\text{W}$  anomalies (mostly positive) in old komatiites (2.4 – 3.8 Ga) and young volcanic rocks with positive anomalies of 12 Ma Ontong Java Plateau and 6 Ma Baffin Bay [1] and with negative anomalies of those such as the Loihi and Samoa basalts [2]. Recently, Kruijer and Kleine [3] proposed that the <sup>182</sup>W excesses for an OJP sample by Rizo et al. [1] may result from the nuclear field shift effect leading to defect of <sup>183</sup>W, as the NTIMS analyses utilized a double normalization involving the <sup>183</sup>W/<sup>184</sup>W ratio.

**Experimental:** High-precision W isotope ratio measurement with MC-ICP-MS (Thermo co. Ltd., NEPTUNE PLUS) equipped with desolvating nebulizer (ARIDAS II) following the chemical separation using both cation and anion exchange resin has been developed. We have measured the W standard solution (SRM 3163) and obtained the isotopic compositions with a precision of  $\pm 5$ ppm. However, the standard solution, which was processed by the cation or anion exchange chemistry in the same way as for rock samples, has systematic

<sup>182</sup>W/<sup>184</sup>W drift of -5ppm, which was also observed by [4] and Kruijer and Kleine [3]. This shift likely resulted from the nuclear field shift effect as mentioned by Kruijer and Kleine [3]. Therefore, we corrected the measured W isotope ratios of samples with the standard solution processed by the same method as that of the samples. This technique led to obtaining of the W isotopic compositions with reproducibility of several ppm.

**Results and Discussion:** We have obtained negative  $\mu^{182}\text{W}$  for the basalts with the high <sup>3</sup>He/<sup>4</sup>He isotopic composition from the Loihi, Hawaii, through the developed analytical method. This result is consistent with that of Mundl et al., [2]. As the Earth's core should have a negative  $\mu^{182}\text{W}$  value of ca. -210, the Loihi sample we analyzed probably contains a component with a signature of core-mantle interaction. We have obtained the high-precision W isotope data for the fresh drilled basalts from Louisville. Louisville is known to have been originated from the primordial deep mantle source. We will discuss the obtained results and the early evolution of the deep mantle.

Acknowledgement – JSPS Grant-in-Aid has supported this project. We are grateful to M. Kawamura for experimental help and Y. Orihashi, T. Hanyu, M. Tejada for providing samples.

**References:** [1] Rizo H. et al. *Science*, 352, 809 (2016). [2] Mundl A. et al. *Science*, **356**, 66 (2017). [3] Kruijer T.S. and Kleine T. *Chem. Geol.*, 485, 24 (2018). [4] M. Willbold, et al. *Nature*, **477**, 195 (2011).

## Noble gas partition between metal-silicate melts

H Sumino<sup>1\*</sup>, T Tanaka<sup>1</sup>, H Kuwahara<sup>2</sup>, S Kishi<sup>1</sup>, R Nomura<sup>3</sup>, K Mibe<sup>4</sup>, C Jackson<sup>5</sup>, S Tateno<sup>6</sup>, H Kagi<sup>7</sup>  
<sup>1</sup>Department of Basic Science, University of Tokyo, Tokyo 153-8902, Japan. <sup>2</sup>Geodynamics Research Center, Ehime University, Ehime 790-8577, Japan. <sup>3</sup>Hakubi Center, Kyoto University, Kyoto 606-8501, Japan. <sup>4</sup>Earthquake Research Institute, University of Tokyo, Tokyo 113-0032, Japan. <sup>5</sup>Geophysical Laboratory, Carnegie Institution of Washington, Washington, DC 20015-9801, USA. <sup>6</sup>Earth-Life Science Institute, Tokyo Institute of Technology, Tokyo 152-8550, Japan, <sup>7</sup>Geochemical Research Center, University of Tokyo, Tokyo 113-0033, Japan. \*email:sumino@igcl.c.u-tokyo.ac.jp

**Introduction:** Analyses of ocean island basalts reveal a geochemical reservoir characterized by unradiogenic, “primordial” noble gas signatures (e.g., high  $^3\text{He}/^4\text{He}$  and low  $^{40}\text{Ar}/^{36}\text{Ar}$  ratios), likely residing in the deep mantle. There has been much debate about the area holding the “primordial” noble gases deep in the Earth [1], including that the “primordial” noble gases have been retained in the deepest region of the mantle since 4.4 Ga [2], or in the core since the core-mantle separation [3,4]. However, the validity of latter strongly depends on the quantity of noble gases the core incorporates during accretion and can hold in the present day.

**Experimental:** In order to investigate noble gas partitioning behavior between the core and mantle, noble gases were dissolved into metal-silicate melts under high temperature and pressure conditions, and then the samples were quenched, recovered, and analyzed for noble gas concentrations.

At the Geophysical Laboratory, Carnegie Institution of Washington, argon partitioning experiments at 1 GPa and 2000 K were conducted using a piston cylinder apparatus. Argon was added as a liquid to a Pt (outer)-graphite (inner) double capsule containing a Fe metal-silicate mixture, and the capsule was welded shut while held in a bath of liquid  $\text{N}_2$ .

The other two series of samples were synthesized at the Geodynamics Research Center, Ehime University. Noble-gas doped silicate glass and iron were melted and equilibrated under high pressure and temperature (8-70 GPa, 1700-1900 K) using a multianvil apparatus (2000~2300 K, 3-8 GPa) and a laser-heated diamond anvil cell (2000-4000 K, 10-70 GPa).

The sample capsule was cut and the polished surface of the section was investigated with scanning electron microscope and Raman spectroscopy. The chemical compositions of silicate and metal phases were determined with electron microprobe. And then, the noble gases in the samples were extracted by an ultraviolet laser ablation apparatus and analyzed using a noble gas mass spectrometer at the University of Tokyo.

**Results and Discussion:** The partition coefficient  $D$ , where  $D = (\text{noble gas in metal phase})/(\text{noble gas in silicate phase})$ , of argon at 1 GPa varied widely from orders of  $10^{-4}$  to  $10^{-1}$ . This resulted from heterogeneous argon distribution

in the metal phase, which seems significantly controlled by contaminant phases, such as silicate inclusions and micro- or nano-argon bubbles. Therefore the lowest  $D$  so far determined would yield the best estimate,  $7 \times 10^{-5}$ , which is three orders of magnitude lower than the values reported by the previous work [5].

On the other hand,  $D$  for neon, argon, krypton and xenon at 8 GPa obtained with the samples synthesized with multianvil apparatus were in the order of  $10^{-3}$ , which is consistent with the previous work [5]. However, it was revealed from the Raman spectra that crystallization of clinopyroxene had occurred in the samples synthesized at pressures of 6 GPa or higher, suggesting that the obtained  $D$  values are significantly underestimated because a previous study showed that noble gas content in pyroxene crystal is smaller than those in glass (melt) by about  $10^{-4}$  [6].

At present, we have not determined helium partition coefficient in the all pressure range as it was difficult to retain enough amount of helium in high-pressure and temperature apparatus during the experiments. We confirmed that the silicate phase obtained with laser-heated diamond anvil cell contained a sufficient amount of noble gas. However, we have not determined amount of the noble gas contained in the metal phase because it was too small to be selectively analyzed with the laser ablation system for noble gas extraction. Further experiments are necessary to obtain the noble gas concentration contained in the metal phase in order to determine the partition coefficients at higher pressure, at least 30 GPa with which the elemental partition between iron and silicate melt would have occurred during core formation [7].

## References:

- [1] Porcelli, D. and Ballentine, C.J., *Rev. Mineral. Geochem.*, **47**, 411 (2002).
- [2] Mukhopadhyay, S., *Nature*. **486**, 101 (2012).
- [3] Trierloff, M. and Kunz, J., *Phys. Earth Planet. Inter.*, **148**, 13 (2005).
- [4] Bouhifd, M.A., Jephcoat, A.P., Heber, V.S. and Kelley, S.P., *Nature Geo.*, **6**, 982 (2013).
- [5] Matsuda, J., Sudo, M., Ozima, M., Ito, K., Ohtaka, O. and Ito, E., *Science*, **259**, 788 (1993).
- [6] Heber, V.S., Brooker, R.A., Kelley, S.P. and Wood, B.J., *Geochim. Cosmochim. Acta*, **71**, 1041 (2007).
- [7] Richter, K., *Earth Planet. Sci. Lett.* **304**, 158 (2011).

## Ab Initio Applications to the Element Partitioning between Core and Mantle

T Tsuchiya, A Ohba, Z Xiong Ehime University, Japan

\*email: tsuchiya.taku.mg@ehime-u.ac.jp

Metal-silicate element partitioning is a key to understanding the chemical interaction between the core and mantle and their evolution. We are particularly interested in the liquid-liquid partitioning under high P,T condition to consider the early-Earth differentiation processes. From the theoretical point of view, element partitioning is determined based on free energy balance in exchange reactions. However, determination of free energy in particular of liquids is not easy because the evaluation of entropy of liquids is not easy. In this study we employ the thermodynamic integration (TI) method, which is funded by statistical mechanics (Kirkwood, 1935) and enable us to compute free energy differences between reference and target systems. The TI routine is implemented into our ab initio molecular dynamics (AIMD) simulation program, and our TI-AIMD code can be applicable not only to liquids but also to solids, where ideal gas and Einstein crystal are chosen for the reference systems respectively, and the reference systems are directly switched to the ab initio (target) systems (Taniuchi and Tsuchiya, 2018). This technique has successfully been applied to predict the melting temperature of MgO up to 4 TPa (Taniuchi and Tsuchiya, 2018). Metal-silicate potassium partitioning, helium partitioning, and argon partitioning have also been studied (Xiong et al. 2018).

Calculated results imply that the potassium partitioning behavior strongly depends on the composition of liquid iron. Potassium basically prefers silicate melt associated with the its usual lithophilic behavior, but this feature was found to

change if liquid iron contains oxygen. The solubility of potassium in liquid iron increased with increasing the oxygen content there. In contrast, the partitioning behaviors of noble gases were found to depend strongly on pressure. This can be understood by the size of vacant spaces in the melt structures. Helium and argon were both partitioned into silicate melt under low pressure primarily due to larger vacant spaces, but they changed to prefer liquid iron under high pressure because the vacant spaces in silicate melts were rapidly compressed with pressure (Xiong and Tsuchiya, in prep.). The technique is further extended to compute the water partitioning between liquid iron and molten silicate. So far we consider only a simple exchange reaction of water ( $H_2O$ ) with no oxidation-reduction reaction. Calculations are yet to be converged and still ongoing, but in the moment water prefers liquid iron to silicate melt at 135 GPa and 5000 K (Ohba, diploma thesis, Ehime Univ. 2018). This behavior is consistent with some experiments conducted at much lower pressures (e.g., Iizuka-Oku et al., 2017). Water was found to dissociate to atomic states in liquid iron without formation of molecular  $H_2O$ .

Some preliminary simulations of metal-silicate element partitioning suggest that the outer core could be a reservoir of several geochemically interesting elements. Our TI-AIMD might be a very useful technique but very careful attention has to be paid for the numerical accuracy of free energy integration to obtain reliable results of element partitioning. Also, since the TI processes need huge computations, so far simple compositions of silicate and iron only can be taken for practical reasons

## On the core-mantle thermal and chemical coupling: Review and perspectives

T Nakagawa<sup>1\*</sup> <sup>1</sup>Department of Earth Sciences, The University of Hong Kong, Pokfulam Road, Hong Kong.

\*email: ntakashi@hku.hk

**Introduction:** On the core-mantle thermal and chemical coupling in terms of the long-term evolution of Earth's mantle and core, there are mainly two approaches for explaining the magnetic evolution provided from paleomagnetic data [1] and heat budget across the Earth [2]. They are based on numerical mantle convection simulations and parameterized mantle convection model imposing the bottom thermal and chemical boundary conditions at the core-mantle boundary.

**Parameterized approach:** Owing to the great progress on the heat transfer in the deep planetary interior so that may include the heat transport by partial melting [3], it is available to access the core-mantle evolution with semi-analytical approach rather than to use a massively parallel computing. Recent investigations have been pointed out that the heat transfer across the core-mantle boundary could range up to 20 TW and the age of the inner core seems to be around 500 Myrs or younger, which seems to be consistent with interpretations of paleomagnetic data [4].

**Massively parallel computing of mantle convection simulations:** However, the parameterized approach could not be addressed for various complicated processes expected in the global-scale mantle dynamics modeling. For instance, the mantle dynamics associated with phase transition and extremely variable viscosity can be only addressed in numerical mantle convection models. In this modeling approach, the coupled core-mantle evolution seems to be influenced from the onset timing of plate-like behavior that is generated by the yield criteria of oceanic lithosphere [5].

**Incorporating into the chemical evolution of Earth's core:** In the recent accomplishment of semi-analytical model of thermal and chemical evolution

of the Earth's core [6], the chemical diffusive processes may be played for the significant role in thermal and magnetic evolution of the Earth's core. Moreover, the chemical evolution associated with the inner core growth may also be greatly important for the thermal and magnetic evolution of Earth's core [7]. Regarding the recent mineral physics accomplishments, the dissolution processes of magnesium or silicon seem to have a great impact to the dynamo actions in the early Earth [8] [9] and pointed out by thermal evolution model [10].

**Synthesis and perspectives:** In this presentation, I would provide the current status of core-mantle coupling research in terms of long-term evolution of thermal, chemical and magnetic evolution so that can be explained for the geophysical observations, paleomagnetic and mineral physics interpretations using two modeling approaches: 1. Semi-analytical parameterized mantle convection and 2. Massively parallel computing of mantle convection simulations. At the end of presentation, I will provide the future direction of coupled evolution of core-mantle dynamics with both mantle convection and geodynamo simulations that has been provided for the preliminary results [11].

**References:** [1] Biggin, A. J., et al., *Nature* **526** (2015). [2] Jaupart, C., et al. *Treatise on Geophysics* **7** (2007). [3] Driscoll, P., and D. Bercovici, *Phys. Earth Planet. Int.* **236** (2014). [4] Biggin, A., J., *Nature Geoscience* **1** (2008). [5] Nakagawa, T., and Tackley, P. J., *G-cubed* **16** (2015). [6] [7] Labrosse, S., *C. R. Geoscience* **346** (2014). [8] Badro, J., et al., *Nature* **536** (2016). [9] Hirose, K., et al., *Nature* **543** (2017). [10] O'Rourke, J., and Stevenson, D., *Nature* **529** (2016). [11] Olson, P., et al., *Phys. Earth Planet. Int.* **214** (2013).

## Hydrogen incorporation mechanisms in nominally anhydrous mantle minerals: NMR spectroscopy and first-principles calculation

Xianyu Xue<sup>1\*</sup> <sup>1</sup>Institute for Planetary Materials, Okayama University, Misasa, Tottori 682-0193, Japan.

\*email: xianyu@okayama-u.ac.jp

**Introduction.** Water, even when present in trace amounts in ‘nominally anhydrous’ major mantle minerals, could have significant effects on mantle properties. As the effects of water on mineral properties strongly depend on how it is incorporated in the crystal structure, a fundamental understanding of the structure is indispensable. Most of the studies on hydrogen incorporation in ‘nominally anhydrous’ minerals have been carried out using infrared spectroscopy, which revealed a number of bands in the 3300~3700  $\text{cm}^{-1}$  region due to O-H stretching vibrations that have been interpreted in terms of presence of H in Mg vacancies, and/or Si vacancies and/or interstitial sites. However, the spectral interpretations are often controversial. Solid-state NMR spectroscopy, in combination with first-principles calculations, on the other hand, has proven to be unique in unravelling detailed local structural information, including defect structures.

We have been applying a combined solid-state NMR and first-principles calculation approach to study hydrogen defects in major mantle minerals, such as olivine, pyroxene and garnet, and have gained much new insight that could not be readily obtained from other techniques. The information also shed light onto the interpretation of the corresponding infrared spectra. Here, I review some of our findings on  $\text{Mg}_2\text{SiO}_4$  forsterite (Xue, X., Kanzaki, M., Turner, D., and Loroeh, D. 2017 *Am. Mineral.*, 102, 519-536) and  $\text{MgSiO}_3$  enstatite (Xue X., Kanzaki M., Jiang J., Djirar A-E & Gregson C., in preparation), both synthesized at high pressures and temperatures.

**Experimental & Calculation Methods.** A  $\text{Mg}_2\text{SiO}_4$  forsterite sample containing about 0.5 wt%  $\text{H}_2\text{O}$  was synthesized at 12 GPa, 1200°C, and several  $\text{MgSiO}_3$  enstatite samples with 0.1 to 0.3 wt%  $\text{H}_2\text{O}$  were synthesized at a range of pressures between 7 and 14 GPa and 1200°C, all in a Kawai-type multi-anvil press. The recovered samples (to ambient condition) were confirmed to be nearly pure target phase.

$^1\text{H}$  MAS and static NMR spectra were obtained at ambient condition using a Varian 9.4 T Unity-Inova NMR spectrometer. First-principles calculations of NMR parameters were performed with the GIPAW method using the Quantum-ESPRESSO package. A number of model structures of  $2 \times 1 \times 2$  supercell for  $\text{Mg}_2\text{SiO}_4$  forsterite and  $1 \times 1 \times 2$  supercell for  $\text{MgSiO}_3$  enstatite, with one Si replaced by 4H ((4H)<sub>Si</sub> defect) or one Mg replaced by 2H ((2H)<sub>Mg</sub> defects) were studied. The structures were first fully relaxed before NMR calculation.

### Results and Discussions

*Mg<sub>2</sub>SiO<sub>4</sub> forsterite.*  $^1\text{H}$  static and MAS NMR spectra were obtained at spinning rates up to 30 kHz. The  $^1\text{H}$  static NMR spectrum contains both a broad and a narrower component. The  $^1\text{H}$  MAS NMR spectra also revealed two main components, a broader peak near 2.4 ppm that has extensive spinning sidebands and a narrower peak at 1.2 ppm with much less prominent spinning sidebands. There is also a very weak narrow peak near 7.3 ppm in the MAS NMR spectra.

First-principles calculation revealed that the lowest-energy structures for forsterite with a (4H)<sub>Si</sub> defect are characterized by having one H point away from the center of the tetrahedron and the rest near the vacant tetrahedra, which may account for the experimentally observed two main components in the  $^1\text{H}$  static and MAS NMR spectra, with the differences in peak width due to different extent of dipolar couplings; whereas the lowest-energy (2H)<sub>Mg</sub> defects matches well with the observed very weak narrow  $^1\text{H}$  NMR peak near 7.3 ppm. Thus, most of the hydrogen defects observed for forsterite synthesized at 12 GPa and 1200°C are in the form of (4H)<sub>Si</sub> defects, with only minor (2H)<sub>Mg</sub> defects.

*MgSiO<sub>3</sub> enstatite.* The  $^1\text{H}$  MAS NMR spectra for the enstatite samples synthesized at different pressures show systematic differences. The spectra for both orthoenstatite and clinoenstatite at 7 GPa are dominated by two narrow peaks near 5.8-5.9 and 7.8-7.6 ppm of equal intensities, whereas those of clinoenstatite (14 GPa) are much broader with peak maxima (or shoulders) recognized near 0.3, 3, 5.8, 8 and 12 ppm. The spectra for the intermediate pressure (12 GPa) contain both sets of components.

First-principles calculation suggests that the  $^1\text{H}$  NMR spectra for both orthoenstatite and clinoenstatite at 7 GPa are consistent with (2H)<sub>Mg</sub> defects; those of clinoenstatite (14 GPa) are consistent with (4H)<sub>Si</sub> as the predominant hydrogen defects, with broad  $^1\text{H}$  NMR peak width resulting from strong  $^1\text{H}$ - $^1\text{H}$  dipolar interactions from clustering of the 4H in the Si vacancy. The presence of  $^1\text{H}$  NMR peak of large chemical shift (12 ppm) for the latter suggests that some of the protons have strong hydrogen bonding, which is different from (4H)<sub>Si</sub> defects in forsterite that are characterized by weak hydrogen bonding and small  $^1\text{H}$  chemical shifts. This difference is explainable by the difference in connectivity of  $\text{SiO}_4$  tetrahedra between forsterite and enstatite.

**Acknowledgements.** This study has been supported by Kakenhi No. 17H01174 to X.X. The work reviewed here is the result of collaboration with M. Kanzaki, J. Jiang and participants of Misasa International Student Program ((2015: D. Turner & D. Loroeh: forsterite project; 2016: A-E. Djirar & C. Gregson: enstatite project).

## Probing hydrogen by single-crystal neutron diffraction in deep mantle hydrous minerals

N Purevjav<sup>1\*</sup>, T Okuchi<sup>1</sup>, N Tomioka<sup>2</sup>, X Wang<sup>3</sup> and C Hoffmann<sup>3</sup>

<sup>1</sup>Institute for Planetary Materials, Okayama University, Misasa, Tottori 682-0193, Japan.

<sup>2</sup>Kochi Institute for Core Sample Research, Japan Agency for Marine-Earth Science and Technology, Nankoku, Kochi 783-8502, Japan.

<sup>3</sup>Chemical and Engineering Materials Division, Neutron Sciences Directorate, Oak Ridge National Laboratory, Tennessee, TN 37831, USA.

\*email: narangoo@s.okayama-u.ac.jp

**Introduction:** Water in Earth's deep mantle minerals presents as structurally bound hydroxyls within their crystal lattices. Studying such water in the hydrous minerals provide significant information for understanding water inventory and transportation as well as its related geochemical and geophysical evolutions within the deep Earth. To obtain better understanding of the effects of such hydroxyls within the hydrous minerals, it is essential to thoroughly investigate hydrogen position, its occupancies and bonding geometries in the relevant mineral's crystal lattice. Single crystal neutron diffraction is the most suitable probe for investigating such hydrogen in the minerals with high precision, where the neutron is sensitive for light atoms such as hydrogen. Thus, we applied the method for the first time for the major water reservoirs of the deep mantle, which are mantle transition zone minerals hydrous wadsleyite [ $\beta$ -Mg<sub>2</sub>SiO<sub>4</sub>] and hydrous ringwoodite [ $\gamma$ -Mg<sub>2</sub>SiO<sub>4</sub>]. These studies are the first applications of single crystal neutron diffraction for the deep mantle hydrous minerals and aimed to investigate their hydrogen positions, occupancies and bonding geometries with high precision.

**Experimental:** Single crystals of hydrous wadsleyite and hydrous ringwoodite were synthesized by using a scaled-up Kawai type cell combining with our pre-established a slow-cooling method at their relevant pressure and temperature conditions of the deep mantle [1]. Synthesized crystals were confirmed to be chemically, physically and optically uniform by spectroscopic and diffraction techniques. The well characterized single crystals of these minerals were measured by neutron time of flight single-crystal Laue diffraction at Spallation Neutron Source, Oak Ridge National Laboratory. This state-of-the-art instrument was used to obtain datasets with a superior spatial resolution, even from the tiny crystal volume of these studies. The crystals were separately measured at 100 K, in different experimental periods. Each dataset was obtained over durations of two or three days.

**Results and Discussion:** Positions of hydrogen in wadsleyite and ringwoodite crystal lattices were contrasted by their negative scattering length density distributions in the observed difference Fourier maps. Such negative scattering lengths of hydrogen provides good contrast to accurately determine its position from the surrounding positive scattering length

density distributions of the other atoms (Mg, Si and O). We successfully determined atomic positions, occupancies, and temperature factors of the all the atoms without any constraints for these minerals crystal lattices. The determined H-O bond distances were 0.999(5) Å and 1.10(4) Å for wadsleyite and ringwoodite, respectively.

In wadsleyite, we investigated that there is only one hydrogen site within its crystal lattice and it was exchanged by the Mg cations at one of the specific M3 octahedra. From its refined hydrogen site occupancy, we calculated 1.36 wt.% of H<sub>2</sub>O in the current wadsleyite sample. By deducing the refinement result, we determined the maximum allowable H<sub>2</sub>O concentration in wadsleyite lattice, which was 3.33 wt.% [2]. There are no other hydrogen sites. In ringwoodite, we investigated that there were charge vacancies in both octahedral and tetrahedral sites, meanwhile the total charge vacancy was fully compensated by single hydrogen site locating only at octahedra. The calculated H<sub>2</sub>O was 1.9 wt.% in the current ringwoodite sample. The current structure refinement result suggests that H<sub>2</sub>O concentration in ringwoodite lattice is not explicitly constrained by the occupancy limitation of the hydrogen site itself. It suggests that the ringwoodite may contain even larger amount of H<sub>2</sub>O than that has been reported previously (max ~ 2.7 wt.% , by Ye et al., 2012).

Therefore, determined H<sub>2</sub>O concentrations in hydrous wadsleyite and hydrous ringwoodite by single crystal neutron diffraction were consistent with those of the estimated amounts by combination of IR, SIMS and x-ray diffraction works [2, 3]. Thus our studies suggest that single crystal neutron diffraction is potential choice for quantitatively analyzing the water in the minerals, even at level of a few wt.% concentrations.

By following the studies, we also applied the single crystal neutron diffraction for dense hydrous magnesium silicate phase E, which is the major reservoir of the water in the subducting slab. The details will be introduced in the talk.

**References:** [1] Okuchi, T. et al., *Am. Mineral.*, **100**, 1483 (2015). [2] Purevjav, N., Okuchi, T., Tomioka, N., Wang, X. and Hoffmann, C. *Sci. Rep.* **6**, 34988 (2016). [3] Purevjav, N., Okuchi, T., Wang, X., Hoffmann, C. and Tomioka, N. *Acta Cryst.* **B74**, 115 (2018).

## First principles determination of the dissociation boundary of phase H (MgSiO<sub>4</sub>H<sub>2</sub>) and possible existence of ice VII at lower mantle conditions.

J. Tsuchiya<sup>1\*</sup> and K. Umemoto<sup>2</sup> <sup>1</sup>Geodynamics Research Center, Ehime University, Japan. <sup>2</sup>Earth-Life Science Institute, Tokyo Institute of Technology, Japan  
\*email:junt@ehime-u.ac.jp

**Introduction:** It is believed that water is carried into the Earth's deep interior by hydrous minerals such as dense hydrous magnesium silicates (DHMSs) in the descending cold plate. A number of studies have been conducted to determine the high-pressure behaviors of DHMSs. In recent years, we discovered a new DHMS, phase H, stable at lower mantle pressure condition above ~ 40 GPa and the solid solution formed by phase H and  $\delta$ -AlOOH has been proposed as the most important carrier of water to the deepest part of Earth's mantle [1-3]. However, the MgSiO<sub>4</sub>H<sub>2</sub> phase H has been reported to decompose into H<sub>2</sub>O and MgSiO<sub>3</sub>-bridgmanite at relatively low pressure condition about 52 GPa at 0 K by first principles calculation [1]. High temperature dissociation phase boundary between phase H and MgSiO<sub>3</sub>+H<sub>2</sub>O has not been determined so far, since the hydrogen disordered ice VII phase is stabilized above ~100 K. Here we report the dissociation phase boundary of phase H at high pressure and temperature condition by determining the free energies of H<sub>2</sub>O ice-VII [4] and MgSiO<sub>3</sub> Bridgmanite and discuss the stability of H<sub>2</sub>O ice-VII in the mantle which is recently identified in the natural diamond inclusion [5] and possible scenario of the transportation of water into deep Earth interiors.

**Experimental:** Umemoto et al. 2010 successfully calculated the phase boundary of order-disorder phase transition between ice VII and VIII. Here we follow the same method to calculate Gibbs free energy of ice VII. The calculation of ice VII was modeled using supercell (2 × 2 × 2 unit cells) containing 16 H<sub>2</sub>O molecules. This supercell has 90 × 90 = 8100 possible hydrogen configurations, satisfying the ice rule. However, the number of the hydrogen configurations can be reduced to 52 after considering symmetry.

The first principles calculation is based on the density functional theory with the generalized gradient approximation (GGA) to the exchange-correlation functional. Norm conserving pseudopotentials were used and those potentials were extensively tested in previous studies. All structural parameters are fully relaxed at a static 0 K at 0, 10, 20, 30, 40, 50, 60, 80, 100 and 120 GPa using damped variable cell shape molecular dynamics implemented in the Quantum-Espresso codes.

In this study, 144 phonon frequencies of the ice supercell are calculated based on density functional perturbation theory (DFPT). Zone-center phonon mode ( $\Gamma$  point) is sampled for the calculation of partition function  $Z_{\text{QHA}}$ .

For the determination of dissociation phase boundary, we used the Gibbs free energy of phase H, CaCl<sub>2</sub>-type SiO<sub>2</sub>, and MgSiO<sub>3</sub> perovskite determined based on DFPT and QHA.

**Results and Discussion:** The present result indicates that the dissociation phase boundary of phase H intersects with cold geotherm around 60 GPa. Several previous melting temperatures of ice are higher than that of cold geotherm. Therefore, there is a possibility that the dissociation of phase H produces superionic ice phase at the middle of lower mantle around 1500 km depth. The crystal chemical reactions between superionic ice and surrounding minerals have not been solved yet. But high diffusivity of hydrogen in superionic ice may produce reaction faster than that in solid ice but different from water, liquid phase of H<sub>2</sub>O.

**References:** [1] Tsuchiya, J., *Geophys. Res. Lett.*, **40**, 4570. [2] Nishi, M. *et al.*, (2014), *Nature Geosci.* **7**, 224 (2013). [3] Ohira, I. *et al.*, *Earth Planet. Sci. Lett.*, **401**, 12 (2014) [4] Umemoto, K., *et al.*, *Chem. Phys. Lett.*, **499**, 236 (2010). [5] Tschauner, O. *et al.*, *Science*, **359**, 1136 (2018).

## High water solubility of ringwoodite at mantle transition zone temperature

Hongzhan Fei\*, Tomoo Katsura

Bayerisches Geoinstitut, University of Bayreuth, Bayreuth, D95447, Germany

\*email:Hongzhan.fei@uni-bayreuth.de

The mantle transition zone, a potential water reservoir in the Earth's interior, is suggested to contain more than 1 wt.% of water, at least locally, by the natural water-rich ringwoodite inclusion (Pearson et al. 2014), electrical conductivity (e.g. Kelbert et al., 2009), and mineral viscosity data (Fei et al. 2017). However, laboratorial mineral physics experiments showed that the water solubility in ringwoodite significantly decreases with increasing temperature. Although ringwoodite can store up to 2.6 wt.% water at relatively low temperatures (~1600 K), under the realistic mantle transition zone condition at ~2000 K, the water solubility is less than 0.3 wt.% (e.g., Ohtani et al. 2000), which is against the conclusion of water rich mantle transition zone. This argument implies that the water solubility in ringwoodite at transition zone temperatures might have been under estimated.

To clarify the water storage capacity of ringwoodite in the mantle transition zone, we revisited the water solubility in both Fe-free and Fe-bearing ringwoodite. Mixtures of MgO, SiO<sub>2</sub>, FeO, and Mg(OH)<sub>2</sub> powders with bulk compositions of Fo100, Fo90, and Fo75 plus 1.5 to 22 wt.% H<sub>2</sub>O were used as starting material. The mixtures were loaded in a PtRh capsule and annealed at 23 GPa, 1600-2000 K, for 0.7 to 6 hours. The run products appeared as coexisting of ringwoodite, hydrous melt, and akimotoite. The

water contents in ringwoodite were analyzed by Fourier transformation infrared spectroscopy with Koch-Muller and Rhede (2010) calibration.

The experimental results show that, although the water solubility in ringwoodite decreases with increasing temperature, even at 2000 K, both Fe-free and Fe-bearing ringwoodite can still store more than 1.0 wt.% H<sub>2</sub>O, much higher than those reported by Ohtani et al. (2000). The water solubility has negligible Fe-content dependence at 2000 K, whereas that in Fe-free ringwoodite is higher than Fe-bearing one at lower temperatures. The high water solubility at 2000 K agrees to the water-rich mantle transition zone inferred from mineral viscosity and the natural inclusion. The relatively low water content in ringwoodite reported in previous studies is probably due to disequilibrium with SiO<sub>2</sub> buffers or insufficient H<sub>2</sub>O in the starting materials.

### References:

- Pearson et al. (2014), *Nature* 507, 221.
- Kelbert et al. (2009), *Nature* 460, 1003.
- Fei et al. (2017), *Sci. Adv.* 3, E1603024.
- Ohtani et al. (2000), *PCM* 27, 533.
- Koch-Muller and Rhede (2010), *Am. Min.* 97, 770.

## In situ vibrational spectroscopy of the dehydration of talc in the system MgO-SiO<sub>2</sub>-H<sub>2</sub>O

Shigeru Yamashita<sup>1\*</sup>

<sup>1</sup>Institute for Planetary Materials, Okayama University, Misasa, Tottori 682-0193, Japan.

\*email:shigeru@misasa.okayama-u.ac.jp

Dehydration kinetics of talc is important to understand transport of H<sub>2</sub>O into the mantle wedge during subduction processes. Experimental results from in-situ observation of the dehydration of talc at 800 °C and 2.4 GPa under the presence of excess amounts of forsterite are presented.

**Experimental:** A pellet of 50/50 mixture (in weight proportion) of natural, stoichiometric-pure Mg-talc (<38 μm grain size) and synthetic forsterite together with distilled H<sub>2</sub>O was loaded in the Ir gasketed sample chamber of an externally heated hydrothermal diamond anvil cell (HDAC) fitted to micro-FTIR and micro-Raman spectrometers. Pressure in the HDAC was monitored with the pressure- and temperature-dependent Raman shift of the fundamental Si-O stretch vibration of forsterite (~857 cm<sup>-1</sup> at ambient condition, Gillet et al., 1991; Wang et al., 1993). To ensure the highest precision of the Raman shift, the 557 nm Kr line was acquired simultaneously as reference. Temperature was controlled to ±1 °C with chromel-alumel thermocouples in contact with the diamond anvils near the sample chamber. Near infrared (NIR) bands assigned to the combination modes of the fundamental Mg-O-H bending + stretch vibrations (~4200 to ~4400 cm<sup>-1</sup>, Madejova et al., 2011) and Raman band assigned to the fundamental Mg-O-H bending (~680 cm<sup>-1</sup>, Madejova et al., 2011) were recorded as a scale of the talc abundance.

**Results:** Upon heating to 800 °C, the sample chamber became thinner while the gasket deformed, which let the sample pellet in contact with both the upper and the lower diamond anvils. At 800 °C and 2.4 GPa, the talc NIR (**Fig. 1**) and Raman bands both monotonously decreased in the intensity with time while Raman bands due to the fundamental Si-O stretch of enstatite (~660, ~690, ~1010, and ~1040 cm<sup>-1</sup>, Huang et al., 2000) appeared and grew. No phase other than talc, forsterite, enstatite, and H<sub>2</sub>O fluid was observed during the experiment, which indicates that the dehydration reaction, talc + forsterite = 5 enstatite + H<sub>2</sub>O, was successfully reproduced. The time decay of the intensities of the talc NIR bands was adequately fitted by an Avrami (JMAK)-type sigmoidal curve with the exponent of

2 and the rate constant of  $2.1 \pm 0.2 \times 10^{-5} \text{ min}^{-2}$ . This translates into a half-lifetime of ~180 min for the talc (a half of the talc disappears in that time). This half-lifetime differs only a small factor from those obtained by previous works for the forsterite-deficient (silica-saturated) reaction, talc = 3 enstatite + quartz + H<sub>2</sub>O, under similar temperature conditions (e.g., Bose and Ganguly, 1994; Chollet et al., 2009).

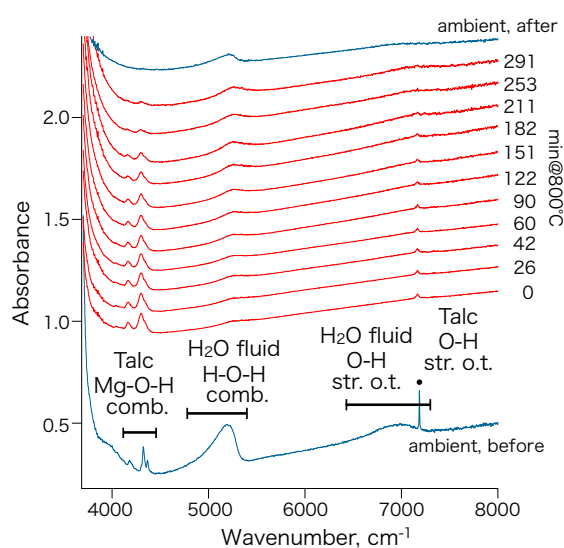


**Figure 1.** Time decay of the talc NIR bands of the sample pellet at 2.4 GPa and 800 °C. The NIR beam was aimed at 100 x 100 μm sample spot. Spectra are offset from each other in absorbance for clarity.

**References:** Bose and Ganguly, *Amer. Mineral.*, 79, 692-699, 1994; Chollet et al., *Earth Planet. Sci. Lett.*, 284, 57-64, 2009; Gillet et al., *J. Geophys. Res. Lett.*, 96, 11,805-11,816, 1991; Huang, et al., *Amer. Mineral.*, 85, 473-470, 2000; Madejova et al., *EMU Notes, Mineral.*, 9, 171-226, 2011; Wang et al., *Amer. Mineral.*, 78, 469-476, 1993.

## Structures of hydrous sodium silicate melts under high pressure and high temperature

T Ohashi<sup>1\*</sup>, T Sakamaki<sup>1</sup>, K Funakoshi<sup>2</sup>, M Muranushi<sup>1</sup>, C Shito<sup>1</sup>, Y Shibazaki<sup>3</sup> and A Suzuki<sup>1</sup> <sup>1</sup>Department of Earth Science, Graduate School of Science, Tohoku University, Sendai, Miyagi 980-8578, Japan. <sup>2</sup>Neutron Science and Technology Center, Comprehensive Research Organization for Science and Society (CROSS), Tokai 319-1106, Japan. <sup>3</sup>National Institute for Materials Science (NIMS), Tsukuba 305-0044, Japan.

\*email: tomonori.ohashi.s8@dc.tohoku.ac.jp

**Introduction:** The behaviors of high-pressure silicate melts, which is controlled by their physico-chemical properties, are important to understand the magma activity in the deep Earth. Particularly, the H<sub>2</sub>O content significantly affects the properties, such as density (e.g., [1]) and viscosity (e.g., [2, 3]). Since such macroscopic properties are known to be largely determined by the microscopic structure, there are considerable interests in revealing how the structures change with increasing pressure.

**Experimental:** We performed structural investigations of hydrous Na<sub>2</sub>O·8/3SiO<sub>2</sub> (NS8/3) melts containing 5 wt% (NS8/3\_H5) and 9 wt% H<sub>2</sub>O (NS8/3\_H9) were determined under high pressure and temperature conditions by the in-situ synchrotron X-ray diffraction (XRD). The dry NS8/3 glass was prepared by quenching a molten mixture of reagent powders SiO<sub>2</sub> and Na<sub>2</sub>CO<sub>3</sub>, and H<sub>2</sub>O was added as distilled water. The in-situ XRD study was conducted by using a cubic-type multi-anvil apparatus named MAX80 at the AR-NE5C beamline of PF-AR at KEK, Japan. The experimental pressure and temperature conditions were about 1.5–3.0 GPa and 550–970 °C, respectively. The design of our high-pressure cell assembly is based on the idea developed by Yamada and coworkers [4].

**Results and Discussion:** The total structure factors,  $S(Q)$  of both liquids show that the position of the first sharp diffraction peaks (FSDP) shift to higher- $Q$  with pressure. This positional shift indicates the intermediate-range order structure of present melts become compact. The obtained reduced radial distribution functions,  $G(r)$  are depicted in Fig. 1, and indicate different pressure evolutions in the average Si-O bond lengths ( $r_{\text{Si-O}}$ ) depending on their water contents. The  $r_{\text{Si-O}}$  in the NS8/3\_H9 liquid shows the monotonic decrease with increasing pressure, however, the  $r_{\text{Si-O}}$  of the NS8/3\_H5 liquid hardly changes after its contraction below 1.6 GPa. The structure of the NS8/3\_H9 melt is assumed to be slightly more depolymerized than the NS8/3\_H5 melt at ambient

pressure [5]. This difference might be due to a phenomenon that the number of strongly hydrogen-bonded SiOH groups, which are favored in the vitreous and molten sodium silicates [6], increase more significantly during pressure-induced ...SiOSi... network breakage in the molten NS8/3\_H9 than in the NS8/3\_H5 melt. This increases Si(-NBO)/Si(-BO) ratio (NBO: non-bridging oxygen, BO: bridging oxygen), so that the  $r_{\text{Si-O}}$  gets shorter.

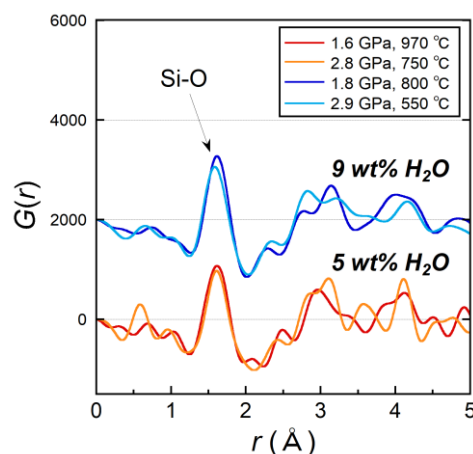


**Figure 1** The reduced radial distribution functions,  $G(r)$ , of the present melts at various pressure and temperature.

**References:** [1] Sakamaki, T., Suzuki, A. and Ohtani, E., *Nature*, **439**, 192 (2006). [2] Suzuki, A., Ohtani, E., Terasaki, H., Nishida, K., Hayashi, H., Sakamaki, T., Shibazaki, Y. and Kikegawa, T., *Phys. Chem. Miner.*, **38**, 59 (2011). [3] Poe, B.T., Romano, C., Liebske, C., Rubie, D.C., Terasaki, H., Suzuki A. and Funakoshi, K., *Chem. Geol.*, **229**, 2 (2006). [4] Yamada, A., Inoue, T., Urakawa, S., Funakoshi, K., Funamori, N., Kikegawa, T., Ohfuji, H. and Irifune, T., *Geophys. Res. Lett.*, **34**, L10303 (2007). [5] Zotov, N. and Keppler, H., *Am. Mineral.*, **83**, 823 (1998). [6] Xue, X. and Kanzaki, M., *Geochim. Cosmochim. Acta*, **68**, 5027 (2004).

## Simultaneous deformation of Calcium Perovskite and Pyrope

AR Thomson<sup>1\*</sup>, SA Hunt<sup>1</sup>, J Van Driel<sup>1</sup>, JP Brodholt<sup>1</sup> and DP Dobson<sup>1</sup>

<sup>1</sup>Department of Earth Sciences, University College London, UK.

\*email: a.r.thomson@ucl.ac.uk

**The DT cup apparatus:** The DT-cup [1,2] is a unique high-pressure deformation apparatus that uses a modified 6-8 split-cylinder geometry, and is capable of generating pressures of  $\sim 25$  GPa. At high-pressure conditions, modified wedges allow uniaxial shortening of the experimental assembly using differential actuators incorporated into main ram. This setup permits controlled strain-rate experiments to be performed to large total-strains. Housed in a modified V6 Paris-Edinburgh load frame, the DT-cup is small enough to be easily transported for *in-situ* diffraction experiments at European synchrotron sources. Beam-line I12 (JEEP), a multi-functional engineering beamline, at Diamond Light Source (DLS) is one such destination well-equipped to perform deformation experiments using monochromatic and/or white-beam X-rays. Here we present recent experiments performed at DLS to study the relative deformation behaviour of CaTiO<sub>3</sub> perovskite and pyrope garnet samples.

**Background:** Calcium perovskite and garnet are both major mineral components of the Earth's mantle that are particularly abundant in subducting assemblages. Subducting oceanic crust converts into eclogite and/or garnetite assemblages throughout upper mantle, and consists of up to 90% garnet by 500 km depth [3]. Subsequently calcium perovskite stabilises beyond  $\sim 600$  km, becoming the third most abundant mineral throughout the lower mantle, composing up to  $\sim 30\%$  of slab assemblages. Previous studies have suggested that garnet can be both stronger [4] or weaker [5] than olivine at upper mantle conditions, and that calcium perovskite is likely to develop the strongest seismic anisotropy due to LPO amongst common phase assemblages of the upper/lower mantle boundary region [6]. However, despite their high abundances and potential importance in understanding subduction dynamics, relatively little is known about the rheological properties of either calcium perovskite or garnet throughout mantle conditions. *In-situ* deformation experiments provide simultaneous measurements of stress and strain-rate, enabling a quantitative determination of rheological properties at mantle conditions.

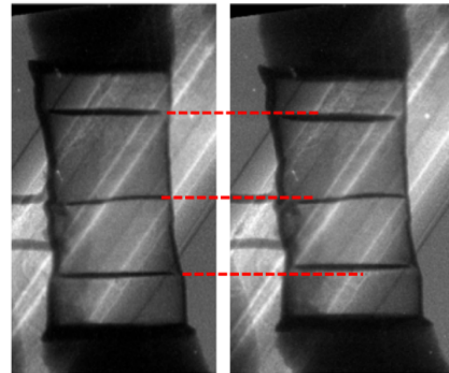


**Figure 1.** X-ray radiographs of CaTiO<sub>3</sub> (upper sample) and pyrope (lower sample) before (left) and during (right) deformation at high pressure-temperature conditions.

**Experimental techniques:** Fine-grained powders of synthetic CaTiO<sub>3</sub> and natural pyrope garnet (Dora Maira) were loaded into 7/3 multi-anvil assemblies. Thin Au marker foils were placed at either end of each sample to monitor strain throughout the experiments and Molybdenum furnaces were used to generate high temperatures, which were monitored using radial thermocouples terminating near the sample position. During initial experiments, conditions of up to  $\sim 6$  GPa and temperatures up to  $\sim 1600$  K were investigated. Angle dispersive diffraction patterns, generated by the diffraction of monochromatic x-rays ( $\lambda \sim 0.22\text{\AA}$ ) from each sample in turn, were collected using a Pilatus 2M CdTe detector. Diffraction patterns were collected alternately with radiographic images of the sample lengths (Figure 1). Combining both measurements allows simultaneous monitoring of both stress, strain and *in-situ* texture development in calcium perovskite and pyrope garnet samples, which deformed at strain rates between  $2 \times 10^{-6}$  and  $1 \times 10^{-5} \text{ s}^{-1}$ .

**References:** [1] Hunt, S.A. et al. (2014) *Reviews of Scientific Instruments*, 85, 085103. [2] Hunt, S.A. & Dobson, D.P. (2017) *Reviews of Scientific Instruments*, 88, 126106. (2017). [3] Stixrude, L., and Lithgow-Bertelloni, C. (2012) *Annual Review of Earth and Planetary Sciences*, 40, 569–595. [4] Li, L. et al. (2006) *American Mineralogist*, 91, 517–525. [5] Hunt, S.A. et al. (2010) *Physics of the Earth and Planetary Interiors*, 179, 87–95. [6] Kawai, K., and Tsuchiya, T. (2015) *Geophysical Research Letters*, 42, 2718–2726.

## D111-type apparatus for high-pressure deformation experiments and its application to a rheological study of hcp-iron

Y. Nishihara<sup>1\*</sup>, S. Doi<sup>1</sup>, D. Yamazaki<sup>2</sup>, N. Tsujino<sup>2</sup>, T. Yoshino<sup>2</sup>, T. Kubo<sup>3</sup>, and M. Imamura<sup>3</sup>

<sup>1</sup>Geodynamics Research Center, Ehime University, Matsuyama, Ehime 790-8577, Japan.

<sup>2</sup>Institute of Planetary Materials, Okayama University, Misasa, Tottori 682-0193, Japan.

<sup>3</sup>Department of Earth and Planetary Sciences, Kyushu University, Fukuoka 819-0395, Japan.

\*email: yunishi@sci.ehime-u.ac.jp

**Introduction:** To study rheological properties of materials in the Earth's deep interior, high-pressure deformation experiments have been carried out using various deformation devices including rotational Drickamer apparatus [1] and deformation-DIA apparatus [2]. A new type apparatus, deformation T-Cup (DT-Cup), which is based on Kawai-type multi-anvil apparatus, was developed by Hunt et al. [3]. In the DT-Cup, by driving two second-stage anvils using differential actuators, well-controlled deformation experiments can be conducted up to confining pressure of 18 GPa. However, more improvement was needed to achieve experiments at the condition of the Earth's lower mantle ( $P > 23$  GPa).

To study the rheological properties at the lower mantle condition experimentally, we have installed a "D111-type apparatus" that is an improved version of DT-Cup with larger dimension. This apparatus has been used to study rheological behavior of the deep Earth materials including hcp-iron, bridgmanite and ringwoodite. In this presentation, we introduce specification of the D111-type apparatus and recent results obtained by using this apparatus.

**Experimental:** A D111-type guide-block (Fig. 1) was installed on a synchrotron beamline NE7A at PF-AR, KEK, Tsukuba, Japan in 2017. Combining this guide-block with the MAX-III press, it acts as a deformation apparatus "D111-type apparatus". The D111-type apparatus can be used under maximum press load of 700 tonf which enables us to conduct quantitative deformation experiments at the lower mantle pressures.

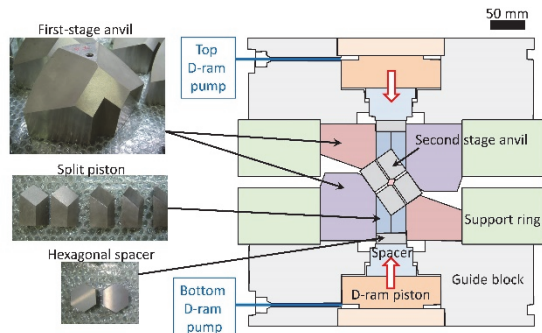


**Figure 1** Schematic illustration of D111-type guide-block.

High-pressure was generated using Kawai-type assembly with octahedral pressure medium and eight second stage anvils. Deformation experiments were

conducted by advancing top and bottom differential-rams (D-ram) at high pressure and high temperature conditions. Sample stress was measured by two-dimensional X-ray diffraction using monochromatized synchrotron X-ray (50–60 keV) and CMOS X-ray detector (Dexela 2923). Sample strain was measured by X-ray radiography.

**Results and Discussion:** Well-controlled deformation experiments with constant strain rate was achieved at press load up to 350 tonf. Maximum pressure and temperature in deformation experiments are  $\sim 27$  GPa and  $\sim 1700$  K, respectively. Maximum pressure exceeds 30 GPa at room temperature before heating. These clearly show capability of deformation experiments at the lower mantle conditions.

Based on the uniaxial deformation experiments of hcp-iron (Fig. 2), steady state stresses were determined under conditions up to 22.6 GPa and 873 K. A preliminary analysis of these data suggests that power-law dislocation creep with stress exponent of  $\sim 5$  is dominant at  $>700$  K whereas power-law breakdown occurs at lower temperatures. However, more experimental data are required to give an accurate constraint on the inner core viscosity.

We have also carried out deformation experiments on the other deep Earth materials including bridgmanite and ringwoodite. Results from these experiments will be briefly given in presentation.

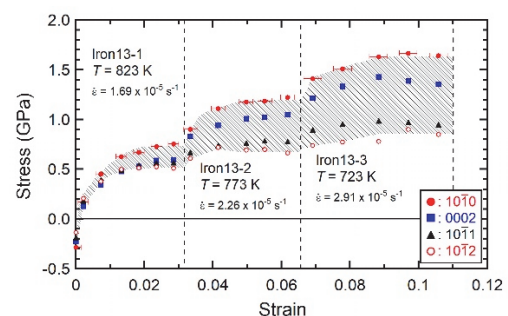


**Figure 2** Stress-strain relationship in a temperature-step deformation experiment of hcp-iron at  $P = 16.3\text{--}16.5$  GPa,  $T = 723\text{--}823$  K and uniaxial strain rate of  $\sim 2 \times 10^{-5} \text{ s}^{-1}$ .

**References:** [1] Yamazaki, D. et al., *Rev. Sci. Inst.*, **72**, 4207 (2001). [2] Wang, Y. et al., *Rev. Sci. Inst.*, **74**, 3002 (2003). [3] Hunt, S. et al., *Rev. Sci. Inst.*, **85**, 085103 (2014).

## Creep strength of bridgmanite

N Tsujino<sup>1\*</sup>, D Yamazaki<sup>1</sup>, Y Nishihara<sup>2</sup>

<sup>1</sup>Institute for Planetary Materials, Okayama University, Misasa, Tottori 682-0193, Japan.

<sup>2</sup>Geodynamics Research Center, Ehime University, Matsuyama, Ehime 790-8577, Japan.

\*email:tsujino@okayama-u.ac.jp

**Introduction:** One dimensional viscosity models of the Earth's mantle proposed by geophysical observations [e.g., 1] suggested that the lower mantle had the largest viscosity in the Earth's mantle. In order to understand mantle dynamics in the Earth's interior, it is important to know the viscosity of the Earth's lower mantle. However, there are large variations of viscosity in the lower mantle between suggested models because of limitation of locations for geophysical observations. Therefore it is important to determine viscosity of lower mantle minerals by high pressure experiments in order to discuss mantle dynamics. Bridgmanite would be the most abundant mineral in the lower mantle. This mineral could dominate the lower mantle viscosity. In this study, we conducted in-situ stress-strain measurements of uniaxial deformation experiments of bridgmanite aggregate using D-111 type high pressure apparatus.

**Experimental:** In-situ measurements were conducted using MAX III with D111 type guide block at PF-AR NE7A beam line. Mg-pure bridgmanite aggregates were used as starting material. Experimental conditions are 1473-1673 K and 24-27 GPa. Strain of bridgmanite was measured by X-ray radiographies taken using an imaging system composed of a YAG crystal and a CMOS camera. WC second cubic anvils with cone (6.5°) to take 2D X-ray diffraction, was used along X-ray path. Two-dimensional X-ray diffraction patterns were corrected for 240 s using flat panel detector. To calculate pressure and the stress magnitude of bridgmanite, (112) X-ray diffraction peaks were used.

**Results and Discussion:** Largest strain was reached to approximately 20%. It is confirmed that strain rate can be well controlled using stroke speed of differential rams. Steady state creep were observed at 1473 K – 1673 K and  $5 \times 10^{-6} - 3.8 \times 10^{-5}$  /s. The creep strength of bridgmanite in this study is the largest in constituent mantle minerals reported by D-DAI apparatus at  $10^{-5}$  /s.

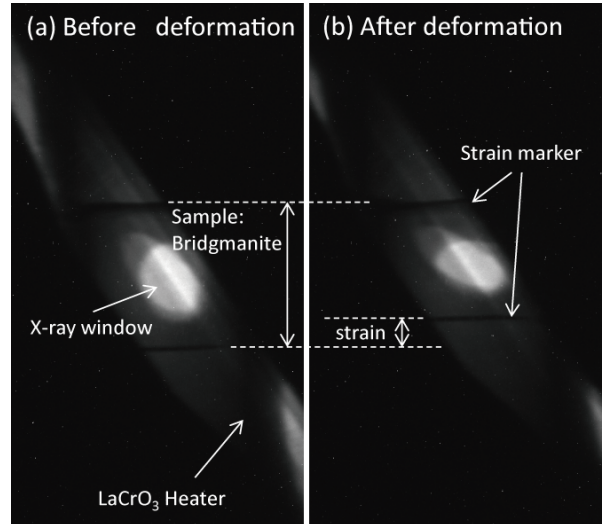


**Figure 1** X-ray radiographs of (a) before deformation and (b) after deformation.

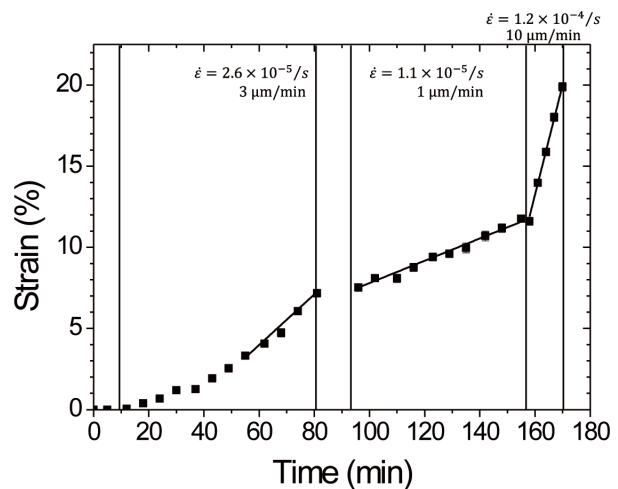


**Figure 2** Strain versus time for deformation experiments. This experiment consists of the tests with three different strain rates

**References:** [1] [1] A.M. Forte & J.X. Mitrovica, *Nature*, 410, 1049-1056, 2001.

# Ab-Initio Investigation of Iron Self-Diffusion: Implications for the Plasticity of Earth's Inner Core

<sup>1,\*</sup>S. Ritterbex and <sup>1</sup>Taku Tsuchiya,

<sup>1</sup>Geodynamics Research Center, Ehime University 2-5 Bunkyo-cho, Matsuyama, Ehime 790-8577, Japan, \*email: ritterbex.sebastian\_arthur\_willem.us@ehime-u.ac.jp

The mechanical properties of Earth's inner core are essential for understanding the evolution and dynamics of the core. However, little is known about the mechanical properties of iron at inner core conditions. Therefore, long-standing questions remain open about the viscous strength of the inner core (Yoshida et al., 1996; Karato, 1999), about the origin of its seismic anisotropy (Deuss, 2014) and about its rotational dynamics (Buffett, 1997). All these issues rely on plastic deformation of the inner core, which is barely constrained.

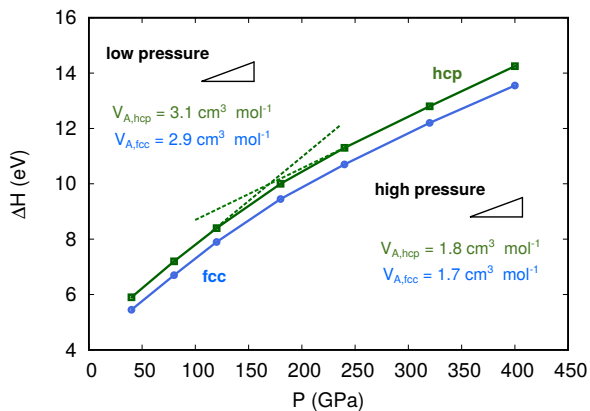


**Figure 1:** Defect energetics as a function of pressure for hcp and fcc iron. The tangents to the curves represent the activation volume of vacancy diffusion at the appropriate pressures.

Under conditions of the Earth's deep interior, the rate of plastic deformation is expected to be constrained by atomic diffusion. Experimental studies on diffusion in iron-nickel alloys at elevated pressure and temperature conditions finally rely on extrapolation to inner core conditions (Yunker and Van Orman, 2007; Reaman et al., 2012). Here, we investigate vacancy diffusion in iron at the appropriate inner core conditions. We use a density

functional approach to calculate all quantities entering the diffusion coefficient, including the role of pressure (Fig. 1) and temperature, and quantify the self-diffusion coefficient of hcp iron according to transition state theory (TST).

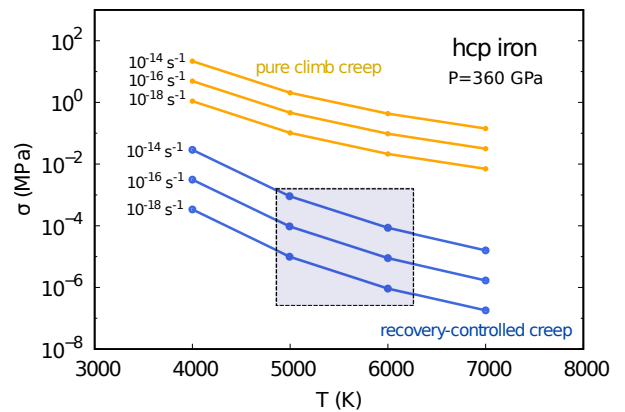


**Figure 2:** Deformation mechanism map including the rate-limiting bounds for climb-controlled dislocation creep in hcp iron at 360 GPa. The blue rectangle suggests the most likely mechanism to operate under conditions of the inner core.

Vacancy diffusion controls many deformation mechanisms such as dislocation creep, an effective strain producing mechanism in metals. We derived a creep model (Weertman, 1955; Nabarro, 1967) to quantify the rate limiting bounds of climb-controlled dislocation creep in hcp iron and provide the first theoretical estimates of the inner core viscosity (Fig. 2).

## Imaging subducted slabs in the mantle from inversion of seismic waveforms

Kenji Kawai<sup>1\*</sup>, Anselme Borgeaud<sup>1</sup>, Yuki Suzuki<sup>1</sup> <sup>1</sup>Department of Earth and Planetary Science, University of Tokyo, Tokyo 113-0033, Japan \*email:kenji@eps.s.u-tokyo.ac.jp

**Introduction:** Seismic tomographic studies have inferred the three-dimensional seismological structure in the Earth's deep interior [e.g., 1, 2]. Some subducted slabs are found to be stagnant above or below 660 km discontinuity, while others fall through the lower mantle and reach the lowermost mantle (see [3] for details), suggesting the whole-mantle convection rather than the layered mantle convection. Recent waveform inversion studies with better resolution especially for the low velocity anomaly have found vertically continuous low-velocity columns in the lower mantle and suggested that the thermochemical plumes rooted in the D" region are associated with the prominent hotspots [4]. Hence, seismic tomographic studies have contributed to understanding the mantle convection.

It has been, however, difficult to estimate how long it takes for the Earth's mantle to migrate between the Earth's surface and the core-mantle boundary (CMB) since the seismic tomographic studies provide information on the current Earth's deep interior. In order to better understand the Earth's evolution and dynamics dating inside the Earth is essential. Therefore, we try to infer the detailed seismic velocity structure in the mantle transition zone and D" region beneath Central America and the Northern Pacific because continuous subduction of oceanic plates beneath the North and South American plates has been taking place since more than 200 Myr ago [5] and investigate the fate of subducted oceanic lithosphere and the thermal and chemical evolution of the Earth.

**Data and Method:** The used events are deep- and intermediate-focus events recorded at broadband seismic stations of the USArray, Canadian Northwest Experiment (CANOE), Global Seismographic Network (GSN-IRIS/USGS), Southern California Seismic Network (SCSN), Pacific Northwest Seismic Network (PNSN), Berkeley Digital Seismic Network (BDSN), and Canadian National Seismograph Network (CNSN). The data are filtered in the period range of 8 or 12.5 to 200 s using a Butterworth bandpass filter. The 3D model is obtained by linearized inversion with respect to a spherically symmetric initial model.

We formulated the inverse problem of waveform inversion for localized 3-D seismic structure, computing partial derivatives of waveforms with respect to the elastic moduli at arbitrary points in

space for anisotropic and anelastic media [6, 7] and applied our method to the assembled dataset to invert for 3-D shear wave structure

**Results and Discussion:** The inferred model showed the presence of two distinct slabs at the CMB beneath Central America and Venezuela and one prominent slab beneath the Northern Pacific due to subduction 200 Myr ago [5], and how these slabs possibly modulate the formation of passive upwelling (called "passive plume") of hot basal mantle material [8, 9]. It then showed how such plumes interact with slabs subducting in the upper mantle and tearing of the subducted slab takes place based on high-resolution seismic images [10].

The inferred imaging enables us to date the slab at some depth taking into account the geological events investigated based on plate reconstruction and estimate a viscosity contrast between the upper and lower mantle of 9-12, which is about 5 times smaller than that estimated from post-glacial rebound [11, 12]. Also, it implies that subduction from the Earth's surface down to the base of the mantle affects the surface environment in two ways: 1) intermittent and localized subduction to the base of the mantle cools down the CMB, influencing convection in the outer core, and thus the geodynamo and geomagnetic field. Increased heat flux from the core to the mantle can trigger geomagnetic reversal; 2) Subduction to the CMB modulate the formation of passive plumes, which if they reach the Earth's surface lead to volcanism that can affect the composition of the atmosphere and temperature of the Earth's surface. This study suggests the coupling between Earth's deep mantle and Earth's surface.

**References:** [1] Romanowicz, B., *Annu. Rev. Earth Planet. Sci.*, **31**, 303–28, 2003. [2] Dziewonski, A.M. et al., *EPSL*, **299**, 69–79, 2010. [3] Fukao, Y. et al., *Annu. Rev. Earth Planet. Sci.*, **37**, 19–46, 2009. [4] French, S.W., & Romanowicz, B., *Nature*, **525**, 95–99, 2015. [5] Müller, R.D. et al., *Annu. Rev. Earth Planet. Sci.*, **44**, 107–138, 2016. [6] Kawai, K. et al., *GJI*, **197**, 495–524, 2014. [7] Konishi, K. et al., *GJI*, **199**, 1245–1267, 2014. [8] Suzuki, Y. et al., *EPS*, **68**:198, 2016. [9] Borgeaud, A.F.E., et al., *Sci. Adv.*, **3**, e1602700, 2017. [10] Borgeaud, A.F.E., *PhD Thesis, Univ. Tokyo*, 2019. [11] Hager, B., *JGR*, **89**, 6003–6015, 1984. [12] Forte, A. M., & Mitrovica, J. X., *Nature*, **410**, 1049–1056, 2001.

## Electrical resistivity and thermal conductivity of fcc Fe: Implications for the Mercury's core

H Gomi<sup>1\*</sup>, T Yoshino<sup>1</sup> <sup>1</sup>Institute for Planetary Materials, Okayama University, Misasa, Tottori 682-0193, Japan.  
\*email:hitoshi.gomi@okayama-u.ac.jp

**Introduction:** The Mercury's magnetic field may be sustained by the geodynamo motion in the liquid Fe core. However, its strength is about 1% of that of Earth. This weak magnetic field may imply a partly stratified core [1, 2]. Gomi et al. [3] pointed out that the geometry of the thermal stratification depends critically on the depth dependency of the thermal conductivity. In this study, we conducted first-principles calculations on the face-centered cubic (fcc) Fe to constrain the electrical resistivity and the thermal conductivity of the Mercury's core.

**Methods:** We calculated the electrical resistivity and the thermal conductivity of fcc Fe by means of the Korringa-Kohn-Rostoker method combined with the coherent potential approximation (KKR-CPA) [4]. The CPA was adopted to treat the disorder effects due to the atomic vibrations and the magnetic fluctuations on the electronic band structure [5-7]. Within the alloy analogy model, the thermal atomic displacements were represented by a discrete set of  $N_v$  displacement vectors  $\Delta R_v(T)$ , where  $|\Delta R_v(T)| = \sqrt{\langle u^2 \rangle}$  is the root mean square displacement of atoms, which is based on the Debye model without zero point vibration. The lattice parameter and the Debye temperature are obtained from the equation of state of fcc Fe [8]. In addition to the non-magnetic state, the magnetic disorder was simulated by the local magnetic disorder (LMD) approach. The conductivity was calculated by the Kubo-Greenwood formula with the vertex correction.

**Results and Discussion:** The calculated electrical resistivities and thermal conductivities with LMD state are consistent with the literature data at 0 GPa [9, 10], whereas the non-magnetic results show smaller resistivity and larger thermal conductivity. This suggests the importance of the magnetic scattering at low pressures. However, our calculation predicts that the magnetic contribution banishes at higher pressures than 20 GPa. Figure 1 compares the present results and previous experiments [11-14] on the electrical resistivity at  $\sim 5$  GPa. Note that, within the fcc stability field, previous measurements have a large variation. Our calculated resistivity values are between Secco and Schloessin [11] and Silber et al. [14].

We further calculated the electrical resistivity and the thermal conductivity of fcc Fe up to 50 GPa and 3000 K. The thermal conductivity increases with increasing pressure and temperature (Figure 2). This means that, if the inner core is absent, the thermal stratification starts from the bottom, and, after the onset of the inner core, a thick thermal stratified layer may develop at the top of the fluid core [3].

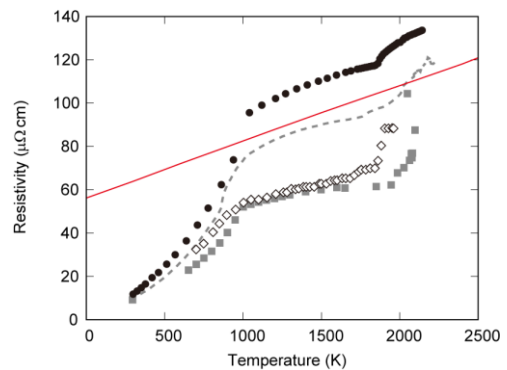


**Figure 1** Electrical resistivity of Fe at  $\sim 5$  GPa. Red solid line indicates the present calculations of fcc Fe with LMD. Gray broken line, gray squares, open diamonds, and black circles are previous experiments by Secco and Schloessin [11], Deng et al. [12], Pommier [13] and Silber et al. [14], respectively.

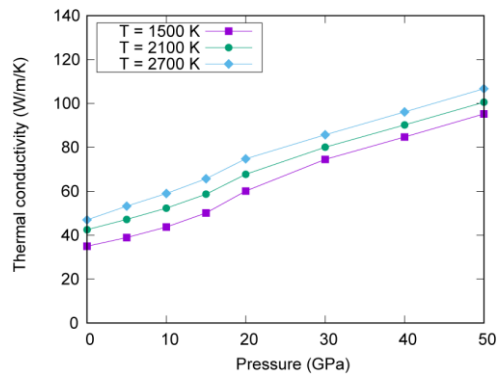


**Figure 2** Thermal conductivity of fcc Fe at high pressure and temperature. Thermal conductivity increases with increasing pressure and temperature.

**References:** [1] Christensen, U. R., *Nature*, **444**, 1056 (2006). [2] Stanley, S., et al., *Earth Planet. Sci. Lett.*, **234**, 27, (2005). [3] Gomi, H., et al., *Phys. Earth Planet. Inter.*, **224**, 88, (2013). [4] Akai, H., *J. Phys.: Cond. Matt.*, **1**, 8045, (1989). [5] Glasbrenner, et al., *Phys. Rev. B*, **89**, 174408, (2014). [6] Ebert, H., *Phys. Rev. B*, **91**, 165132, (2015). [7] Kou, S., and Akai, H., *Solid Stat. Commun.*, **276**, 1, (2018). [8] Tsujino, N., et al., *Earth Planet. Sci. Lett.*, **375**, 244, (2013). [9] Ho, C. Y., et al., *J. Phys. Chem. Ref. Data*, **1**, 279, (1972). [10] Ho, C. Y., et al., *J. Phys. Chem. Ref. Data*, **12**, 183, (1983). [11] Secco, R. A., Schloessin, H. H., *J. Geophys. Res.*, **94**, 5887, (1989). [12] Deng, L., et al., *Geophys. Res. Lett.*, **40**, 33, (2013). [13] Pommier, A., *Earth Planet. Sci. Lett.*, **496**, 37, (2018). [14] Silber, R. E., et al., *Sci. Rep.*, **8**, 10758, (2018).

## Study on transport properties of liquid iron and iron alloy under high temperature and high pressure using the laser shock technique

K Miyanishi<sup>1\*</sup>, N Ozaki<sup>1,2</sup>, S Ohmura<sup>3</sup>, M Harmand<sup>4</sup>, A Krygier<sup>5</sup>, T Nishikawa<sup>2</sup>, Y Umeda<sup>2</sup>, K Shigemori<sup>1</sup>, Y Sakawa<sup>1</sup>, T Sano<sup>1</sup> and R Kodama<sup>1,2</sup>

<sup>1</sup>Institute of Laser Engineering, Osaka University, <sup>2</sup>Graduate school of engineering, Osaka University, <sup>3</sup>Faculty of Engineering, Hiroshima Institute of Technology, <sup>4</sup>IMPMC, Sorbonne Université, <sup>5</sup>LLNL

\*email:miyanishik@ile.osaka-u.ac.jp

**Introduction:** Information on the thermal and electrical transport properties of iron alloys under high-pressure and high-temperature conditions corresponding to the earth's outer core is necessary to clarify the convection phenomena of the earth and the cooling history. In particular, the transport properties in the outer core–mantle boundary condition strongly influence the mantle convection, the outer core convection generating the earth's magnetic field, the growth and inner flow of the inner core, and so on. However, there are very few experimental examples concerning high-pressure and high-temperature liquid iron/iron-alloy which correspond to the outer core conditions, and only a few cases have been reported for pure iron [1]. It is required to investigate transport coefficients of liquid iron alloys containing light elements to simulate actual outer core, experimentally. The laser shock technique has several advantages to exploring iron-alloys under high-pressure and high-temperature condition. As there is no mechanical restriction on pressure generation, producing the pressure of even TPa is easy, and high heating rate exceeding  $10^{15}$  K / s is possible, and it is a closed system that is not affected by surroundings. Therefore the technique is effective for generation and observation of high-pressure and high-temperature liquid iron-alloys. In this research, we report electrical conductivity deduced from optical reflectivity, pressure and temperature measurements of laser shock compressed iron and iron-silicon (Fe-Si) alloy at and above the earth's outer core conditions.

**Experimental:** Target assemblies containing polypropylene (CH), aluminum, quartz, iron or iron-

silicon alloy and magnesium oxide (MgO) window were shock compressed by the laser shock technique at the GEKKO XII laser facility, the Institute of Laser Engineering, Osaka University. Iron and iron-silicon alloy were formed by electron beam evaporation on the MgO window. Laser beams with a wavelength of 527 nm were focused onto the target. A focal spot was 1 mm in diameter with a flat-top spatial intensity distribution resulting in a planar shock front. Temporal shape of the laser pulse was approximately a flat-top with a full-width at half-maximum of 2.5 ns. The velocity interferometer system for any reflector (VISAR) measures a particle velocity and a reflectivity at the interface between iron or iron-silicon alloy and MgO. The pressure was evaluated using measured particle velocity and a known equation of state of MgO[2]. The optical pyrometer measures the temperature at the interface through the MgO window.

**Results and Discussion:** The pressures determined from the measurement results were from 200 to 400 GPa, and the temperatures were up to 15000 K. We observed, in the case of iron, a decrease in reflectivity as the pressure increased, whereas in the case of the iron-silicon alloy, a continuous increase following a discontinuous decrease at around 250 GPa in the reflectivity. These results suggest that the trends in change of electrical conductivity in iron and iron-silicon alloy are significantly different in the pressure and the temperature conditions.

**References:** [1] K. Ohta, Y. Kuwayama, K. Hirose, K. Shimizu, Y. Ohisi: *Nature*, **534**, 95 (2016). [2] S. Root, L. Shulenburg, R. W. Lemke et al.: *Phys. Rev. Lett.*, **115**, 198501 (2015).

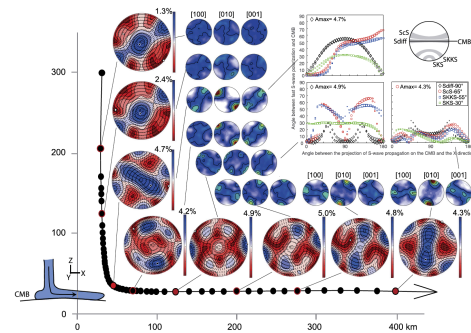
## Deformation, crystal preferred orientations, and seismic anisotropy in the Earth's D'' layer

D. Mainprice\*Geosciences Montpellier, CNRS & Université de Montpellier, F-34095 Montpellier cedex 5, France.

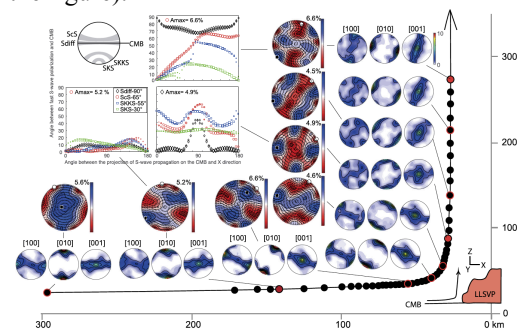
\*email: david.mainprice@umontpellier.fr

We use a forward multiscale model that couples atomistic modeling of intracrystalline plasticity mechanisms (dislocation glide  $\pm$ twinning) in MgSiO<sub>3</sub>post-perovskite (PPv) and periclase (MgO) at lower mantle pressures and temperatures to polycrystal plasticity simulations to predict crystal preferred orientations (CPO) development and seismic anisotropy in D''. We model the CPO evolution in aggregates of 70% PPv and 30% MgO submitted to simple shear, axial shortening, and along corner-flow streamlines, which simulate changes in flow orientation similar to those expected at the transition between a downwelling and flow parallel to the core–mantle boundary (CMB) within D'' or between CMB-parallel flow and upwelling at the borders of the large low shear wave velocity provinces (LLSVP) in the lowermost mantle. Axial shortening results in alignment of PPv [010] axes with the shortening direction. Simple shear produces PPv CPO with a monoclinic symmetry that rapidly rotates towards parallelism between the dominant [100](010) slip system and the macroscopic shear.

These predictions differ from MgSiO<sub>3</sub>post-perovskite textures formed in diamond-anvil cell experiments, but agree with those obtained in simple shear and compression experiments using CaIrO<sub>3</sub> post-perovskite. Development of CPO in PPv and MgO results in seismic anisotropy in D''. For shear parallel to the CMB, at low strain, the inclination of ScS, Sdiff, and SKKS fast polarizations and delay times vary depending on the propagation direction. At moderate and high shear strains, all S-waves are polarized nearly horizontally. Downwelling flow produces Sdiff, ScS, and SKKS fast polarization directions and birefringence that vary gradually as a function of the back-azimuth from nearly parallel to inclined by up to 70° to CMB and from null to ~5%. Change in the flow to shear parallel to the CMB results in dispersion of the CPO, weakening of the anisotropy, and strong azimuthal variation of the S-wave splitting up to 250 km from the corner.



Evolution of the PPv CPO and of the S-waves polarization anisotropy predicted for the 70% PPv +30% MgO aggregate along a corner flow line simulating the change in flow direction associated with the transition from a downwelling to shearing parallel to the CMB (cf. sketch at the bottom left of the figure).



Evolution of the PPv CPO and of the S-waves polarization anisotropy predicted for the 70% PPv +30% MgO aggregate along a corner flow line simulating the change in flow direction associated with the transition from shearing parallel to the CMB to upwelling at the border of a LLSVP (cf. sketch at the bottom right of the figure)

Transition from horizontal shear to upwelling also produces weakening of the CPO and complex seismic anisotropy patterns, with dominantly inclined fast ScS and SKKS polarizations, over most of the upwelling path. Models that take into account twinning in PPv explain most observations of seismic anisotropy in D'', but heterogeneity of the flow at scales <1000 km is needed to comply with the seismological evidence for low apparent birefringence in D''. account twinning in PPv explain most observations of seismic anisotropy in D'', but heterogeneity of the flow at scales <1000 km is needed to comply with the seismological evidence for low apparent birefringence in D''

**Reference:** Tommasi A. et al. *Earth and Planetary Science Letters* 492 (2018) 35–46.

## Azimuthal anisotropy in the lowermost mantle beneath Philippine from ScS–S travel times

S Tanaka<sup>1\*</sup> <sup>1</sup>D-Earth, JAMSTEC, 2-15 Natsushima-cho, Yokosuka, 237-0061, Japan.

\*email: stan@jamstec.go.jp

**Introduction:** Seismic anisotropy in the lowermost mantle has been detected by splitting of diffracted S and ScS phases, the discrepancy of shear wave splitting of SKS and SKKS, to date. In many cases, the propagation direction of such seismic waves is restricted due to the combination of sources and receivers. Thus, the azimuthal anisotropy using ray paths passing in multi-directions has been rarely discussed. Now, seismic networks and large-scale seismic arrays have been increasing especially in the eastern Asia where there are also many earthquakes. It is a good opportunity to examine an azimuthal variation of travel times passing through the outside of the Pacific Large Low Shear Velocity Province, where the existence of anisotropy in the lowermost mantle is expected.

**Data and Method:** I used the seismograms of earthquakes occurred in Mariana, east China, Indonesia, and Vanuatu that are record with the seismic stations belonging to IRIS GSN and PASSCAL, Thai Metrological Department, F-net, JISNET, NECESSArray (Fig.1). This geometry gives a good condition that the mid-points of seismic ray paths are located near Philippine with various azimuths.

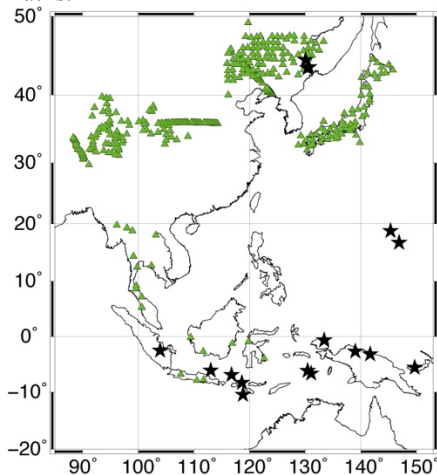


**Figure 1** Distribution of hypocenters (solid stars) and stations (green triangles).

I measured ScS–S differential travel times using a waveform cross-correlation method, which can effectively cancel the heterogeneity in the crust and upper mantle and the uncertainty of hypocenters. The differential travel times are compared with theoretical travel times by PREM [1] with correction of physical dispersion due to anelasticity for the typical period of 10 s, that for ellipticity of the Earth [2], finally I obtained about 500 residuals. Even though I used the differential travel times, the ScS–S residuals show the large scattering and the correlation with the residuals

of S travel times are much larger than that of ScS phases. This means that the raw ScS–S residuals are affected by heterogeneity in the upper part of the lower mantle where only S waves are propagated. Thus, we applied the further corrections using 3D mantle heterogeneity models.

**Results and Discussion:** We used S-wave 3D models of S16U6L8 [3], S4BL16 [4], S40RTS [5], SEMUCB-WM [6], and a P-wave 3D model of GAP-P4 [7] with conversion rate  $d\ln V_s/d\ln V_p=1.7$  [8]. I found that the scatter of the ScS–S residuals are much improved and that the correlation coefficient between the residuals of ScS–S and ScS are increased and that between ScS–S and S are much reduced when the GAP-P4 model are used for the correction, probably due to its high spatial resolution in the upper lower mantle. As a result, only the ScS–S residuals corrected with the modified GAP-P4 can be used to infer seismic anisotropy in the lowermost mantle.

Then I fitted  $\cos 2\theta$  and  $\cos 4\theta$  curves with least square to obtain the characteristics of the azimuthal variation of the ScS–S residuals, clearly indicating that  $\cos 2\theta$  component is significant with the fastest direction (the minimum ScS–S) is along ESE–WNW.

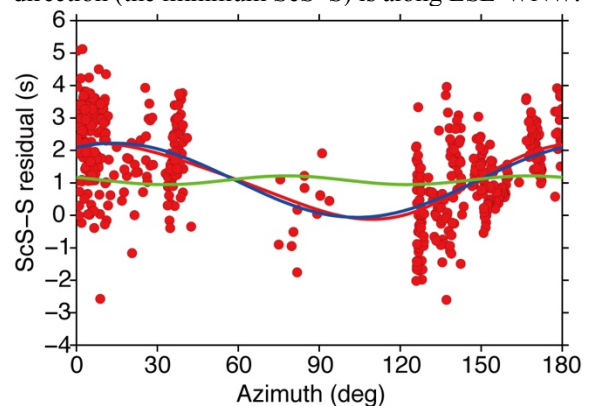


**Figure 2** Azimuthal variation of ScS–S residual corrected with the modified GAP-P4. Red, blue, and green lines are the fitted curve composed of  $\cos 2\theta$  and  $\cos 4\theta$ ,  $2\theta$ ,  $4\theta$  components, respectively.

**References:** [1] Dziewonski, A.M. and Anderson, D.L., *Phys. Earth Planet. Inter.*, **25**, 297 (1981). [2] Kennett, B.L.N. and Gudmundsson, O., *Geophys. J. Int.*, **127**, 40 (1996). [3] Liu, X.F. and Dziewonski, A.M., In: *The Core-Mantle Boundary Region*, 21 (1998). [4] Masters, G., et al., In: *Earth's Deep Interior: Mineral Physics and Tomography from the Atomic to the Global Scale*, *Geophysical Monograph* **17**, 63 (2000). [5] Ritsema, J., et al., *Geophys. J. Int.* **184**, 1223 (2011). [6] French, S.W. and Romanowicz, B., *Nature* **525**, 95 (2015). [7] Obayashi, M., et al., *Geophys. Res. Lett.* **40**, 5652 (2013). [8] Karato, S., *Geophys. Res. Lett.*, **20**, 1623 (1993).

## Topography of the western Pacific LLSVP constrained by S wave multipathing

Sunil K. Roy<sup>1,2</sup>, Nozomu Takeuchi<sup>1\*</sup>, D. Srinagesh<sup>2</sup>, M. Ravi Kumar<sup>2,3</sup> and Hitoshi Kawakatsu<sup>1</sup> <sup>1</sup>Earthquake Research Institute, University of Toyo, Bunkyo-ku, Tokyo 113-0032, Japan <sup>2</sup>CSIR-National Geophysical Research Institute, Hyderabad, 500007, India <sup>3</sup>Institute of Seismological Research, Gandhinagar, 382009, India.  
\*email:takeuchi@eri.u-tokyo.ac.jp

**Summary of Our Finding:** We found that SHdiff phases generated by earthquakes in the Fiji-Tonga, recorded in India, are accompanied by secondary pulses. We interpreted them as a consequence of multipathing of S waves caused by the Pacific Large Low-Shear-Velocity Province (LLSVP). We analyzed the differential travel times between SHdiff and the secondary pulse, together with the absolute SHdiff arrival times, to constrain the thickness and velocity perturbations in the western end of the Pacific LLSVP. Our preferred model shows a lateral variation in the thickness of the LLSVP; the southern part of our study region revealing a thicker (300 km) low velocity region compared to the northern part (200 km). However, the velocity perturbations of the LLSVP appear to be comparable (-1.5%). The results are consistent with a scenario that the LLSVP is a chemically distinct pile with significant surface topography.

**Discussion:** In this study, we showed that the observed waveforms can be explained without much alteration of the existing tomography models [1]. Our observations suggest that the western edge of Pacific LLSVP extends in the NE-SW direction from 129.5°E to 136.5°E and has a smaller-scale topography. There is a variation in the topography of the western edge of the Pacific LLSVP from 300 km to 200 km, from south to north. The observations also suggest that the edge of the LLSVP (i.e., our study region) has both significant thickness and surface topography, which favors the LLSVP as a chemically distinct pile. The existence of topography whose scale length is much smaller than the whole Pacific LLSVP suggests some dynamic process at the western edge such as a regional plume, instability of dome-like structure, or push due to downwelling from the outside [2,3].

Sharpness of the top of LLSVP is important to constrain the origin of this large anomaly. The amplitude of the secondary phase decreases if the

thickness of the transition zone is greater than ~60 km. Although precise quantification is difficult, considering the observed amplitudes of the secondary pulses being more than ~30% of the first pulse for most of the cases, a gradual transition from the ambient mantle to the LLSVP is unlikely and the LLSVP should be a distinct region.

It is debated whether the origin of the LLSVP is thermal or chemical [4-6]. Our results favor a chemical origin because of the following reasons. If the thermal anomalies were the origin, we expect predominance of smaller scale anomalies with complex geometry that compose plume clusters [6]. Such smaller scale features were required to explain the sharp sides observed in previous seismological studies [7,8]. However, to explain the secondary pulses observed in this study, we need quasi-horizontal upper boundary of the lower velocity region, otherwise we hardly expect phases with similar apparent velocity and arrival time as those for the SHdiff phase. To further constrain the origin, we probably need to analyze Pdiff and its post- or pre-cursors, which is a future research topic.

**References:** [1] Takeuchi, N., *Earth Planet. Sci. Lett.*, **319-320**, 55–64, (2012). [2] Tan, E. & Gurnis, M., *J. Geophys. Res.: Solid Earth*, **112**(B6), (2007). [3] Tan, E., Leng, W., Zhong, S., & Gurnis, M., *Geochem. Geophys. Geosyst.*, **12**(7) (2011). [4] McNamara, A. K. & Zhong, S., *Nature*, **437**, 1136–1139 (2005). [5] Bull, A. L., McNamara, A. K., & Ritsema, J., *Earth Planet. Sci. Lett.*, **278**, 152–162 (2009). [6] Davies, D. R., Goes, S., Davies, J., Schuberth, B., Bunge, H.-P., & Ritsema, J., *Earth Planet. Sci. Lett.*, **353-354**, 253–269 (2012). [7] Ni, S., Tan, E., Gurnis, M., & Helmberger, D., *Science*, **296**(5574), 1850–1852 (2002). [8] To, A., Romanowicz, B., Capdeville, Y., & Takeuchi, N., *Earth Planet. Sci. Lett.*, **233**(1), 137–153 (2005).

## Measurements of high pressure-temperature thermal conductivity of the Earth's lower mantle minerals in a laser-heated diamond anvil cell

K Ohta<sup>1\*</sup>, A Hasegawa<sup>1,2</sup>, T Yagi<sup>2</sup>, Y Okuda<sup>1</sup>, K Onga<sup>1</sup>, K Hirose<sup>3,4</sup>, & Y Ohishi<sup>5</sup>

<sup>1</sup>Department of Earth and Planetary Sciences, Tokyo Institute of Technology, Meguro, Tokyo 152-8551, Japan,

<sup>2</sup>National Metrology Institute of Japan, National Institute of Advanced Industrial Science and Technology, Tsukuba, Ibaraki 305-8563, Japan, <sup>3</sup>Earth-Life Science Institute, Tokyo Institute of Technology, Meguro, Tokyo 152-8551, Japan, <sup>4</sup>Department of Earth and Planetary Science, The University of Tokyo, Bunkyo, Tokyo 113-0033, Japan, <sup>5</sup>Japan Synchrotron Radiation Research Institute, Sayo, Hyogo 679-5198, Japan.

\*email:k-ohta@geo.titech.ac.jp

As given by the Fourier's law, heat conduction in material is characterized by thermal conductivity, a function of thermal diffusivity, density, and isobaric heat capacity. The thermal transport properties of the Earth's constituents are important information to understand thermal evolution and the heat budget of the Earth. Thus, the experimental determination of thermal conductivity of deep Earth materials are required.

The diamond anvil cell (DAC) is capable of accessing the pressure-temperature conditions of the Earth's deep interior, and is compatible with laser optical techniques. The pulsed light heating thermoreflectance (TR) method has been applied to a DAC in order to measure thermal conductivity and diffusivity of condensed material [1,2]. This TR with DAC method successfully obtained the thermal conductivity of the Earth's lower mantle minerals to the pressure condition equal to the Earth's core-mantle boundary (135 GPa) but at room temperature [3,4]. To extend measurable temperature range, the TR method may be combined with a laser-heated DAC (LHDAC) technique that is able to generate the pressure-temperature condition equivalent to the center of the Earth.

We recently developed a new instrument to measure the thermal diffusivity (and thus thermal conductivity) of sample *in-situ* at high pressure and temperature based on the combination of the TR method and the LHDAC system (Fig. 1). A symmetric-type DAC is used for high-pressure generation. The sample is loaded into a sample hole drilled at the center of preindented rhenium gasket. We use a double-sided high-power CW laser heating technique to generate stable high temperature conditions of sample in a DAC. Temperature generated by the CW lasers is determined from thermal radiation spectra from the heated sample. A pulsed pump laser and a CW probe laser are also irradiated to the sample to determine heat diffusion time through the sample via the thermoreflectance phenomena. Details of the thermoreflectance technique in a DAC may be found in our previous studies [2-4].

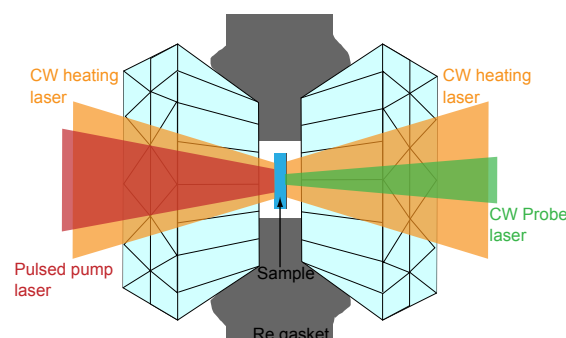


**Figure 1** Schematic illustration of the cross section of the DAC and the arrangement of four laser beams for TR pump laser, TR probe laser and heating CW lasers.

As a performance test of the developed system, we examined thermal conductivity of Pt at 40 and 56 GPa and high temperatures up to 1910 K. We found positive pressure and temperature dependence of the conductivity of Pt, which is in good agreement with the previous study employing the flash heating method in a LHDAC [5].

We also measured the thermal conductivity of the major minerals in the Earth's lower mantle, MgO periclase, MgSiO<sub>3</sub> bridgmanite, post-perovskite and CaSiO<sub>3</sub> perovskite *in-situ* at high pressures and high temperatures. These are the first experimental demonstrations of thermal conductivity of the lower mantle minerals at the conditions below the mid-part of the Earth's lower mantle. The new thermal conductivity measurement system will shed light on the controversial thermal transport properties of the Earth's deep interior [6].

**References:** [1] Hsieh, W.-P. et al., *Phys. Rev. B*, **80**, 180302 (2009). [2] Yagi, T. et al., *Meas. Sci. Technol.*, **22**, 024011 (2011). [3] Imada, S. et al., *Geophys. Res. Lett.*, **41**, 4542–4547 (2014). [4] Okuda, Y. et al., *Earth Planet. Sci. Lett.*, **474**, 25–31 (2017). [5] McWilliams, R. S. et al., *Phys. Earth Planet. Inter.*, **247**, 17–26 (2015). [6] Kavner, A. and Rainey, E.S.G., *Deep Earth: Physics and Chemistry of the Lower Mantle and Core*, 31–42 (2016).

## Sound velocity of liquid Fe–Ni–S–Si under pressure

H Terasaki<sup>1\*</sup>, I Yamada<sup>1</sup>, A Kamiya<sup>1</sup>, R Tsuruoka<sup>1</sup>, T Kondo<sup>1</sup>, Y Higo<sup>2</sup>, A Machida<sup>3</sup>

<sup>1</sup>Department of Earth and Space Science, Osaka University, Toyonaka, Osaka, 560-0043, Japan. <sup>2</sup>Japan Synchrotron Radiation Research Institute, Sayo, Hyogo, 679-5198, Japan. <sup>3</sup>National Institute for Quantum and Radiological Science and Technology, Sayo, Hyogo, 679-5148, Japan.

\*email:terasaki@ess.sci.osaka-u.ac.jp

**Introduction:** Most of the terrestrial planets has a liquid core, which mainly consists of Fe–Ni and also contains possibly some light elements. Silicon has been considered as a major candidate of the light element in Mercury core since Si tends to dissolve into Fe in reduced condition and Mercury interior is expected to be reduced due to its large metallic core. However, it is found from recent X-ray spectroscopy of the MESSENGER spacecraft that surface on Mercury contains 1–4 wt% of sulfur [1]. The S content on the surface suggests that certain amounts of S and Si are likely to dissolve into liquid iron based on partitioning of S and Si between metal and silicate melts [2]. This indicates that both S and Si are likely to be contained in the Mercury core. Thus, elastic properties of liquid Fe–Ni–S–Si are important to understand the interior structures of Mercury and properties of its liquid outer core. In this study, we measured sound velocity of liquid Fe–Ni–S–Si under pressure to obtain their elastic properties.

**Experimental:** The experiments were carried out at BL04B1 and BL22XU beamlines, SPring-8 synchrotron facility. High pressure was generated using 1500 ton Kawai-type or 180 ton cubic multianvil press. Used size for truncated edge lengths were 5 mm for Kawai-press and 6 mm for cubic press. We used two Fe–Ni–S–Si sample compositions (Fe-11wt%Ni-6wt%S-4wt%Si and Fe-11wt%Ni-3wt%S-8wt%Si). The sample pellet was sandwiched by single crystal sapphire buffer rods. High temperature was generated using cylindrical graphite or TiC resistive heater.

The P-wave velocity was measured using the pulse-echo overlap method. The LiNbO<sub>3</sub> transducer, which generated the ultrasonic wave, was attached on the backside of the tungsten carbide anvil. The echo signals from the sample interfaces were detected using a high resolution digital oscilloscope to measure the P-wave travel time in the sample. The sample length was determined from X-ray radiography image of the sample. The P-wave velocity ( $V_p$ ) was measured up to 16.3 GPa and 2010 K in this study.

**Results and Discussion:** The effect of temperature on the  $V_p$  of both Fe–Ni–S–Si compositions are quite small in the range of present conditions. The  $V_p$  of both compositions increase mildly with increasing pressure. Compared to the reported  $V_p$  of liquid Fe–Ni [3], the  $V_p$  of liquid Fe–Ni decreases approximately 1.6% by addition of 6wt%S and 4wt%Si and 3.1% by addition of 3wt%S and 8wt%Si. Therefore, addition of S reduces the  $V_p$  effectively whereas that of Si increases the  $V_p$  in the Fe–Ni–S–Si system. The elastic data obtained in this study is applicable to estimate the core size and composition of the Mercury Fe–Ni–S–Si core.

**References:** [1] Nittler, L.R. et al., *Science*, **333**, 1847 (2011). [2] Chabot, N.L. et al., *Earth Planet. Sci. Lett.*, **390**, 199 (2014). [3] Kuwabara, S. et al., *Phys. Chem. Mineral.*, **43**, 229 (2016).

# Sound velocity of liquid Fe-P alloy under high pressure based on inelastic X-ray scattering measurements

Y. Nakajima<sup>1,2\*</sup>, D. Kinoshita<sup>1</sup>, Y. Kuwayama<sup>3</sup>, K. Hirose<sup>3,4</sup>, A. Iwamoto<sup>1</sup>, S. Tateno<sup>4</sup>, D. Ishikawa<sup>2,5</sup>, A.Q.R. Baron<sup>2</sup>

<sup>1</sup>Department of Physics, Kumamoto University, <sup>2</sup>Materials Dynamics Laboratory, RIKEN SPring-8 Center,

<sup>3</sup>Department of Earth and Planetary Science, The University of Tokyo, <sup>5</sup>Earth and Life Science Institute, Tokyo Institute of Technology, <sup>5</sup>SPring-8/JASRI

\*email:yoichi@kumamoto-u.ac.jp

**Introduction:** The Earth's liquid outer core is composed mainly of iron with several wt.% nickel. The density and velocity of the outer core are 10% less and 4% higher, respectively, than that of Fe-Ni alloy, indicating that the core contains lighter components [1]. The nature of the light elements in the core is key to understanding the Earth's building blocks, planetary accretion and core formation processes, and subsequent chemical and thermal evolution of the core. The influence of possible lighter elements on the elastic parameters of liquid Fe under high-pressure and -temperature relevant to the core conditions is fundamental to constrain the light elements in the core.

Phosphorous is one of the candidates for light elements in the core because it is found in iron-meteorites [2] and depleted in the silicate mantle relative to chondrites [3]. In this study, we determined the P-wave velocity of liquid Fe-P alloy under static high-pressure conditions to 80 GPa based on inelastic X-ray scattering (IXS) measurements in a laser-heated diamond-anvil cell LH-DAC.

**Experimental:** We performed high-pressure IXS measurements at the beamline BL43LXU of the SPring-8 synchrotron facility [4]. The sample was Fe<sub>3</sub>P (hereafter called Fe<sub>75</sub>P<sub>25</sub>), which was packed into the sample chamber of a rhenium gasket together with two single-crystal sapphire discs that acted as both thermal and chemical insulators. The sample was compressed with 300 μm culet diamond anvils and heated up from both sides by using a couple of Yb<sup>3+</sup>-doped YAG fiber lasers. The pressure was determined based on diamond Raman-shift and the temperature was measured by a spectroradiometric method.

During heating, X-ray diffraction measurements performed. Sample melting was judged from the disappearance of diffraction peaks from solids and the appearance of diffuse signals from liquid using IXS spectra of liquid sample were collected by a high resolution IXS spectrometer with an energy resolution of ~2.8 meV using a Si(999) backscattering geometry at 17.79 keV. The incident X-ray beam size was ~5 μm [5]. Scattered X-rays were collected in an energy range of ±30 meV by an array of 12 of 24 Si analyzers at different momentum

transfers ( $Q$ ) between 3–6 nm<sup>-1</sup>. The collected IXS data was analyzed for the excitation energy ( $E$ ) of longitudinal acoustic (LA) phonon mode of the liquid sample. From the obtained  $E$ - $Q$  dispersion relation, we determined the P-wave velocity of the samples. We performed IXS measurements on liquid Fe<sub>75</sub>P<sub>25</sub> at 34–80 GPa and 2450–2800 K.

**Results and Discussion:** The P-wave velocity ( $V_P$ ) data obtained for liquid Fe<sub>75</sub>P<sub>25</sub> are plotted as a function of pressure in Figure 1. The Murnaghan equation of state (EoS) was fitted to the  $P$ - $V_P$  data, with an assumption of no temperature effect on  $V_P$  of liquid Fe<sub>75</sub>P<sub>25</sub> under the present high-pressure conditions and 1 bar density data. The  $V_P$  of liquid Fe<sub>75</sub>P<sub>25</sub> is almost identical to that of liquid Fe [6], whereas the bulk modulus and density derived from the EoS fitting are slightly lower. This exhibits that phosphorus has negligible effect on  $V_P$  of Fe, which can be by cancelling out each effect of P on the bulk modulus and density of liquid Fe.

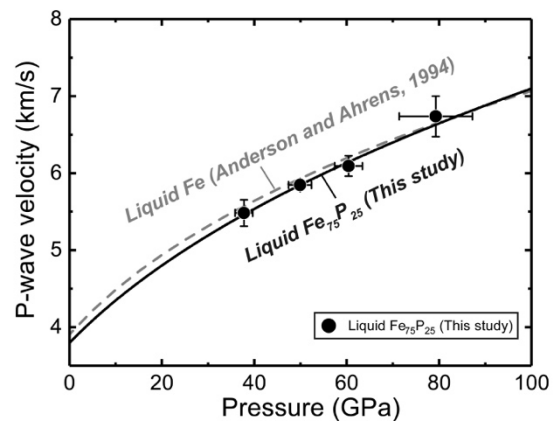


**Figure 1** Sound velocity of liquid Fe<sub>75</sub>P<sub>25</sub>. The solid line is a fitting to the obtained P-wave velocity of liquid Fe<sub>75</sub>P<sub>25</sub>, which is compared with that for pure Fe based on shock-compression data [6].

**References:** [1] Birch, *J. Geophys. Res.*, **57**, 227 (1952). [2] Skála and Císařová, *Phys. Chem. Mine.*, **31**, 721 (2005) [3] McDonough, *Treatise on Geochem.*, **Vol.2**, 547 (2003) [4] Baron, *SPring-8 Inf. Newsl.*, **15**, 14 (2010). [5] Baron et al., *AIP Conf. Proc.*, **2054**, 020002 (2018) [6] Anderson and Ahrens, *J. Geophys. Res.*, **99**, 4273 (1994)

# Sound velocities of CaSiO<sub>3</sub> perovskite (“breyite”) and some implications for chemical compositions around the 660 km discontinuity.

T Irifune<sup>1,2\*</sup> and S Gréaux<sup>1,2</sup> <sup>1</sup>Geodynamics Research Center, Ehime University, Matsuyama, Japan; Earth-Life Science Institute, Tokyo Institute of Technology, Tokyo, Japan.

\*email:irifune@dpc.ehime-u.ac.jp

**Introduction:** Precise measurements of sound velocities of high-pressure minerals at high pressure and high temperature are important to constrain the chemical compositions of the deep mantle (e.g. [1]). The GRC + JASRI group has been developing techniques for such measurements using ultrasonic pulse-echo interferometry, and has enabled to perform sound velocity measurements under the pressure and temperature conditions of the uppermost region of the lower mantle, by a combination of Kawai-type multianvil apparatus and synchrotron in situ X-ray observations (e.g. [2], [3], [4]). The group has made such measurements on a number of important mantle minerals, such as garnets with various chemical compositions, wadyleite, ringwoodite, akimotoite, stishovite, etc., as well as rocks such as pyrolite and MORB. However, the velocity measurements on CaSiO<sub>3</sub>-perovskite (CaPv) have not been made because of unavailability of adequate sintered polycrystalline samples of CaPv, as this phase is known to become amorphous at the ambient pressure upon release of pressure. Meanwhile, CaPv was recently discovered as an inclusion in natural diamond of ultra-deep origin [5], and named as “Breyite”, after the name of Prof. Gerhard Brey of Goethe University, which has been approved by the IMA.

**Experimental:** Sound velocity measurements were conducted at the BL04B1, SPring-8, using SPEED-1500. The basic technique is similar to those reported earlier ([2], [3]), but we expanded the pressure and temperature conditions toward the uppermost region of the lower mantle. A bulk glass starting material of CaSiO<sub>3</sub> composition was loaded in the cell, and first converted to CaPv at 21 GPa, 1300 K in 1 hour. The ultrasonic and in situ X-ray observations were made upon decreasing temperature at fixed press loads. We made five

independent such runs to see the mutual consistency of the results. Further details of the present sound velocity measurements on CaPv have been reported in [6].

**Results and Discussion:** Successful measurements of sound velocities of cubic CaPv have been made at pressures up to about 23 GPa and temperatures between 600 K and 1700 K. Significant decreases in both V<sub>p</sub> and V<sub>s</sub> were observed at temperatures below 600 K, suggesting the cubic to tetragonal transition of CaPv at the lower temperatures. We obtained elastic moduli of cubic CaPv as K<sub>0</sub> = 248(3) GPa and G<sub>0</sub> = 126(1) GPa. The present shear modulus is substantially lower than those predicted based on ab initio calculations (e.g. [7], [8]), while the bulk modulus is consistent with those theoretically predicted. The present result shows that the subducted oceanic crust of basaltic compositions, which have 20-30 vol.% of CaPv in the uppermost lower mantle, would have sound velocities significantly lower than those of the surrounding mantle, suggesting that the presence of a basalt rich layer may be responsible for the low-velocity signature recently found in some regions atop of the lower mantle [9].

**References:** [1] Li, B and Liebermann, R. C., *Phys. Earth Planet. Inter.*, **233**, 135 (2014). [2] Higo, Y. et al., *Phys. Earth Planet Inter.*, **166**, 167 (2008). [3] Irifune, T. et al., *Nature*, **451**, 814 (2008). [4] Higo, Y et al., *Rev. Sci. Instrum.*, **89**, 014501 (2017). [5] Nestola et al., *Nature*, **555**, 237 (2018), [6] Gréaux et al., *Nature*, **565**, 218 (2019). [7] Stixrude, L. et al., *Phys. Rev. B*, **75**, 024108 (2007), [8] Tsuchiya, T., *Phys. Earth Planet. Inter.* **188**, 142 (2011), [9] Schmandt, B. et al., *Science*, **344**, 1265 (2014).

## Internally-consistent multiple constraints on the mineralogy and seismology of Earth's lower mantle

JF Lin<sup>1\*</sup> <sup>1</sup>Department of Geological Sciences, The University of Texas at Austin, Austin, TX78712, USA

\*email: afu@jsg.utexas.edu

**Introduction:** The mineralogical model, seismic observations and thermal state of the Earth's lower mantle are key parameters to understand chemistry and dynamic processes of planet. However, it remains much debated on the chemical composition and origins of seismic observations of the lower mantle even after decades of experimental and theoretical efforts [1]. Direct comparison on the velocity and density profiles between seismic observations, such as PREM and AK135, and mineral physics modeling from laboratory elasticity data has been widely used to constrain the composition of lower mantle. However, many previous studies used limited range and/or number of physical parameters with high uncertainties for the comparison [1]. It's thus crucial to obtain reliable and multiple physical parameters such as  $V_P$ ,  $V_S$ , and  $\rho$  of single-crystal (Al,Fe)-bearing bridgmanite and ferropericlasite at relevant lower mantle P-T conditions in order to derive reliable geophysical and geochemical models of the region.

**Experimental:** Here we have synthesized high-quality single-crystal and polycrystalline bridgmanite and ferropericlasite crystals using 5000-ton Kawai apparatus at Misasa. We have used these well-characterized crystals such as bridgmanite ( $\text{Mg}_{0.93}\text{Fe}_{0.08}\text{Al}_{0.10}\text{Si}_{0.90}\text{O}_3$  (Fe8-Al10-Bgm) with  $\text{Fe}^{3+}/\Sigma\text{Fe}\sim 0.6$ ), to measure their  $V_S$ ,  $V_P$  and  $\rho$  at high pressures using combined Brillouin light scattering (BLS), impulsive stimulated light scattering (ISLS) and X-ray diffraction (XRD) techniques in a diamond anvil cell (DAC) [2-3].

**Results and Discussion:**  $V_S$ ,  $V_P$ , and  $\rho$  of polycrystalline and single-crystal ferropericlasite and (Fe,Al)-bearing bridgmanite crystals have been measured at lower-mantle pressures. Single-crystal results are used to derive full elastic constants of ferropericlasite and bridgmanite at lower-mantle pressures. Specifically, velocity profiles of Fe8-Al10-Bgm increase monotonically with pressure up to 83 GPa [2-3]. However, the spin transition of iron in ferropericlasite and Fe-bearing bridgmanite causes a significant drop in the  $V_P$  at high pressures. Our results also show significant Fe and Al effects on the velocity of bridgmanite:  $V_S$  of Fe8-Al10-Bgm is slightly lower than that of  $\text{MgSiO}_3$  and Al-bearing bridgmanite at high

pressures, while its  $V_P$  is significantly decreased when compared with the extrapolation of  $\text{MgSiO}_3$  and Al-bearing bridgmanite [1-3].

We used the measured elasticity of bridgmanite and ferropericlasite, together with literature reports on high pressure and temperature data of these minerals, to quantitatively evaluate the effects of the temperature, spin transition as well as Fe and Al substitution on the elasticity of ferropericlasite and/or bridgmanite. These results are then used to calculate their adiabatic bulk and shear moduli ( $K_S$  and  $\mu$ ) [3, 4].

The elasticity data of bridgmanite and ferropericlasite are then used to model an internally-consistent one-dimensional seismic and adiabatic temperature profile of lower mantle by taking into account of the Fe/Al partitioning and the spin transition [4]. Following the thermodynamic and elastic modeling, we derive an internally-consistent mineralogical model and adiabatic temperature profile of lower mantle, that can reproduce consistent seismic profiles in  $V_P$ ,  $V_S$ , and  $\rho$  at the whole lower-mantle pressures ranging from 28 to 130 GPa [4]. We will present these results and their implications in the workshop to address the forefront scientific questions in our understanding of the mineralogy and seismic profiles of the lower mantle.

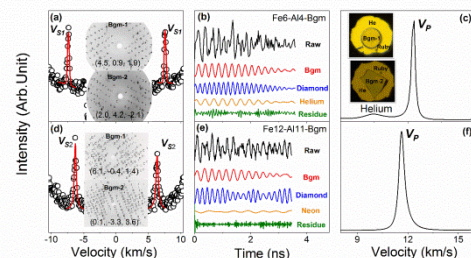


**Figure** Representative experimental Brillouin light scattering (BLS), impulsive stimulated light scattering (ISLS), and X-ray diffraction (XRD) spectra of single-crystal (Al,Fe)-bearing Bgm at 25 GPa. Inserts in (c) show photos of two Fe6-Al4-Bgm crystals loaded in sample chambers with helium medium at 25 GPa.

**References:** [1] Lin, J.F. *et al.*, *Nature*, **564**, E18, (2018). [2] Fu, S. *et al.*, *Geophys. Res. Lett.*, **45**, (2018). [3] Fu, S. *et al.*, *Earth Planet. Sci. Lett.*, **503**, 1 (2018). [4] Fu, S. *et al.*, *in prep.* (2019).

# Nanoscale texture and transformation timescale of dense $\text{Mg}_2\text{SiO}_4$ polymorphs in shocked meteorites: comparison between natural occurrences by high-resolution TEM and experimental results by fast XFEL diffraction

T Okuchi\* <sup>1</sup>Institute for Planetary Materials, Okayama University, Misasa, Tottori 682-0193, Japan.

\*email:okuchi@misasa.okayama-u.ac.jp

**Introduction:** Primitive meteorites often show significant features of impact metamorphism. One of such features are occurrence of dense high-pressure polymorphs of silicate minerals in heavily shocked portions of the meteorites. By transmission electron microscopy, it was discovered that some fraction of olivine ( $\alpha$ - $(\text{Mg,Fe})_2\text{SiO}_4$ ) crystals in such meteorites were transformed into its variety of denser polymorphs, which even include a recently-discovered new structure ( $\varepsilon$ - $(\text{Mg,Fe})\text{Mg}_2\text{SiO}_4$ ) that has a unique nano-scaled microtexture (Figure 1). While the impact events that induced such transformations must have played essential roles in early history of planetary evolutions 4.5 billion years before, there has been no successful study to transform olivine crystals into its denser polymorphs by means of shock-compression experiments in a laboratory. Thus, temperature and stress conditions of the impact events were still left ambiguous and controversial.

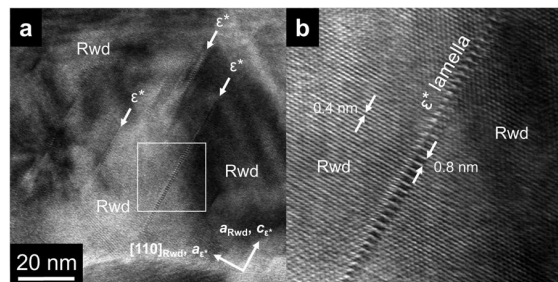


**Figure 1** Microtexture of  $\varepsilon$ - $(\text{Mg,Fe})_2\text{SiO}_4$  occurring within  $\gamma$ - $(\text{Mg,Fe})_2\text{SiO}_4$ , which was observed by high-resolution TEM at Kochi JAMSTEC (Tomioka and Okuchi, 2017).

**Experimental:** Here we experimentally reproduced a part of such transformation processes of  $\alpha$ - $\text{Mg}_2\text{SiO}_4$  forsterite olivine into its denser polymorphs, which was successfully observed with sub-nanosecond time resolution, by means of ultrafast x-ray diffraction scheme using x-ray free electron laser source at SACLA, SPring-8 (Figure 2). The single crystals of forsterite were shock-compressed by irradiation of strong visible laser beam of nanoseconds of pulse length, which was focused into  $\sim 200 \mu\text{m}$  in diameter. Then its structure was then immediately analyzed by free electron laser beam of femtoseconds of pulse length, which was focused into even smaller dimension where the strongest shock compression was occurring.

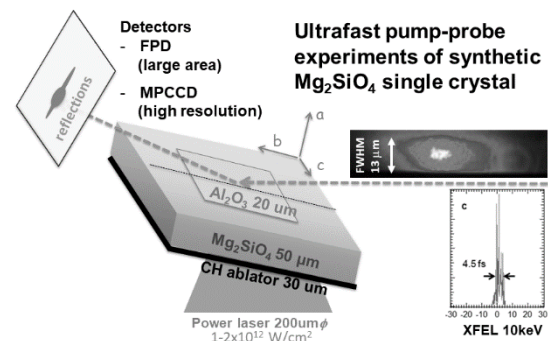


**Figure 2** Experimental setup for laser-driven shock compression experiments coupled with fast XFEL diffraction analysis (e.g., Albertazzi et al., 2017).

**Results:** The olivine crystals were compressed uniaxially along the a-axis until its dimension was reduced down to  $\sim 90\%$  of its original, and then rapidly transformed into a denser structure having a different space group, most possibly that of  $\varepsilon$ - $\text{Mg}_2\text{SiO}_4$  or  $\gamma$ - $\text{Mg}_2\text{SiO}_4$  by means of an ultrafast slip deformation process which completed only within a few nanoseconds. Our current results have significant implication on the growth process and reaction kinetics of the olivine's dense polymorphs naturally occurring within the meteorites, as well as on the nature of ancient impact events in the early solar system.

**Acknowledgment:** The author thanks MEXT X-ray Free Electron Laser Priority Strategy Program, SACLA Priority Strategy Proposal Program for "Ultrafast Processes under Extreme Conditions", and JSPS Grant-in-Aid for Scientific Research.

## References:

- Tomioka, N. & T. Okuchi, A new high-pressure form of  $\text{Mg}_2\text{SiO}_4$  highlighting diffusionless phase transitions of olivine. *Sci. Rep.* 7, 17351 (2017).  
 Albertazzi, B., N. Ozaki, V. Zhakhovskiy, A. Faenov, H. Habara, M. Harmand, N. J. Hartley, D. K. Initsky, N. Inogamov, Y. Inubushi, T. Ishikawa, T. Katayama, H. Koyama, M. Koenig, A. Krygier, T. Matsuoka, S. Matsuyama, E. McBride, K. Migda, G. Morard, H. Ohashi, T. Okuchi, T. Pikuz, N. Purevjav, O. Sakata, Y. Sano, T. Sato, T. Sekine, T. Seto, K. Takahashi, K. A. Tanaka, Y. Tange, 16 T. Togashi, K. Tono, Y. Umeda, T. Vinci, M. Yabashi, T. Yabuuchi, K. Yamauchi, H. Yumoto & R. Kodama, Dynamic fracture of tantalum under extreme tensile stress, *Sci. Adv.* 3, e1602705 (2017).

## Low-frequency micro-Raman spectroscopy and its application to mineral sciences

M Kanzaki\* <sup>1</sup>Institute for Planetary Materials, Okayama University, Misasa, Tottori 682-0193, Japan.

\*email:mkanzaki@okayama-u.ac.jp

**Introduction:** Because of advent of simple and cheap Raman system with single monochromator plus CCD detector, low-frequency Raman (below  $\sim 200\text{ cm}^{-1}$ ) becomes nearly obsolete in last two decades. This is due to lower frequency limit of Raman filters (+ dichroic filter) used for those spectrometers. However, this situation has changed in last few years, as Ondax Inc. introduced new Raman filter which allows measurement down to  $\sim 5\text{ cm}^{-1}$ . Simultaneously, terahertz spectroscopy (corresponding far-infrared region) is now available to non-specialists. Therefore, new era of terahertz-region spectroscopy has arrived.

Although low-frequency region is not quite necessary for phase identification of materials (one of most used applications), it contains rich information of dynamics and local structure of materials. Boson peak in glasses and soft mode of phase transition are a few well known examples. In the talk, a few examples of applications to minerals are given to demonstrate ability of low-frequency Raman spectroscopy.

**Experimental:** For micro-Raman measurement, a home-build spectrometer with single-monochromator and CCD detector was used. Two Ondax SureBlock filters are adopted to the system to obtain low-frequency Raman spectra. We also employed a Ondax NoiseBlock filter, which works as a dichroic mirror. 488 nm solid laser with laser power of 80 mW was used. See [1] for details of the instrument.

For high-temperature measurements, a wire-heater was used, and temperature was calibrated against 5~6 standard materials with known melting points [2].

**Results and Discussion:** First example is soft mode of  $\alpha\text{-AlPO}_4$ -moganite. This is a high-pressure phase synthesized at 5 GPa, 1500 °C [3]. Similar to  $\text{SiO}_2$ -moganite and other silica phases such as quartz, temperature-induced phase transition is expected. This supposed transition was studied using present micro-Raman system up to 600 °C. Two low-frequency modes ( $60$  and  $74\text{ cm}^{-1}$ ) were detected at room temperature. The  $74\text{ cm}^{-1}$ -mode significantly shifted toward  $0\text{ cm}^{-1}$  with temperature as shown in Fig. 1. This behavior is well fitted with an order parameter equation as shown in Fig. 1, confirming that the mode is soft mode. The transition temperature ( $T_c$ ) was determined as 415 °C. First-principles calculation of vibrational modes of  $\alpha\text{-AlPO}_4$ -moganite predicted two low-frequency modes, and atomic displacements for the  $74\text{ cm}^{-1}$ -

mode matched well toward to route for the expected high-temperature structure.

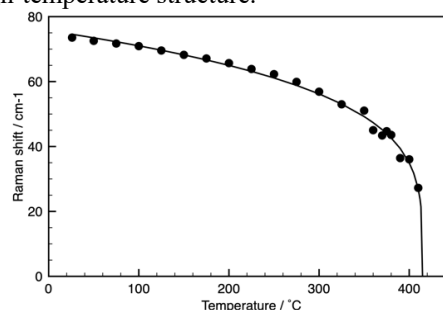


**Figure 1** Soft mode Raman shift of  $\alpha\text{-AlPO}_4$ -moganite versus temperature (solid circles). The solid line represents curve fitting using an order parameter equation ( $\omega_s = A|T_c - T|^\beta$ ).

Second example is low-frequency peak observed in natural minerals. We found a very intense (and broad) low-frequency Raman peak in a  $\text{CO}_2$ -containing melanophlogite as shown in Fig. 2 [4]. Melanophlogite is one of rare silica minerals with a clathrate structure. Heating study of this sample revealed that this feature is due to  $\text{CO}_2$  in the structure and is likely due to librational and translational modes of  $\text{CO}_2$  molecules in cages, as degassing reduced its intensity. Degassing behavior which is related to diffusion of  $\text{CO}_2$  in cages of the structure, can be studied by observing this and also  $\text{CO}_2$  vibrational peaks [4]. Low-frequency peaks are also found in several zeolites which are likely originated from molecular  $\text{H}_2\text{O}$  clusters in the large cages of zeolites.

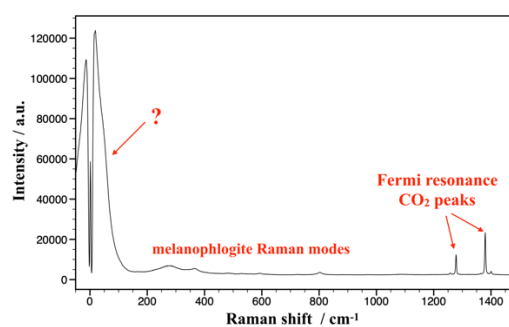


**Figure 2** Raman spectrum of  $\text{CO}_2$ -containing melanophlogite from Fortunillo, Italy at ambient conditions.

**References:** [1] <http://www.misasa.okayama-u.ac.jp/pukiwiki/index.php?Micro-Raman> spectroscopy [2] Kanzaki, M., *J. Mineral. Petrol. Sci.*, **113**, 126 (2018). [3] Kanzaki, M. and Xue, X. *Inorg. Chem.*, **51**, 6164 (2012). [4] Kanzaki, M., *J. Mineral. Petrol. Sci.*, **114** (2019) in press.

## The effect of water on Fe–Mg interdiffusion rates in ringwoodite and implications for the electrical conductivity in the mantle transition zone

B H Zhang<sup>1\*</sup>, T Yoshino<sup>2</sup>, C C Zhao<sup>2</sup>, <sup>1</sup>Institute of Geochemistry, Chinese Academy of Sciences, Guiyang 550081, China; <sup>2</sup>Institute for Planetary Materials, Okayama University, Misasa, Tottori 682-0193, Japan.

\*zhangbaohua@vip.gyig.ac.cn

**Introduction:** Ringwoodite [ $\gamma$ -(Mg,Fe)<sub>2</sub>SiO<sub>4</sub>] is the major component of the lower mantle transition zone (MTZ), which can contain significant amount of water in its crystal structure. Therefore, the MTZ is considered to be a large water reservoir in deep Earth [1, 2]. It has been demonstrated that the incorporation of even tens of wt. ppm water could significantly affect physical properties of ringwoodite including seismic wave velocity and electrical conductivity [3].

Among various atoms in ringwoodite, Fe–Mg is the fastest diffusing species, providing the upper limit of related processes and the effect of water on its  $D_{\text{Fe–Mg}}$  might be larger than that in olivine [4]. To verify this speculation, we determined the water effect on  $D_{\text{Fe–Mg}}$  of synthetic Fe-free (Mg<sub>2</sub>SiO<sub>4</sub>) and Fe-bearing (Fe<sub>0.2</sub>Mg<sub>1.8</sub>SiO<sub>4</sub>) ringwoodite aggregates under high temperature and high pressure in this study. The role of water in homogenization of chemical heterogeneities in the MTZ was discussed and the possible MTZ water storage was estimated by means of the inferred conductivity of ringwoodite from present  $D_{\text{Fe–Mg}}$  data.

**Experimental:** We determined the kinetics of Fe–Mg interdiffusion in ringwoodite aggregates as a function of water content (up to ~6000 wt. ppm H<sub>2</sub>O) at 20 GPa and 1373–1673 K by the diffusion couple method. Element maps and diffusion profiles of ringwoodite diffusion couple were analyzed by EPMA. The dependence of Fe–Mg interdiffusivity ( $D_{\text{Fe–Mg}}$ ) on Fe concentration was determined using a Boltzmann-Matano method.

**Results and Discussion:** The experimentally reported  $D_{\text{Fe–Mg}}$  in ringwoodite within  $0 \leq X_{\text{Fe}} \leq 0.1$  could be fitted by the relation  $D_{\text{Fe–Mg}}(\text{m}^2/\text{s}) = D_0 X_{\text{Fe}}^n C_{\text{H}_2\text{O}}^r \exp[-(E^* + \alpha C_{\text{H}_2\text{O}})/RT]$ , where  $E^* = (1 - X_{\text{Fe}})E_{\text{Mg}} + X_{\text{Fe}}E_{\text{Fe}}$  ( $E_{\text{Mg}} = 140 \pm 5$  kJ/mol,  $E_{\text{Fe}} = 4 \pm 2$  kJ/mol),  $D_0 = 5.59^{+2.90}_{-1.91} \times 10^{-10}$  m<sup>2</sup>/s,  $n = -0.21 \pm 0.10$ ,  $r = 0.25 \pm 0.03$ , and  $\alpha = -24 \pm 4$ . The water content exponent  $r$  of 0.25 suggests a non-negligible role of water in enhancing Fe–Mg interdiffusion in ringwoodite.

The length scale over which the chemical heterogeneities are homogenized by Fe–Mg interdiffusion in the MTZ is estimated to be only a few hundred meters even assuming the whole Earth age.

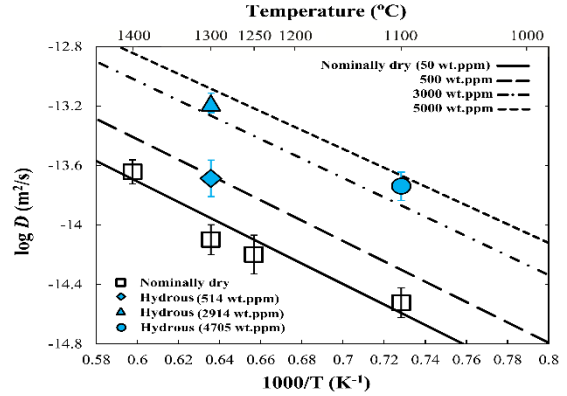


**Figure 1** Arrhenius plot of the variation of  $D_{\text{Fe–Mg}}$  for  $X_{\text{Mg}} = 0.94$  in the nominally dry and wet ringwoodite diffusion couples displayed as a function of inverse temperature at 20 GPa.

Comparison between the conductivities predicted from Fe–Mg interdiffusion and those obtained from magnetotelluric surveys suggest that around 0.1 wt.% water can account for the high conductivity anomalies ( $\sim 10^{-0.6} - 10^{-1}$  S/m) observed in the lower part of the MTZ.

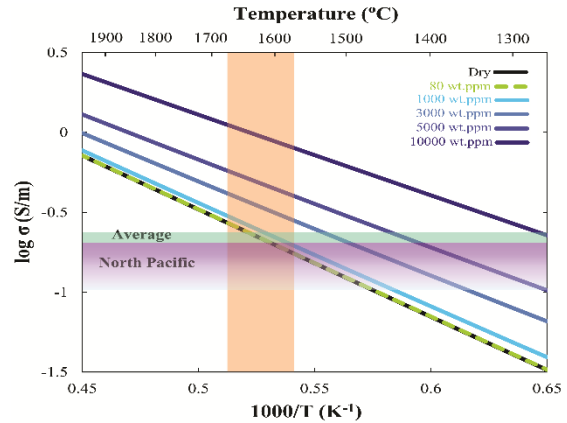


**Figure 2** Ringwoodite electrical conductivity as a function of inverse temperature and H<sub>2</sub>O content. Calculations are shown for dry ringwoodite [3] as well as hydrous (this study). The light blue and purple regions denote ranges of conductivity values observed in the global average model [5] and in the North Pacific Ocean [6], respectively.

**References:** [1] Inoue et al., *GRL*, **22**, 117 (1995). [2] Ohtani et al., *PEPI*, **143**, 255 (2004). [3] Yoshino et al., *Nature*, **451**, 326 (2008). [4] Hier-Majumder et al., *JGR*, **110**, B02202 (2005). [5] Kelbert et al., *Nature*, **460**, 1003 (2009). [6] Shimizu et al., *GJI*, **180**, 1030 (2010).

## Probing basalt–5.75H<sub>2</sub>O–CH<sub>4</sub> system by *in situ* vibrational spectroscopy

N Chertkova<sup>1\*</sup>, S Yamashita<sup>2</sup>, H Ohfuji<sup>1</sup>, T Irifune<sup>1</sup>, H Kadobayashi<sup>1</sup>, Y Yamamoto<sup>3</sup>

<sup>1</sup>Geodynamics Research Center, Ehime University, 2-5 Bukyo-cho, Matsuyama, 790-8577, Japan

<sup>2</sup>Institute for Planetary Materials, Okayama University, Misasa, Tottori 682-0193, Japan

<sup>3</sup>National Institute of Advanced Industrial Science and Technology, Tsukuba, Ibaraki 305-8569, Japan

\*email:chertkova.nadezda.sj@ehime-u.ac.jp

**Introduction:** Volatile components released from sediments in subduction zones are involved in melting, island-arc volcanism, and the chemical alteration of the mantle wedge above subducting plates. Increase of melt fraction triggered by the presence of volatile components has a major effect on seismic velocities [1-3] and should be considered in construction of geodynamic models. Experimental data on fluid and rock interaction can provide essential information for understanding of these processes and interpretation of observed seismic parameters.

**Experimental:** Experiments were carried out in an externally heated Mao-type diamond anvil cell [4] with modified cell assembly and increased opening angle. Doubly-polished MORB glass pieces were loaded into the sample chamber of DAC together with methane hydrate fluid source [5], pressurized, then heated in the temperature range to 1000 °C. Phase relationships were monitored during heating under the optical microscope, employing *in situ* micro-Raman and infrared spectroscopy [4,6]. During experiments temperature was measured by the thermocouple, attached to the gasket, and pressure was determined using the Raman spectrum of optical pressure sensor [4,7].

**Results and Discussion:** Microphotographs taken during experiments are shown on Fig. 1. During heating above 100 °C, a decomposition of solid methane hydrate into methane and water took place (Fig. 1b). Upon further heating to 700 °C, crystallization of coesite crystals in the fluid was observed (Fig. 1c). At temperatures above 800 °C clinopyroxene and garnet crystals were coexisting with homogeneous fluid phase (Fig. 1c).

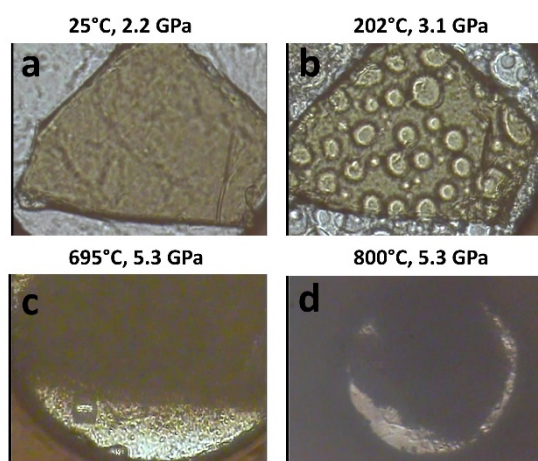


**Figure 1** Microphotographs of the phases observed during DAC experiments in the system basalt–5.75H<sub>2</sub>O–CH<sub>4</sub>: (a) starting basaltic glass with solid methane hydrate at room temperature; (b) basaltic glass with decomposed methane hydrate; (c) crystallization of coesite crystals during heating; (d) fine-grained clinopyroxene and garnet, surrounded by supercritical fluid.

Observed mineral phases are in consistency with the subsolidus association described in the dry basaltic system with the similar MORB composition [8]. Though previous studies, which employed quenching techniques, reported the presence of immiscibility gaps in the basaltic systems with C–O–H components at temperatures below 1600 °C and pressures below 6 GPa [9,10], results of this study showed stability of homogeneous silica-rich fluid phase at temperatures above 800 °C and pressures above 3.2 GPa, with separation of supercritical fluid into several components during quenching.

**References:** [1] Hammond, W.C. and Humphreys, E.D., *J. Geophys. Res.*, **105**, 10975 (2000). [2] Wiens, D.A. and Smith, G.P., *Geophysical Monograph -AGU*, **138**, 59 (2003). [3] Chantel, J., Manthilake, G., Andraut, D., Novella, D., Yu, T. and Wang, Y., *Science advances*, **2**, e1600246 (2016). [4] Chertkova, N., Ohfuji, H., Nomura, R., Kadobayashi, H. and Irifune, T., *High Pressure Res.*, **38**, 337 (2018). [5] Kadobayashi, H., Hirai, H., Ohfuji, H., Ohtake, M. and Yamamoto, Y. *J. Chem. Phys.*, **148**, 164503 (2018). [6] Chertkova, N. and Yamashita, S. *Chem. Geol.*, **409**, 149 (2015). [7] Chertkova, N., Yamashita, S., Ito, E. and Shimojuku, A. *Mineral. Mag.*, **78**, 1677. [8] Yasuda, A., Fujii, T. and Kurita, K. *J. Geophys. Res.: Solid Earth*, **99**, 9401. [9] Zhang, P. F., Tang, Y. J., Hu, Y., Zhang, H. F., Su, B. X., Xiao, Y. and Santosh, M. *Int. Geology Rev.*, **54**, 1443-1455 (2012). [10] Litasov, K. D., Shatskiy, A. and Ohtani, E. *EPSL*, **391**, 87 (2014).



## Effect of iron content on thermal conductivity of olivine with implications for cooling history of rocky planets

Youyue Zhang<sup>1\*</sup>, Takashi Yoshino<sup>1</sup>, Akira Yoneda<sup>1</sup>, Masahiro Osako<sup>2</sup>.

<sup>1</sup>Institute for Study of the Earth's Interior, Okayama University, Misasa, Tottori 682-0193, Japan

<sup>2</sup>Division of Physical Sciences, National Museum of Nature and Science, 3-23-1, Hyakunincho, Shinjuku-ku, Tokyo 169-0073, Japan

\*email: zhangyouyue@s.okayama-u.ac.jp

**Introduction:** Knowledge of thermal transport properties of mantle materials is essential for understanding the thermal state and dynamics of the Earth and planetary interiors. Previous studies have suggested that temperature and pressure dependences of thermal conductivity can affect mantle convection and plate tectonics involving subduction dynamics. Olivine is the most abundant mineral in the Earth's upper mantle and chemical composition of olivine in the Earth's upper mantle is characterized by high forsterite content around Fo<sub>90</sub>. For other terrestrial planets, Mercury is believed to have a FeO-poor mantle along with end member silicates, whereas olivine in the Martian mantle would be more Fe-rich, speculated to be Fo<sub>67</sub>. Recent studies suggested that surface of some asteroids is dominated by Fe-rich olivine of composition from Fo<sub>49</sub> to Fo<sub>70</sub>. Hence, the effect of Fe content in olivine on thermal conductivity could be significant for understanding the thermal structure and cooling history of these terrestrial planets and asteroids.

**Experimental:** In this study, by combining multi-anvil high pressure experimental technique and pulse heating method, thermal conductivity and diffusivity of olivine were determined simultaneously. Thermal properties of olivine with six different Fe contents (Fo, Fo<sub>90</sub>, Fo<sub>70</sub>, Fo<sub>50</sub>, Fo<sub>31</sub>, Fo<sub>0</sub>) were measured under the Earth's upper mantle condition in a 5000-ton Kawai type multi-anvil press. For Fo<sub>90</sub>, Fo<sub>70</sub>, Fo<sub>50</sub> and Fo<sub>31</sub>, we measured thermal conductivity and diffusivity up to 10 GPa and 1000 K. For fayalite (Fo<sub>0</sub>), taking into consideration of the relatively low transition temperature to spinel phase under high pressure, the measurement condition was limited up to 8 GPa and 700 K. And for Forsterite, we took data up to 5 GPa and 1000 K.

**Results and Discussion:** Thermal conductivity of olivine was varied by different Fe contents and the lowest value appeared at composition about Fo<sub>31</sub> at room temperature. The thermal conductivity of Fo<sub>31</sub> was about 70% of Fo<sub>90</sub> and 35% of Fo. For olivine, the temperature dependence of thermal conductivity and diffusivity can be described by an empirical form as  $A + B / T$ . The pressure dependence can be expressed by a linear function as  $a + bP$ . As temperature increases, the difference in  $\lambda$  among olivine samples with various Fe contents tends to become smaller. According to the fitting equation, the absolute  $\lambda$  value of Fo<sub>31</sub> at 800 K correspond to 72, 74 and 77% of the value of Fo<sub>90</sub> at 6, 8 and 10 GPa,

respectively. Meanwhile, at temperatures higher than 500 K, the minimum value appears at composition of Fa.

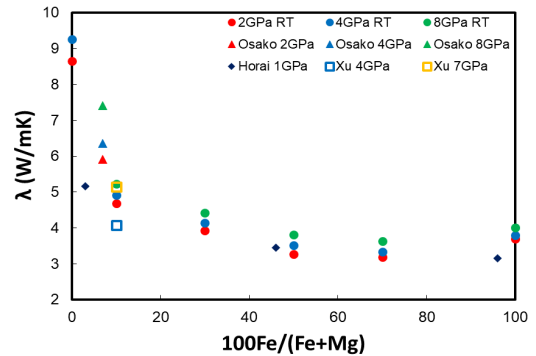


**Figure 1** Compositional dependence of thermal conductivity  $\lambda$  of olivine at room temperature.

Compared with single crystal olivine, the grain boundary scattering of polycrystal olivine lowered the absolute value of thermal conductivity and reduced the pressure dependence of thermal conductivity at room temperature and temperature dependence of thermal conductivity under high temperature.

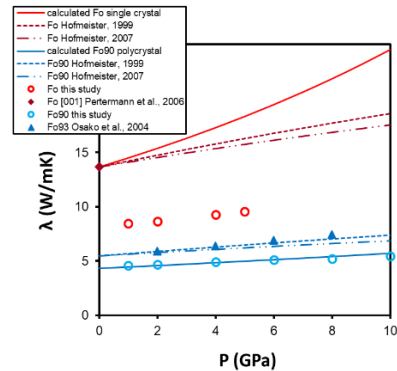


**Figure 2** Comparison of thermal conductivity of olivine single crystal  $\lambda_{\text{single}}$  and polycrystal  $\lambda_{\text{poly}}$  with models' predictions.

Heat capacity of olivine calculated from  $\lambda$  and  $\kappa$  is independent of pressure and is controlled by nearly constant thermal expansion coefficient of Fo<sub>70</sub> and Fo<sub>50</sub> with increasing temperature.

The composition dependent thermal conductivity of olivine suggests a warmer upper mantle and thicker crust of Mars than expected. The Fe-poor mantle of Mercury indicates a much higher speed of heat loss than other terrestrial planets. Olivine dominant asteroids with high Fe content have longer cooling history and smaller thermal inertia on the surface.

## Measurement of T-dependent electrical resistivity of solid and liquid Fe and Pt at fixed P

Innocent C. Ezenwa<sup>1\*</sup>, Takashi Yoshino<sup>1</sup>

<sup>1</sup>Institute for Planetary Materials, Okayama University, Misasa, Tottori 682-0193, Japan.

\*email: [iezenwa@okayama-u.ac.jp](mailto:iezenwa@okayama-u.ac.jp)

**Introduction:** Knowledge of the thermal and electrical conductivity of solid and liquid Fe and its relevant alloys at P and T conditions is essential for understanding the cooling history of planetary cores and modelling their dynamo. The general understanding of the electrical transport properties of the transition metals at lower P will perhaps give insight in understanding Fe behavior at the inaccessible planetary core conditions. Theoretical investigation has suggested that the electrical and thermal conductivity of solid and liquid Fe at Earth's core conditions are similar in value [1]. At ambient T, experimental investigation showed that hcp  $\epsilon$ -phase of Fe becomes paramagnetic at  $\sim 18$  GPa while Pt is paramagnetic and crystalize fcc at ambient conditions. Since Fe and Pt have an unfilled  $d$ -band electronic structure and at high P both exhibits closed packed crystal structures, experimental determination of the transport properties of molten Pt at lower P conditions is important for understanding the behavior of molten Fe preceding  $\epsilon$ -phase at  $\sim 80$  GPa.

**Experimental:** We develop a technique and cell design for the investigation of the electrical resistivity of metals that keeps it free from contamination in the multianvil press. And, we

report measurements on Fe and Pt. The sample was kept pure by making the electrodes and the sample the same composition while the thermocouple (TC) is placed close to the sample and taking through the gasket. The major challenge of TC breakage during compression and/or heating was overcome by shielding the TC with a cylindrical hollow coiling ring made of the same composition as the TC leads. The use of current polarity reversal to eliminate biased voltage as deployed in previous studies was adopted.

**Results and Discussion:** The resistivity of both Fe and Pt increases and decreases with T and P respectively, was observed. On melting, Fe result at 3 GPa agrees with very recent data by Silber et al. [2] which showed an increasing difference in the resistivity value of solid and liquid with increasing P. While, Pt resistivity on melting at 3 GPa appears constant comparable to its 1 atm value. Experiment is on-going to measure resistivity of liquid Fe and Pt at higher P.

**References:** [1] Wagle, F., Steinle-Neumann, G., *Geophys J. Int.*, **213**, 237, (2018). [2] Silber, R.E. et al., *Sci. Rep.*, **8**, 10758 (2018).

## Melting process in Hawaii plume: Report from a large volume multi-anvil laboratory in Guangzhou Institute of Geochemistry

E.Takahashi<sup>1,2\*</sup>, S.Gao<sup>1,2</sup>, J.Wang<sup>1</sup> and Li Li<sup>1</sup> <sup>1</sup>Guangzhou Institute of Geochemistry, Chinese Academy of Sciences, 510640, China, <sup>2</sup>Earth and Planetary Sciences, Tokyo Institute of Technology, Tokyo Japan

\*email: takahashi@gig.ac.cn

**Introduction:** Mantle plumes originate either from the bottom of the mantle (CMB; core-mantle boundary, Davies, 1990) or the base of the upper mantle (600-700 km depth, White and McKenzie, 1995). In order to produce large amount of tholeiite magma in the shield building stage of the Hawaiian plume its potential temperature is considered to be at least 300°C higher than asthenosphere judging from the peridotite dry solidus at 3 GPa (base of the Pacific plate).

However, if large amount of recycled eclogite component is involved in the genesis of LIP magmas, estimated PMT of the plumes based on peridotite dry solidus should be overestimated in great amount. Based on melting study of the Columbia River basalts, Takahashi [1] proposed that temperature of the Yellowstone plume may be only ~100°C higher than normal asthenosphere. In order to evaluate the role of recycled eclogite in magma genesis of Hawaiian plume, we carried out high-P and high-T melting experiments.

**Experimental:** High-pressure experiments at 2.9, 5 and 8 GPa were carried out using a Boyd-England-type piston cylinder and a 2500 ton cubic-type multi-anvil press recently moved from EPS Tokyo Institute of Technology to Guangzhou Institute of Technology. Under both dry and hydrous conditions, layered basalt/peridotite starting materials were used. Fertile lherzolite KLB-1 (Takahashi [2]) was employed as peridotite component, and two basalt components were used as recycled crust component: 1) Columbia River basalt (CRB72-180, Takahashi [1]) which is relatively enriched in K, Ti and LREE ( $K_2O \approx 1\text{wt}\%$ ,  $TiO_2 = 3.15\text{wt}\%$ ), N-type MORB (NAM-7, Yasuda [3]).

**Results:** Melts formed by reactive melting of dry eclogite and peridotite changes dramatically in the temperature range across the solidus of peridotite KLB-1 from basalt (below dry solidus) to picrite (20-40°C above dry solidus). Basaltic melts are not saturated with olivine both at 2.9, and 5 GPa and therefore they are separated by peridotite matrix by Opx film. Chemical reaction between the basalt melt and the peridotite matrix proceeds only slowly by solid-diffusion across the Opx film. In hydrous experiments, solidus of peridotite decreases significantly and therefore the reaction between hydrous melt and the partially molten peridotite matrix proceeds at temperatures below peridotite dry solidus.

Melting study of alkali-basalt/peridotite layered sample showed much lower solidus temperature than MORB/peridotite sample mainly due to  $K_2O$ . Melting starts as deep as 200km depth and composition of initial melts at pressures higher than 120km are similar to K-rich alkali acidic rocks (phonolite, hawaiiite) as long as melting is limited in basalt layer. On the other hand, silica-poor alkali magmas (basanite, nephelinite) are produced in the presence of volatiles which widen partial melting of peridotite as well as mafic component.

**Genesis of Hawaiian tholeiite magma:** Iron rich-nature of Hawaiian tholeiite is difficult to reproduce by reaction melting of MORB/peridotite but is reproduced by CRB72-180/peridotite. Recycled mafic component in Hawaii plume, therefore, may be higher in FeO than modern MORB which is consistent with Fe-rich nature of mafic rocks in early Earth and estimated model recycle time of Hawaii plume (>2Ga). Based on present experiments, we propose that potential temperature of the Hawaii plume may be only 100-150°C above that of normal asthenosphere. Tholeiite magma in the shield building stage may be formed slightly under hydrous condition near the dry solidus of peridotite (1450-1500°C at about 3 GPa). Our model predicts lower plume temperatures than most previous estimates. Change in plume flux of Hawaii hot spot through time may be related to the amount of entrained eclogite than potential temperature.

**Origin of alkali magma:** Post shield stage phonolite and hawaiiite magmas in Hawaii were considered to be fractionation product of alkali basalts under crustal magma chambers (e.g., Frey et al, 1990). However, our experimental results revealed an alternative scenario that phonolite and hawaiiite magma were derived from partial melting of alkali basaltic blocks at deeper part (150-200km) of the plume. On the other hand, basanite and nephelinite which appears in rejuvenated stage may represent partial melt of peridotite portion of the plume beneath Pacific plate. We discuss magma genesis in Hawaii plume based on our melting experiments and occurrence of diverse magma types both geographically and in growth history of a given shield volcano.

**References:** [1] Takahashi et al, *Earth Planet. Sci. Lett.* (1998) [2] Takahashi, *J. Geophys. Res.*, (1986), [3] Yasuda et al., *J. Geophys. Res.* (1994)

## Silicic melt obtained from the melting experiments of mantle peridotite reacted with slab melt

N. Tsuchiya<sup>1\*</sup> and D. Yamazaki<sup>2</sup>

<sup>1</sup>Department of Geology, Iwate University, Morioka 020-8550, Japan. <sup>2</sup>Institute for Planetary Materials, Okayama University, Misasa, Tottori 682-0193, Japan. \*email: tsuchiya@iwate-u.ac.jp

**Introduction:** Island arc magmatism along convergent plate margins is one of the major processes of continental crust generation, and the net flux from mantle to crust is considered to be basaltic [1]. On the other hand, Archean trondhjemite-tonalite-granodiorite (TTGs) are considered to have formed during subduction by partial melting of hydrated oceanic crust transformed into garnet amphibolite to eclogite (slab melting), slab melting is of particular importance to crust-forming processes in the planet Earth [2-4]. In this study, the partial melting of peridotite modified by reaction with felsic slab melts, was experimentally investigated at 1.5 GPa for H<sub>2</sub>O saturated conditions in the relatively low temperature range from 1000 to 1075°C, and the generation of andesitic melts is discussed.

**Results and Discussion:** Starting materials are 1) synthesized peridotite (H<sub>2</sub>O: 12.59%), 2) synthesized peridotite plus 40%, 20%, and 5% of slab melt (H<sub>2</sub>O: 0.7 to 12%), and 3) Ichinomegata lherzolite plus 40% of adakitic granite (H<sub>2</sub>O: more than 10%). All the experiments were carried out using a piston cylinder apparatus and Au capsules. In the case of starting materials 1), no glass were observed both at 1000 and 1050°C. Starting materials 2) to 3), the quenched glasses obtained at 1000°C were dacitic in composition (SiO<sub>2</sub> = 67-68%, MgO = 0.5-1.1%), and the volume of melt was 18 to 32%. The quenched glasses obtained at 1050°C were andesitic in composition (SiO<sub>2</sub> = 57-64%, MgO = 1.5-4.5%), and the volume of melt was 20 to 34%. The quenched glasses obtained at 1075°C were andesitic in composition (SiO<sub>2</sub> = 56-61%, MgO = 3-4%). All of those glasses are coexisting with olivine (Fo 89-91%), orthopyroxene, and clinopyroxene.

These results indicates the possibility that calc-alkaline dacitic to andesitic melts can be generated by the reaction of slab melts with mantle peridotite. Moreover, this suggests that calc-alkaline dacites to andesites can be formed by direct partial melting of the hydrous upper mantle contaminated with slab melts. These results were not consisting with the previous results [5, 6], which probably resulted from higher SiO<sub>2</sub> content in starting peridotite.

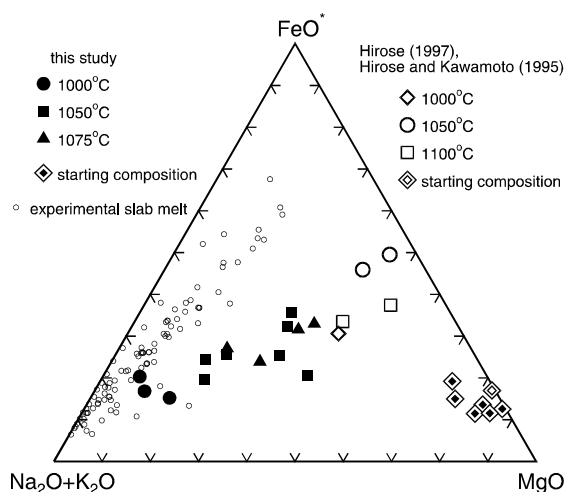


**Figure 1** AFM diagram of glass compositions obtained from this study. Data from [5, 6], and experimental slab melt compiled by [7] are also plotted for comparison.

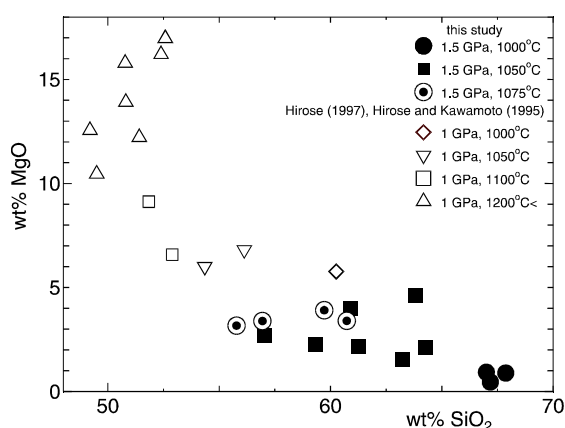


**Figure 2** MgO-SiO<sub>2</sub> diagram of glass compositions obtained from this study. Data from [5, 6] are also plotted for comparison.

**References:** [1] Kay, R. W., and Kay, S. M., *Geological Society Special Publication* **24**, 147-159 (1986). [2] Martin, H., *Geology*, **14**, 753-756 (1986). [3] Defant, M.J. and Drummond, M.S., *Nature*, **347**, 662-665 (1990). [4] Rollinson, H., *Nature*, **389**, 173-176 (1997). [5] Hirose, K., and Kawamoto, T., *Earth and Planetary Science Letters*, **133**, 463-473 (1995). [6] Hirose, K., *Geology*, **24**, 44-46 (1997). [7] Tsuchiya, N., Kimura, J.-I. and Kagami, H., *Journal of Volcanology and Geothermal Research*, **167**, 134-159 (2007).

## Pressure dependence of graphitization: Implications for rapid recrystallization of carbonaceous material in Earth's crust

Y. Nakamura<sup>1,\*</sup>, T. Yoshino<sup>2</sup>, and M. Satish-Kumar<sup>3</sup>

<sup>1</sup>Geological Survey of Japan, National Institute of Advanced Industrial Science and Technology, AIST, Tsukuba Central 7, 1-1-1 Higashi, Tsukuba 305-8567, Japan

<sup>2</sup>Institute for Planetary Materials, Okayama University, Misasa, Tottori 682-0193, Japan

<sup>3</sup>Department of Geology, Faculty of Science, Niigata University, 2-8050 Ikarashi, Nishi-ku, Niigata 950-2181, Japan \*E-mail:yoshi-nakamura@aist.go.jp

**Introduction:** Graphitization of carbonaceous material (CM) to graphite is one of the most important and sensitive thermal indicators for very low-grade to amphibolite facies metamorphism (150–650 °C) [1]. Although there are many reasons for investigating natural graphitization, most studies ultimately focus on its application as a user-friendly thermal indicator during metamorphism, independent of bulk chemistry and the mineral assemblage. Hence, many researchers have widely investigated natural graphitization in metamorphic rocks. On the other hand, the kinetics of graphitization has been debated for several decades. Laboratory experiments have shown that the synthesis of graphite from amorphous carbon at 1 atm requires a very high activation energy of  $\sim 1000$  kJmol<sup>-1</sup> [2]. For example, previous experimental kinetic data suggest that, even at 700 °C, synthesizing graphite from amorphous carbon would require a duration of  $\sim 10^{40}$  min ( $\sim 1.9 \times 10^{34}$  years) [3]. Thus, besides temperature, further extrinsic factors such as pressure and deformation during metamorphism should also be considered.

**Experiment:** HPHT experiments for the kinetics of graphitization were performed at the Institute for Planetary Materials (IPM). Three different high-pressure apparatuses were used in this experiment: (1) a piston-cylinder (PC) high-pressure apparatus, (2) a DIA-type high-pressure apparatus (AMAGAEL), and (3) a Kawai-type multi-anvil high-pressure apparatus.

**Results and Discussion:** Natural carbonaceous material from sedimentary rocks in the Shimanto accretionary complex and the Hidaka metamorphic belt, underwent systematic changes in crystallinity and morphology with increasing pressure (0.5 to 8.0 GPa) and durations (10 min to 24 h) at 1200 °C. To assess the pressure dependence of graphitization, we adopt two approaches for formulating the graphitization kinetics using a power law rate model (Fig. 1A) and a Johnson–Mehl–Avrami–Kolmogorov model (Fig. 1B). Activation volumes of  $-21.7 \pm 3.0$  to  $-33.7 \pm 17.3$  cm<sup>3</sup> mol<sup>-1</sup>, and  $-1.5 \pm 0.3$  to  $-4.0 \pm 1.7$  cm<sup>3</sup> mol<sup>-1</sup> are obtained for pressures from 0.5 to 2.0 GPa and 2.0 to 8.0 GPa, respectively (Fig. 1). Such negative activation volumes are closely related to nanostructural reorganization in the precursor material based on TEM observations. The experimental data are applied to the Arrhenius-type equation of graphitization, extrapolated to geological

$P$ – $T$ – $t$  conditions. Our model predicts that carbonaceous material undergoing metamorphism for  $\sim 10$  Myr at pressures of 0.5–1.0 GPa will begin to crystallize at 380–500 °C and will transform to fully ordered graphite at 480–700 °C, depending on the peak pressure. Thus, natural graphitization in Earth's crust might proceed much more rapidly than previously estimated, owing to the large negative activation volumes of the reaction. Our model is applicable to a wide range of  $P$ – $T$ – $t$  conditions and provides a new pathway not only for more precise geothermometry, but also geospeedometry and geobarometry.

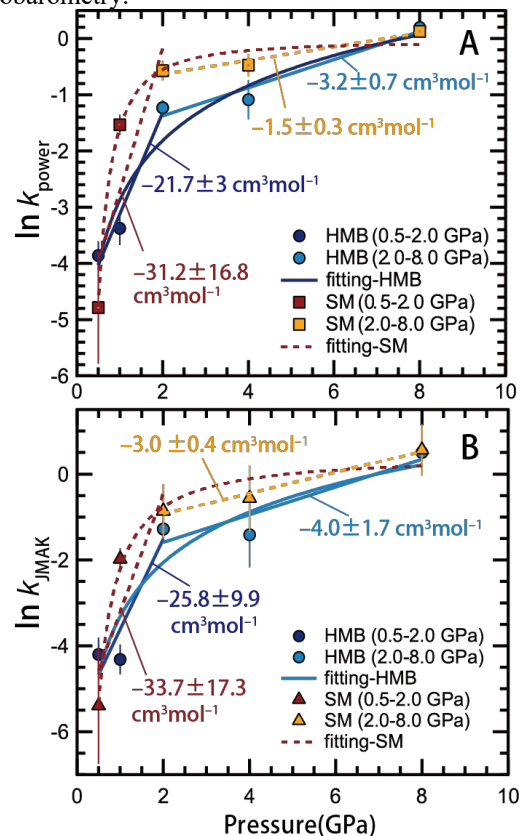


**Figure 1.** Log-linear plots of pressure (GPa) and  $\ln k_{\text{power}}$  (A) and  $\ln k_{\text{JMAK}}$  (B) for both samples. The  $\ln k_{a,p}$  as a function of pressure are fitted by power rate and linear regressions.

**Reference:** [1] Buseck, P. and Beyssac, O. *Elements*, **10**, 421 (2014). [2] Fischbach, D.B. *Nature*, **200**, 1281 (1963). [3] Bustin, R.M., Rouzaud, J.-N., and Ross, V., *Carbon*, **33**, 679 (1995).

## Electrical conductivity measurement of rhyolitic and andesitic glasses

Y Haraguchi<sup>1</sup>, T Yoshino<sup>2</sup>, S Yamashita<sup>2</sup>, M Nakamoto<sup>1</sup>, M Suzuki<sup>1</sup>, K Fuji-ta<sup>1\*</sup> and T Tanaka<sup>1</sup>

<sup>1</sup>Graduate School of Engineering, Osaka University, Suita, Osaka 565-0871, Japan.

<sup>2</sup>Institute for Planetary Materials, Okayama University, Misasa, Tottori 682-0193, Japan.

\*email: [fujita@fsao.eng.osaka-u.ac.jp](mailto:fujita@fsao.eng.osaka-u.ac.jp)

**Introduction:** Magneto-Telluric (MT) soundings have been developed to seek electrical conductivity structure of volcanic body and its underground structures. In particular, to interpret melt process and properties of rock and/or mineral beneath the volcano, it is crucial to obtain electrical conductivity data of rock and mineral in the laboratory. To compare with results from MT observation and those of laboratory measurement, we can have much knowledge of subsurface electrical conductivity structure of volcanic region. Despite the accumulation of much MT data and laboratory data, the interpretation for electrical conductivity structure and conductivity variation in the laboratory remain unknown. Particularly, electrical conductivity behavior of volcanic rock in the melt region and glass transition zone is not elucidated yet.

In the present work, our studies examine and focus on electrical conductivity change of rhyolite and andesite glasses.

**Experimental:** We synthesized rhyolite glasses using the piston cylinder apparatus. Glass samples were synthesized at 1 GPa.

Electrical conductivity measurements were conducted at 1 to 3 GPa using a DIA-type cubic anvil press with maximum load of 2000 ton and 6-axis apparatus. In our experiments, the sample assembly was designed to have high insulation resistance as shown in Figure 1. The cell assembly mainly consists of pyrophyllite, ZrO<sub>2</sub>, Al<sub>2</sub>O<sub>3</sub> and MgO to keep high insulation [1]. Before starting conductivity measurement, the assembly was pre-heated below 500-600 K to exclude the contained water and moisture. The glass sample with dimensions of 1.0-1.6 mm in diameter and 1.0 mm in thickness was surrounded by single crystal quartz. To avoid chemical reaction between sample and surrounded quartz, we conducted preparatory experiments and carefully inspected reactivity in high temperature range using the SEM.

**Results and Discussion:** After conducting pre-heating to purge contained water and moisture around the assembly, stable conductivity data were

obtained. Between 500 and 1600 K, the conductivity of rhyolite (Water contents: 0 wt% and 4 wt%) seemed to stabilize and show linear trend as expected from Arrhenius equation. We succeeded in electrical conductivity measurement to have stable and reversible values up to 1600 K. The conductivity linearly increased with increasing temperature. Using the linear trend of Arrhenius law, the activation energy of rhyolite was estimated. We also examined conductivity behavior of andesitic glasses. From the specific data, we observed minute electrical conductivity variation around the glass transition temperature which were estimated from viscosity [2] for rhyolite and andesite glasses. Our results suggest that the relation between the change of electrical conductivity and glass transition temperature estimated electrical conductivity can be used for prediction such as explosive event in volcanic region.

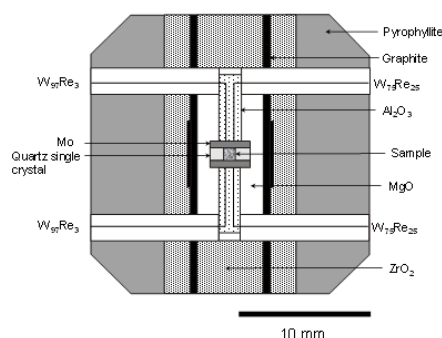


**Figure 1** Construction of cell assembly for electrical conductivity measurements of rhyolitic and andesitic glasses.

## References:

[1] Fuji-ta, K., et al., *Tectonophysics*, **504**, 116–121 (2011).

[2] Giordano, D., et al., *Journal of Volcanology and Geothermal Research*, **142**, 105-118 (2005).

## The Measurement of Seebeck coefficient under Pressure using Six-axis Multi-Anvil Press

Y Mori<sup>1\*</sup>, N. Nakano<sup>1</sup>, T. Yoshino<sup>2</sup>

<sup>1</sup>Department of Science, Okayama University of Science, Ridai 1-1, Kita-ku, Okayama 700-0005, Japan.

<sup>2</sup>Institute for Planetary Materials, Okayama University, Misasa, Tottori 682-0193, Japan.

\*email:mori@das.ous.ac.jp

Magnesium silicide ( $Mg_2Si$ ) is a semiconductor with the promising because the thermoelectric material because of a harmless to the human body and a large deposit. The phase diagram of the material is very simple however it is difficult to synthesize the high purity  $Mg_2Si$ , because the melting point of  $Mg_2Si$  is close to the boiling point of Mg at high temperature region. Therefore we have studied the high-pressure synthesis by means of a piston cylinder method and a hot pressing method to synthesize to the stoichiometric compound [1]. As a result, the high quality  $Mg_2Si$  without the unreacted starting materials was synthesized, but the thermoelectric performance never improved dramatically. Morozova et al. reported that the Power factor of Al-doped  $Mg_2Si$  at 2 GPa increased by 10 times of the ambient pressure [2]. In order to understand the behavior under high-pressure, it is necessary to develop the measurement technique of the Seebeck coefficient and the electric resistance under high-pressure and high-temperature.

In this paper, we developed the thermoelectric measurement system at high-temperature and high-pressure using six-axis multi-anvil press.

The pressure was generated by the six-axis multi-anvil press, which was installed in the Institute for Planetary Materials, Okayama University. High-pressure cell consists of a pyrophyllite body as a pressure medium, zirconia tube as heat insulator. Two graphite sheets as a heater were put the center position and the off-set position in the high-pressure cell to make the monotonous temperature gradient as shown in Fig. 1. The temperature on the both surfaces of sample was controlled, individually by the heaters, and measured by two thermocouples made of W-Re. There were 4-leads for the electrical conductivity and 2-leads for the thermal electro motive force. The sample which size was 2.25 mm in height and 3.0 mm in diameter was formed by an ultrasonic machining.

The pressure experiment was carried out from 1.0 GPa to 2.5 GPa. The temperature condition was from 472 K to 873 K with 50 K intervals and the temperature difference for the temperature gradient was from minus 20 K to plus 10 K.

Figure 2 shows the results of thermal electro motive force at 1 GPa under several temperature. The value of Seebeck coefficient under pressure was evaluated by an inclination of the line, and the absolute value of that was decreased with increasing pressure.

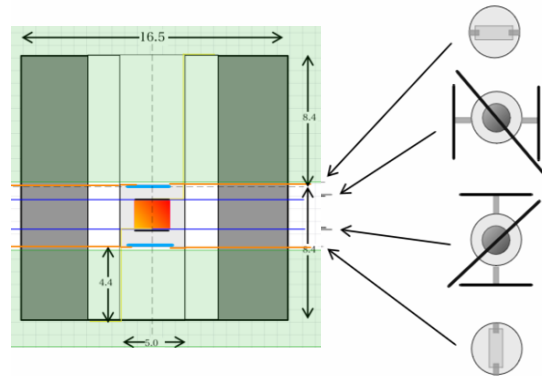


**Figure 1** Schematic image of high-pressure cell for the measurement. Two sheet heaters of graphite were put the center position and the off-set position to make the temperature gradient in the sample.

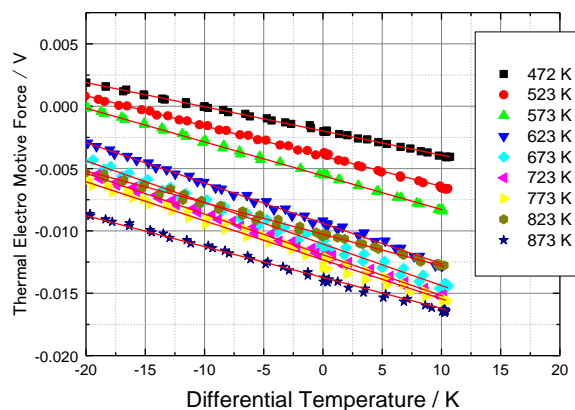


**Figure 2** Thermal electro motive force of  $Mg_2Si$  as a function of differential temperature at various temperatures under 1 GPa. The seebeck coefficient is calculated by the inclination.

**Acknowledgement:** The study was performed by “Joint Usage / Research Centre” program by MEXT at the Institute for Planetary Materials, Okayama University. The work was supported by JSPS KAKENHI Grant Number 17K06847 and 26420731, and Foundation for “Okari GAP”, Okayama University of Science.

### References:

- [1]Y. Mori, Y. Kaihara, S. Nakamura, T. Yoshino and K. Takarabe., *phys. stat. solidi. (c)*, **2013**, 10, 1847-1849.
- [2]N. V. Morozova, S. V. Ovsyannikov, I. V. Korobeinikov, A. E. Karkin, K. Takarabe, Y. Mori, S. Nakamura, V. V. Shchennikov, *J. Appl. Phys.*, **2014**, 115, 213705 1-9.

## Redox kinetics of olivine revealed by diffusion profile of oxygen fugacity and its implication to the redox evolution of the uppermost mantle

C Zhao<sup>1\*</sup> T Yoshino<sup>1</sup> <sup>1</sup>Institute for Planetary Materials, Okayama University, Misasa, Tottori 682-0193, Japan.  
\*email:zhaocc@s.okayama-u.ac.jp

**Introduction:** The evolution of the redox state of the mantle through time has been a focus of hot debate. Recent study implies that the redox state of the slab may not significantly be changed during subduction [1]. Thus, ferric iron transported by oxidized slab is expected to change the redox state of the upper mantle. However, concentrations of Cr, V, and the V/Sc ratio of the oldest known rocks indicate that the upper most mantle has remained at approximately FMQ over the past 3.5 Gyrs [2, 3]. Therefore, it seems that although oxidized slab is continuously subducted into mantle, the redox state of the upper mantle does not change systematically.

It is possible that the mantle represents an almost infinite buffer reservoir and renders the addition of oxidized slab ineffective. On the other hand, the possible extremely slow reaction speed between slab and the uppermost mantle materials might disable the oxidized component to be an effective redox changer. However, the mechanism of the interaction between them remains unclear, which is of great urgent to investigate.

**Experimental:** Olivine (MgO, SiO<sub>2</sub> and Fe<sub>2</sub>O<sub>3</sub> oxide mixture) with 5 wt% Pt powder used as oxygen sensor was first synthesized using gas mixture furnace at iron-wustite (IW) buffer and Ni-NiO (NNO) buffered condition at 1300 °C. Diffusion couple method is adopted to investigate the redox kinetics of olivine, within which pre-sintered piece of oxidized and reduced olivine was stacked face to face. Diffusion experiments were conducted for different durations at 1 GPa, 1100-1300 °C using piston cylinder apparatus.

After recovery, oxygen fugacity profiles were calculated from iron fraction in Pt alloy and iron content in olivine measured by EPMA [4]. Diffusion coefficients were obtained using Boltzmann-Matano method through fitting and calculation of iron content in Pt alloy as a function of distance from Matano interface. Water content after diffusion was measured using FTIR.

**Results and Discussion:** Except one couple, the water content of all the other couples shows < 10 wt. ppm. Redox process in olivine could be viewed as a diffusion-controlled process. Diffusion coefficient in oxidized olivine shows obvious oxygen fugacity dependence, while that in reduced one shows small dependence (Fig. 1).

The activation enthalpy is calculated to be 235 kJ/mol, which is comparable with that for Fe-Mg diffusion in olivine. However, the magnitude is 2-4 orders higher. Since the activation enthalpy and magnitude are comparable with that of diffusion of

hydrous defects related to Mg-vacancies [5], it is possible that even extremely small amount of water could dominate redox kinetics in olivine.

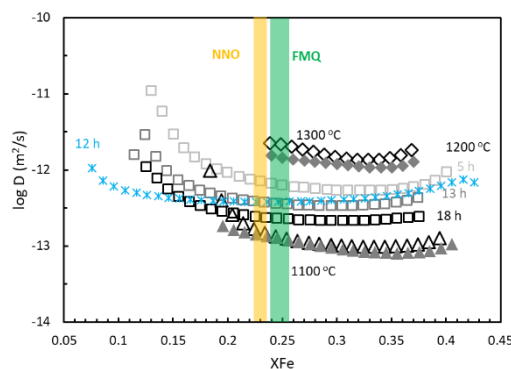


**Figure 1** Diffusion coefficient as a function of iron content in Pt alloy. Unfilled and filled symbols are data from Pt capsuled and MgO capsuled samples, respectively. Blue star line is diffusion coefficient from magnetite-containing couple.

The diffusion length calculated indicate that the influence exerted by slab on the reduced mantle is very limited (< 4 km at 1600 °C even for 4500 Ma's stagnation in the upper mantle) (Fig. 2). Therefore, it is possible that the extremely slow redox process prevents subducted slab to change the redox state of the upper mantle. Once subducted more, the oxidized slab can bring redox budget to deep mantle as it keeps dry condition.

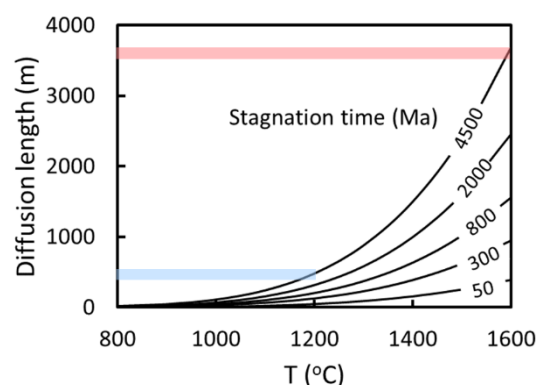


**Figure 2** Diffusion length calculated for subducting slab stagnated at the upper mantle for different durations.

**References:** [1] Lee, C.A., et al., *Nature*, **468**, 681 (2010). [2] Canil, D., *Earth Planet. Sci. Lett.*, **195**, 75 (2002). [3] Li, Z.A. and Lee, C.A., *Earth Planet. Sci. Lett.*, **228**, 483 (2004). [4] Faul, U.H., et al., *Phys. Chem. Mineral.*, (2017). [5] Padron-Navarta, J.A., et al., *Earth Planet. Sci. Lett.*, **392**, 100 (2014).

## Electrical conductivity of hydrous olivine: revisited by various approaches

T. Yoshino<sup>1\*</sup>, W. Sun<sup>1,2</sup>, C. Zhao<sup>1</sup>, N. Sakamoto<sup>3</sup>, H. Yurimoto<sup>3,4</sup>

<sup>1</sup>Institute for Planetary Materials, Okayama University, Misasa, Tottori 682-0193, Japan. <sup>2</sup>Earth-Life Science Institute, Tokyo Institute of Technology, Tokyo, Japan. <sup>3</sup>Isotope imaging laboratory, Creative Research Institute, Hokkaido University, Japan. <sup>4</sup>Department of Natural History Sciences, Hokkaido University, Sapporo, Hokkaido 060-0810, Japan.

\*email:tyoshino@misasa.okayama-u.ac.jp

**Introduction:** Magnetotelluric (MT) studies have constructed the profiles and structures of electrical conductivity in the mantle up to the uppermost lower mantle. A major conductivity anomaly is found in the oceanic upper mantle at ~100 km depth near the mid ocean ridge. It shows high conductivity about  $10^{-2}$  to  $10^{-1}$  S/m and is characterized by strong anisotropic feature [1]. The origin of the conductivity anomalies is still in debate. One of major hypotheses to explain this anomaly is olivine hydration.

Many researchers have studied effect of water on electrical conductivity of olivine. Although several groups have measured the electrical conductivity of mantle materials at high pressure, they have provided inconsistent results with regard to the effect of water. Some studies suggested that olivine with the maximum soluble H<sub>2</sub>O content at the top of the asthenosphere has lower conductivity less than 0.1 S/m, which is a typical value of conductivity anomaly observed in the oceanic mantle, and has weak anisotropic feature [2-4]. In contrast, more recently, electrical conductivity measurement of single crystal olivine at relatively high temperature have shown higher conductivity with high activation energy [5], suggesting that small amounts of water account for the conductivity anomaly.

In this study, we revisit the effect of water on electrical conductivity of olivine based on H-D inter-diffusion in olivine single crystal and conductivity measurement of buffered sintered samples.

**Experimental:** Hydrogen in octahedral site vacancy has thought to be a main charge carrier to link lattice hydrogen diffusion and proton conduction. Recent FTIR and NMR investigation and first principle calculation indicated that concentration of hydrogen in M site was negligibly small. The other candidate of electric carrier for hydrous olivine is  $[2\text{H}]_{\text{Mg}}^{\times}$  diffusion. The activation enthalpy obtained for hydrogen self-diffusion in olivine is 1.1-1.8 eV, while that for proton conduction is around 0.7 eV. To investigate H-site specific effect on electrical conductivity of hydrous olivine, we have performed the conductivity measurements for the forsterite aggregates buffered by MgO and SiO<sub>2</sub>. To estimate electrical conductivity at higher temperatures, hydrogen self-diffusion coefficients determined from

inter-diffusion in H- and D-doped olivine single crystal couples at the upper mantle conditions (3-13 GPa and 1000–1300 K).

**Results and Discussion:** FTIR spectra of MgO-buffered forsterite aggregates shows strong sharp absorption peaks at high wave numbers, while those of SiO<sub>2</sub> buffered samples are characterized by smaller water content and broad absorption bands at low wave numbers. Thus, this broad band seems to be related to H in Mg site. The activation enthalpy of SiO<sub>2</sub> buffered sample is higher than MgO-buffered one, suggesting that the main charge carrier is different between them. Low activation energy (~0.7 eV) is comparable to the previous results by conductivity measurements at lower temperatures. Hydrogen in Si site vacancy in association with proton shows dominant conduction mechanism at low temperatures and in MgO buffered condition.

Hydrogen self-diffusion is highly anisotropic with highest mobility along [100] orientation. The geometric average hydrogen self-diffusion coefficient is showed as a function of temperature and water  $D_{\text{H}} = 10^{-7.7 \pm 0.8} (C_{\text{H}_2\text{O}})^{0.61 \pm 0.01} \exp(-\frac{130 \pm 17 \text{ kJ/mol}}{RT}) \text{ m}^2/\text{s}$ . This activation energy is consistent with conductivity measurement for the SiO<sub>2</sub>-buffered sample and single crystal [6] determined at high temperatures. Combined with the Nernst-Einstein relation, the present results suggests that the most of literature data overestimate effect of water on conductivity of hydrous olivine because of sample heterogeneity. Although previous studies used single crystal synthesized by diffusion, the single crystals used in these experiments have not reached equilibrium from the viewpoint of hydrogen diffusion. At high temperatures to relevant mantle condition, a main electrical charge carrier of hydrous olivine seems to be  $[\text{V}]_{\text{Mg}}^{\times}$  in association with migration of  $[2\text{H}]_{\text{Mg}}^{\times}$ .

**References:** [1] Evans et al., *Nature*, **437**, 249 (2005). [2] Yoshino et al., *Nature*, **443**, 973 (2006). [3] Poe et al., *Phys. Earth Planet. Inter.*, **181**, 103 (2010). [4] Yang et al., *Earth Planet. Sci. Lett.*, **317-318**, 241 (2012). [5] Dai and Karato, *Earth Planet. Sci. Lett.*, **408**, 709 (2014).

## H<sub>2</sub>O-enhanced ionic conductivity of olivine

T. Katsura<sup>1,2\*</sup>, H.-F. Fei<sup>1</sup>, D. Druzhbin<sup>1</sup> <sup>1</sup>Bayerisches Geoinstitut, University of Bayreuth, 95440 Bayreuth, Germany, <sup>2</sup> Center for High Pressure Science & Technology Advanced Research, 100094 Beijing, China.

\*email: tomo.katsura@uni-bayreuth.de

**Introduction:** A magnetotelluric study showed a high-conductivity ( $10^{-1}$ - $10^{-2}$  S/m) layer (HCL) at 70~120 km depths in the asthenosphere beneath young plates near the East Pacific Rise [1], which is higher than dry olivine conductivity by more than one order of magnitude. Although many studies attributed this high conductivity to olivine proton conduction, which is driven by migration of  $H_1^+$ , its magnitude in this region should be small because of the small amounts of H<sub>2</sub>O in the depleted MORB mantle [2]. Furthermore, the relatively small activation enthalpy of the proton conduction does not agree to the HT location of the HCL.

Although the olivine conduction mechanism that dominates at asthenospheric temperatures will be the ionic conduction ( $\sigma_{V_{Mg}}$ ), which is driven by migration of  $V_{Mg}''$ , conductivity measurements at ambient pressure demonstrated its small magnitudes. Our diffusion study, however, showed that the olivine Mg self-diffusivity ( $D_{Mg}$ ) almost linearly increases with increasing H<sub>2</sub>O content ( $C_{H_2O}$ ) [3]. This result implies enhancement of  $\sigma_{V_{Mg}}$  by H<sub>2</sub>O incorporation, which may interpret the HCL. To prove this hypothesis,  $\sigma_{V_{Mg}}$  was measured as a function of  $C_{H_2O}$  in this study [4].

**Experimental:** Samples for conductivity measurement were discs of natural-olivine single crystals with initial  $C_{H_2O} = 50$  wt. ppm. They were surrounded by single-crystal MgO, and sandwiched by Mo foils, which were loaded in a multi-anvil cell. When a higher H<sub>2</sub>O content was intended, a tiny amount of brucite was added next to the Mo foils. Impedance spectroscopy in the frequency range of  $10^7$  to  $10^{2-0}$  Hz was conducted in the three different crystallographic orientations at  $P = 2 - 10$  GPa. The  $T$  conditions were up to 2200 and 1700 K for low- ( $C_{H_2O} = \sim 20$  wt. ppm) and high- $C_{H_2O}$  samples, respectively. Several heating and cooling cycles were repeated to confirm essentially no change in conductivity after the first cooling. The  $C_{H_2O}$ 's were measured by means of FT-IR spectroscopy with the Withers' calibration [3] after recovery.

**Results and Discussion:** Results of conductivity measurement show that slopes of the logarithmic conductivity ( $\log \sigma$ ) to the reciprocal temperature ( $1/T$ ) increase with increasing  $T$  due to

mixed contribution of the  $\sigma_{V_{Mg}}$  and hopping conductivity. These two mechanisms were numerically separated by assuming their parallel contributions. The activation energy and volume of  $\sigma_{V_{Mg}}$  were obtained as  $E_a = 250 - 450$  kJ/mol. and  $V_a = 3.2 - 5.3$  cm<sup>3</sup>/mol., which are identical to those of  $D_{Mg}$  within the errors ( $E_a = 200 - 400$  kJ/mol. and  $V_a = 1.0 - 4.3$  cm<sup>3</sup>/mol.) [3, 6].

Significant anisotropy was found in  $\sigma_{V_{Mg}}$ , which is  $\sigma_{[001]} \gg \sigma_{[100]} \approx \sigma_{[010]}$ . This characteristic is identical to those of  $\sigma_{V_{Mg}}$  under dry conditions [7] and of  $D_{Mg}$  [6].

The  $C_{H_2O}$ 's with and without brucite were 20 - 40 and 200 - 500 ppm wt. ppm, respectively. By assuming a proportionality to a power of  $C_{H_2O}$ , the  $C_{H_2O}$  exponent was found  $r = 1.3 \pm 0.2$ . This exponent is identical to that of  $D_{Mg}$  ( $r = 1.2 \pm 0.2$ ).

These results suggest that  $\sigma_{V_{Mg}}$  increases with increasing  $C_{H_2O}$ . Since the increase in  $D_{Mg}$  with  $C_{H_2O}$  starts at least at  $C_{H_2O}$  of 1 ppm, the increase in  $\sigma_{V_{Mg}}$  will start at this  $C_{H_2O}$  as well. Hence, an increase in  $C_{H_2O}$  from 1 to 100 wt. ppm, for example, is expected to increase  $\sigma_{V_{Mg}}$  by 2.5 orders of magnitude. Thus, H<sub>2</sub>O incorporation will tremendously enhance  $\sigma_{V_{Mg}}$ .

Under the  $P$ - $T$  conditions at the top of the asthenosphere under a 5-Ma old plate, namely 3 GPa and 1650-1700 K [1], the isotropic  $\sigma_{V_{Mg}}$  of olivine with  $C_{H_2O} = 100$  wt. ppm will be  $4 \times 10^{-2}$  S/m. This conductivity is identical to or even higher than that of the top of the asthenosphere in the isotropic model ( $1 \sim 4 \times 10^{-2}$  S/m). Ref [2] also reported by a half order of anisotropy, which can be duplicated by the higher conductivity in the [001] direction than the [100] and [010] direction. Thus the HCL can be attributed to the H<sub>2</sub>O enhanced  $\sigma_{V_{Mg}}$ .

**References:** [1] Katsura, T. et al. *Tectonophysics*. **717**, 162 (2017). [2] Baba, K. et al., *J. Geophys. Res.* **111**, B02101 (2006). [3] Fei, H.-Z. et al., *Earth Planet Sci. Lett.*, **484**, 204 (2018). [4] Fei, H.-Z. et al., submitted. [5] Withers, A. et al. *Chem. Geol.*, **334**, 92 (2012). [6] Chakraborty, S. et al., *Phys. Chem. Min.* **21**, 489 (1994) [7] Constable, S. et al. *J. Geophys. Res.* **83**, 3397 (1992).

## Simultaneously generation of ultra-high pressure and high temperature by combining boron-doped diamond heater and sintered diamond anvils

L Xie<sup>1\*</sup>, K Nishida<sup>1</sup>, T Ishi<sup>1</sup>, C Artem<sup>1</sup>, B Dimitry<sup>1</sup>, T Katsura<sup>1</sup>

<sup>1</sup> Bayerisches Geoinstitut, Univ. of Bayreuth, 95440 Bayreuth, Germany.

\*email: Longjian.Xie@uni-bayreuth.de

**Introduction:** The Kawai-type multi-anvil press (MAP) is one of the most widely used high-pressure-temperature (P-T) apparatus. It generates uniform and stable high-pressure-temperature conditions in a relatively large volume. However, traditional MAPs has limited P-T conditions. Recently, significant efforts have been made for development of pressure generation technique using sintered diamond (SD) anvils and of temperature generation technique using boron-doped diamond heater.

Thanks to these efforts, the maximum pressure of MAPs exceeds 100 GPa [1], which is close to the core mantle boundary. The temperature range has been expanded to 4000 K at pressures to 15 GPa using boron-doped diamond (BDD) heater [2]. However, simultaneous generation of ultrahigh pressure (UHP) and ultrahigh temperature (UHT) is still difficult. The BDD heater was quite recently developed, and has not been implemented in cell assemblies for SD experiments. In this study, we try to simultaneously generate UHP (up to 80 GPa) and UHT (up to 3000 K) by combining BDD heater and SD anvils in MAP.

**Experimental:** High P-T experiments were conducted using the multi-anvil apparatus, SPEED-Mk.II, at BL04B1, SPring-8, Japan. First-stage anvils are made of tungsten carbide with 27-mm

truncation. Second-stage anvils are made of SD and have edge and truncation lengths of 14.0 and 1.5 mm, respectively. The pressure medium is 5.7-mm MgO octahedron. The tube heater of BDD powder with a 1.6-mm length and 0.5- and 0.7-mm inner and outer diameters, respectively were placed normal to two opposite faces of the anvil truncation. Temperatures were measured using a 0.05-mm thick W-Re thermocouple. A sintered block of MgO, mixed with diamond for suppression of MgO grain growth, was used as a pressure marker.

**Results and Discussion:** We succeeded to generate temperature as high as 3000 K at 27 GPa with SD anvils. The pressure generation of current cell assembly is similar with WC anvils due to the diamond support of BDD heater. Large thermal pressure (~2 GPa per 1000 K) can be generated in the current cell assembly. The improvement of higher pressure generation efficiency is needed in future work.

### References:

- [1] Yamazaki, D., Ito, E., Yoshino, T., Tsujino, N., Yoneda, A., Guo, X., Xu, F., Higo, Y., Funakoshi, K., *Phys. Earth Planet. Inter.*, **228**, 262-267 (2014).
- [2] Xie, L., Yoneda, A., Yoshino, T., Yamazaki, D., Tsujino, N., Higo, Y., Tange, Y., Irifune, T., Shimei, T., Ito, E., *R. Sci. Instrum.*, **88**, 093904 (2017).

## High pressure generation in the Kawai-type multianvil apparatus

D. Yamazaki, Institute for Planetary Materials, Okayama University, Misasa, Tottori 682-0193, Japan.  
email:dy@misasa.okayama-u.ac.jp

High pressure and temperature generations are the most essential importance in the experimental study of the Earth's interior. In this context, the Kawai-type multianvil apparatus (KMA) has been widely used as well as the diamond anvil cell (DAC) (cf. Ito et al., 2015). The conspicuous advantages of the KMA over the DAC are the capability to compress a large volume sample, ~1000 times larger than that of DAC, and create a quasi-hydrostatic environment owing to squeezing an octahedral pressure medium by eight cubic anvils (Kawai and Endo, 1970). Moreover, it is possible to keep the specimen in homogeneous and stable conditions at high temperature by adopting an internal heating system. These advantages makes it possible to measure physicochemical properties of the Earth's minerals precisely under high pressure and temperature conditions (e.g., Nishiyama et al., 2004).

Generated pressure in the KMA with tungsten carbide (WC) anvils had been limited to ~25 GPa (e.g., Keppler and Frost, 2005) for a long time. However, recent development of harder WC material, TJS01 (Fuji Die Co., Ltd.) containing a small amount of Ni binder (<0.2 %), opened new era to attain the pressure much higher than 25 GPa. Kunimoto et al. (2016) generated pressures up to 50 GPa at room temperature using 14 mm edge length TJS01 anvils. Later, Ishii et al., (2017) generated pressures up to 65 GPa at room temperature and 48 GPa at 2000 K using the 26 mm edge length applying higher press load. On the other hand, the attainable pressure with sintered diamond (SD) anvils has been gradually extended from 1998 to present and the attainable pressure has been extended to ~95 GPa by optimizing the pressure medium and gasket (Ito et al., 2005; Tange et al., 2008; Ito et al., 2010). In the previous our study (Yamazaki et al., 2014), we used new type of SD anvils, "C2-grade" and we could extend the generated pressure to 109 GPa. In this study, we report on the recent progress of high pressure generation in the KMA with WC (TJS01) and SD ("C2-grade") anvils.

In situ X-ray diffraction experiments at high-pressure and temperature were conducted at beamline BL04B1, SPring-8 synchrotron radiation facility using the DIA type press (SPEED-Mk.II) (Katsura et al., 2004). Energy dispersive powder X-ray diffraction technique was adopted with a polychromatic X-ray beam at a diffraction angle of ~6° in conjunction with a germanium solid-state detector. The sample was irradiated by the collimated beam with a size of 50 μm horizontally and 100 μm vertically. A multi-channel analyzer was used to acquire diffracted photons in a range of 20-140 keV through the sandwiched gaskets (anvil gaps). The energies of the photons were calibrated using characteristic fluorescence X-ray lines of Cu, Mo, Ag, Ta, Pt, Ag and Pb, or radiation sources of <sup>55</sup>Fe, <sup>57</sup>Co and <sup>133</sup>Ba. The precision in the energy measurements was approximately 30-100 eV per channel. During

acquisition of diffracted photons, sample was rotated around the vertical axis between 0° and 6° with respect to the direction of the incident X-ray beam by oscillating the press to average diffraction profile and to minimize the effect of grain growth (Katsura et al., 2004).

In the pressure generation tests with WC anvils, we measured the generated pressure at 50-100 ton intervals. After compression at room temperature, we heated the sample up to 1500 K. We conducted several tests for the pressure generation with WC anvils and pressure reached 71.3 GPa at press load of 7.5 MN at room temperature. Pressure generation efficiency against press load in the present study is higher than that in previous study by Ishii et al. (2017).

In SD experiments, we annealed the sample at every 5-10 GPa interval up to 800-1000 K during compression to relax stress and to reduce the probability of explosion of the specimen (i.e. so called "blow out"). The pressure reached 112.7 GPa at 8.0 MN and 300 K before annealing. Although the pressure generation efficiency of this run is higher than the previous study (Yamazaki et al., 2014) due to usage of smaller gaskets, the run was terminated by blow-out while increasing temperature up to ~550 K. In the next run, we successfully increased the press load up to 13.0 MN despite using 14 mm edge length anvils because the harder first stage anvil with the transverse rupture strength (TRS) of 4410 MPa (F09 grade, Fuji Die Co., Ltd.). In the previous study (Yamazaki et al., 2014), we used more brittle materials for the first stage anvil (F10 grade, Fuji Die Co., Ltd.) with TRS=3820 MPa and the maximum press load was limited to ~10 MN. As a result, in this study the pressure reached 120.3 GPa at room temperature after annealing at 760 K, although the generation efficiency in this run was lower than that in M1626 and was virtually identical (within ±5%) to previous experiment (Yamazaki et al., 2014).

POSTER

## Viscosity of Lower Mantle Estimated from the Common Diffusivity of Creep and Grain Growth

A Okamoto<sup>1\*</sup> T Hiraga<sup>1\*</sup> <sup>1</sup>Earthquake Research Institute, University of Tokyo, Tokyo, Yayoi 113-0032, Japan.  
\*email:aokamoto@eri.u-tokyo.ac.jp

**Introduction:** Grain-size reduction caused by the post-spinel transformation and subsequent grain growth during the whole mantle convection should control viscosity of the lower mantle, if it deforms by diffusion creep which is a grain-size sensitive mechanism [1]. Thus, to estimate viscosity of the lower mantle, grain growth has to be taken into consideration.

**Results and Discussion:** Our group has recently conducted high-temperature creep and grain growth experiments on forsterite + enstatite aggregate (FoEn) [2] and forsterite + periclase aggregate (FoPer) [3] and found that grain boundary (GB) diffusivities extracted from both creep and grain growth rates in both polymineralic systems are essentially identical (Fig. 1). These results indicate that the creep and grain growth are controlled by a common diffusion mechanism in both systems where the slowest diffusion species, which is silicon, is contained or absent in the constituent elements of the secondary phase.

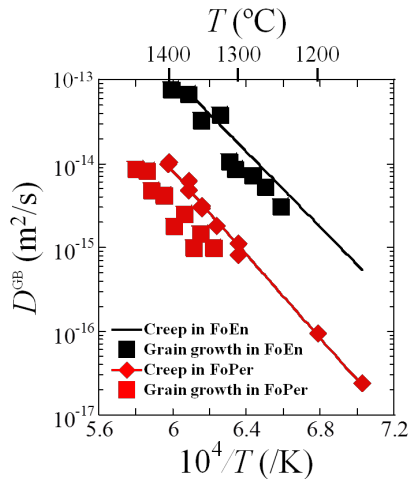


**Figure 1** Arrhenius plot of extracted grain boundary diffusivities from the creep and grain growth rates.

**Application to lower mantle:** When creep and grain growth rates are determined by the common diffusivity, grain size and viscosity of the aggregate can be described in terms of material constants, diffusivity and time. We applied these relationships to the lower mantle to calculate grain size and viscosity at each depth and age of the mantle during one cycle of the whole mantle convection. We used lattice diffusivities of constituent elements in bridgmanite and post-perovskite estimated from ab initio simulations [4][5][6] and diffusion experiments [7][8][9]. Calculations show that grain size and viscosity in downwelling mantle are ~0.2 mm and  $10^{18} \sim 10^{20}$  Pa·s while those in upwelling mantle are ~0.5-10 mm and  $10^{20} \sim 10^{24}$  Pa·s (Fig. 2).

Thus, we predict a large viscosity variation within lower mantle. The viscosity profile estimated from a joint inversion of convection and glacial rebound data [10] is well within such variation (Fig. 2b).

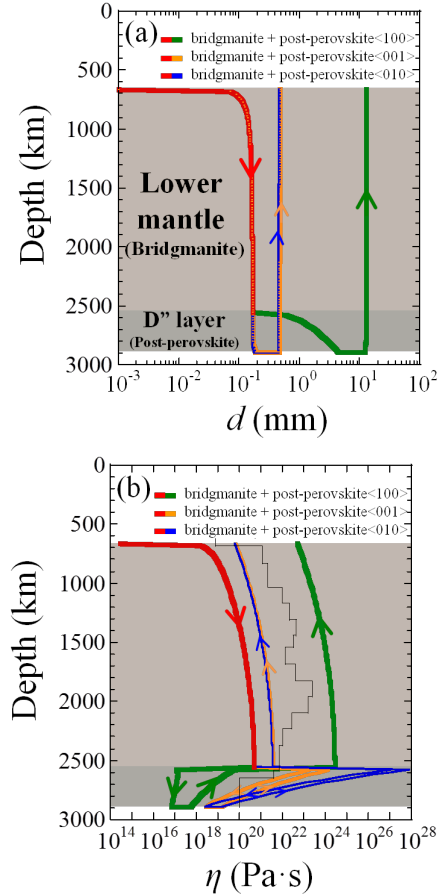


**Figure 2** Calculated depth profiles of grain size and viscosity in the lower mantle during whole mantle convection. (a) Grain size,  $d$ . Grain growth of post-perovskite is calculated based on diffusion at different crystallographic axes which are represented by different colors. (b) Viscosity,  $\eta$ , of the lower mantle deforming by diffusion creep. Colors correspond to that in (a). Viscosity profile proposed by [10] is shown by a black solid line.

**References:** [1] Solomatov, V.S. and Reese, C.C. *J. Geophys. Res.*, **113**, B07408 (2008). [2] Nakakoji, T. and Hiraga, T. *J. Geophys. Res.*, **123**, 9513-9527 (2018). [3] Okamoto, A. and Hiraga, T. in prep. [4] Ammann, M.W. et al. *Phys. Chem. Miner.*, **36**, 151-158 (2009). [5] Ammann, M.W. et al. *Rev. Mineral. Geochem.*, **71**, 201-224 (2010a). [6] Ammann, M.W. et al. *Nature.*, **465**, 462-465 (2010b). [7] Xu, J. et al. *J. Geophys. Res.*, **116**, B12205 (2011). [8] Yamazaki, D. et al. *Phys. Earth Planet. Inter.* **119**, 299-309 (2000). [9] Dobson, D.P., *Phys. Earth Planet. Inter.* **139**, 55-64 (2003). [10] Mitrovica, J.X. and Forte, A.M. *Earth Planet. Sci. Lett.* **225**, 177-189 (2004).

## Grain growth textures and kinetics in pyrolitic and basaltic materials under lower mantle conditions

T Kubo<sup>1\*</sup> and M. Imamura<sup>1</sup> <sup>1</sup>Dep. Earth Planet Sci., Kyushu University, Fukuoka 819-0395, Japan.

\*email: kubotomo@geo.kyushu-u.ac.jp

Peridotite and basaltic materials of deep slabs cause significant grain-size reduction across the upper and lower mantle boundary through the post-spinel and post-garnet transformations, respectively. The grain-size sensitive creep possibly becomes dominant in both materials, and therefore the grain-size evolution controls viscosity variation and convective mixing of chemical heterogeneities in the lower mantle. Here we report on the results of grain growth experiments in pyrolitic and MORB materials under lower mantle conditions.

Each material consists of 3-4 phases in the lower mantle; those are bridgmanite, Ca-perovskite, and ferropericlasite (+majoritic garnet at the top of the lower mantle) in pyrolite, and bridgmanite, Ca-perovskite, stishovite, and aluminous phase in MORB. Grain growth experiments in these assemblages were conducted using a Kawai-type multi-anvil apparatus at ~25-27 GPa, 1873-2373K, and for 1-3000 min. XRD and FE-SEM with EDS mapping were used to examine phase identification, grain growth texture and grain size of each phase.

Grain growth textures in pyrolite and MORB materials at ~27 GPa are shown in Fig. 1. In the case of pyrolite material, the minor phase of ferropericlasite were solely located at the grain boundary of the major phase of bridgmanite. The  $d_I/d_{II}$  ratio was roughly constant and estimated to be about 1.8 ( $d_I$ : grain size of primary phase,  $d_{II}$ : grain size of secondary phase). These observations suggest that the grain growth of bridgmanite was controlled by Zener pinning and Ostwald ripening of ferropericlasite. Zener relationship (the  $d_I/d_{II}$  ratio with the volume fraction of minor phase) in the pyrolitic lower-mantle assemblages is almost consistent with that obtained in the olivine-enstatite system (Tasaka and Hiraga, 2013). The grain size evolution in peridotite materials will be discussed based on the grain growth kinetics of the pinning phase of ferropericlasite and the Zener relationship.

In MORB material, the volume fractions are similar, however the grain sizes are

slightly different among the 4 phases. Stishovite and bridgmanite are larger than others, and stishovite exhibits columnar shape. Because each phase is not connected, Ostwald ripening likely controls the grain growth in all phases. The average grain size of 4 phases in the MORB material is smaller than that in the pyrolitic material, which roughly corresponds to the difference of ~300 K in temperature. Quantitative analysis of grain growth kinetics in each phase of MORB material will be presented. We also discuss the difference in grain size evolution and the possible contrast in viscosity between pyrolitic and basaltic materials in the lower mantle.

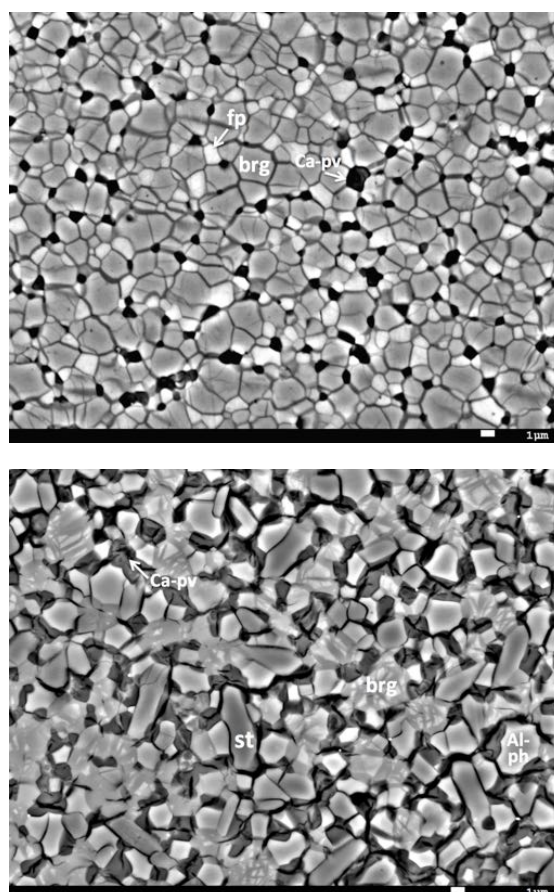


**Figure 1** Grain growth textures in pyrolitic (top, 27GPa 1800°C 60min) and basaltic (bottom, 27GPa 2100°C 60min) materials under lower mantle conditions.



## Technical development toward understanding the melting temperature of the materials at high pressure using ultra-fast spectroradiometry

R Sinmyo<sup>1\*</sup> <sup>1</sup>Department of Earth and Planetary Science, University of Tokyo, Bunkyo, Tokyo 113-0033, Japan.  
\*email:sinmyo@eps.s.u-tokyo.ac.jp

**Introduction:** Melting is the most important phenomena for understanding the co-evolution of the Earth's mantle and core. Researchers have attempted to simulate melting of materials at high-pressure and -temperature conditions for understanding the melting temperature, phase relationships and element partitioning of the materials at the core-mantle boundary. However, the melting temperature and phase relationships of terrestrial materials are not yet understood well, partly because of the unstable/heterogeneous heating in the laser-heated diamond anvil cell (LHDAC) experiments. This project aims to understand the melting temperature and the phase relationships under high-pressure conditions by using newly developed ultra-fast spectroradiometry.

**Experimental:** High-pressure and -temperature conditions were generated by using LHDAC and internal-resistance-heated diamond anvil cell (IHDAC) [1]. Metallic iron, boron-doped diamond, and silicate materials were used for the sample. DC source was used for heating in IHDAC. A function generator was used for controlling power source and spectrometer to synchronize heating and temperature measurements. A bipolar source was connected to the function generator for the amplification of the square-wave pulse for heating in some runs. The slew rate of the bipolar source was several hundred volts/microsecond in theory. Voltage and current were monitored by a high-speed digital logging system.

A fast CCD camera was attached to an astigmatism-reduced spectrometer for stationary 2-D high-resolution fast spectroradiometry. For ultra-fast 2-D spectroradiometry, galvanometer mirror was combined with optical filters and photomultiplier tubes. Streak camera was used for one run to obtain time-resolved spectra.

**Results and Discussion:** In IHDAC experiments, the temperature of the iron sample started fluctuating at certain temperature upon increasing voltage [1]. Such fluctuation is likely due to a morphology change upon melting. Since the onsets of fluctuation coincide with the jump of the resistance and disappearance of XRD signals from the solid sample, the voltage-temperature relationships can be used as a criterion for the melting. However, in the previous study, temperatures were determined by a conventional spectrometer and thus the spectra can be obtained < ~ 2 frames/sec (~ 500 milliseconds/frame), which might be too slow to resolve dynamics of the transition from solid to liquid. In this study, 2-D fast spectroscopy was combined with LHDAC and IHDAC setup. The spectroscopic measurements were successfully synchronized with the pulse or short-time heating in IHDAC and LHDAC. Spectra were obtained in ~50 frames/sec (~20 milliseconds/frame) by a newly developed system for the full 2-D image using a fast CCD camera. In contrast, several microseconds can be resolved by using the streak camera. Although the streak camera provides the fastest measurements, the signals were relatively weak so that accumulations are necessary for several ten seconds. Obtained spectra showed that the increase or decrease of temperature ends within several ten microseconds in square-wave pulse heating experiments using IHDAC. Such a short time can not be resolved by conventional spectroscopy. By a combination of DAC experiments and ultra-fast spectroscopy, it is promising to determine the melting temperature of terrestrial materials more precisely.

**References:** [1] Sinmyo, R., Hirose, K. and Ohishi, Y. *Earth Planet. Sci. Lett.*, **510**, 45-52 (2019).

## Pressure scales at multi-megabar pressure

T Sakai<sup>1\*</sup> <sup>1</sup>Geodynamics Research Center, Ehime University, Matsuyama, Ehime 790-8577, Japan.

\*email:sakai@sci.ehime-u.ac.jp

**Introduction:** The pressure conditions of deep interior of super-Earths much higher than that of the center of the Earth, and reach several hundreds of gigapascal (GPa). Above 500 GPa, a lot of phase transitions are predicted by theoretical studies for oxides, silicates [1]. Although diamond anvil cell (DAC) is widely used as an experimental tool to generate very high pressure, its pressure is usually limited up to about 300 GPa. In order to beyond the limit of conventional diamond anvils, the double stage diamond anvil cell (ds-DAC) technique was invented by Dubrovinsky et al. [2], and it is thought as a promising technique to generate ultra-high static pressures. We have also developed a ds-DAC technique by precisely fabricating 2<sup>nd</sup> stage anvils using a focused ion beam system. Using ultra-fine (< 10 nm) nano-polycrystalline diamond as 2<sup>nd</sup> stage micro-anvils, we succeeded to generate a pressure above 400 GPa [3] based on the equation of state of rhenium (Re-EoS) proposed by Anzellini et al. [4], while it is about 630 GPa according to the Re-EoS reported in Dubrovinsky et al. [2]. Although we conclude that the most likely pressure achieved was in a range of 430–460 GPa based on a calibration experiments using the platinum pressure scale [5] to 280 GPa, it should be confirmed the consistency between various pressure scales at multi-megabar conditions. Here, the consistency between equations of state (EoS) for rhenium (Re), Gold (Au), platinum (Pt) and periclase (MgO) at multi-megabar condition will be discussed.

**Experimental:** We performed the compression experiment of Pt and MgO using a conventional DAC with a 40  $\mu\text{m}$  double beveled culet. Pt and MgO were compressed up to about 308 GPa. The samples were annealed at each pressure condition using a laser heating system. For this run, MgO EoS described by Keane equation was used as a pressure standard [6]. In the second run, Au and Pt samples were compressed up to about 350 GPa with a silicate glass which was used as a pressure medium. Culet size of diamond anvils was 20  $\mu\text{m}$ . Second run was a cold compression without a laser annealing. Powder X-ray diffraction experiments were performed at BL10XU, SPring-8.

**Results and Discussion:** First, we determined a Pt-EoS based on MgO scale [6]. And then, Re-EoS's parameters were obtained based on the Pt-EoS using a compression data of Re and Pt reported in Sakai et al. [3]. The new Re-EoS was shown in Figure 1 as "Keane-MgO calibration". As shown in Figure 1, we could not reproduce the Re-EoS reported by

Dubrovinsky et al. [2] in any Pt scales calibrations [7,8] and by our new Re-EoS. Since Re-EoS by [2] was calibrated by Yokoo-Au scale [5], the difference between Au and Pt scale is a key to discuss this discrepancy. Simultaneous compression study of Au and Pt (second run) yields the volume-volume relation of these materials at high pressure condition. Using this relation, we can check the pressure difference between Au and Pt scale by [5]. As a result, Yokoo-Au scale and Yokoo-Pt scale are "roughly" consistent, and the pressure difference between these scales (10-20 GPa) cannot account for the discrepancy (>100 GPa). The discrepancy between Re-EoS by [2] and others should be explained by the experimental problem caused by a large/steep pressure gradient in the ds-DAC experiments.

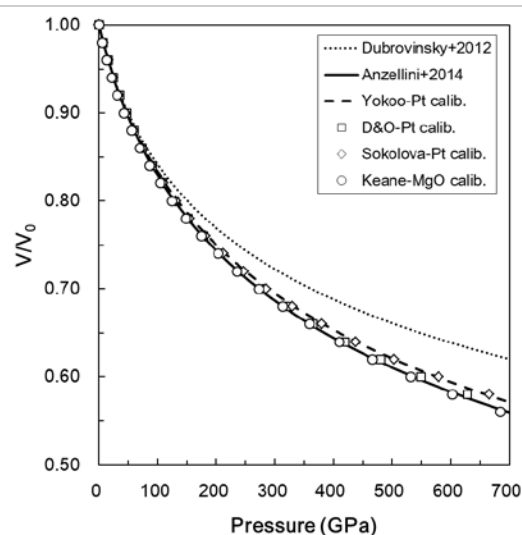


**Figure 1** Compression curves of rhenium based on several pressure standards.

**References:** [1] Tsuchiya, T., and Tsuchiya, J., *Proc. Natl. Acad. Sci.* **108**, 1252-1255. (2011) [2] Dubrovinsky, L., et al., *Nat. Commun.* **3**, DOI:10.1038/ncomms2160 (2012). [3] Sakai, T., et al., *High Press. Res.* **38**, 107-119. DOI:10.1080/08957959.2018.1448082 (2018). [4] Anzellini, S., et al., *J. Appl. Phys.* **115**, DOI:10.1063/1.4863300 (2014). [5] Yokoo M., et al., *Phys. Rev. B* **80**, 104114. (2009). [6] Sakai, T., et al., *Sci. R ep.* **6**, DOI:10.1038/srep22652 (2016). [7] Dorogokupets, P.I. and Oganov, A.R., *Phys. Rev. B* **75**, 024115. (2007). [8] Sokolova, T.S., et al., *Com p. Geosci.* **94**, 162-169. (2016).

## Polycrystalline diamond sintered from ultradispersed nanodiamonds

M Nishi<sup>1,2\*</sup>, K Yamamoto<sup>1</sup>, Y Zhou<sup>1</sup>, T Irifune<sup>1,2</sup>

<sup>1</sup> Geodynamics Research Center, Ehime University, Ehime 790-8577, Japan.

<sup>2</sup> Earth-Life Science Institute, Tokyo Institute of Technology, Tokyo 152-8550, Japan.

\*email:nishi@sci.ehime-u.ac.jp

**Introduction:** NPD is a binder-less nanodiamond aggregate (~50 nm) synthesized by direct conversion of graphite under high pressure and temperature [1]. Although NPD has extremely high hardness exceeding that of single-crystalline diamond, it is difficult to obtain the large size of the NPD above 1 cm<sup>3</sup>, because extreme high pressure conditions are required. Here we show nanodiamond polycrystalline sintered from ultradispersive nanodiamond under relatively moderate pressure and temperature conditions.

**Experimental:** We used a multi-anvil apparatus to sinter the nanodiamonds at 8-15 GPa and 1600-2300°C, where the diamond is thermodynamically stabilized. The starting materials were enclosed in metal capsules. The microstructures and chemical compositions of the recovered samples were examined using a field-emission scanning electron microscope with energy-dispersive X-ray spectroscopy. Well-sintered polycrystalline were subjected to the Knoop indentation test to evaluate its hardness.

**Results and Discussion:** We succeeded in recovering the well-sintered polycrystalline diamonds with grain size of ~10-30 nm in some runs (Figure 1). Full width at half maximum of XRD peaks decreased with increasing temperature due to the grain growth of diamond particles. The color, hardness, and grain size of the sintered polycrystalline changed depending on the capsule materials as well as the pressure and temperature conditions. These features might be affected by the porosity, the grain

size, and the impurities. Further studies are required to synthesize the polycrystalline with high hardness comparable to NPD.

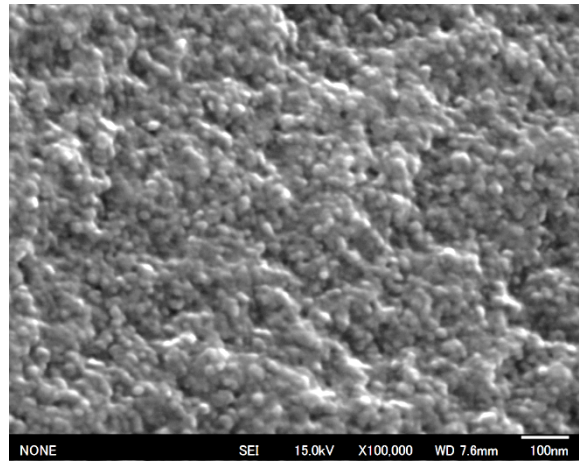


**Figure 1** SEM image of the recovered diamond polycrystalline.

**References:** [1] T. Irifune, A. Kurio, S. Sakamoto, T. Inoue, H. Sumiya., *Nature*, **421**, 599 (2003).

## Development of ultrasonic measurement technique toward whole lower mantle conditions

Y Higo<sup>1\*</sup>, T Irifune<sup>2</sup>

<sup>1</sup>JASRI, SPring-8, Kouto, Hyogo 679-5198, Japan.

<sup>2</sup>GRC, Ehime University, Matsuyama, Ehime 790-8577, Japan

\*email:higo@spring8.or.jp

**Introduction:** Elasticity data on mantle minerals under high pressure and high temperature are critical to interpret the seismic velocity and density profiles in the Earth's deep interior. However, ultrasonic measurements of elastic wave velocities under high pressure and high temperature have been limited to those corresponding to the mantle transition region (<24GPa, <1673K), because of the technical difficulties [1]. Since only a small sample can be used in the experiment under the lower mantle conditions, ultrasonic echoes are very weak and cannot perform a precise elastic measurement. In this study, to overcome this problem, the high-frequency arbitrary waveform generator, post amplifier and high-speed semiconductor relay were installed in BL04B1 at SPring-8 [2].

**Experimental:** For test measurement, pure polycrystalline alumina rod (General Electric (GE) brand Lucalox<sup>TM</sup>;  $\phi = 1.0\text{mm}$ ,  $L = \sim 0.5\text{mm}$ ) was used as a test sample. Since alumina is very hard and there is no phase transition under the condition of the upper part of the lower mantle, numbers of elastic data, which can be compared is reported. An assembly of eight cubic anvils of WC with edge length of 26 mm and truncated corner of 3.0 mm has been used in Kawai-type multi-anvil apparatus (SPEED-1500). Travel times for both P- and S-waves passing through the sample were measured by the ultrasonic interferometry, and each sample length under pressure was determined from the X-ray image of the sample using a high-resolution CCD camera. At the same time, X-ray diffraction data from the sample were acquired, and the generated pressures were monitored throughout the run.

The travel time of ultrasonic waves through the sample was determined by a pulse echo overlap method. The ultrasonic transducer was used to generate and receive ultrasonic pulses. In this study, a high-frequency waveform generator (Tektronix AWG 710 B) was introduced to drive an ultrasonic transducer in high frequency and high voltage signals, enabling the generation of a high-frequency burst sinewave signal of 60–80MHz range, and a low-noise post-amplifier (Thamway T142-4029A) was also introduced to amplify the burst sine wave signal (2 Vpp: voltage peak to peak) from the high-

frequency generator to 30 Vpp for generating powerful ultrasonic pulses (Fig. 1).

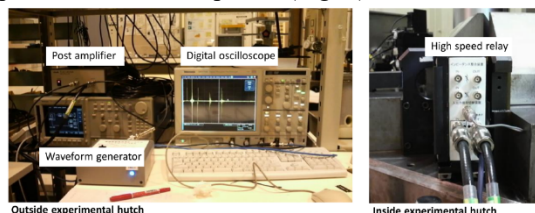


**Figure 1** Images of the installed ultrasonic measurement system. Waveform generator, post-amplifier, and digital oscilloscope located outside of the experimental hutch. High-speed semiconductor relay device located beside the high-pressure press inside the experimental hutch.

**Results and Discussion:** We have successfully measured elastic wave velocities of alumina up to ~30GPa, which corresponds to the lower mantle P-T condition. The waveforms observed very clear, and the echoes of P-wave and S-wave were identifiable at high pressure and high temperature (Fig. 2). Precise elastic wave velocity measurement of the lower mantle minerals will be attained using this system. More recently, higher pressure ultrasonic measurements of Mg-perovskite have been started, combined with the sintered diamond anvils. In this presentation, the recent experimental results of Mg-perovskite and other mantle minerals under high pressure will also be present.

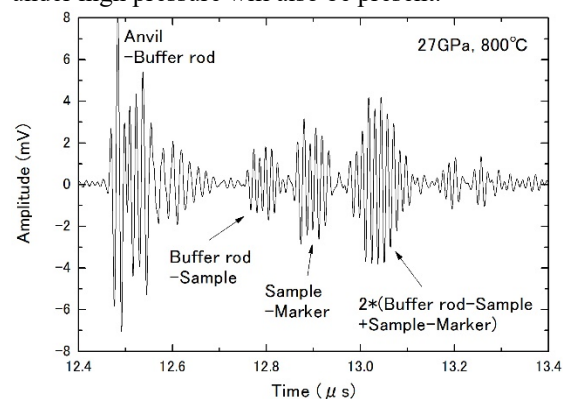


**Figure 2** Example of waveform data of  $\text{Al}_2\text{O}_3$  for the P-wave signal measured at high pressure and temperature, ~27 GPa and ~800 °C.

**References:** [1] Higo, Y., Kono, Y., Inoue, T., Irifune, T., Funakoshi, K., *J. Synchrotron. Rad.* 16, 762 (2009) [2] Higo, Y., Irifune, T., Funakoshi, K., *RSI*, 89, 014501 (2018)

## Importance of various Al substitutions in bridgmanite

T Inoue<sup>1,2,3\*</sup>, M Noda<sup>3</sup>, S Kakizawa<sup>3</sup>, T Kuribayashi<sup>4</sup>, A Sano<sup>5</sup> and T Hattori<sup>5</sup>, <sup>1</sup> Department of Earth and Planetary Systems Science, Graduate School of Science, Hiroshima University, Higashi-Hiroshima, Hiroshima 739-8526, Japan, <sup>2</sup> Hiroshima Institute of Plate Convergence Region Research (HiPeR), Hiroshima University, Higashi-Hiroshima, Hiroshima 739-8526, Japan, <sup>3</sup> Geodynamics Research Center (GRC), Ehime University, Matsuyama, Ehime 790-8577, Japan, <sup>4</sup> Department of Earth Science, Graduate School of Science, Tohoku University, Sendai 980-8578, Japan, <sup>5</sup> J-PARC Center, Japan Atomic Energy Agency, Tokai, Naka, Ibaraki 319-1195, Japan.

\*email:toinoue@hiroshima-u.ac.jp

**Introduction:** Bridgmanite should be a major constituent mineral in the Earth's lower mantle, and [1] reported that bridgmanite can incorporate almost Al<sub>2</sub>O<sub>3</sub> component in lower mantle. The Al substitution mechanism is supposed to be complicated, because there are two types of Al substitution mechanisms in anhydrous bridgmanite, Tschermak and oxygen vacancy substitutions (e.g. [2]). However, the pure Tschermak and oxygen vacancy substitutions bridgmanite has not been reported so far in low Al content, when we checked the previous studies carefully (e.g. [3, 4]). The previous studies have used powder samples as the starting materials, so we considered that the absorbed water may affect the results, because we have a knowledge of the possible existence of hydrous bridgmanite which has a water content of ~0.8 wt%. Therefore, we tried to investigate the possible existence of the Al substitution mechanism in bridgmanite as a function of Al content in extremely anhydrous condition.

**Experimental:** The high pressure experiments were conducted at 28 GPa and 1600-1700°C for 1 hour using a Kawai type apparatus. Some different Al content samples were prepared as the starting materials along the ideal substitution line of Tschermak and oxygen vacancy substitutions, respectively. Glass rods were used as the starting materials to eliminate the absorbed water on the sample surface. Moreover, the glass rods were enclosed in a rhenium capsule to prevent the water

incorporation from the surrounding cell assembly. In addition, all parts of the cell assembly were dried just before the synthesis experiments. The chemical compositions of the starting materials were examined by SEM-EDS, and the recovered samples were identified by X-ray and neutron (in J-PARC) diffractions and SEM-EDS.

**Results and Discussion:** Our results show that it is possible to exist both Tschermak and oxygen vacancy substitution bridgmanites in low Al content in anhydrous condition. The maximum Al content for pure oxygen vacancy substitution bridgmanite was less than ~0.025 pfu in total cation of 2, and the existence of pure oxygen vacancy substitution component is restricted to be less than Al=~0.1 pfu. The present result combining with our previous study in hydrous condition, shows that hydration in Al-bearing bridgmanite should occur easily if hydrogen exists in the system (lower mantle) in pyrolite (MgO-excess) composition. Thus the large deviation from the Tschermak substitution in the previous studies mainly should come from the hydration from the absorbed water.

**References:** [1] Irifune, T., *Nature*, **370**, 131 (1994). [2] Kojitani, H., Katsura, T. and Akaogi, M., *Phys. Chem. Mineral.*, **34**, 257 (2007). [3] Irifune, T. Koizumi, T. and Ando, J., *Phys. Earth Planet. Inter.*, **96**, 147 (1996). [4] Kubo, A. and Akaogi, M., *Phys. Earth Planet. Inter.*, **121**, 85 (2000).

## Stability field of hydrous aluminosilicates from the mantle transition zone to the shallow part of the lower mantle

A Suzuki<sup>1\*</sup> <sup>1</sup>Department of Earth Science, Graduate School of Science, Tohoku University, Sendai, Miyagi 980-8578, Japan.

\*email:akio.suzuki.c5@tohoku.ac.jp

**Introduction:** Water is transported into the deep Earth's interior by hydrous minerals in the descending slabs. Previous studies showed that hydrous aluminosilicates would be stable in the sedimentary layer of subducting slab. Discovery of phase Egg in the diamond inclusion also supports that hydrous aluminosilicate could exist in the Earth's deep interior. Topaz-OH II was synthesized by Kanzaki [1] at the pressure of 14 GPa and the temperature of 1400 °C, but no experiment has been reported under higher pressure conditions. In the high pressure and high temperature experiment using starting materials of  $\text{Al}_2\text{SiO}_4(\text{OH})_2$  composition have reported stable regions only at 26 GPa [2]. The phase relation of  $\text{Al}_2\text{SiO}_4(\text{OH})_2$  aluminosilicates between 14 and 26 GPa is important for the discussion of water transport from the mantle transition layer to the shallow part of the lower mantle.

**Experimental:** In this study, quenching experiments and in situ X-ray diffraction studies on the phase relation of  $\text{Al}_2\text{SiO}_4(\text{OH})_2$  were conducted in the pressure range of 12.0–32.2 GPa and in the temperature range of 800–1600 °C. Quenching experiments were carried out using a Kawai-type apparatus at Tohoku University. The recovered samples were analyzed by XRD and SEM. In situ X-ray diffraction studies were carried out at the beamline BL04B1 at SPring-8. Energy dispersive method using a pure-Ge solid state detector was adopted to collect X-ray diffraction data.

**Results and Discussion:** We observed the coexistence of  $\delta$ - $\text{AlOOH}$  and stishovite at 31.0 GPa

and 1500 °C and the formation of phase Egg together with corundum at 30.6 GPa and 1600 °C. These results indicate that phase Egg is stable at least up to 30.6 GPa and 1600 °C, which is higher pressure and temperature condition than that reported previously. Aluminous phase D, which was reported by Pamato et al. [2], was not observed in the present study. Phase Egg should be the important water carrier after the avalanche of the stagnant slab up to the depth of approximately 900 km in the lower mantle.

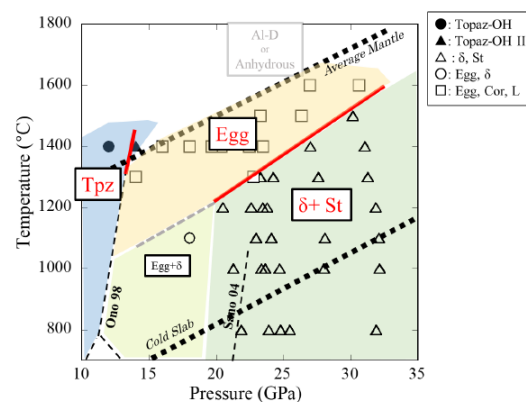


**Figure 1** Phase diagram of  $\text{Al}_2\text{SiO}_4(\text{OH})_2$  composition under high pressure and high temperature.

**References:** [1] Kanzaki, M., *Amer. Mineral.*, **95**, 1349 (2010). [2] Pamato, M.G., et al., *Nature Geosci.*, **8**, 75 (2014).

## Reaction between forsterite and nitrogen fluid at high pressure and high temperature

H Kagi<sup>1\*</sup>, T. Kubo<sup>1</sup>, A. Shinozaki<sup>2</sup>, T. Okada<sup>1</sup>, H. Ohfuji<sup>3</sup>, A. Nakao<sup>4</sup> <sup>1</sup> Geochemical Research Center, Graduate School of Science, The University of Tokyo, Hongo 7-3-1, Tokyo 113-0033, Japan. <sup>2</sup> Faculty of Science, Hokkaido University, Kita 10 Nishi 8, Kita-ku, Sapporo 060-0810, Japan. <sup>3</sup> Geodynamics Research Center, Ehime University, Bukyo-cho 2-5, Ehime 790-8577, Japan. <sup>4</sup> Institute for Physical and Chemical Research (RIKEN), Hirosawa 2-1, Wako, 351-0012, Japan. \*email:kagi@eqchem.s.u-tokyo.ac.jp

**Introduction:** Nitrogen is the essential element in the biosphere and its geochemical behavior dramatically changes with its chemical species. In the crust, nitrogen exists as  $\text{NH}_4^+$  substituting for  $\text{K}^+$  in silicate minerals. However, with increasing depth in the Earth, uncertainties on geochemical behavior of nitrogen remain unrevealed. Recently, Yoshioka et al. (2018) investigated solubility of nitrogen in the major minerals of the Earth's transition zone and the lower mantle [1]. As mentioned, chemical speciation of nitrogen strongly depends on oxygen fugacity. Under the reduced condition in the deep Earth, the nitrogen speciation could be as  $\text{NH}_4^+$  or  $\text{N}^{3-}$ . Interactions and reactions between mantle minerals and nitrogen have to be investigated for understanding geochemical behavior of nitrogen. In this study, we focused on a possibility of reaction between a representative upper-mantle mineral, forsterite ( $\text{Mg}_2\text{SiO}_4$ ), and nitrogen and tried to constrain the chemical states of nitrogen in the mantle.

**Experimental:** For high pressure experiments, diamond anvil cells (DACs) equipping a pair of type Ia diamond anvils were used. Starting samples were a single crystal synthetic forsterite ( $\text{Mg}_2\text{SiO}_4$ ) or powdered synthetic forsterite. After loading the starting material, nitrogen was introduced to the sample hole by soaking the cell into liquid nitrogen and the pressure was applied after sealing the sample and nitrogen. Before heating samples,  $\text{N}_2$  was loaded to a gasket hole with a sample and pressure was increased to approximately 5 GPa, which corresponds to representative pressure in the shallow upper mantle where forsterite is the most abundant mineral and stable phase. A carbon dioxide laser and/or a fiber laser were used to heat forsterite loaded in the DACs. Generated temperature in the sample ranged from 1300 K to 3500 K. Heated samples were quenched to room temperature and characterized with various methods. X-ray diffraction (XRD) patterns were obtained at BL-18C of the Photon Factory, KEK. Sample images were obtained with field-emission scanning electron microscope (SEM, JSM-7000F; JEOL). Chemical speciation of nitrogen was investigated using X-ray photoelectron spectroscopy (XPS, PHI 5000, VersaProbe II; ULVAC-PHI, Inc.) equipped

with a monochromatic Al  $\text{K}\alpha$  X-ray. for compensating charge-up on the sample surface

**Results and Discussion:** Figure 1 shows a representative X-ray diffraction pattern of powder forsterite sample recovered from reaction with  $\text{N}_2$ . After the reaction, orthopyroxene ( $\text{MgSiO}_3$ ) was detected. Moreover, a small peak assignable to the most intense reflection of  $\text{Si}_3\text{N}_4$  was detected. The present results indicate that the following decomposition reaction occurs in  $\text{N}_2$  fluid at high pressure and high temperature.

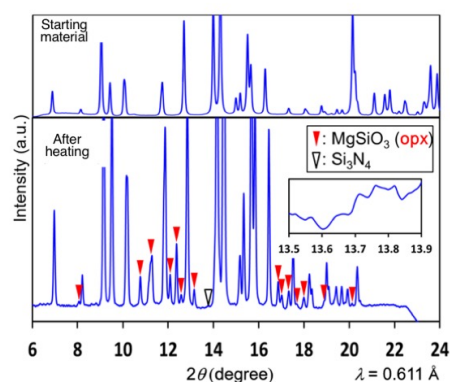


**Figure 1** X-ray diffraction patterns of powder forsterite sample before heating and after heating at high pressure in the DAC. After heating with the  $\text{CO}_2$  laser at 1400 K and subsequently with the fiber laser at 1800 K, formation of orthopyroxene was observed. The inset shows enlarged angle region corresponding to the most intense reflection of  $\text{Si}_3\text{N}_4$ .

Dissolution of forsterite into nitrogen fluid was also observed from the surface texture of a single crystal of forsterite. The chemical composition of forsterite surface suggested the preferential dissolution of  $\text{MgO}$  component and incongruent melting of forsterite which results in crystallization of orthopyroxene and periclase. XPS spectra revealed three nitrogen species,  $\text{NH}_4^+$ ,  $\text{N}_2$ , and  $\text{N}^{3-}$ , in forsterite. The present study was conducted under coexisting with  $\text{N}_2$  fluid without controlling  $f\text{O}_2$ . It is worthwhile to note that the three nitrogen species was found from forsterite heated with  $\text{N}_2$ .

**References:** [1] Yoshioka, T. et al., Earth and Planetary Science Letters **488**, 134 (2018).

## Behavior of light elements in the early stage of Earth's evolution: In-situ high-pressure and temperature neutron diffraction measurements on iron-silicate-water-sulfur system

R Iizuka-Oku<sup>1\*</sup>, H Gotou<sup>2</sup>, K Fukuyama<sup>1</sup> and H Kagi<sup>1</sup>, <sup>1</sup>Geochemical Research Center, Graduate School of Science, The University of Tokyo, Tokyo 113-0033, Japan, <sup>2</sup>Institute for Solid State Physics, The University of Tokyo, Kashiwa, Chiba 277-8581, Japan.

\*email: riizuka@eqchem.s.u-tokyo.ac.jp

**Introduction:** The Earth's core is considered to consist of Fe alloy and some light elements (O, S, Si, H, C). Hydrogen (H) is the most abundant element in the universe and one of the promising candidates existing in the Earth's core. However, its amount dissolved in the core and its process are still unknown because H cannot be detected by X-ray diffraction (XRD) and it easily escapes from iron by the release of pressure. Recently, H content in *fcc*-Fe at high pressure and temperature (high-PT) has been determined using *in-situ* neutron diffraction measurements at J-PARC [1], suggesting that H had preferentially dissolved into iron before any other light elements have dissolved in the very early stage of Earth's evolution. It is important to further study the partitioning of the other light elements between iron hydride (not pure iron) and silicates. To clarify the effects of multi light elements on the core-mantle segregation in the Earth's formation, we have focused on sulfur (S) and investigated its effect on hydrogenation of iron.

**Experimental:** As a starting material, Fe fine powder was pelletized with/without S powder and placed at the center of the graphite sample capsule. Powder mixture of quartz (SiO<sub>2</sub>), brucite Mg(OD)<sub>2</sub> (or MgO for comparison of the water existence) surrounds the Fe pellet. Sample composition of Fe:Mg(OD)<sub>2</sub>:SiO<sub>2</sub>=2:1:1 of molar ratio with 5wt.% of S simulates an ideal condition of the primitive Earth.

*In-situ* high-PT neutron experiments were carried out using a six-axis multi-anvil press "Atsuhime" installed at PLANET (BL11), MLF, J-PARC. An originally improved multi-anvil 6-6 type assembly was applied. Three samples were pressurized up to 6-7 GPa and then heated up to ~700 °C step by step. The reaction processes (dehydration of Mg(OD)<sub>2</sub>, phase transformations of Fe (*bcc*-*fcc*) and FeS, formation of silicates) were carefully checked in real time. The diffraction patterns of *fcc*-Fe were measured at 550°C and 700°C for several ~10 hours and analyzed using the Rietveld refinement method to determine structural and atomic parameters of *fcc*-Fe and sub-products. The recovered samples were examined by XRD and a scanning electron microscope (SEM) - Energy Dispersive X-ray Spectroscopy (EDS) to more precisely identify the products, their compositions, and the elements partition.

**Results and Discussion:** The cell volume changes in *fcc*-Fe and subphase of FeS-V were investigated for every hour during long-time measurements at 700°C as shown in Fig. 1. For the sample including water,

the volume of *fcc*-Fe was significantly increased with time at 700°C, whereas the sample without water showed no change regardless of temperatures. The cell volume of FeS-V did not increase for ~10 hours, suggesting that the formation of FeS was promoted in the existence of water, but its hydrogenation was negligible. Fe gradually incorporated D in the existence of water and FeD<sub>x</sub> formed. The D content at 700°C even after >10 hours was  $x \sim 0.10$  at a maximum. The value was small compared to that ( $x=0.23$ ) by our previous study on Fe-silicate-D<sub>2</sub>O system without S. From the SEM results, the inhibition of deuterization might be due to the formation of FeS layer surrounding Fe pellet, whereas such a thick FeS layer was not observed when using the Fe+S pellet. The sample without water did not include FeS layer nor Fe-bearing silicates.

It is suggested that both S and Fe were not mobile and could not react with each other without the existence of water. H and S can be preferentially incorporated into solid Fe at lower-T (~700°C) before melting, i.e. in the very early stage of the Earth's formation. The other light elements (C, O, Si) could have dissolved into molten iron hydride and/or FeS in the later process of Earth's core-mantle differentiation at much higher-PT condition.

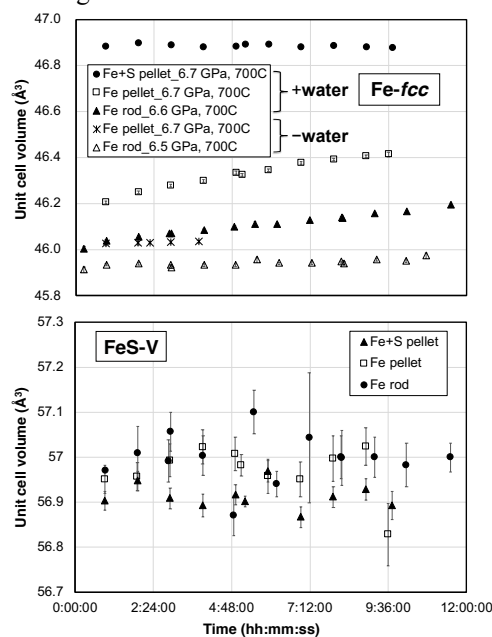


**Figure 1** Time changes in unit cell volume of *fcc*-Fe (upper) and FeS-V (lower) at 700°C. FeS-V was observed only in the sample including water.

**References:** [1] Iizuka-Oku, R., *et al.*, *Nature Commun.*, **8**, 14096 (2017).

## Structural study on new high-pressure forms of $\text{Al}_2\text{SiO}_5$

T Kuribayashi<sup>1\*</sup>, Y Zhou<sup>2</sup>, T Irifune<sup>2,3</sup> and H Ohfuji<sup>2</sup>

<sup>1</sup>Department of Earth Science, Graduate School of Science, Tohoku University, Sendai 980-8578, Japan.

<sup>2</sup>Geodynamics Research Center, Ehime University, Matsuyama 790-8577, Japan.

<sup>3</sup>Earth-Life Science Institute, Tokyo Institute of Technology, Tokyo 152-8550, Japan.

\*email: t-kuri@m.tohoku.ac.jp

**Introduction:** Recently, two new high-PT forms of  $\text{Al}_2\text{SiO}_5$  phases (kyanite-II and kyanite-III) have been synthesized at the conditions of 14-17 GPa and 2300-2400 K for kyanite-II and 17-23 GPa and 2400-2500 K, respectively (Zhou et al. 2018). They reported that kyanite-II is a completely new phase, and kyanite-III corresponds to the phase with  $\text{V}_3\text{O}_5$  type structure based on the similarity of the lattice parameters and X-ray powder profile. Therefore, the crystal structures of these two phases are needed to be determined to discuss about their crystal chemistry and physical properties.

**Experimental:** The samples of kyanite-II and kyanite-III synthesized by Zhou et al. (2018) were used for present SC-XRD experiments. The synthesized conditions are 2550K and 16.2 GPa for kyanite-II (OS2991) and 2750K and 19.3 GPa for kyanite-III (OS2992), respectively. Single crystal pieces of Kyanite-II ( $0.06 \times 0.04 \times 0.04 \text{ mm}^3$ ) and Kyanite-III ( $0.06 \times 0.07 \times 0.02 \text{ mm}^3$ ) used for X-ray analysis were carefully selected because twinning property were commonly revealed in polarized microscope observation. SC-XRD experiments were conducted using an automated four-circle X-ray diffractometer (Rigaku, AFC-7S) with monochromatized  $\text{MoK}\alpha$  radiation ( $\lambda = 0.71073 \text{ \AA}$ ). X-ray reflection intensity data were collected up to  $2\theta_{\text{max}} = 60^\circ$  ( $\sin\theta/\lambda \approx 0.70$ ). Space groups of the phases were determined as  $P1$  for kyanite-II and  $C2/c$  for kyanite-III based on the analyses of the systematic absence rules in the distributions of X-ray reflection intensity data.

Crystal structure determination and refinement for two phases were succeed, yielding  $R = 4.83\%$  for kyanite-II with space group  $P1$  and  $R = 3.26\%$  for kyanite-III with space group  $C2/c$ . The X-ray reflection intensity data with  $F_o > 4\sigma(F_o)$  were used for structure determinations and refinements of both samples. No corrections for crystal absorption were applied because of the small absorption coefficient values and small size of crystals. Initial structural parameters of both phases were obtained from the charge flipping method with Superflip software (Palatinus and Chapuis, 2007). Extinction corrections were applied for both analyses. Anisotropic displacement parameters were used for Al, Si and O atoms. Neutral atomic scattering factor of each atom specie (Al, Si and O) was taken from International Tables for Crystallography Volume C

(2004). All calculations for structural refinements were performed by SHELXL97 with WinGX.

**Results and Discussion:** The crystallographic information of each new phase obtained through refinements are as following: triclinic,  $P1$ ,  $Z = 6$ ,  $a = 7.0560(7) \text{ \AA}$ ,  $b = 9.4372(8) \text{ \AA}$ ,  $c = 6.7755(7) \text{ \AA}$ ,  $\alpha = 96.763(7)^\circ$ ,  $\beta = 99.177(8)^\circ$ ,  $\gamma = 108.127(7)^\circ$  and  $V = 416.51(7) \text{ \AA}^3$  for kyanite-II, and monoclinic,  $C2/c$ ,  $Z = 4$ ,  $a = 9.2964(9) \text{ \AA}$ ,  $b = 4.7084(7) \text{ \AA}$ ,  $c = 6.6289(10) \text{ \AA}$ ,  $\beta = 111.300(9)^\circ$  and  $V = 270.33(7) \text{ \AA}^3$  for kyanite-III. Calculated densities of these phase are 3.877 and 3.982 ( $\text{g}\cdot\text{cm}^{-3}$ ) for kyanite-II and kyanite-III, respectively.

The crystal structure of kyanite-II is shown in Figure 1. The structure has two tetrahedral (T1 and T2), eight octahedral (Oct1 to Oct8) and fifteen oxygen sites. T2 and M8 polyhedra are characteristic in kyanite-II structure. T2 tetrahedron shares a face with M8 octahedron and T2 and M8 sites are too close each other, therefore they cannot be occupied simultaneously. Also, T2 shares an edge with adjacent T2. T1 shares a corner with T2. The mean T1 and T2 distances are 1.651  $\text{ \AA}$  and 1.743  $\text{ \AA}$ . The mean octahedral Oct-O distances implies that the distribution of Si and Al in octahedral sites are disordered arrangement.

On the other hand, the crystal structure of kyanite-III is shown in Figure 2. The structure has two octahedral and three oxygen sites. Based on its chemical formula, Si and Al should occupy Wyckoff  $4b$  site and Wyckoff  $8f$  site, respectively. The crystal structure of kyanite-III is similar to that of  $\text{V}_2\text{TiO}_5$ . The  $\text{V}_2\text{TiO}_5$  structure is slightly different from  $\text{V}_3\text{O}_5$  type structure in view of space group. The mean octahedral Si-O and Al-O distances implies that the distribution of Si and Al in octahedral sites are disordered arrangement as well as that of kyanite-II.

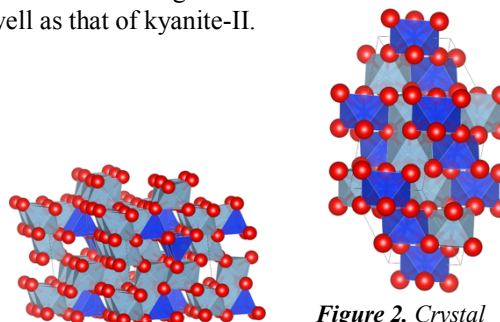


**Figure 1.** Crystal structure of kyanite-II

**Figure 2.** Crystal structure of kyanite-III

## Static compression of B2 KCl to 230 GPa and its $P$ - $V$ - $T$ equation of state

S Tateno<sup>1\*</sup>, T Komabayashi<sup>2</sup>, K Hirose<sup>1,3</sup> <sup>1</sup>Earth-Life Science Institute, Tokyo Institute of Technology, Tokyo 152-8550, Japan, <sup>2</sup>School of GeoSciences and Centre for Science at Extreme Conditions, University of Edinburgh, Edinburgh EH9 3FE, U.K. <sup>3</sup>Department of Earth and Planetary Science, The University of Tokyo, Tokyo 113-0033, Japan.

\*email: tateno@elsi.jp

**Introduction:** Potassium chloride is often used as a pressure gauge and pressure-transmitting medium in high-pressure experiments using a diamond-anvil cell due to the chemically inert and soft natures. Cold compression experiments on KCl in a helium pressure medium performed up to 160 GPa reported its highly compressible nature comparable to solid argon [1]. Walker et al. reported that B2 KCl exhibits low-thermal expansivity up to 8 GPa and 873 K [2], which was supported by recent theoretical calculations [1]. Precise evaluation of its thermal EoS is of great importance for high  $P$ - $T$  experiments in the DAC. Here we present a new EoS for B2-type KCl from our high  $P$ - $T$  experiments to 230 GPa/300 K and 60 GPa/2600 K in a laser-heated DAC.

**Experimental:** High  $P$ - $T$  conditions were generated using laser-heated DAC techniques. Diamond-anvils with a culet size of 300, 120, or 40  $\mu$ m were used depending on the target pressure. The starting material was powder of KCl that was mixed with platinum black that served as an internal pressure standard [3] and laser absorber. We used SiO<sub>2</sub> glass (runs 1 and 2) or argon (runs 5 and 6) for thermal insulation. Argon was cryogenically loaded into the sample chamber.

Angle-dispersive XRD measurements were conducted at BL10XU, SPring-8. Heating was performed from both sides of the sample by employing a pair of 100 W Yb fiber lasers.

**Results and Discussion:** Four separate sets of experiments were performed to measure the unit-cell volume of B2 KCl and Pt at 84.8–229 GPa at 300 K (runs 1 and 2) and 4.2–59.4 GPa at 300–2560 K (runs 3 and 4). We made efforts to minimize the effects of the deviatoric stress by employing thermal annealing and choosing the diffraction lines for calculating the unit-cell volume, which was based on the gamma plot [4]. As a result, our  $P$ - $V$ - $T$  data represent much lesser nonhydrostatic conditions than in the case of a He pressure medium without thermal annealing.

To construct a thermal EoS for B2 KCl, all the data were analyzed in the framework of a thermal pressure EoS based on the Mie-Grüneisen-Debye model with a Vinet form at 300 K. Fitting all the high-temperature data simultaneously yielded  $K_0 = 18.3(3)$ ,  $K_0' = 5.6(3)$ ,  $\gamma_0 = 2.3(2)$ , and  $q = 0.8(2)$ . Our compression curve is in good agreement with the recent results by Dewaele et al. [1] to ~50 GPa, above which the two curves, however, deviate from each other slightly (Figure 1). The comparison between the previous EoS reported by Dewaele et al. [1] and ours

with calibration against various Pt scales indicates that our EoS gives a lower pressure at a given volume of KCl. In other words, our compression curve gives a smaller volume at a given pressure, which may arise due to the different stress state developed in the sample chamber.

The calculated thermal pressure is almost pressure insensitive due to the small Grüneisen parameter. This is in good agreement with Dewaele et al. [1], in which the thermal pressure is assumed to be independent of volume. The present study revealed that KCl shows a small thermal pressure at any given pressure. For instance, the thermal pressure of KCl is as small as ~10 GPa at 3000 K, then increases to ~15 GPa at 4000 K regardless of the pressure, which are ~50% smaller than the case for Pt, Au, or MgO. The determined low thermal pressure of B2 KCl validates the use of a KCl medium as a high- $T$  pressure marker. This would add another advantage of KCl over the other materials to the soft and chemically inert natures.

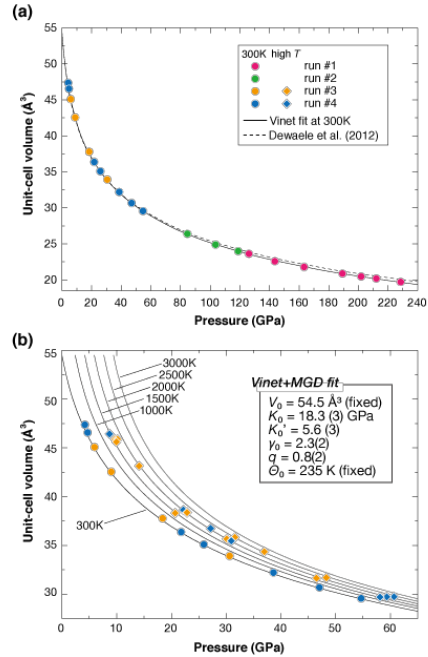


**Figure 1** (a) Volume data for B2 KCl and fit to the Vinet EoS at room temperature. (b) Volume data for 300 K and high-temperature and isothermal compression curve based on the Mie-Grüneisen-Debye model.

**References:** [1] Dewaele, A. et al., *Phys. Rev. B*, **85**, 214105 (2012). [2] Walker, D. et al., *Gephys. Res. Lett.* **87**, 805 (2002). [3] Sokolova, T.S. et al., *Comp. Geosci.*, **94**, 162 (2016). [4] Sing, A.K. and Takemura, K., *J. App. Phys.*, **90**, 3269 (2001).

## Quantitative analysis from stigmatic isotope imaging of SIMS

S. Itoh\* <sup>1</sup>Dept. Earth Planet.Sci., Kyoto University, oiwakecho sakyoku, Kyoto 606-8502, Japan.

\*email:sitoh@kueps.kyoto-u.ac.jp

### Introduction:

Direct ion imaging with secondary ion mass spectrometry (SIMS) has been developed in various fields, such as Material sciences, Earth and planetary sciences, life sciences. Especially, quantitative direct ion imaging techniques has recently developed using stigmatic direct ion imaging methods (e.g., Nittler, 1996; Yurimoto et al., 2003).

### Experimental:

In this study, we try to develop the stigmatic secondary ion imaging methods using Cameca ims-4fE7 SIMS at Kyoto University. The imaging detector system consists of micro-channel plate (MCP), florescent screen and Cooled 16bit charged-coupled device (CCD) camera (BU-LN52 Bitrun Co.). This conventional imaging system needs to estimate the calibration parameter with conversion from ion to electron, and from electron to photon. In Fig.1., the conversion between ADU/s/pixel and secondary ion intensity are shown. The integrated ADU is about  $10^4$ /pixel. The CCD image is  $512 \times 512$  pixel. The magnification of secondary ion image is about  $0.4 \mu\text{m}/\text{pixel}$ . The five area denotes  $50 \times 50$  pixel. The calculation of conversion equation shows the average value of five area.

### Results and Discussion:

In principle, each micro-channel of MCP would be different conversion parameter for electron converted from secondary ions. Therefore, in order to estimate the qualitative ion imaging using this system, we need to estimate the error of this conversion parameter in different location of each channel.

In this talk, we introduce the estimation of calibration parameter between the light output count rate read by CCD camera and the count rate of secondary ions incident on MCP with different experimental session. We will estimate the error of each nonlinear exponent parameter for five places ( $50 \times 50$  pixels) and these different parameters cause the error of about 5%. We will discuss it in detail with quantitative isotope imaging with application of high-pressure experiments.

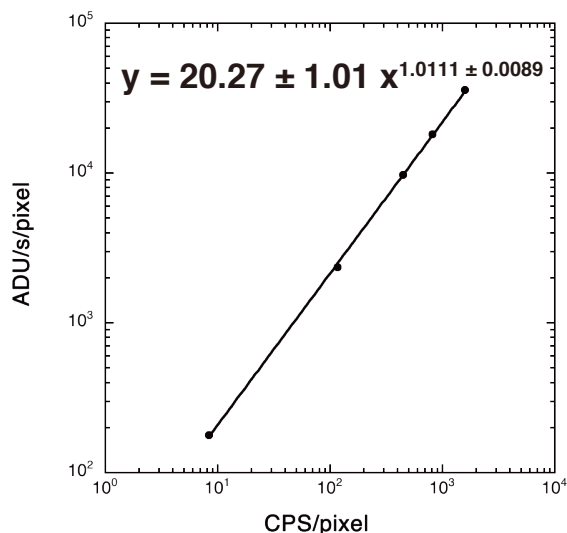
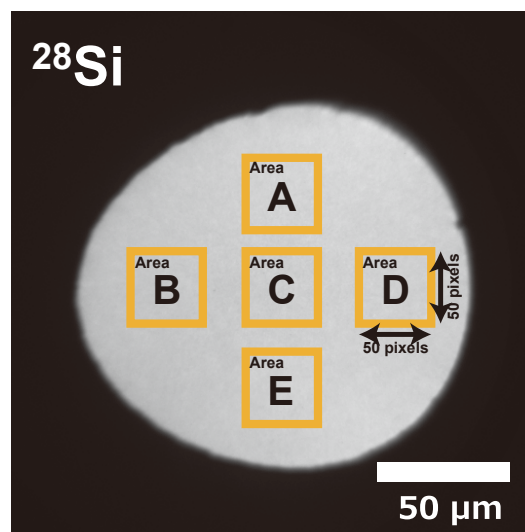


**Figure 1** Stigmatic  $^{28}\text{Si}$  secondary ion image using CCD camera. The plot diagram shows the relationship between ADU/s/pixel and secondary ion count rate.

**References:** [1] Nittler, L.R. (1996) Quantitative Isotopic Ratio Ion Imaging and its Application to Studies of Preserved Stardust in Meteorites. doctoral dissertation Washington Univ. [2] Yurimoto, H., Nagashima, K., Kunihiro, T. (2003) High precision isotope micro-imaging of materials. Appl. Surf. Sci., 203-204, 793-797.

## Controlling factor of whole-rock PGE concentrations in mantle peridotite

T. Kogiso<sup>1\*</sup> and N. Akizawa<sup>2</sup> <sup>1</sup>Graduate School of Human and Environmental Studies, Kyoto University, Kyoto, Kyoto 606-8501, Japan. <sup>2</sup>Atmosphere and Ocean Research Institute, The University of Tokyo, Kashiwa, Chiba 277-8564, Japan. \*email: kogiso.tetsu.6s@kyoto-u.ac.jp

Platinum-group elements (PGE) are thought to be concentrated strongly in the metallic core in the Earth's interior, because they have strong affinity for metallic phases. This results in very low PGE abundances in the silicate mantle, and it in turn enables PGE in the mantle to be used as a sensitive indicator of the contribution of metallic phases to mantle chemistry. Thus, the abundances of PGE in the mantle are an important key for understanding the core-mantle differentiation process during Earth's formation and the chemical interaction between the mantle and core through Earth's history.

The PGE abundance in the mantle have been estimated based on whole-rock PGE concentrations of natural mantle peridotites. However, whole-rock PGE concentrations in peridotite samples are enormously scattered in general, and therefore it is difficult to estimate the average abundances of PGE in the mantle. This implies that even the best ever estimation of the average PGE abundances in the mantle [1,2] would contain large uncertainties. Accurate knowledge about the behaviors of PGE in mantle peridotite is thus necessary for the precise estimation of the mantle PGE abundances, but it is still to be quantitatively clarified how and by what whole-rock PGE concentrations in mantle peridotite are controlled and modified.

Recent micrometer-scale analytical studies have revealed that the major host phases of PGE in mantle peridotite are base-metal sulfides (BMS) and platinum-group minerals (PGM) [e.g., 3-5]. It is therefore important to reveal the origin of the BMS and PGM in peridotite for deciphering what controls whole-rock PGE concentrations in peridotite. BMS are commonly found in peridotite samples, and some of BMS, such as those included in major silicate minerals, potentially preserve pristine PGE signatures of the mantle [3]. However, many BMS are found in grain boundaries between silicate minerals, and they are most likely to be formed in metasomatic processes during transportation to the Earth's surface [5]. The origin of PGM is much difficult to be investigated, because PGM have been

rarely discovered in peridotites due to their very small size (< several  $\mu\text{m}$ ). Most of the PGM ever found in peridotite samples were associated with BMS, and are likely to originate from subsolidus exsolution from BMS [5-6]. These observations suggest PGE hosts in peridotite are considerably affected by secondary processes.

On the other hand, experimental studies revealed that some of PGM can coexist with mantle minerals at mantle temperatures, even at above solidus of fertile peridotite, whereas BMS tend to be molten at such high temperatures [7 and references therein]. Model calculations on the basis of experimental data showed that partial melting of fertile peridotite can just roughly explain the correlations between PGE and major element concentrations in natural peridotite if PGM remain as solid phases in the residue [8]. However, the modelling can't yet fully reproduce the PGE variations in peridotite, especially those in depleted harzburgite samples [8]. In addition, there have been so far no reports of the existence of PGM that certainly originated from residue of peridotite partial melting.

Thus, it is still uncertain how PGE host minerals in peridotite were formed, and therefore it's unclear whether whole-rock PGE concentrations of peridotite preserve pristine mantle signatures. Further detailed petrological studies on the occurrence of BMS and PGM in peridotite would be necessary for unraveling the origin of PGE hosts.

**References:** [1] Becker, H. et al., *Geochim. Cosmochim. Acta*, **70**, 4528 (2006). [2] Fischer-Gödde, M. et al., *Chem. Geol.*, **280**, 365 (2006). [3] Alard, O. et al., *Nature*, **407**, 891 (2000). [4] Kogiso, T. et al., *Geochem. Geophys. Geosyst.*, **9**, Q03018 (2008). [5] Lorand, J.-P. et al., *Earth Planet. Sci. Lett.*, **289**, 298 (2010). [6] Akizawa, N., et al., *Chem. Geol.*, **475**, 87 (2017). [7] Brenan, J. et al., *Rev. Mineral. Geochem.*, **81**, 1 (2016). [8] Aulbach, S. et al., *Rev. Mineral. Geochem.*, **81**, 239 (2016).

## Sulfur and carbon isotope fractionation under mantle conditions

F Maeda<sup>1</sup>, Y Horioka<sup>1</sup>, S Kamada<sup>1,2\*</sup>, S Aoyama<sup>3</sup>, S Ozawa<sup>1</sup>, M Satish-Kumar<sup>3</sup>, A Suzuki<sup>1</sup>

<sup>1</sup>Department of Earth Science, Graduate school of Science, Tohoku Univ., Sendai, Miyagi 980-8578, Japan.

<sup>2</sup>Frontier Research Institute for Interdisciplinary Sciences, Tohoku Univ., Sendai, Miyagi 980-8578, Japan.

<sup>3</sup>Department of Geology, Faculty of Science, Niigata University, Nishi-ku, Niigata 950-2181, Japan.

\*email:seijikmd@m.tohoku.ac.jp

**Introduction:** Isotopic compositions of sulfur and carbon are important tracers for chemical evolutions and ancient processes through the Earth history. A recent study for isotope ratio of S reported that the mantle was depleted in <sup>34</sup>S based on analyses of natural mid-ocean ridge basalt (MORB) glasses [1]. As sulfur is a candidate of light elements in the core because of the siderophile nature, this depletion in <sup>34</sup>S might be caused by a chemical reaction between the mantle and the core during the magma ocean. Isotope ratios of <sup>12</sup>C and <sup>13</sup>C ( $\delta^{13}\text{C}$ ) have been examined for the mantle samples such as carbonate, diamond, and volcanic CO<sub>2</sub>. [e.g., 2] These analyses indicated a characteristic  $\delta^{13}\text{C}$  value for the mantle as  $-5\text{‰}$ . In contrast, some diamonds from the deep mantle showed highly negative  $\delta^{13}\text{C}$  values such as  $\delta^{13}\text{C}$  of  $-20\text{‰}$  [e.g., 3,4]. Origin of the mantle  $\delta^{13}\text{C}$  and the negative  $\delta^{13}\text{C}$  of diamonds has been debated [3,5]. Since the isotope fractionations in the Earth interior can play key roles to understand the isotopic compositions of sulfur and carbon, pressure ( $P$ ) and temperature ( $T$ ) effects on the isotope fractionations were recently examined using high  $P$ - $T$  experiments [5-7]. However, the experimental simulations are still not sufficient in particular for pressures and systems in the Earth. Present experiments investigated the sulfur isotope fractionation between the silicate melts and metallic melts and carbon isotope fractionation between carbonate and diamond or graphite at 3-10 GPa and 1500-1800 °C in order to reveal the  $P$ - $T$  effects on the sulfur and isotope fractionations in the magma ocean and the carbon isotope fractionations in the modern mantle.

**Experimental:** High pressure and temperature experiments were conducted by using a Kawai-type multi anvil press installed at Tohoku University. Starting materials were mixtures of oxides for silicate phases and mixtures of FeS and Fe for metallic phases in the experiments for sulfur, and mixtures of natural magnesite (Mg<sub>0.994</sub>Fe<sub>0.003</sub>Ca<sub>0.003</sub>CO<sub>3</sub>), reagent-grade SiO<sub>2</sub>, and sp-2 graphite in the experiments for carbon. Capsules made of hBN and Al<sub>2</sub>O<sub>3</sub> were used and surrounded by a graphite heater for the sulfur experiments. An MgO capsule with a LaCrO<sub>3</sub> heater was used for the carbon experiments. Temperatures were measured with W/Re thermocouples. The compositions of recovered samples were analyzed by SEM-EDS at Tohoku University and the sulfur and carbon isotope ratios of that were analyzed by IRMS at Niigata University.

**Results and Discussion:** Sulfur isotope ratios only in metallic phases were analyzed because amounts of sulfur in silicate phases were not sufficient for the analyses. Sulfur in the metal phases were extracted using Cr(II) reduction method [8]. The pressure effects on  $\delta^{34}\text{S}$  were not observed. In contrast, the temperature effects on  $\delta^{34}\text{S}$  were negative. The present results indicate that S isotope fractionations are difficult to occur in the present pressure range (3-5 GPa) under high-temperature conditions corresponding to the magma ocean. On the other hand, an indirect-pressure effect on the sulfur isotope fractionation is possible at higher pressures corresponding to the bottom of the magma ocean (30-60 GPa): coordination numbers (CN) of cations in silicate melts increase at such pressures [9]. Since heavy isotopes prefer bonds of lower CN [e.g., 10, 11], it is expected that the heavy isotope (i.e., <sup>34</sup>S) is depleted in silicate melts under high-pressure conditions corresponding to the deep magma ocean. The negative  $\delta^{34}\text{S}$  of mantle can hence be explained by the indirect pressure effect on the sulfur isotope fractionation. Carbon isotope ratios were measured for both of carbonates and diamond/graphite. The differences of  $\delta^{13}\text{C}$  values between carbonates and diamond/graphite were approximately 10-11 ‰. These values were larger compared with previous studies, showing the carbon isotope fractionation of 1-3 ‰ [5,7], but were consistent with a previous report for isotope fractionations between a carbonated-silicate and graphite [7]. The large difference of  $\delta^{13}\text{C}$  between carbonate and diamond/graphite can yield due to non-equilibrium conditions for the carbon isotopes, or reduction of carbonates as shown by Mizutani et al. [7].

**References:** [1] Labidi J. et al., *Nature*, **501**, 208-211. (2013) [2] Denies P. *Earth Sci. Rev.*, **58**, 247-278. [3] Walter M.J. et al., *Science*, **334**, 54-57. (2011) [4] Bulanova G.P. et al. *Contrib. Miner. Petrol.* **160**, 489-510 (2010) [5] Satish-Kumar M. et al., *Earth Planet. Sci. Lett.*, **310**, 340-348. (2011) [6] Labidi J. et al., *Geochim. Cosmochim. Acta*, **175**, 181-194. (2016) [7] Mizutani, S. et al. *Earth Planet. Sci. Lett.*, **392**, 86-93. (2014) [8] Canfield D.E. et al., *Chem. Geol.*, **54**, 149-155. (1986) [9] Bajgain S. et al., *Nat. Commun.*, **6**, 8578. (2015) [10] Criss R.E. Oxford University Press, Inc., *New York*, 254. (1999) [11] Schauble E.A. In *Geochemistry of Non-Traditional Stable Isotope*, **55**, 65-111. (2004)

## The major element composition of the Hadean crusts: constraints from Sm-Nd isotope systematics and high-pressure melting experiments

N M Kondo<sup>1,2\*</sup>, T Kogiso<sup>1</sup>

<sup>1</sup>Graduate School of Human and Environmental Studies, Kyoto University, Nihonmatsu-cho, Sakyo-ku, Kyoto, Japan.

<sup>2</sup>Geodynamics Research Center, Ehime University, 2-5 Bunkyo-cho, Matsuyama, Ehime, Japan.

\*email: kondo.nozomi.xg@ehime-u.ac.jp

**Introduction:** The mantle composition and dynamics have been evolved through formation and re-mixing of crust. Therefore, in order to understand the history of the mantle chemical and dynamical evolution, we have to know the initial condition of the crustal formation and recycling. Previous studies have investigated the crustal formation in the early Earth from zircons <4.4 Ga, and from isotopic record in the Archean rocks (ex. Nebel et al. 2014; Rizo et al, 2013). These clues have suggested formation of the primary crust from mantle melting before 4.4 Ga, formation of the evolved crust (secondary, ...) from melting of pre-existing (primary, ...) crust and re-mixing of these crusts. However, the rock record before 4.0 Ga (the Hadean) has never or scarcely found, and therefore, the major element composition of the Hadean crusts have been unrevealed. The major element composition controls physical properties such as density and viscosity of melt and crust, and these physical properties in turns controls the formation and recycling of the crust. Therefore, in this study we constrained the major element composition of the Hadean primary and secondary crust and discussed about the formation and fate of these Hadean crusts.

**Strategy:** We combined the Sm-Nd isotope systematics and high-pressure melting experiments in order to constrain the major element composition of the Hadean primary and secondary crust. For the primary crust, we firstly estimated melting condition of mantle at the Hadean silicate (mantle and crust) differentiation from the Sm-Nd systematics in the early Archean rocks, that have higher and lower  $^{142}\text{Nd}/^{144}\text{Nd}$  ratio than that of the present mantle. The  $^{142}\text{Nd}/^{144}\text{Nd}$  anomalies are distinct in the early Archean rocks, and diminish from the late Archean to the present. Due to the short half-life of the  $^{146}\text{Sm}$  (68 Myr), the parent nuclide of the  $^{142}\text{Nd}$ , the  $^{142}\text{Nd}/^{144}\text{Nd}$  anomalies and diminishing of them have been interpreted as the Sm/Nd fractionation at the Hadean silicate differentiation and re-mixing of the Hadean depleted mantle (high Sm/Nd and  $^{142}\text{Nd}/^{144}\text{Nd}$  ratio) and enriched crust (low Sm/Nd and  $^{142}\text{Nd}/^{144}\text{Nd}$  ratio). Since the degree of the Sm/Nd fractionation depends on two variables, the timing and melting condition of the Hadean silicate differentiation, we can constrain these two variables from two Sm-Nd systematics,  $^{146}\text{Sm}$ - $^{142}\text{Nd}$  and  $^{147}\text{Sm}$ - $^{143}\text{Nd}$  systems. Then, we estimated the major element composition of the melt generated at the

Hadean silicate differentiation from the melting condition constrained from the Sm-Nd systematics and data of high-pressure melting experiments of a primitive mantle (Fallon et al. 2008; Hirose & Kushiro 1993; Walter 1998; Davis et al. 2011; Kondo et al. 2016) . For the secondary crust, we conducted high-pressure melting experiments of synthesized starting material with the hydrous primary crust composition, using piston-cylinder high-pressure apparatus at Graduate School of Human and Environmental Studies, Kyoto University, and determined the major element composition of melt.

**Result and discussion:** For the Hadean primary crust, the estimated melting condition at the Hadean silicate differentiation was extremely small melt fraction at shallow upper mantle pressures. Then, as the result, the major element composition of the melt was estimated to be Ti-basaltic at 1 GPa, Ti-K-rich picritic at 3 GPa, and Ti-Fe-P-rich komatiitic at 7 GPa. Then, we discussed the probable composition of the Hadean primary crust to be Ti-Fe-P-rich komatiitic by estimating the condition of the Hadean mantle (mantle potential temperature, tectonics, and thickness of lithosphere). We also discussed the formation of the Hadean primary crust by estimating the density and viscosity of the Ti-Fe-P-rich komatiitic melt. For the Hadean secondary crust, the solidus and melting phase relation of the hydrous Hadean primary crust was determined from 1-3 GPa, and the major element composition of the melt was revealed to be Ti-Fe-P rich mafic. Then, we discussed the subduction and melting of the hydrous Hadean primary crust by comparing the solidus and subduction P-T pass of the early Archean and the present subduction zones. We also discussed the formation of the Hadean secondary crust by estimating the density and viscosity of the Ti-Fe-P rich mafic melt.

**Summary:** We constrained the major element composition of the Hadean primary and secondary crust by combining the Sm-Nd systematics and high-pressure melting experiments. The Hadean primary crust would have formed at extremely small melt fraction and had Ti-Fe-P-rich komatiitic composition. The Hadean secondary crust would have formed subduction-related melting of the hydrous Hadean primary crust and had Ti-Fe-P-rich mafic composition.

## Completion of the seismic observation with Thai Seismic Array (TSAR)

S Tanaka<sup>1\*</sup> <sup>1</sup>D-Earth, JAMSTEC, 2-15 Natsushima-cho, Yokosuka, 237-0061, Japan.

W. Siripunvaraporn<sup>2</sup>, S. Boonchaisuk<sup>2</sup>, S. Noisagool<sup>2</sup> <sup>2</sup>Faculty of Science, Mahidol University, Bangkok, Thailand.

K. Kawai<sup>3</sup>, Y. Suzuki<sup>3</sup> <sup>3</sup>Graduate School of Science, Univ. Tokyo, Hongo, Bunkyo-ku, Tokyo, 113-0033, Japan.

T. Kim<sup>4</sup>, Y. Ishihara<sup>4</sup> <sup>4</sup>CEAT, JAMSTEC, Showa-cho, Kanazawa-ku, Yokohama, 236-0001, Japan.

H. Kawakatsu<sup>5</sup>, N. Takeuchi<sup>5</sup>, K. Miyagawa<sup>5</sup>, R. Iritani<sup>5</sup> <sup>5</sup>ERI, Univ. Tokyo, Yayoi, Bunkyo-ku, Tokyo, 113-0032, Japan.

\*email: stan@jamstec.go.jp

**Introduction:** Thailand occupies an important area to study the lowermost mantle below the western Pacific where is the western edge of the Pacific Large Low Shear-Velocity Province (LLSVP) and the deep part of the inner core. However, the density of seismic stations has not been so high compared with the neighboring regions, (e.g., China and India). Furthermore, tectonics in Thailand is interesting to understand geology of the Indochina peninsula and a moderate size earthquake occurred in the northern Thailand in 2014. Thus, Japanese and Thai seismologists have been keen for seismic observation in this area.

Under the project “Seismic and geoelectromagnetic observation for core and mantle”, which is one of the KAKENHI grants for innovative area “Core-mantle co-evolution and interaction”, we finally got the opportunity for the broadband seismic observation named Thai Seismic Array (TSAR) from January, 2016 with deploying 2 pilot stations and the array was completed with 40 stations in Feb. 2017. After about 2 years operation, the dismantlement of the TSAR stations has been completed in January 2019. Here we briefly report this observation.

**Observation:** Geographical distribution of the TSAR stations is shown in Fig. 1. The typical station interval is about 100 km except for the western area of the main Thailand. Originally, we had a plan to deploy the stations in the Malay peninsula. Unfortunately, due to heavy rain and severe flooding in January and February 2017, we changed the deployment area from the Malay peninsula to the current area. As a result, we obtained a dense network in the western area.

We could organize only 1 deployment team. Thus, in order to complete the deployment of 40 stations except for 2 pilot stations, we tripped 4 times during November 2016 to February 2017. The maintenance and data collection trips are conducted by Thai members in summer, and by both Japanese and Thai members in winter. Due to probably severe flooding and activities of local creature, the sensors and data logger at nearly half of the stations were damaged. And lightning probably affected the GPS clocks. The dismantlement trips were conducted in December 2018 and January 2019.

**Results and Discussion:** In the period from January 2017 to December 2018 in which more than about half of stations works, there were 245 earthquakes with magnitude greater than or equal to 6.0 [1]. Among these, the nuclear explosion in North Korea is included. And the focal depths of 48 earthquakes are greater than or equal to 100 km, which are mainly distributed in the southwestern Pacific and south America. Such deep earthquakes are expected to provide the good data to obtain the structure of the mantle and core. Additionally, we had a moderate earthquake with magnitude of about 5 occurred in the western area of Thailand, of which epicenter is 14.90°N, 99.14°E determined by Thai Meteorological Department, on December 30, 2018 and 8 TSAR stations in the western area successfully recorded this event. Thus, the TSAR data will contribute to hypocenter relocation and the further understanding of the source mechanism.

Although we sent back the instruments belonging to the ERI, Univ. Tokyo just after the dismantlement, 3 sets of the instruments belonging to JAMSTEC are left in Bangkok. They will be reinstalled in the active fault area in the northern Thailand for the continuing collaboration with Mahidol Univ.

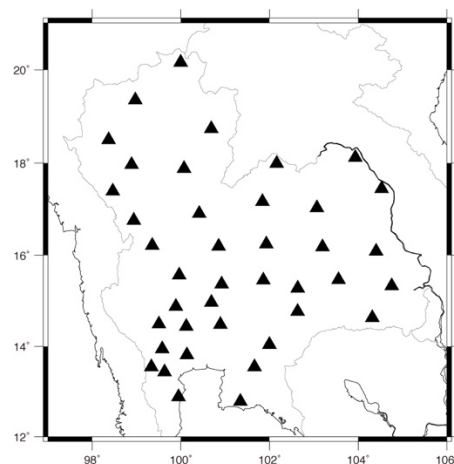


**Figure 1** Distribution of the full TSAR stations (solid triangles).

**References:** [1] <https://earthquake.usgs.gov/earthquakes/search/>

### **S-to-P scattering in the lower mantle near subduction zones**

S Kaneshima<sup>1\*</sup> <sup>1</sup>Department of Earth and Planetary Science, Kyushu University, Fukuoka, Nishi-ku, Motoooka, 819-0395, Japan.

\*email:kane@geo.kyushu-u.ac.jp

We investigate S-to-P scatterers in shallow to mid-lower mantle beneath subduction zones, where deep seismicity extends down to the bottom of the upper mantle. By array processing broadband and short period wave form data obtained at seismic networks, we seek anomalous later phases in the P coda. The later phases usually arrive along off-great circle paths and significantly later than S-to-P conversion at the "660 km" discontinuity. They are thus adequately regarded as scattered waves, rather than conversion at a global horizontal discontinuity, and indicate that a spatial change in elastic properties by several percent occurs at the scatterers as abruptly as the post-spinel transformation, probably caused by compositional heterogeneity. We locate prominent S-to-P scatterers beneath Pacific subduction zones. Nearly half of 137 S-to-P scatterers located in this study and previous studies by the authors are shallower than 1000 km, and the number of scatterers decreases with depth. In this presentation we focus on the S-to-P scatterers in the mantle beneath Samoa hot spot north of the Tonga-Fiji subduction zone, where seismic tomography has revealed a large-scale upwelling from the Pacific LLSVP at the base of the mantle. In the depth range from 900 to 1200 km we have found a few scatterers near the edge of a plume-like body with low shear velocity.

## Core-mantle interaction inferred from a core surface flow model

M Matsushima<sup>1\*</sup> <sup>1</sup>Tokyo Institute of Technology, Tokyo 152-8551, Japan.

\*email:masaki.matsushima@eps.sci.titech.ac.jp

**Introduction:** Fluid motions in the Earth's metallic liquid outer core are responsible for the dynamo process by which the geomagnetic field is generated and maintained. Such core fluid flow can be estimated from geomagnetic field data, such as spatial distribution of geomagnetic field and its temporal change referred to as secular variation. This implies that spatial and temporal variations of fluid flow in the core provide information on any interaction between the core and mantle. To investigate possible core-mantle interaction, a core surface flow model is obtained using a geomagnetic field model.

**Method:** Following the method of [1], inside a viscous boundary layer at the core-mantle boundary (CMB), magnetic diffusion is assumed to significantly contribute to temporal change of geomagnetic field, and the radial dependence of core flow is expressed in terms of a spiral similar to the Ekman spiral. Below the boundary layer, magnetic diffusion is neglected as in the frozen-flux approximation, and instead of the tangentially geostrophic constraint as used in [1], the tangentially magnetostrophic constraint is imposed on the flow; that is, the effect of magnetic field through the Lorentz force is taken into account. Since it is better to adopt a geomagnetic field model covering longer duration, COV-OBS.x1 [2] which covers the range between 1840 and 2015 is adopted.

**Results and Discussion:** Any heterogeneous structure due to temperature or heat flux at the CMB should have a strong effect on the core flow when a thermal convection occurs in the outer core. The heterogeneity successively influences the flow pattern. Therefore, average of fluid flow is expected to show possible core-mantle interaction. Hence, fluid flows inside and below the boundary layer are averaged over the time from 1840 to 2015 covered by the COV-OBS.x1 model.

It turns out, however, that mean amplitudes of upwelling and downwelling flows as well as mean horizontal flows are smaller than those at respective times, as shown in Fig. 1. This result suggests that compositional convection is dominant in the Earth's outer core, because possible thermal heterogeneity

due to the lowermost mantle structure has little effect on the core surface flow. It should be noted that there is a noticeable mean upwelling flow corresponding to a counterclockwise vortex beneath the south of Africa, and that the location is just outside the tangent cylinder, an imaginary cylinder parallel to the rotational axis and attached to the equator of the inner core. This may indicate that the vortex corresponds to an edge of columnar convective motion, although the other edge is unclear.

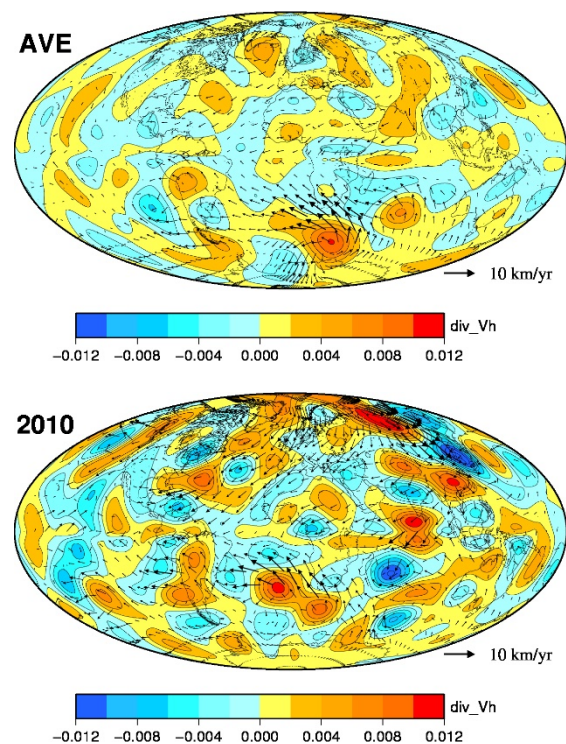


**Figure 1** Core flows inside the boundary layer at the core-mantle boundary (upper) averaged in the range from 1840 to 2015 and (lower) for the epoch of 2010. Arrows show the horizontal velocity, and color contours denote upwellings and downwellings.

**References:** [1] Matsushima, M., *Geophys. J. Int.*, **202**, 1495 (2015). [2] Gillet, N., Barrios, O., and Finlay, C. C., *Earth Planets Space*, **67**, 71 (2015).

## Variation of the intensity of the paleomagnetic field during 38-50 Ma deduced from the marine sediments recovered from the northwest Atlantic

Y Yamamoto<sup>1\*</sup>, H Fukami<sup>1</sup>, W Taniguchi<sup>1</sup>, P.C. Lippert<sup>2</sup>

<sup>1</sup> Center for Advanced Marine Core Research, Kochi University, Kochi 783-8502, Japan.

<sup>2</sup> Department of Geology and Geophysics, University of Utah, Salt Lake City, UT 84112, USA.

\*email:y.yamamoto@kochi-u.ac.jp

**Introduction:** Variations of the intensity of the paleomagnetic field (paleointensity), which provide clues about the evolution of the geodynamo, are recorded in rocks and sediments. Marine sediments give relative paleointensity (RPI) continuously in time. For the period of 0-2 Ma global RPI stacks [1][2] have been reported based on numerous regional RPI records. For the period of 2-3 Ma there have been increasing number of regional RPI records [3][4]. However, published RPI records older than ~3 Ma are very limited in time and space: 14.5-18.5 Ma [5], 17.5-26.5 Ma [6], 23-41 Ma [7] from the equatorial Pacific; 23-34 Ma from the South Atlantic [8]. We have conducted a paleomagnetic study on the marine sediments recovered in the northwest Atlantic to extend our knowledge of the RPI variation in further geologic past, and report on the preliminary RPI results for the period of about 38-50 Ma.

**Experimental:** Integrated Ocean Drilling Program (IODP) Expedition 342 recovered hemipelagic sediment drifts from Sites U1403 and U1408 in the northwest Atlantic, off the coast of Newfoundland [9]. Piston cores of the two sites were subjected to a series of the paleomagnetic measurements including analyses of natural, anhysteretic, and isothermal remanent magnetizations (NRM, ARM, and IRM). Excluding the intervals showing signs of probable dissolution of primary magnetic minerals (low ARM intensity intervals) and inhomogeneous magnetic grain sizes (mainly for low ARM/IRM intervals), RPIs were estimated based on ratios of NRM/ARM and NRM/IRM.

**Results and Discussion:** Considering age models of the studied cores [10][11], the resultant RPI records cover the Chrons 18 (38.5-41.1 Ma), 19 (41.1-42.9 Ma), 20 (42.9-46.4 Ma), 21r (47.8-48.6 Ma), and 22n (48.6-49.3 Ma). These records are characterized by RPI minima always at chron boundaries and large fluctuations between highs and lows during each chron. Such characteristics are commonly recognized in the published RPI records back to 41 Ma [1-8]; this is first record to show that they persist at least since 49.3 Ma.

For the Chron 18 interval, we obtained RPI results from both sites, which are approximately 380 km apart (Figure 1). Our results show common features, including RPIs that are generally high during C18n.2n (39.6-40.0 Ma) and low during C18r (40.0-41.1 Ma). Prominent RPI lows, which appear to be almost equivalent to the RPI minima at other chron boundaries (*i.e.*, during Chrons 19, 20, 21r, and 22n), are also commonly recognized at ~40.5 Ma. We suggest that the RPI lows might be related to a failed geomagnetic reversal.

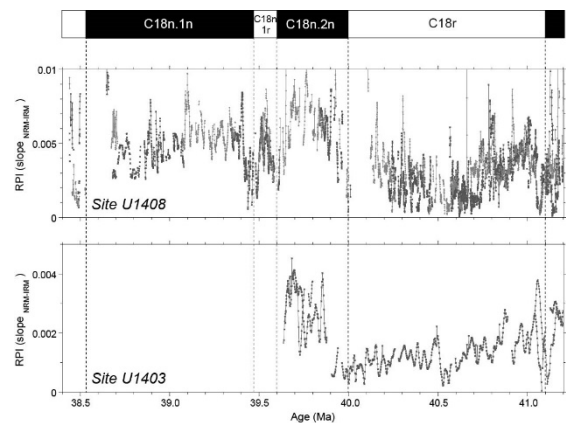


**Figure 1** Chron 18 RPI results from Site U1408 (upper panel) and U1403 (lower panel).

**References:** [1] Channell, J.E.T. et al., *Earth planet. Sci. Lett.*, **283**, 14–23 (2009). [2] Valet, J.-P. et al., *Nature*, **435**, 802–805 (2005). [3] Yamazaki, T. and Oda, H., *Geochem. Geophys. Geosyst.*, **6**, Q11H20 (2005). [4] Sakuramoto, Y. et al., *J. Geophys. Res. Solid Earth*, **122**, 7525–7543 (2017). [5] Ohneiser, C. et al., *Earth planet. Sci. Lett.*, **374**, 227–238 (2013). [6] Channell, J.E.T. and Lanci, L., *Earth planet. Sci. Lett.*, **387**, 77–88 (2014). [7] Yamamoto, Y. et al., *Geophys. J. Int.*, **196**, 694–711 (2014). [8] Tauxe, L. and Hartl, P., *Geophys. J. Int.*, **128**, 217–229 (1997). [9] Norris, R.D. et al., *Proc. IODP*, **342**, doi:10.2204/iodp.proc.342.101.2014 (2014). [10] Boulila, S. et al., *Earth Planet. Sci. Lett.*, **486**, 94–107 (2018). [11] Yamamoto, Y. et al., *Proc. IODP*, **342**, doi:10.2204/iodp.proc.342.207.2018 (2018).

# Toward adjoint tomography of the large low seismic velocity provinces beneath the western Pacific Ocean

M Obayashi<sup>1\*</sup>, T Miyoshi<sup>2</sup>, and J Yoshimitsu<sup>1</sup>

<sup>1</sup>Japan Agency for Marine-Earth Science and Technology, 2-15 Natsushima, Yokosuka 237-0061, Japan.

<sup>2</sup>National Research Institute for Earth Science and Disaster Resilience, 3-1 Tennodai, Tsukuba 305-0006, Japan.

\*email: obayashi@jamstec.go.jp

**Introduction:** It is well-known that there is a large low seismic velocity provinces (LLSVP) where the seismic velocity changes sharply above the core-mantle boundary (CMB), however it is unclear how it is distributed above the CMB. In recent years, the detailed S-wave velocity structure around the CMB was inferred from waveform inversion [1, 2]. In our previous study, we found an NE-SW running low S-wave velocity structure within the LLSVP lying beneath the western Pacific Ocean using analyses of travel times and the finite frequency inversion. To clarify the detail structure and its relationship with old subduction, we determine a three-dimensional (3D) P and S-wave velocity structure beneath the western Pacific Ocean based on waveform tomography using the combination of Spectral-element method (SEM) [3] and adjoint method [4]. We show here some preliminary results with computational costs.

**DATA and Method:** We collected the seismic waveforms of three components obtained at seismic broadband stations from ~700 earthquakes occurred from 2008 to 2015. Distribution of seismic stations used in this study is shown in Fig. 1. Removing the response of each instrument from the original records, we transferred into displacement waveforms with a bandpass filter (10-150 sec) to use the inversion. We constructed global Earth model based on S40RTS [5] as an initial 3D model in inversion to calculate synthetic displacements and adjoint waveforms using the SEM. Our SEM structural model was parameterized using 1.6 billion grid points to produce waveforms of a shortest period of 10 sec. The forward and adjoint simulation were conducted using a flat 600 Message Passing Interface (MPI) on Data Analyzer (DA) system in Japan Agency for Marine-Earth Science and Technology (JAMSTEC). The model parameters  $V_p$  and  $V_s$  were updated iteratively by gradient method using the misfit kernels (Fig. 2) based on the adjoint sources to minimize the misfit between observed waveforms and synthetic waveforms. Here, we show some preliminary results: estimation of computational costs, forward modelling, and trial inversion.

**Results and Discussion:** This study requires large computational cost to calculate forward and backward waveforms in the 3D whole Earth. We estimated the calculation time on the DA system. The time step of the solver was 0.1045 sec and 30 min waveforms were calculated. As a result, the

calculation time was required approximately 2 and 9 hours for conducting forward and adjoint simulation, respectively for each event. If the calculation is conducted as 4 independent parallel job, it takes 3 weeks to obtain one iterative results when ~200 events are used in inversion. We succeed construction of the iterative model using the misfit kernels of a few events as trial, synthetic waveforms by iterative model were improved clearly. We are planning to apply differential travel times of some core phases. we are expected to revise the LLSVP from initial 3D model more efficient.

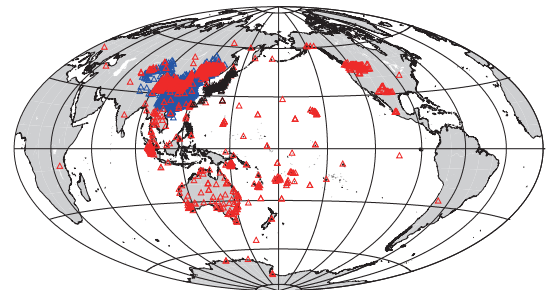


**Figure 1** Distribution of seismic stations used in this study. Black, red and blue triangles indicate F-net, IRIS and Chinese stations, respectively.

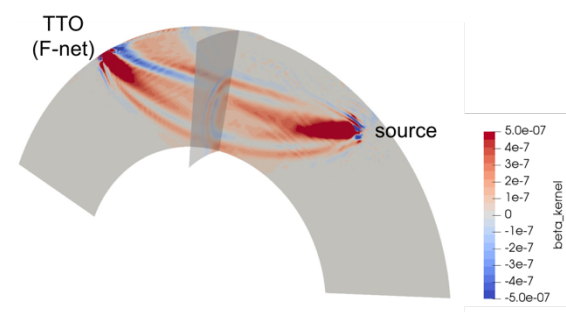


**Figure 2** Example of beta kernel for the earthquake occurred in Fiji on July, 2011. The kernel was calculated using S and ScS waves.

**Acknowledgements:** We used seismic waveforms obtained by IRIS and NIED F-net stations and SPECFEM3D Globe package used in this study.

**References:** [1] Konishi, K., Kawai, K., Geller, R.J., and Fuji, N., *Geophys. J. Int.*, **199**, 1245-1267 (2014). [2] Yuan, K. and Romanowicz, B., *Science*, **357**, 393-397 (2017). [3] Komatitsch, D. and Tromp, J., *Geophys. J. Int.*, **149**, 390-412 (2002). [4] Tromp, J., Tape, C., and Liu, Q., *Geophys. J. Int.*, **160**, 195-216 (2005). [5] Ritsema, J., Deuss, A., van Heijst, H. J., and Woodhouse, J. H., *Geophys. J. Int.*, **184**, 1223-1236 (2011).

## Using S-P wave search the depth of mantle 660-discontinuity beneath Kuril Region where subduction slab do not exist

G. Hao , Faculty of Science , Kyushu University , Fukuoka ,Japan

### Introduction

The depth of the 660-km seismic discontinuity is investigated at the Kuril Region , by using the broadband earthquake event data from provided by IRIS. We processed about 50 events occur at Kuril Region and Sea of Okhotsk , depth range from 100 to 600 km. In these data , about 20 of them show clear S660P phases , which S wave propagate to the 660-km discontinuity and convert to P wave then recorded by arrays at USA . These S660P wave propagate away from the subducting slab to America and Alaska. For shallower and intermediate depth(100 ~ 300km) earthquake, the S-to-P conversion occur at the 660-km discontinuity that do not cross with the subducting slab. For deeper events (400 ~ 600km), the conversions occur within or near the boundary of the slab (due to the dip angle of the slab ). We estimate the depth of 660-km discontinuity by computing the depth of conversion points of S-to-P wave , the depth of 660-km discontinuity at Kuril and Okhotsk region that do not cross with the subducting slab is about  $660 \pm 5$  km, indicate that there is no comprehensive depression at this region . Results of deeper events suggest that, at the vicinity of the slab, the 660-km discontinuity have 10 to 15 km depression, consistent with previous research. In addition , for comparing with the wave that propagate within/near and away from the subducting slab, we also process some deep events data that recorded by

arrays at Europe, suggest that discontinuity has about 10km depression (get results from only two events).

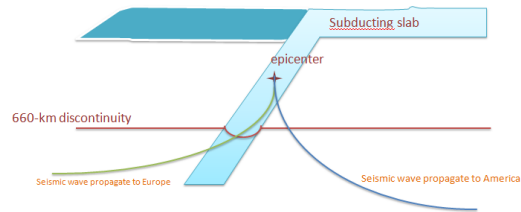


Figure 1 : the structure of subducting slab and ray path of seismic waves processed in this research

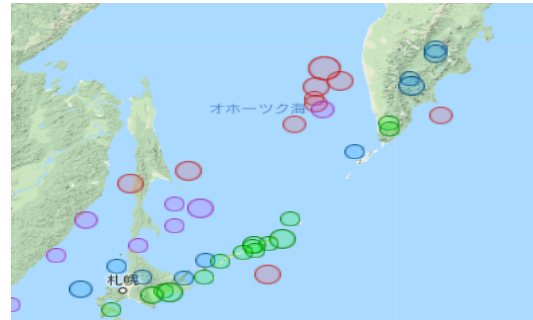


Figure 2: the earthquake events and their depth(getting deeper from green to red )

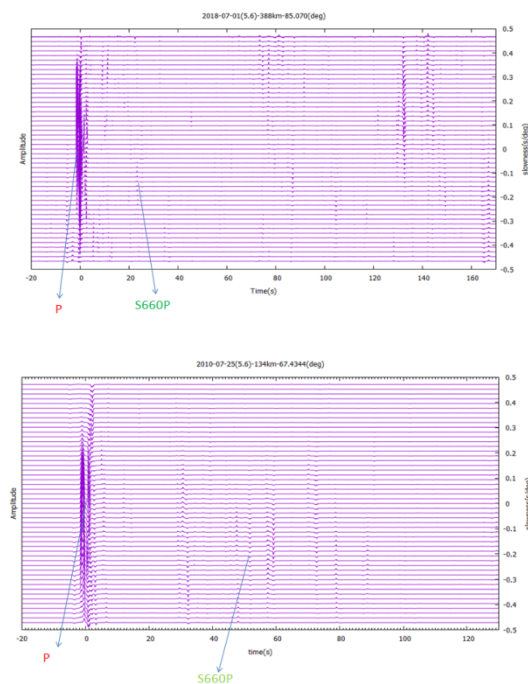


Figure 3 : two examples (113km & 388km) that S660P can be seen clearly, and the relatively arrival time of P & S660P

## Sharpness of the hemispherical boundary in the inner core beneath the northern Pacific

R Iritani<sup>1\*</sup>, H Kawakatsu<sup>1</sup>, N Takeuchi<sup>1</sup> Earthquake Research Institute, University of Tokyo, Bunkyo-ku, Tokyo 113-0032, Japan.

\*email:ryohei9@eri.u-tokyo.ac.jp

**Introduction:** Hemispherical heterogeneity in the topmost of the Earth's inner core, faster velocity and higher attenuation in the eastern hemisphere and slower velocity and weaker attenuation in the western hemisphere, has been revealed by seismological studies. The understanding of this feature is an important key to give constraint on the physical state and the growth process of the inner core. However, it is not achieved consensus on the transition structure between two hemispheres, because of the difficulty to analyze complex core-sensitive data and the limitation of earthquake and seismic array distribution. We previously developed a waveform inversion based on simulated annealing and analyzed core phase data observed by globally deployed seismic array. Using this approach, we provided continuous depth profiles of velocity and attenuation structures and revealed the presence of intricate heterogeneous structures in the top 300 km of the inner core [1, 2]. In this study, we apply this waveform inversion approach to core phase data sets that propagate beneath the northern Pacific to investigate the nature of the transition structure in this region.

**Data:** Data set used in this study consists of two directional event-station pairs, seismograms observed by permanent European stations for events at Fiji-Tonga region, and USArray for events near Indonesia (Fig. 1). We analyze the broadband vertical component of collected core phase data containing PKIKP and PKP phases (i.e. the epicentral distance between 145 – 155 degree). Each data is filtered by 0.5 – 1.5 Hz bandpass filter. Resultant analyzed waveforms for EU stations and USArray are 2,108 and 1,172 traces respectively.

**Observations:** Waveform inversion based on simulated annealing is employed for each event data to measure traveltime and attenuation in the inner core. As a result, traveltime anomalies observed by EU stations show obvious positive anomaly suggesting mainly propagating the eastern hemisphere, while traveltimes observed by USArray show relatively smaller (or no) anomalies suggesting effects by both of two hemispheres. On the other hand, attenuation parameters for both arrays show similar trend that suggests high attenuation corresponding to the eastern hemisphere.

To investigate a hemispherical transition boundary in sampling region, we conduct a ray theory based forward modeling of traveltime by

changing a shape of boundary from meridian boundary to eyeball shaped boundary, and its position. We compute root-mean-square (RMS) of residual between observations and theoretical traveltimes computed with each boundary model. Then, an eyeball shaped boundary, that is located at longitude of 158°E on the equatorial line and latitude of 80°N at the northernmost point, obtained as the preferred hemispherical boundary, which derives the minimum RMS value. Finally, we investigate a sharpness of the boundary by varying a width of hemispherical transition. We assume linear variation from the eastern and western hemisphere in a given width and compute RMS. As a result, the width of 600 km at the surface of the inner core shows smaller RMS than sharp boundary. The obtained transition structure is shown in Fig. 2.

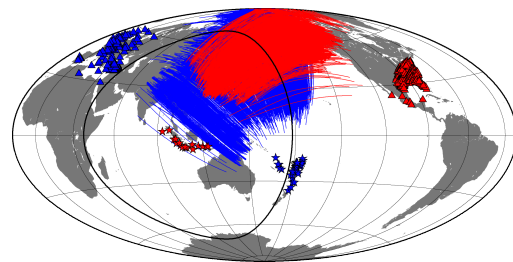


**Figure 1** The distribution of events (star) and stations (triangle), and ray paths propagating in the inner core (solid line). Red and blue denotes the data for EU stations and USArray respectively. Black line is proposed hemispherical boundary in [3].

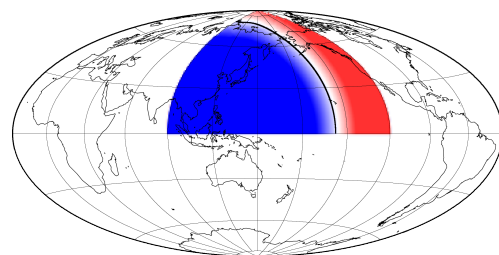


**Figure 2** The preferred hemispherical transition boundary projected on the Earth's surface. The black line is the hemispherical boundary and areas colored by blue and red denote the eastern and western hemisphere.

### References:

- [1] Iritani, R., N. Takeuchi, and H. Kawakatsu, *Phys. Earth Planet. Inter.*, **230**, (2014).
- [2] Iritani, R., N. Takeuchi, and H. Kawakatsu, *Earth Planet. Sci. Lett.*, **405**, (2014).
- [3] Tanaka S., and H. Hamaguchi, *J. Geophys. Res.*, **102**, (1997).

## Sample-scale geochemical variation of the Inada granitic body, Ibaraki, Japan -toward the reduction of geoneutrino flux estimation errors-

Kazuki Minami<sup>1</sup>, Kenta Ueki<sup>2\*</sup>, Tsuyoshi Iizuka<sup>3</sup>, Sanshiro Enomoto<sup>4,5</sup> and Hiroyuki K.M. Tanaka<sup>1</sup>

<sup>1</sup>Earthquake Research Institute, University of Tokyo, Bunkyo-ku, Tokyo 113-0032, Japan.

<sup>2</sup>Department of Solid Earth Geochemistry, Japan Agency for Marine-Earth Science and Technology, Yokosuka 237-0061, Japan.

<sup>3</sup>Department of Earth and Planetary Science, University of Tokyo, Bunkyo-ku, Tokyo 113-0033, Japan.

<sup>4</sup>Kavli Institute for the Physics and Mathematics of the Universe, University of Tokyo, Kashiwa 277-8583, Japan

<sup>5</sup>Department of Physics, University of Washington, Seattle, WA 98195, United States

\*email: kenta\_ueki@jamstec.go.jp

**Introduction:** Geoneutrino observation at anti-neutrino observatory "KamLAND" in Kamioka (Hida City, Gifu Prefecture), is expected to bring us direct information on the abundance of radiogenic elements in the deep earth [1]. As crustal rocks exhibit a higher concentration of geoneutrino producing radiogenic elements (Uranium and thorium) than mantle rocks, it is necessary to subtract the contribution of geoneutrino from the Japanese crust from the observation value in Kamioka to estimate geoneutrino flux from core and mantle. For the purpose, we are developing a 3D compositional map of Japanese crust [2]. Geoneutrino flux calculated using the compositional map exhibits a large error (~ 80%) at present. We found that information on the spatial correlation of the rock chemical composition on various spatial scales such as a single rock suite scale (m to km scale), and outcrop or sample size scale (m-cm) is fundamental to reduce the estimation error of crustal geoneutrino flux as small as the observation error of the neutrino on KamLAND.

**Geological background and Method:** In this study, we present a sample-scale (cm scale) geochemical heterogeneity of a granitic body of Inada, Ibaraki prefecture, Japan. Inada granite is a Cretaceous granite in the Ryoke belt [3].

We collected rock samples from Inada granite, in order to evaluate the variance of chemical compositions in the single rock sample (~500g). Grid sampling was conducted in two quarries in the Inada area. The sample was subdivided into several cubic samples with a weight of about 25g using a diamond saw. Each cubic split was polished on a grinder, rinsed in an ultrasonic bath to avoid surface contamination. Major and some trace

element concentrations of each cubic sample were determined by X-ray fluorescence spectrometer (XRF) at the <sup>1</sup>Earthquake Research Institute, University of Tokyo. Also, we conducted analysis by an ED-XRF at Japan Agency for Marine-Earth Science and Technology to evaluate the mm scale spatial distribution of elements in each split.

**Result:** Wide compositional variations in a single rock sample (~500g) such as 73~77 SiO<sub>2</sub> wt% were observed. Based on the data, we evaluated the relationship between compositional variance and the size of the sample. SiO<sub>2</sub> concentration was positively correlated with the modal concentration of quartz, indicating the granite experienced mm to cm scale geochemical process to derive the heterogeneous distribution of quartz. Our result indicates that, in addition to the kilometer or meter scale variations, cm-scale geochemical variation should be considered to evaluate geochemical variation of granitic rocks. Also, this result will be combined analysis with the geochemical database for the basement rocks of Japanese islands with geographical coordinates [4] to evaluate multi-scale spatial correlations of rock compositions.

**References:** [1] The KamLAND Collaboration, *Nature Geosci.* **4**, 647-651 (2011). [2] Takeuchi, N., Ueki, K., Iizuka, T., Nagao, J., Tanaka, A., Enomoto, S., Shirahata, Y., Watanabe, H., Yamano, M. and Tanaka, H., *Phys. Earth Planet. Int* (2019) in press. [3] Arakawa, Y. and Takahashi, Y. *Contrib. Mineral. Petrol.*, **101**, 46-56 (1989). [4] Haraguchi, S., Ueki, K., Yoshida, K., Kuwatani, T., Mohamed, M., Horiuchi, S. and Iwamori, H., *Jour. Geol. Soc. Japan*, **124**, 1049-1054.

## ***Ab initio* anharmonic lattice dynamics for Fe-bearing lower mantle minerals**

Haruhiko Dekura<sup>1\*</sup> and Taku Tsuchiya<sup>1</sup>

<sup>1</sup>Geodynamics Research Center, Ehime University, Matsuyama, 790-8577, Japan.

\*email:dekura.haruhiko.mf@ehime-u.ac.jp

**Introduction:** Determination of lattice thermal conductivity ( $\kappa_{\text{lat}}$ ) of lower mantle (LM) minerals is a key to understanding the dynamics and evolution of the earth's deep interior. Some recent experimental studies have shown that  $\kappa_{\text{lat}}$  of MgO and MgSiO<sub>3</sub> bridgmanite (Brg) are substantially reduced by Fe incorporation [1-5]. In contrast, Okuda et al. (2017) reported a very different result on Brg with a marginal effect of Fe particularly at high pressure [6]. Besides, the effect of Fe on MgSiO<sub>3</sub> post-perovskite (PPv) has never been reported. Therefore, in this study, we investigate  $\kappa_{\text{lat}}$  of Fe-bearing LM minerals (ferropericlase (FP), Brg, and PPv) in the LM pressure and temperature conditions, based on the *ab initio* anharmonic lattice dynamics techniques.

**Computational Methods:** We performed density-functional theoretic calculations combined with the internally consistent density-functional theory plus *U* technique for more precisely describing the Fe-O bond [7]. The harmonic (HFC) and anharmonic force constants (AFC) were then extracted by numerical derivatives of the adiabatic potential surface. The ferrous iron was treated in the high spin state for Brg and PPv, and the low spin state for FP. Using the HFC and AFC determined in this study, we then calculated the  $\kappa_{\text{lat}}$  of the three phases by fully solving the phonon Boltzmann transport equation describing phonon distribution function in the interacting phonon systems [8].

**Results and Discussion:** Calculations demonstrate strong negative solid solution effects of Fe incorporation on  $\kappa_{\text{lat}}$  of the three phases. Our detailed analysis indicates that the strong Fe effect occurs primarily due to the substantial change in harmonic properties. We found that the calculated  $\kappa_{\text{lat}}$  of FP with ~13% iron at ~100 GPa and 300 K is more than 2 times higher than those reported by DAC experiments with ~10–20% iron [3,4], while the  $\kappa_{\text{lat}}$  of Brg (~6% iron) is found to be lower than the experiment with ~7% iron [5]. The values of  $\kappa_{\text{lat}}$  of Brg and PPv under the lowermost mantle condition is found to be almost the same, and they are ~10-20% of the value of  $\kappa_{\text{lat}}$  of FP. This indicates both the FP and Brg/PPv almost equally contributes to the thermal transport properties of deep LM. The effective conductivity for pyrolytic aggregate is also discussed.

### **References:**

- [1] Manthilake, GM. *et al.*, *Proc Natl Acad Sci USA* **108**, 17901 (2012).
- [2] Goncharov, AF. *et al.*, *Phys Earth Planet Inter* **247**, 11 (2015).
- [3] Ohta, K. *et al.*, *Earth Planet Sci Lett* **465**, 29 (2017).
- [4] Hsieh WP. *et al.*, *Proc Natl Acad Sci USA* **115**, 4099 (2018).
- [5] Hsieh WP. *et al.*, *J Geophys Res Solid Earth* **122**, 4900 (2017).
- [6] Okuda, Y. *et al.*, *Earth Planet Sci Lett* **465**, 29 (2017).
- [7] Tsuchiya, T. and Wang, X. *J. Geophys. Res.* **118**, 83 (2013).
- [8] Dekura, H. and Tsuchiya, T. *Phys. Rev. B* **95**, 184303 (2017).

## Melting phase equilibrium relations in MgSiO<sub>3</sub>-SiO<sub>2</sub> system under high pressures

T. Moriguti<sup>1\*</sup>, A. Yoneda<sup>1</sup>, and E. Ito<sup>1</sup>

<sup>1</sup>Institute for Planetary Materials, Okayama University, Misasa, Tottori 682-0193, Japan.

\*email:moriguti@misasa.okayama-u.ac.jp

Melting of silicates played important roles in chemical differentiation in a deep magma ocean in the early Earth. Therefore, melting relations of the MgO-SiO<sub>2</sub> system have been extensively studied since a pioneer work by Bowen and Anderson [1]. Furthermore, chemical differentiation in the deep magma ocean has been simulated extensively based on results of high pressure melting experiments (e.g. [2] and [3]). However, almost all of these works have been carried out on the compositions ranging from MgO to MgSiO<sub>3</sub>, assuming that the bulk mantle composition is peridotitic or close to that derived from CI chondrite. Recently, enstatite chondrite (E-chondrite) has been attracted as the bulk earth source material [4] because the isotope systematics of the Earth and Moon are nearly identical to those of E-chondrite over O, N, Mo, Re, Os, and Cr. In E-chondrite, the silicate composition is characterized by SiO<sub>2</sub>/(SiO<sub>2</sub>+MgO) = ~0.6, which is substantially higher than that of the peridotitic mantle (~0.4).

In this context, understanding of the melting relations over compositions between MgSiO<sub>3</sub> and SiO<sub>2</sub> is indispensable to clarify the mantle fractionation. That also relates to investigations of chemical compositions of the crust at early stage of the Earth. Nevertheless, there have been very limited works on the pressure effect on melting in the MgSiO<sub>3</sub>-SiO<sub>2</sub> system. Available information regarding phase relations in the system has been so far limited to 5 GPa [5]. In this study, we are determining the melting relations in the MgSiO<sub>3</sub>-SiO<sub>2</sub> system at pressures 5 to 20 GPa. Here we present the results obtained at 10 GPa.

**References:** [1] Bowen and Anderson (1914) *Am. J. Sci.* 4th ser. 37, 487-500. [2] Kato and Kumazawa (1985) *Nature* 316, 803-805. [3] Ito and Katsura (1992) *Am. Geophys. Union Monogr.* 67, 315-322. [4] Javoy et al. (2010) *Earth Planet. Sci. Lett.* 293, 259-268. [5] Dalton and Presnall (1997) *Geochim. Cosmochim. Acta* 61, 2367-2373.

## Pressure effect on IR spectra of anhydrous minerals

M Sakurai<sup>1\*</sup>, N Tsujino<sup>1</sup>, <sup>1</sup>Institute for Planetary Materials, Okayama University, Misasa, Tottori 682-0193, Japan.  
\*email:msakurai@okayama-u.ac.jp

**Introduction:** Water incorporation mechanisms in nominally anhydrous minerals in the Earth's mantle are important to understand effect of water on some physical properties (e.g. rheological properties; [1]; electrical conductivity; [2, 3]). Olivine is the most consistent mineral in the upper mantle can contain small amount of water from a few wt.ppm to a few 1000 wt.ppm (e.g. [4]). Many water incorporation mechanisms of olivine were suggested by experimental studies (e.g. [5, 6]) and theoretical studies (e.g. [7]) and were controversial.

In order to study the role of water, the positions of hydrogen ions in crystal sites should be investigated at first.

**Experimental:** In-situ observations at high pressure were conducted at room temperature up to ~ 7.1 GPa using a diamond-anvil cell (DAC). Diamond-anvils (type IIA) with 600  $\mu\text{m}$  culets were used in all experiments. SUS304 stainless steel plates with 300 or 350  $\mu\text{m}$  in thickness were used for gasket. A 400  $\mu\text{m}$  diameter hole was drilled in a gasket, and was pre-indenting to ~280  $\mu\text{m}$  in thickness, then the holes (sample chamber) in the gaskets were shrunk to ~300  $\mu\text{m}$  in diameter. The starting material was placed in this sample chamber with KBr pressure medium. The semicircular shaped starting material was adopted in this study because it is easy to identify the direction of crystal axis under microscope. Small ruby chips were also inserted in the sample chamber as the pressure markers. After set of the sample assembly, DAC was dried up in vacuum oven (~423 K) over 12 hours to prevent the adsorption of water vapor. The pressure was calculated from the ruby pressure scale based on the shift of the fluorescent peak [8].

FT-IR spectra were obtained from a vacuum-type FT-IR spectrometer (FT-IR-6100 and IRT-5000), equipped with mid-IR light, a KBr beam splitter, and a mercury cadmium telluride (MCT) detector. The degree of vacuum reached to 1Pa to reduce interference by moisture. The samples were analysed with a typically  $75 \times 75 \mu\text{m}$  polarized IR beam parallel to crystal axis. The back ground was measured at space where signals from sample and ruby could be avoided. The IR spectra were obtained by averaging typically 256 scans with  $4 \text{ cm}^{-1}$  resolution.

**Results and Discussion:** In this study, we performed in-situ IR observations at high pressures for forsterite (Fo) single crystals using DAC. At first, we developed in-situ IR observation method at high pressure for low water content of nominally anhydrous minerals in the upper mantle. Using this technique, polarized IR spectra parallel to crystal axis of synthetic hydrous Fo were obtained under high pressure for the first time. First principle calculation (DFT

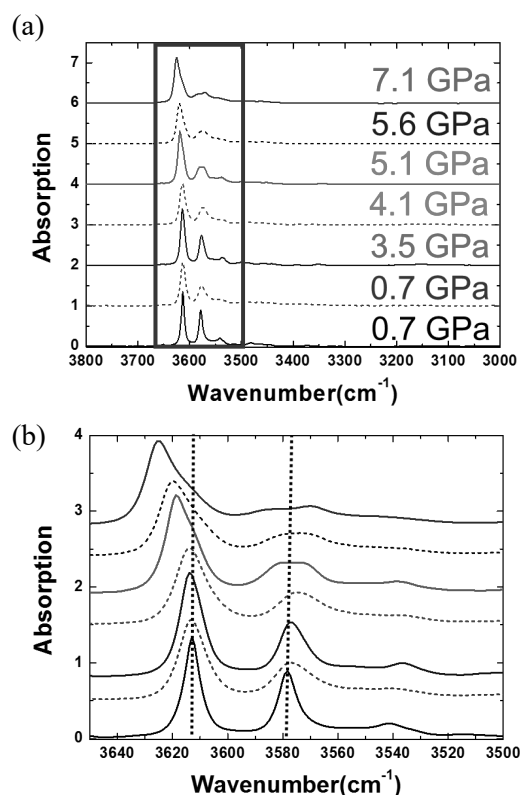


**Figure 1**(a) The pressure effect of polarized absorption IR spectra of synthetic forsterite parallel to a-axis. (b) The enlarged figure of the range of  $3650\text{--}3500 \text{ cm}^{-1}$  in the (a). Vertical positions of the spectra were shifted for a comparison.

calculation) for hydrogen position in Fo was carried out at various pressures. Hydrogen position in Fo was estimated based on the comparison of the vibrational frequencies measured by the FT-IR methods and simulation by the first-principles methods. The band shift observed in experiments under high pressure could be explained by the hydrogen position change in Si Site with pressure calculated by DFT.

**References:** [1] Hirschmann, M., Kohlstedt, D. (2012) *Physics Today*, **65** (3), 40-45. [2] Zang et al. (2012) *Earth Planet. Sci. Lett.*, 357-358, 11-20. [3] Schlechter et al. (2012) *Phys. Chem. Minerals*, **39**, 531-541. [4] Mosenfelder et al. (2006) *Am. Min.*, **91**(2-3), 285-294. [5] Bai, Q., Kohlstedt, D.L. (1993) *Phys. Chem. Minerals*, **19**, 460-471 [6] Berry et al. (2005) *Geology*, **33**(11), 869-872. [7] Umemoto et al. (2011) *Ame. Min.*, **96**, 1475-1479. [8] Mao et al. (1986) *J. Geophys. Res.*, **91**(B5), 4673-4676.

## Deformation experiments on akimotoite

LL Guan<sup>1\*</sup>, D Yamazaki<sup>1</sup> & N Tsujino<sup>1</sup>

<sup>1</sup>Institute for Planetary Materials, Okayama University, Misasa, Tottori 682-0193, Japan.

\*email: guanlongli@s.okayama-u.ac.jp

**Introduction:** The ilmenite structure of  $\text{MgSiO}_3$ , known as akimotoite, is inferred to occur in cold subducting slabs in the bottom of Earth's mantle transition zone and the uppermost lower mantle along a low-temperature geotherm [1]. Akimotoite is thought to be the most anisotropic mineral in the Earth's mantle transition zone [2-3]. The elastic anisotropy caused by the lattice preferred orientation of akimotoite due to slab-induced deformation may be used plausibly to interpret the significant seismic anisotropy observed in mid-mantle (depths 410-670km) [5-8]. However, previous studies did not determine the slip plane or the dominant slip system precisely [9]. Therefore, precisely and detailed lattice preferred orientation of akimotoite is needed. In this study, we conducted deformation experiment to investigate the rheological properties of akimotoite.

**Experimental:** For the preparation of starting material of akimotoite aggregates for deformation experiment, high pressure experiments using  $\text{MgSiO}_3$  glass as starting material, have been performed at 1400 °C, 20-22GPa in the Kawai-type multi-anvil apparatus. The starting material of synthesis experiments was prepared using the following procedures. A mixture of MgO and  $\text{SiO}_2$  with a 1:1 mol ratio was heated in a furnace at 1683°C for 15-45 minutes and quenched to form  $\text{MgSiO}_3$  glass. The glass was powdered in an agate mortar with ethanol for half an hour. We conducted deformation experiment on akimotoite aggregates by using high pressure deformation apparatus, so called D-111 type apparatus installed at Institute for Planetary Materials, Okayama University (Fig.1b). The deformation experiment was performed at 1200 °C, ~21 GPa. Schematic cross-section of cell assembly of pure shear experiments is shown as Fig1a. The original length of akimotoite aggregates was 0.784 mm.

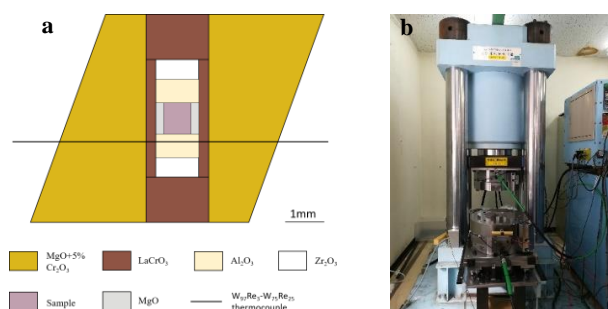


**Figure 1** Schematic cross-sections of cell assemblies of pure shear deformation experiments(a) and photo of D-111 type apparatus installed at Institute for Planetary Materials, Okayama University(b).

**Results and Discussion:** The chemical composition of synthetic glass was analyzed by an electron probe micro-analyzer (EPMA). EPMA mapping showed that Mg and Si were homogeneously distributed in the glass. After synthesis experiments, samples were investigated by X-ray diffraction, electron probe microanalysis and scanning electron microscopy to identify phase, measure

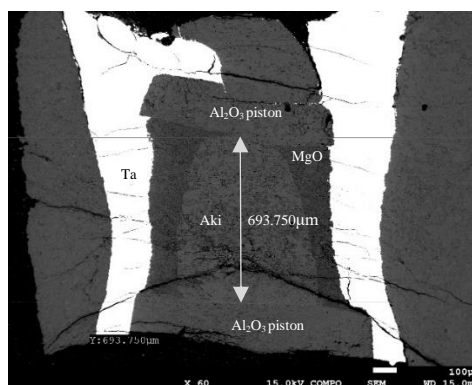


**Figure 2** Scanning Electron Microscope images of the deformed akimotoite aggregates. Sample quenched at ~21 GPa and 1200 °C (run D039).

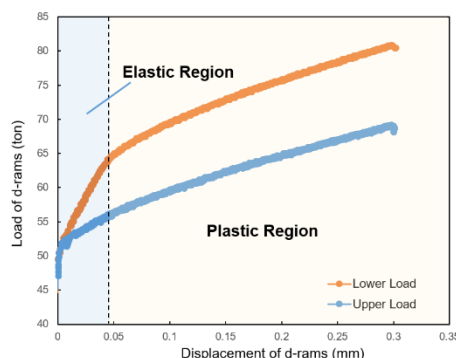


**Figure 3** The relationship between displacement of d-rams and load of d-rams.

chemical composition and observe microstructure, respectively. The recovered sample was well-sintered and no-crack akimotoite aggregates with grain size of 2-8 μm. These akimotoite aggregates were suitable as a starting material for deformation experiments. After deformation, the length of recovered sample was 0.694 mm (Fig 3) with deformation time for 120 min. The strain and average strain rate were estimated to be  $\epsilon \sim 0.12$  and  $\dot{\epsilon} \approx 1.67 \times 10^{-4} \text{ s}^{-1}$ , respectively. Figure 4 shows the relationship between displacement and load of d-rams, suggesting the mechanism change from elastic to plastic deformation with increasing d-ram load (or displacement). Microstructural analysis by using EBSD reveals the lattice preferred orientation pattern and indicates the dominant slip system.

**References:** [1] Akaogi et al., *Phys. Earth Planet. Inter.* 132, 303 (2002). [2] Zhang et al., *Phys. Earth Planet. Inter.* 151, 309 (2005). [3] Weidner & Ito, *Phys. Earth Planet. Inter.* 40, 65 (1985). [4] Wookey et al., *Nature* 415, 777-780 (2002). [5] Nowacki et al., *Geochem. Geophys. Geosys.* 16, 764 (2015). [6] Foley & Long, *Geophys. Res. Lett.* 38, L02303 (2011). [7] Lynner & Long, *Geochem. Geophys. Geosys.* 15, 2262 (2014). [8] Heintz, *J. Geophys. Res.* 111, B09303 (2006). [9] Shiraishi et al., *Nature*, 455, 657 (2008).

## Latest remodeling of multi-axis DAC system for radial XRD experiments

H. Yusa<sup>1\*</sup>, N. Hirao<sup>2</sup>, Y. Mori<sup>3</sup>, and Y. Ohishi<sup>2</sup>

<sup>1</sup>National Institute for Materials Science, Tsukuba, Ibaraki 305-0044, Japan.

<sup>2</sup>Japan Synchrotron Radiation Research Institute (JASRI), Sayo, Hyogo 679-5198, Japan

<sup>3</sup>Department of Applied Science, Okayama University of Science, Okayama 700-0005, Japan

\*email:yusa.hitoshi@nims.go.jp

**Introduction:** Under non-hydrostatic conditions, uniaxial compression causes deviatoric stress in pressurized samples. A radial X-ray diffraction method is one way to solve the deviatoric stress. Several years ago, we have constructed a multi-axis diamond anvil cell (DAC) oscillation system [1] for powder X-ray diffraction experiments to overcome a statistical problem on the analysis from a spotty diffraction pattern taken with a low-emittance synchrotron radiation X-ray. By recent remodeling, the function as a radial X-ray diffraction was added to the multi-axis DAC system [2].

**Experimental:** The multi-axis DAC oscillation system has three axes: horizontal ( $\theta$ ), vertical swivel ( $\omega$ ), and rotating axes ( $\phi$ ) perpendicular to  $\theta$ . The DAC with a laterally large angular aperture ( $70^\circ$ ), which is newly developed for the radial XRD experiments, is inserted into the holder on  $\phi$  axis (Fig. 1). The sample position is adjusted to the center by each axis. The position is remotely controlled with a pulse motor system and the angle was determined by high-precision encoders. The incident X-ray focuses on the sample in a direction perpendicular to compression axis of DAC. A beryllium gasket is used to reduce the diffraction from the gasket materials. The diffracted X-rays are detected with an imaging plate. Since the DAC also has a large aperture ( $70^\circ$ ) in an axis parallel to compression, the oscillating mechanism still works effectively in this system. This system is installed at SPring-8 (BL04B2).

**Results and Discussion:** We tested the system for the radial XRD experiments under uniaxial compression of MgO samples. The sample loaded into the DAC without pressure medium was compressed to 13.8 GPa and subsequently decompressed to ambient pressure. Variation of measured  $d$ -spacing (200) vs. azimuth was plotted in Fig.2. Differential stress was calculated from Singh's method [3]. After the decompression to ambient pressure, residual stress was observed in the sample. Further details will be presented in the poster session.

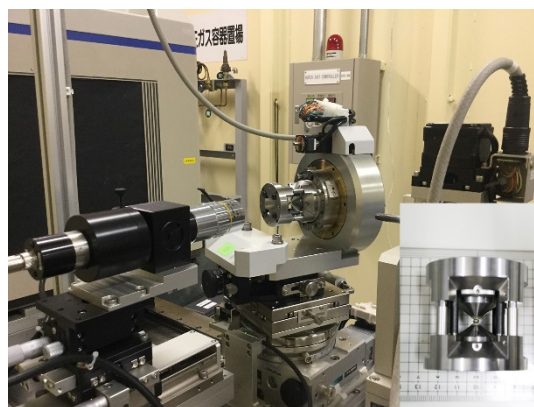


**Figure 1** The multi-axis DAC oscillation system after latest remodeling for radial X-ray diffraction experiments. Inset: The DAC for radial XRD experiments.

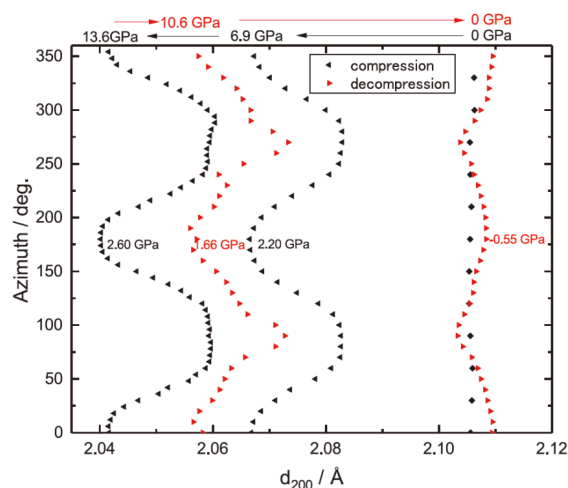


**Figure 2** Variation of  $d$ -spacing (200) of MgO with azimuth under uniaxial compression (black) and decompression (red).

**References:** [1] Yusa, H. Hirao, N. Ohishi, Y. and Mori, Y., *Rev. High Pressure Sci. Technol.*, **21**, 76 (2011). [2] Yusa, Mori, Y. H. Hirao, N. and Ohishi, Y., *Rev. High Pressure Sci. Technol.*, **27**, 220 (2017). [3] Singh, A.K. Balashingh, C. Mao, H.K. Hemley, R. J. and Shu, J., *J. Appl. Phys.*, **83**, 7567 (1998)

## DREAM & Its applications: Software for Management of Samples and Data

Y Yachi<sup>1\*</sup>, T Kunihiro<sup>1</sup>, and E Nakamura<sup>1</sup> <sup>1</sup>Institute for Planetary Materials, Okayama University, Misasa, Tottori 682-0193, Japan.

\*email:yyachi@misasa.okayama-u.ac.jp

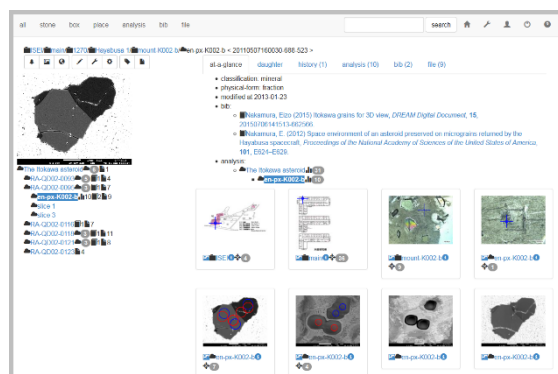


**Figure 1** Visualized sample with DREAM App. The sample is a micrograin returned from the asteroid Itokawa as a part of the Hayabusa mission [3]. DREAM App displays a genetic hierarchy as navigation tree, storage location on floor maps, and analysis spots on surface maps.

It is important to archive samples with data because well-managed samples can be traceable for a long time and reanalyzed with future state-of-art technologies that we cannot even imagine. Institute for Planetary Materials (IPM), Okayama University is constructing DREAM, which is a depository that stores research samples with data to support future research [1], and “DREAM App”, which is a web-based software for sample curation that supports personal and institutional sample and data management [2].

DREAM App allows users to add custom fields to meet the needs for their own sample collection, establish the relationship between an original sample and any sub-samples, track its storage location and weight loss/gain history, correlate any and all geochemical datasets (Figure 1), and show datasets on interactive maps and diagrams (Figure 2). In addition, DREAM App provides a RESTful API to enhance interoperability. With the API, we have developed several client applications. For example, an Android application for sample management registers a new sample at a field site, creates its sub-samples at a laboratory, prints their QR code to label printers, and tracks current locations by just scanning their QR codes. A smart scale for automatic sample weighing updates current weight of a sample by just scanning its QR code with barcode reader. With the application and the smart scale, almost all sample management tasks can be completed with an Android phone or tablet. We also plan to provide a cross platform application, which supports iOS devices such as iPhone and iPad. Furthermore, DREAM App supports seamless sample registration to SESAR (System for Earth

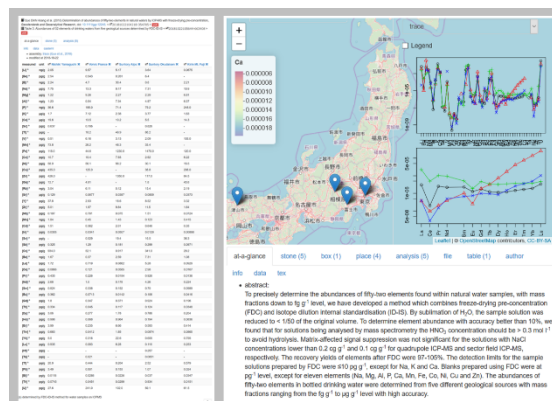


**Figure 2** Data visualization with DREAM App. The visualized data are abundances of 52 elements in natural waters determined by ICP-MS with FDC-ID-IS method [4]. DREAM App displays geochemical data as a formatted table and geochemical diagrams such as spider plot. Sample localities are shown on an interactive map created with Leaflet (javascript library) and OpenStreetMap (tile map service).

Sample Registration) [5], which provides access to the sample catalog via the Global Sample Search, and operates the registry that distributes the International Geo Sample Number (IGSN).

Currently, DREAM stores 21,000 samples, 1,300 places, 4,900 analyses, 650 bibliographies, and 22,000 images. With the seamless sample registration to SESAR, we have obtained IGSNs for 360 samples, which referred in 12 publications. Datasets associated with the publications (500 samples, 260 places, 2,200 analyses, 12 bibliographies, and 600 images) and DREAM App are available at the following URL.

<https://dream.misasa.okayama-u.ac.jp/>

We focus on creating software manuals and user guides to promote the use of our software in any laboratory or institution. In addition, we plan to provide cloud-based sample management software that should help geochemists all over the world manage samples by using the phone in their pocket without IT expert knowledge.

**References:** [1] Kitagawa et al. *Journal of Space Science Informatics Japan*, **3**, 73-77 (2013). [2] Yachi et al. *Geostandards and Geoanalytical Research*, **38**, 95-102, (2013). [3] Nakamura et al. *PNAS*, **101**, E624-E629 (2012). [4] Que et al. *Geostandards and Geoanalytical Research*, **43**, 147-161 (2018). [5] <http://www.geosamples.org/>

## Measurement of thermal conductivity and thermal diffusivity for mantle minerals by the pulse heating method

M Osako<sup>1\*</sup>, A Yoneda<sup>2</sup>

<sup>1</sup>National Museum of Nature and Science, Tsukuba, Ibaraki, 305-0005 Japan, <sup>2</sup>Institute for Planetary Materials, Okayama University, Misasa, Tottori 682-0193, Japan.

\*email:sako@kahaku.go.jp

We have conducted simultaneous measurements of thermal diffusivity and thermal conductivity of mantle minerals under pressure by the plain pulse-heating method in the Kawai-type apparatus at the Institute for planetary materials, Misasa. We adjust the method by Dzhavadov, who measured thermal properties under pressure for a large (20 mm in diameter) specimen, for mantle materials by reducing the size of sample. This method is a predominant one for deep Earth materials because it has some advantages as follows: (1) comparatively small amount of samples compared with other method such that uses cylindrical sample symmetry, (2) applicable to materials with anisotropy in thermal conduction, (3) simple cell assembly. Moreover, this method has potential to obtain specific heat capacity under pressure. We started measurement for upper mantle minerals, olivine and garnet and hydrous phases such as serpentine and talc using a sample of 4.3 mm in diameter and 1mm in length. The pressure range was up to 10 GPa and temperature to 1100 K. In order to extend pressure range, reduction of the sample cell assembly was needed. A new assembly quite similar to our previous one was designed for a sample of 2.6 mm in diameter and 0.6 mm in thickness (Fig. 1). The assembly was installed in an octahedral pressure medium with edges of 14 mm and compressed by anvils with truncated corner of 7 mm (14-7 cell). Test measurements were made using garnet samples (Fig.2). This new cell enables to perform measurements at pressures exceeding 20 GPa, therefore applying to materials of the mantle transition zone. The cell is also applicable to other important minerals, for example, pyroxene, of which specimen has necessarily limited size. A cell assembly of more reduced in size is planned. The coming cell will be used for measurements of MgSiO<sub>3</sub> perovskite (bridgemanite).

Thermal diffusivity or thermal conductivity shows differences among literatures, even though in case of upper-mantle minerals. Measurement of these properties under pressure is indispensable to be performed under considerable approximate conditions due to limited size of the sample. This may cause discrepancies among experimental data. Our measurement by a simple or clear method will settle values of thermal conductivity of thermal diffusivity for the major mantle minerals.

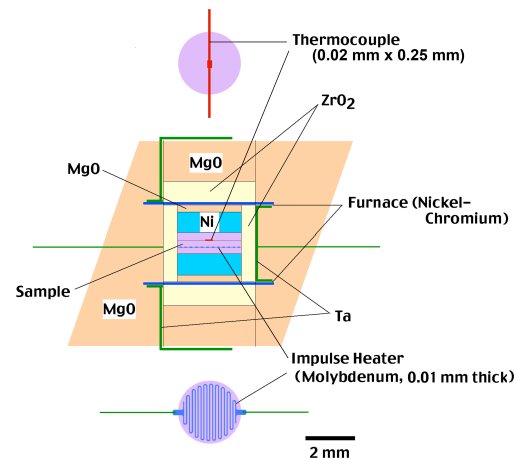


Fig. 1. 14-7 cell assembly for thermal conductivity and thermal diffusivity measurement in the Kawai apparatus (~20GPa). The numeral before the hyphen is edge size of an octahedral pressure medium and after is truncated corner of an anvil.

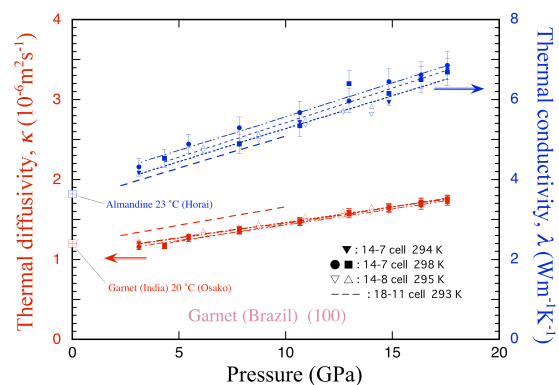


Fig. 2. Thermal conductivity ( $\lambda$ ) and thermal diffusivity ( $\kappa$ ) measurement by various sizes of cell. Errors of  $\lambda$  (ca. 3%) and  $\kappa$  (ca. 2%) come from the uncertainty of heating area, pulse heating power, sample thickness and fitting errors. Systematic errors among runs may come from unexpected deformation and/or displacement in the sample assembly, in particular, at the initial pressurizing; more precise machining of sample preparation is needed to avoid these unfavorable effects.

## References:

- [1] Dzhavadov, L.N., 1995, *High Temp.-High Pressures*, **7**, 49 (1995). [2] Osako, M., E. Ito, A. Yoneda, *Phys. Earth Planet. Inter.*, **143-144**, 311 (2004). [3] Wang, C., A. Yoneda, M. Osako, E. Ito, T. Yoshino, Z. Jin, *J. Geophys. Res.*, **119**, 6277 (2014)

## Low-frequency micro-Raman spectroscopy and its application to mineral sciences

Akira YONEDA<sup>1\*</sup>, Shin-ichiro KOBAYASHI<sup>2</sup>, Seiji KAMADA<sup>3</sup>

<sup>1</sup>Institute for Planetary Materials, Okayama University, Misasa, Tottori 682-0193, Japan.

<sup>2</sup>Department of Earth Science, Graduate school of Science, Tohoku Univ., 6-3, Aoba, Aramaki, Aoba-ku, Sendai, 980-8578

<sup>3</sup>Research Institute for Interdisciplinary Sciences, Tohoku Univ., 6-3, Aoba, Aramaki, Aoba-ku, Sendai, 980-8578

\*email: yoneda@okayama-u.ac.jp

GHz ultrasonic velocity measurements has been developed up to ~15 GPa in diamond anvil cell (DAC). In order for GHz ultrasonic measurement, both P and S wave buffer rods were manufactured through sputtering ZnO piezoelectric film on single crystal rods, such as sapphire, rutile (TiO<sub>2</sub>), and YAG. Several technical breakthroughs have been achieved before observing stable signals from the specimen squeezed in DAC: (1) Wiping by aqueous ammonia on the contact surfaces enhances transmissibility of GHz wave from buffer rod to diamond. (2) Cleaning by lathery detergent and water jet is effective to remove sticky stuff on rear surface of diamond. (3) Steel ball supporter provides easier adjustment of contact between buffer rod and diamond. Consequently, we succeeded to demonstrate performance of GHz-DAC system through measurements on KCl and natural olivine samples.

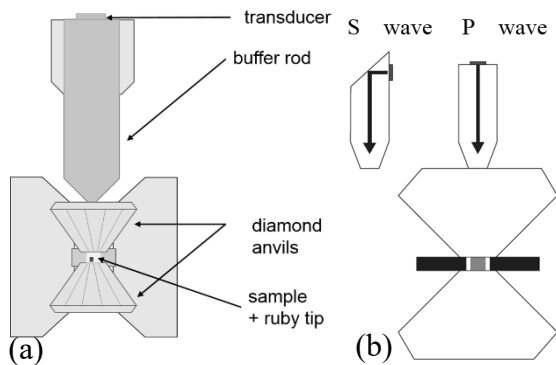


Figure 1. (a) Schematic view of the present GHz-DAC measurement assembly. A ruby tip is shown schematically by black rectangle in the sample cell. (b) Conceptual comparison between P and S wave buffer rods; S wave buffer rod is available by utilizing P-S conversion of ultrasonic wave.

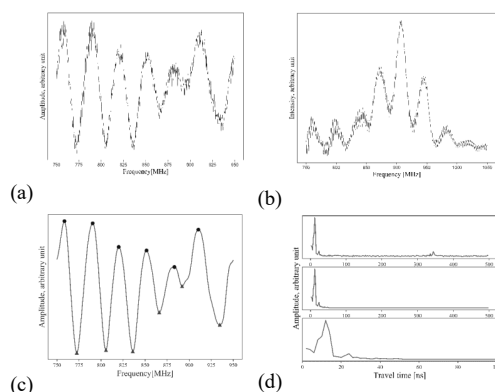


Figure 2. – Amplitude modulation along carrier frequencies. (a) KCl at 1.4 GPa. (b) Natural olivine at 4.5 GPa. (c) Smoothed plot of (a) through Fourier transformation. (d) Fortier coefficients of the raw data of (a). Upper plot is the raw coefficients on data shown in (a). Middle plot shows truncation of longer travel time components. Lower plot is horizontally magnified plot of the middle plot. We can see that coefficients longer than ~50 ns were truncated to be zero.

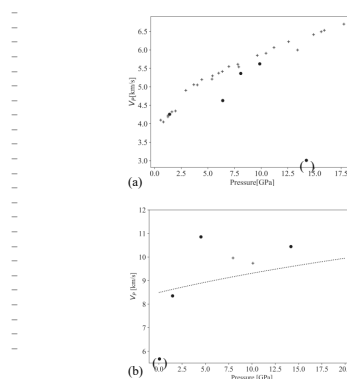


Figure 3. Resulted  $V_P$  of sample. (a) Results on KCl. Present data are shown by solid circle, while those of Campbell and Heinz (1994) by cross shapes. Note that the highest data point in the parenthesis may correspond to measurement of gasket material. (b) Natural olivine. Solid circles and cross shapes indicate data measured under loading and unloading processes. Dotted line shows reference data of Darling et al. (2004). Note that the data point at 0 GPa in the parenthesis may be deviated owing to voids inside specimen.

## High-pressure synthesis of doped black phosphorous

N. Noguchi,<sup>1\*</sup> Y. Fujii,<sup>1</sup> T. Saitoh,<sup>1</sup> and H. Okamura<sup>1</sup>

<sup>1</sup>Graduate School of technology, Industrial and Social Sciences, Tokushima University, Tokushima, Tokushima 770-8506, Japan.

\*email:noguchi.naoki@tokushima-u.ac.jp

**Introduction:** Two-dimensional van der Waals materials are promising fabricated materials for electric components. The nano-sheets made from them by exfoliating are applicable to ultra-compact electronic devices. In particular, phosphorene, which is a single layer of black phosphorus (BP), has two excellent electrical properties derived from the band structure. First, it has a direct band gap of 0.8 eV along with a-axis. Second, the slope of the band dispersion curve promises a high carrier mobility along with the c-axis.

The doping technique to BP is required in order to enhance its designability and stability. It will enable us to control p-n type and the band gap, in addition, increase the resistance to oxidation [1]. We tried to synthesize the single crystals of the doped BP using the piston-cylinder high-pressure apparatus. The high-pressure synthesis method has an advantage which is not in the other methods. The high homogeneity of the dopant elements are achieved by melting starting materials. In this study, we selected three elements: carbon (C), sulfur (S), and palladium (Pd), as dopant.

**Experimental:** The single crystals of doped BP were grown by the gradual solidification method reported in Endo et al. 1982 [2]. Starting materials were molten at about 1000 °C and 1 GPa, and cooled to about 700 °C with a rate of 1 °C/min, and then, were quenched. Powdered red phosphorous mixed with 2-5 wt% the dopant reagent was used as the starting material. Considering high chemical reactivity of molten phosphorus, graphite was used as a sample container. The recovered samples were identified and characterized using by XRD, SEM-EDS, Raman and infrared spectroscopy.

**Results and Discussion:** The single crystals obtained have the maximum size of 500 μm. For the experiments for S- and Pd-doping, their elements were not detected by in BP crystals by energy-dispersive spectroscopy. The shape of the grains of S in the recovered samples shows that the melting occurred, while that of the grains of Pd shows that melting did not occur. For the experiment of C-doping, 5-10 wt% of C element was detected in BP crystals, and was scattered uniformly. The powdered XRD pattern of the C-doped BP was very similar with that of pure BP.

The lattice parameters of C-doped BP matches with that of pure BP within 0.01 Å order [2]. The characteristic Raman bands due to the phonon modes of BP were appeared in the Raman spectra. Their peaks are shifted to 3 ~ 5 cm<sup>-1</sup> compared with the Raman bands of pure BP. The polarized infrared absorption spectra revealed the band gap (Fig.2). The dipole transition between the valence band maximum and the conduction band minimum is allowed for E//c polarization and is forbidden for E//a [3]. The band gap of C-doped BP was 0.341 eV, which is almost same as that of pure-BP (0.335 eV). The situation of the C element in BP has not been revealed yet. There are three possible situations; substitution, adatom, and intercalation. The state analysis such as XPS and XAFS is needed in order to reveal the situation.

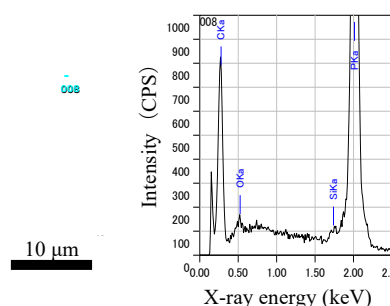


**Figure 1** SEM image (left) and elemental spectrum (right) of C-doped BP crystal.

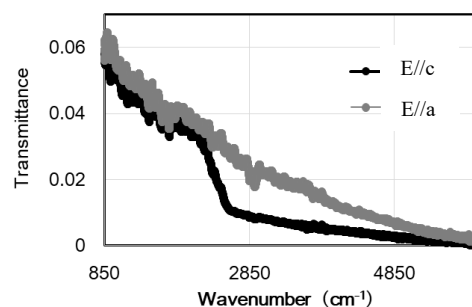


**Figure 2** Polarized infrared absorption spectra of C-doped BP crystal.

**References:** [1] Lv, W. et al., *ACS Appl. Mater. Interfaces*, **10**, 9663 (2018). [2] Endo, S. et al., *J. J. Appl. Phys.*, **21**, L482 (1982). [3] Akahama, Y. and Kawamura H., *Phys. Stat. Sol. b*, **223**, 349 (2001).

## Electrical conductivity of diaspore, $\delta$ -AlOOH and $\epsilon$ -FeOOH

Ran Wang<sup>1\*</sup>, Takashi Yoshino<sup>1</sup>

<sup>1</sup>Institute for Planetary Materials, Okayama University, Misasa, Tottori 682-0193, Japan.

\*email: ranwang@s.okayama-u.ac.jp

**Introduction:** FeOOH and AlOOH are dominant hydrous phases in sedimentary rocks deposited in the sea or lake basins which were considered to be possibly related to the deep water cycle by slab subduction. Therefore, understanding of the electrical conductivity behaviors of these hydrous phases are essential to explore the nature and dynamic process of the Earth's interior.

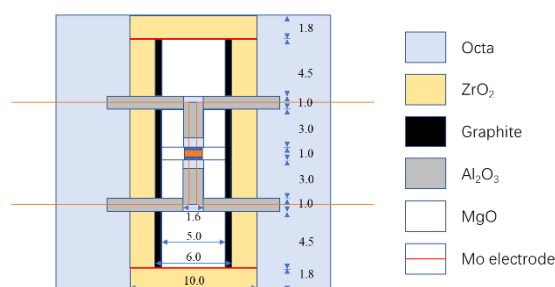


**Figure 1** Cell assembly (25/15) for EC measurement below 8GPa. 25 and 15 represent the lengths of edges of octahedron pressure medium and truncations of tungsten carbide anvils, unit: mm.

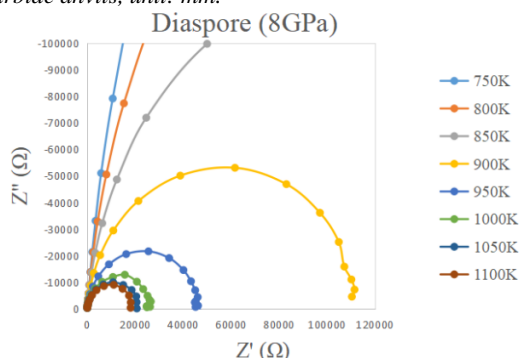


**Figure 2** Impedance spectrum of diaspore at 8GPa.  $Z'$  and  $Z''$  are real and imaginary parts of the impedance, respectively.[1]

**Experimental:** In this study, the powders of a natural single crystal gem-level diaspore ( $\alpha$ -AlOOH)[2] and goethite ( $\alpha$ -FeOOH) were used as the starting material. Diaspore was pre-sintered at 8GPa and 700°C to reduce the porosity before electrical conductivity measurements of diaspore and  $\delta$ -AlOOH was pre-synthesized at 19GPa and 1000°C. The diaspore was kept in a Pt capsule of 2mm diameter. Sintering and synthesis experiments were performed by the 1000ton and 5000ton Kawai-type multianvil apparatus of the Institute for Planetary Materials, Okayama University. Electrical conductivity of diaspore ( $\alpha$ -AlOOH),  $\delta$ -AlOOH and  $\epsilon$ -FeOOH was measured by impedance spectroscopy with a frequency range from 10<sup>-1</sup> to 10<sup>6</sup> Hz at pressures up to 15, 20 and 12 GPa and temperatures of 1200, 1200 and 1000 K well below the dehydration temperatures

of these phases under the relevant pressures. Examples of cell assembly for electrical conductivity measurement and impedance spectroscopy were shown as **Fig 1** and **Fig 2**.

**EC of diaspore,  $\delta$ -AlOOH and  $\epsilon$ -FeOOH**

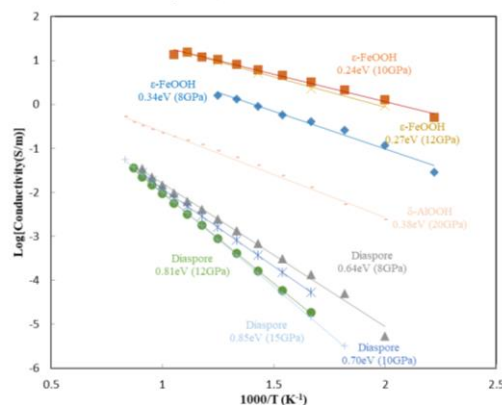


**Figure 3** Electrical conductivity of diaspore,  $\delta$ -AlOOH and  $\epsilon$ -FeOOH as a function of reciprocal temperature.

**Results and Discussion:** **Fig 3** showed the electrical conductivity results of diaspore,  $\delta$ -AlOOH and  $\epsilon$ -FeOOH. For diaspore at 8, 10, and 12 GPa, the relationship between electrical conductivity and reciprocal temperature could be well fitted by the Arrhenius formula:  $\sigma = \sigma_0 \exp[-(\Delta E + P\Delta V)/kT]$  and shows the pre-exponential factor ( $\sigma_0$ ), activation energy ( $\Delta E$ ) and activation volume ( $\Delta V$ ) of  $55.94 \pm 1.16$  S/m,  $0.547 \pm 0.016$  eV and  $1.683 \pm 0.123$  cm<sup>3</sup>/mol, respectively. However, data of diaspore obtained below 6 GPa could not be fitted by the Arrhenius formula, which was thought to be due to the remnant of free water in the sample caused by heating to insufficient temperature to proceed dehydration of interstitial water. Thus, it is quite difficult to measure the electrical conductivity of diaspore at low pressures. The electrical conductivity of diaspore increased with pressures ranging from 8 to 12 GPa by half order of magnitude and then the conductivity change with pressures from 12 to 15 GPa became negligibly small. The dominant conduction mechanism of diaspore is regarded as proton conduction.  $\delta$ -AlOOH and  $\epsilon$ -FeOOH show one and two orders of magnitude higher electrical conductivity than diaspore. Due to isostructural CaCl<sub>2</sub>-type hydroxide structure,  $\delta$ -AlOOH and  $\epsilon$ -FeOOH display the nearly identical activation enthalpy ( $0.384 \pm 0.007$  eV,  $0.330 \pm 0.048$  eV) which is relatively lower than that of diaspore.

### References:

- [1] Yoshino, T., *Surv. Geophys.*, **31**, 163(2010).
- [2] Suzuki, A., *Phys. Chem. Minerals.*, **27**, 689(2000).

## Intrinsic attenuation factor Q of partially molten Fe–S–O system

Chao Liu<sup>1\*</sup>, Takashi Yoshino<sup>1</sup>, Institute for Planetary Materials, Okayama University, Misasa, Tottori 682-0193, Japan.

\*Chaoliu@s.okayama-u.ac.jp

**Introduction:** Heterogeneous seismic structures have been found at the top of the Earth's inner core in terms of attenuation and velocity<sup>1</sup>. The outermost part of the inner core with approximately 30 km thickness shows low attenuation, then attenuation increases beneath this layer<sup>2</sup>. The positive and negative correlations between velocity and attenuation were observed from the uppermost inner core in different areas: Pacific center in the inner core has negative correlation and the rest area has positive correlation<sup>3,4</sup>. In this study, experiments on attenuation of partially molten Fe–S–O system were performed to explain the possibility that could cause seismic anomalies.

**Experimental:** We investigated Fe-S-O system. Sulfur and oxygen are regarded as the representative light element in the Earth's core. Fe samples with 1, 3 and 14 wt. % S were synthesized in piston cylinder apparatus at 900°C and 1 GPa. a small amount of oxygen was included accidentally. In-situ X-ray radiographic observations were performed at the bending magnet beam line BL04B1 at SPring-8. Deformation-DIA press with a facility of cyclic loading was used. This system could produce sinusoidal displacement in a wide range of oscillation periods from 0.2 to 100 s and generating variable amplitudes<sup>5</sup>. Q value characterizing intrinsic attenuation was determined by phase lag of sample strain against the reference material at 1 GPa and up to 1200°C.

**Results and Discussion:** The experimental results show that frequency dependence of attenuation is not remarkable except for a fine grained-sample, whereas decrease of attenuation was found at 1100 and 920°C for Fe- 1 wt. %S and Fe- 14 wt. %S samples, respectively. The attenuation drop would occur with increasing melt fraction. Experiments of Fe-14 wt. %S sample along heating and cooling paths were done to check the influence of grain growth during experiments. Data obtained from both heating and cooling paths show that abrupt change of the attenuation occurred at around 925°C. The Young's modulus calculated from the strain ratio of sample and reference shows strong temperature dependence. An obvious drop occurred between 900 and 980°C in association with the occurrence of partial melting. Relationship between velocity and attenuation anomalies of the Fe–S–O

system shows a positive correlation when melt fraction reaches a certain value. Partial melting could decrease  $Q^{-1}$ , which could explain the relative low attenuation on uppermost 30 km layer throughout the top of the inner core. Combining with the positive correlation between attenuation and velocity, a large amount of partial melting could occur on the uppermost 30 km layer of the rest area except the Pacific hemisphere in the inner core.

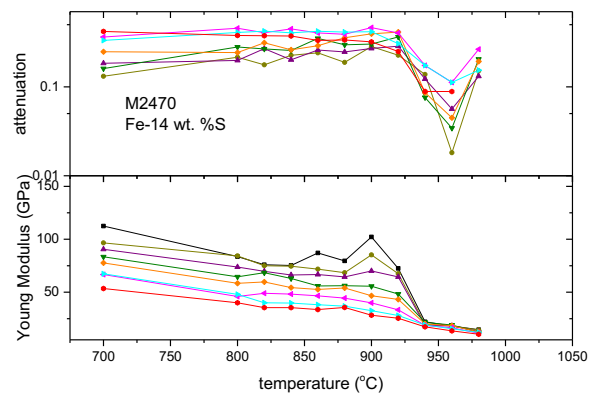


**Figure 1** The experimental results of attenuation and Young Modulus from 14 wt. %S-bearing iron alloy sample measurement.

**References:** 1. Tanaka, S. Depth extent of hemispherical inner core from PKP(DF) and PKP(Cdiff) for equatorial paths. *Phys. Earth Planet. Inter.* 210–211, 50–62 (2012). 2. Ibourichene, A. & Romanowicz, B. Detection of small scale heterogeneities at the Inner Core Boundary. *Phys. Earth Planet. Inter.* 281, 55–67 (2018). 3. Attanayake, J., Cormier, V. F. & Silva, S. M. De. Uppermost inner core seismic structure – new insights from body waveform inversion. *Earth Planet. Sci. Lett.* 385, 49–58 (2014). 4. Godwin, H., Waszek, L. & Deuss, A. Measuring the seismic velocity in the top 15 km of Earth's inner core. *Phys. Earth Planet. Inter.* 274, 158–169 (2018). 5. Yoshino, T., Yamazaki, D., Tange, Y. & Higo, Y. Short-period cyclic loading system for in situ X-ray observation of anelastic properties at high pressure. *Short-period cyclic loading system for in situ X-ray observation of anelastic properties at high pressure.* 105106, (2016).

## Local Organizing Committee

---

- Executive Committee Chairman

Xianyu Xue

- Executive Committee Vice Chairman

Takashi Yoshino

- Program committee

Takashi Yoshino, Xianyu Xue, Takuo Okuchi, Taku Tsuchiya

- Public relations committee

Masami Kanzaki, Shigeru Yamashita, Matthew Izawa

- Location committee

Akira Yoneda, Daisuke Yamazaki, Takuya Moriguti,

Noriyoshi Tsujino, Yusuke Yachi, Hitoshi Gomi, Kaori Anji